2015

Investigation on the promising electrode materials for rechargeable sodium ion batteries

Wei-Jie Li
University of Wollongong, wl347@uowmail.edu.au

UNIVERSITY OF WOLLONGONG

Investigation on the promising electrode materials for rechargeable sodium ion batteries

This thesis is presented as part of the requirements for the Award of the Degree of

Doctor Philoscophy

From

University of Wollongong

By

***Weijie Li*, B. Sc., M.Sc.**

Institute for Superconducting and Electronic Materials (ISEM)

Faculty of Engineering

November 2015

Declaration

I, Weijie Li, declare that this thesis is an original work which was conducted by me using the laboratories at the Institute for Superconducting and Electronic Materials, Faculty of Engineering, University of Wollongong, NSW, Australia, otherwise, I referenced and acknowledged it. In addition, this document has never been submitted to other institutions for qualifications.

Weijie Li

25 November, 2015

Acknowledgements

First of all, the work is supported by the Australian Research Council through a Linkage Project (LP120200432) and Auto CRC 2020, Project 1-111.

I would like to express my deepest gratitude to my supervisors, Dr. Shulei Chou, Prof. Shixue Dou and Prof. JungHo Kim, for their constructive expert supervision for my PHD career. Especially, I also would like to thank Dr. Shulei Chou who also gives me encouragement at the beginning of my PHD career.

I would like to Prof. Huakun Liu and Prof. Jiazhao Wang for their advices and suggestions during the group meeting. I also would like to thank Dr. Tania Silver, who always seriously read every manuscript and polish English during my PHD study.

I would like to express my appreciation to the collaborators, like Dr. Qinfen Gu (Australian Synchrotron), Dr. Jianli Wang (ISEM), Prof. Yong Mook Kang (Dongguk University), who provided important contribution in the my publications during my PHD study.

I would like to thank Dr. Dongqi Shi (ISEM), Dr. Xun Xu (ISEM), Dr. Germanas Peleckis (ISEM), Dr. Tony Romeo (EMC), Dr. Gilberto Casillas-Garcia (EMC)) who gave me much technical assistance over my PhD career. I also thank the university staffs, especially at ISEM, like Ms. Crystal Mahfouz (Administrative Assistant), Ms. Narelle Badger (Administrative Assistant), Ms. Joanne George (Laboratory and Safety Operations Officer), because they gave me lots of administrative assistance.

I also would like to thank my good friends and teammates during my PHD study at ISEM. I would like to express my appreciation to Dr. Jiantie Xu, Dr. Zhijia Zhang, Dr. Shi Yi, Dr. Xuanwen Gao, Dr. Yunxiao Wang, Dr. Xin Liang, Dr. Qi Li, Mr. Jun Wang, Mr. Yuede Pan, Mr. Wenbin Luo, Mr. Rejaul Kaiser, Ms. Qiuran Yang, Ms. Yanfei Xu, Ms. Qiannan Liu, Mr. Zhe Hu, Mr. Mingzhe Chen, Mr. Weihong Lai for their friendness to share their knowledge and experience with me.

Finally, I would like to thank my family, my best friends, and my relatives for their support during my PhD career.

Contents

Abstracts

Renewable energy sources, such as wind and sun, have attracted ever-growing attention due to exhaustion of fossil fuels and environmental concerns. Due to the intermittent nature of the renewable energy, the utilization of these energy sources relies on the availability of large-scale energy storage systems (ESS). In some applications, lithium ion batteries (LIBs) are not suitable candidates because of the low abundance of lithium resources and their high cost. In comparison, sodium is abundant and cheap, and also has similar physical and chemical properties to lithium. Thus, more and more investigations on sodium ion batteries (SIBs) have been emerging in recent years. For the commercial application, the electrode materials need to meet the requirements of non-toxicity, low cost, high specific capacity, and long cycle life. In this doctoral work, promising red phosphorus and Prussian blue analogues were chosen as the objects of study, although their cycling performance is not yet satisfactory. Through reducing the particle size and forming composites with conductive carbon, P/carbon nanotube (CNT) and P/graphene nanoplate (GnP) composites were synthesized. By alloying with other elements, FeP, CoP, and $Sn_{4+x}P_3$@(Sn+P) alloy compounds were prepared. Through optimizing the structure and combining the electrode materials with conductive polyporrole, a series of different Na-enriched $Na_{1+x}FeFe(CN)_6$ and multi-functional polypyrrole coated $Na_{1.72}MnFe(CN)_6$ composites were synthesized, respectively. Moreover, the influences of the morphology and the sodium storage mechanism of these electrode materials were investigated through various characterization techniques, including field emission scanning electron microscopy, transmission electron microscopy, synchrotron X-ray powder diffraction, Mössbauer spectroscopy, Raman spectroscopy, magnetic measurements, thermogravimetric analysis, X-ray photoelectron spectroscopy, and inductively coupled plasma analysis.

Anode material for SIBs

To investigate the reversibility of bulk red P for sodium storage, P/CNT composite was prepared just by simply mixing microsized red phosphorus with CNTs by hand grinding. The thus-prepared P/CNT composite unexpectedly exhibited highly reversible sodium storage. It is concluded that the poor electronic conductivity and huge volume expansion of red P is the main obstacles which inhibit the reversibility and cycling stability of red P. Consequently, we propose two strategies to dissolve these problems in chapter 5-7. One is combination with graphene nanoplate to prepare (P/GnP) composite by the ball-milling method. The particle size was reduced and incorporated in graphene nanoplates, in addition, the phosphorus-

carbon bonds were formed in the P/GnPs composite. This chemical bond improves the electrical connectivity between the P particles and the graphene nanoplates, consequently stabilizing the structure of the composite to achieve high cycling performance and rate capability. As a result, the red phosphorus and graphene nanoplate composite delivered high reversible capacity of 1146 mAh g^{-1} at the current density of 100 mA g^{-1} and excellent cycling stability for 200 cycles with 92.5% capacity retention. Another strategy is forming alloy compounds with active metal element (Sn) or inactive metal element (Fe, Co). As a result, the as-prepared $Sn_{4+x}P_3$ presented a core-shell-like morphology, where the core is the tin phosphide and the shell is the amorphous tin and phosphorus. Such morphology is beneficial to the electrochemical performance. Thus, the composite was denoted as $Sn_{4+x}P_3$@(Sn+P). It showed excellent cycling performance with capacity retention of 92.6% at the current density of 100 mA g^{-1} over 100 cycles. Moreover, the sodium storage mechanism of FeP or CoP was explored by various techiques, it is concluded that the sodium storage mechanism of CoP and FeP involves the reaction of P with Na.

Cathode materials for SIBs

As for Prussian blue cathode, we chose manganese-based $Na_{1.72}MnFe(CN)_6$ (NMHFC) and iron-based $Na_{1+x}FeFe(CN)_6$ as the studied subjects. We utilize the intrinsic oxidation power of the NMHFC, without an external chemical oxidant, to form conducting polymers on the surfaces of NMHFC particles, resulting in improved electronic conductivity, which leads to enhanced cycling performance (67% capacity retention after 200 cycles) and increased rate capability (46% capacity for the 40 C rate). To improve the specific capacity and cycling performance of $NaFeFe(CN)_6$, we optimized its structure by increase the amount of sodium ions per formula unit to reduce the amount of vacancies and coordinating water in the framework. This not only can enhance the cycling stability and the efficiency due to the reduction in the amount of vacancies and crystal water, but also can improve the specific capacity, due to the benefit from more sodium ions entering into the framework. The $Na_{1.56}Fe[Fe(CN)_6]\cdot 3.1H_2O$ (PB-5) sample shows a high specific capacity of more than 100 mAh g^{-1} and excellent capacity retention of 97% over 400 cycles at the 0.2 C rate (20 mA g^{-1}).

List of Abbreviations

Abbreviation	Full name
3D	Three dimensional
a.u.	Arbitrary unit
BET	Brunauer Emmett Teller
cm	Centimeter
mm	Millimeter
nm	Nanometer
CMC	Sodium carboxymethyl cellulose
PAA	Polyacrylic acid
CPE	Constant phase-angle element
CV	Cyclic voltammetry
DEC	Diethyl carbonate
DMC	Dimethyl carbonate
EC	Ethylene carbonate
FEC	Fluoroethylene carbonate
EDS	Energy dispersive x-ray spectroscopy
EIS	Electrochemical impedance spectroscopy
EV	Electric vehicle
FESEM	Field emission scanning electron microscopy
FTIR	Fourier transform inferior red Spectroscopy
JCPDS	Joint committee on powder diffraction standards
HEV	Hybrid electric vehicle
HRTEM	High-resolution transmission electron microscopy
LIB	Lithium-ion battery
SIB	Sodium-ion battery
NMP	1-methyl-2-pyrrolidinone
PPy	Polypyrrole
PVDF	Polyvinylidene fluoride
SAED	Selected area electron diffraction
SEI	Solid electrolyte interphase

SEM	Scanning electron microscopy
FSEM	Field emission scanning electron microscopy
SXRD	Synchrotron X-ray diffraction
TEM	Transmission electron microscopy
STEM	Scanning transmission electron microscopy
PPMS	physical properties measurement system
TGA	Thermogravimetric analysis
XPS	X-ray photoelectron spectroscopy
XRD	X-ray diffraction

List of Symbols

Symbol	**Name**	**Unit**
2θ	Detection angle in XRD	Degree
C-rate	Charged or discharged energies	mA g^{-1}
E_a	Apparent activation energies	kJ mol^{-1}
f	Frequency in the EIS test	Hz
F	Faradic constant = 96485	C
I	Current density	A cm^{-2}
i_0	Exchange currents	A
L	Crystal size	nm
m	Active material weight	g
N	Avogadro's number = 6.022×10^{-23}	mol^{-1}
P	Relative pressure	Pa
P_0	Saturation pressure	Pa
Q	Specific capacity	mAh g^{-1}
Q_c	Specific charge capacity	mAh g^{-1}
Q_d	Specific discharge capacity	mAh g^{-1}
Q_{TSC}	Theoretical specific capacity	mAh g^{-1}

R	Gas constant = 8.319	J K^{-1} mol^{-1}
R_{ct}	Charge transfer resistace	Ω
T	Temperature	K or ℃
t	Time	h or s
W	Warburg impedance	Ω
Z_{im}	Imaginary part of the impedance	Ω
Z_{re}	Real part of the impedance	Ω
σ	Ionic conductivity	S cm^{-1}
η	Coulombic efficiency	%
λ	X-ray wavelength	Å

List of Organizations

Abbreviation	Full time
AIIM	Australian Institute for Innovative Materials
EMC	Electron Microscopy Centre
ISEM	Institute for Superconducting and Electronic Materials
UOW	University of Wollongong
AS	Australian Synchrotron

List of Figures

List of Tables

Chapter 1 Introduction

1.1 General background

The energy crisis and the greenhouse effect have been hot topics worldwide since the 20th century. The fundamental cause of the greenhouse effect is greenhouse gas emissions (GHG), such as CO_2 and CH_4, which are generated by burning fossil fuels for electricity, heat, and transportation. Meanwhile, the excessive utilization of fossil fuels has triggered the energy crisis.[1-4] Thus, the focus of the ever-increasing fuel shortages and the greenhouse effect is the use of fossil fuel, which is motivating us to find sustainable energy sources and make more effective energy savings and emission reductions. Nevertheless, the utilization of various sources of renewable energy, such as solar, wind, and hydropower, is limited by weather and time. Therefore, it is important to rapidly develop an energy storage system (EES) which can integrate the renewable energy into the grid smoothly and effectively.[5-8] At present, there is general agreement that the secondary batteries, among various energy storage technologies, are one of the most promising means for storing electricity on a large scale, due to their flexibility and high energy conversion efficiency. [9-13]

Lithium ion batteries, as one such kind of secondary battery, due to their high energy density, long cycle life, and environmental friendliness, have been generally applied as energy storage device in electric vehicles (EVs), portable devices, mobile phones, etc. Although lithium ion batteries possess many advantages (long cycle life, high energy conversion efficiency, and energy density) which meet the elementary requirements of electrical energy storage (EES), the price of lithium is one point that should be given more consideration from the view of large-scale usage. Recently, the price of lithium has been increasing constantly, owing to the uneven distribution of global lithium reserves, which are often located in remote or politically sensitive areas, and the large consumption associated with the electric vehicle market. Thus, it is crucial to research cheap secondary batteries for EES.[14-38]

In comparison to Li, sodium has abundant natural resources, resulting in its low cost. Moreover, sodium is located below Li in the periodic table, so it possesses similar chemical and physical properties to Li in many aspects. Sodium has a higher redox potential of -2.71 V versus standard hydrogen electrode and lower gravimetric capacity of 1165 mAh g^{-1} compared with lithium (redox potential of -3.01 V and gravimetric capacity of 3829 mAh g^{-1}, respectively).[39-56] This makes the energy density of sodium ion batteries lower than for lithium ion batteries. For the secondary batteries applied in large-scale energy storage

systems, however, this has to be compared with the low cost, so whether the batteries have high energy density becomes less crucial. Therefore, sodium ion batteries are a promising candidate for application in large-scale energy storage systems.

1.2 Challenges for the sodium-ion batteries

Sodium-ion batteries (SIBs) were first investigated for electrochemical energy storage before 1980. Up to the last 10 years, SIBs were becoming one of the hottest research topics for intensive investigations. Many electrode candidates for lithium ion batteries have been tested for sodium ion storage, although their cycling performance, specific capacity, and rate capability are not satisfactory. This is because the ionic radius of Na (0.98 Å) is larger than that of Li (0.76Å), so that the kinetic diffusion and storage mechanisms of Na are different from those of lithium ion batteries (LIBs), causing some problems. For finding cathode materials for SIBs, the challenge is that the intercalation of Na^+ is so difficult compared with Li^+ that the specific energy and power density of SIBs are smaller compared with LIBs. In terms of anode materials for SIBs, there are two main difficulties arising from the bigger ionic radius of Na. One is that the conversion reactions occur at relatively high potentials, eventually resulting in decreases om overall cell voltage, especially in the cases of oxides, fluorides, chlorides, bromides, etc. The other is that the volume expansion is larger than for lithium-based equivalents owing to the bigger ionic radius of Na than that of Li. Usually, these cause mechanical degradation in anode materials, resulting in poor cycle life. Therefore, it is crucial for us to find good new electrode materials with superior energy density for advancing the prospects of SIBs and to enhance their electrochemical properties through the various strategies for controlling the morphology, structure, and size of the particles, and forming composites and compounds. This is not an easy task, however, because most of the sodium-equivalent electrodes are electrochemically inactive; for example, Si cannot store sodium.

1.3 The goals of this work

In this doctoral work, the main goal is to search for promising anode and cathode materials for SIBs with the properties of low cost, long cycle life, and environmental-friendliness. For anode, phosphorus was selected as my research subject due to its low cost, non-toxicity, and high specific capacity. Then, the electrochemical performance of the P-based anode materials has been further improved by forming composites with carbon and preparing alloying compounds. In term of cathode, my main attention has been given to Prussian blue analogues.

Through combining Prussian blue analogues with conductive polymer and optimizing the structure, the cycle life of the Prussian blue cathode materials could be prolonged. Moreover, ex-situ X-ray diffraction (XRD), ex-situ X-ray photoelectron spectroscopy (XPS), ex-situ transmission electron microscopy (TEM), and in-situ XRD have been implemented to investigate the sodium storage mechanisms of these electrode candidate materials.

1.4 Outlines of the thesis

The scope of this doctoral work is briefly summarized below as follows:

Chapter 1 concisely introduces the general background, main challenges, some strategies for enhancing the electrochemical performance of SIBs, and the outline of this study.

Chapter 2 presents a literature review on SIBs, consisting of basic concepts and working principles, electrode materials, and electrolytes.

Chapter 3 presents the chemicals and methods applied to synthesizing electrode materials. This chapter also briefly introduces the characterization methods used to characterize the electrode materials: X-ray diffraction (XRD), synchrotron X-ray diffraction (SXRD), photoelectron spectroscopy (XPS), Raman spectroscopy, thermogravimetric analysis (TGA), scanning electron microscopy (SEM), field emission scanning electron microscopy (FESEM), transmission electron microscopy (TEM), selected area electron diffraction (SAED), energy dispersive X-ray spectroscopy (EDS), Mössbauer spectroscopy, the physical properties measurement system (PPMS), and electrochemical measurements, which include cyclic voltammetry (CV), galvanostatic charge-discharge cycling, and electrochemical impedance spectroscopy (EIS).

Chapter 4 discusses the electrochemical reversibility of commercial microsized red phosphorus in sodium ion batteries. Through simply mixing microsized red phosphorus with carbon nanotubes (CNTs) by hand grinding, highly reversible sodium storage was unexpectedly achieved. The P/CNT composite delivered an initial discharge capacity of 2210 mAh g^{-1}, and 76.6 % of the initial reversible capacity still remained after 10 cycles. CNTs play a crucial role in the reversibility of the P/CNT composite. The network structure of the CNTs serves to effectively buffer the enormous stresses from the volume expansion of the P particles and reduces the rate of pulverization of particles. On the other hand, the CNT network provides pathways for electron transport, which is helpful for maintaining the connections not only between the red phosphorus particles, but also between the red phosphorus and the current collector.

Chapter 5 further improves the cycling performance of red phosphorus, by reducing its particle size and incorporating it with graphene nanoplates. Cheap red P and natural graphite were selected as the starting materials here, and the red phosphorus and graphene nanoplates composite were prepared via a simple and scalable ball-milling method. The phosphorus-carbon bond formed during the milling process improves the electrical connectivity between the P particles and graphene nanoplates, and consequently stabilizes the structure of the composite to achieve high cycling performance and rate capability. As a result, the red phosphorus and graphene nanoplate composite delivered high reversible capacity of 1146 mAh g^{-1} at the current density of 100 mA g^{-1} and an excellent cycling stability of 200 cycles with 92.5% capacity retention.

Chapter 6 presents the electrochemical performance of a novel tin phosphide − $Sn_{4+x}P_3$, which contains the active metal Sn. The as-prepared $Sn_{4+x}P_3$ presents a core-shell-like morphology, where the core is the tin phosphide and the shell is the amorphous tin and phosphorus. Such a morphology is beneficial to the electrochemical performance. Then, the composite was denoted as $Sn_{4+x}P_3$@(Sn+P). It showed excellent cycling performance with capacity retention of 92.6% at the current density of 100 mA g^{-1} over 100 cycles. Moreover, the $Sn_{4+x}P_3$@(Sn+P) electrode exhibited superior high rate capability, with a stable capacity of 165 mAh g^{-1} at the 10 C-rate (5000 mA g^{-1}).

Chapter 7 reports a novel, nanosized FeP and CoP particles, which contain inactive metal Fe and Co. It was synthesized by the ball-milling method for sodium ion batteries. It delivered a high capacity of 764.7 and 770 mAh g^{-1}, respectively. Through ex-situ XRD, XPS and TEM, the sodium storage mechanism of FeP and CoP was explored.

Chapter 8 presents a facile, one-step, soft chemistry approach to the synthesis of ClO_4^- doped polypyrrole-coated $Na_{1.72}MnFe(CN)_6$ composite as a cathode material (NMHFC@PPy) for SIBs. PPy plays multiple important roles in the composite. First, PPy acts as a conductive coating layer, which can increase the electronic conductivity of NMHFC to improve the rate capability. Second, PPy can act as a protective layer to reduce the dissolution of Mn into the electrolyte to improve the cycling performance. Finally, the PPy doped with ClO_4^- can act as an active material to increase the capacity of the composite. As a result, NMHFC@PPy shows high energy density (428 Wh kg^{-1}), enhanced cycling performance (67% capacity retention after 200 cycles), and excellent rate capacity (46% capacity for the 40 C rate).

Chapter 9 reports a series of different Na-enriched $Na_{1+x}FeFe(CN)_6$ samples synthesized by a facile one-step method which utilizes $Na_4Fe(CN)_6$ as the precursor in different concentrations

of NaCl solution. In this method, more sodium ions enter into the framework, which not only can effectively reduce the amount of vacancies and coordinating water, but also can increase the amount of sodium ions per formula unit. As a result, this material not only can enhance the cycling stability and the efficiency, due to the reduction in the amount of vacancies and crystal water, but also can improve the specific capacity, due to the benefit from more sodium ions entering into the framework. The $Na_{1.56}Fe[Fe(CN)_6]\cdot 3.1H_2O$ (PB-5) sample shows a high specific capacity of more than 100 mAh g^{-1} and excellent capacity retention of 97% over 400 cycles. Moreover, through various characterization techniques including synchrotron X-ray powder diffraction (S-XRD), Mössbauer spectroscopy, Raman spectroscopy, magnetic measurements, thermogravimetric analysis, X-ray photoelectron spectroscopy, and inductively coupled plasma analysis, the structure of the as-prepared $Na_{1+x}FeFe(CN)_6$ samples was determined.

Chapter 10 summarizes the overall doctoral work and provides the outlook for further research work on the phosphorus-based anode and Prussian blue cathode materials.

Chapter 2. Literature Review

2.1 Development history of the sodium ion batteries

Historically, battery development can be traced to the invention of the Leyden jar, which can store electric charge, in the city of Leyden in the Netherlands in 1745. Ewald George von Kleist used a set of Leyden jars connected in series to establish a high voltage. From then on, a series of similar devices connected more tightly was called a *battery*. In 1800, Volta, an Italian physics professor, built the first liquid-electrolyte battery in which alternating zinc and copper disks were separated by cardboard and soaked in salt water. In the next 200 years, battery technology developed rapidly. In 1859, Gaston Planté, a French physicist, first developed the rechargeable lead-sulfuric acid battery. In 1899, Jungner invented the nickel-cadmium battery, and then nickel-iron batteries appeared in 1901. In the next 60 years, many researchers worked on studies of rechargeable batteries. In the 1960s, researchers at the Ford Motor Co. developed high-temperature Na-S batteries, in which the electrodes held at 300 ℃ are liquid sodium and sulphur separated by a ceramic electrolyte (β-alumina), sparking investigations into the field of ion transport for energy storage. Subsequently, NGK INSULATORS, LTD. (NGK) and the Tokyo Electric Power Co. (TEPCO), two Japanese companies, worked together on the development of the sodium-sulfur battery, and then, NGK started to produce it on a large scale for commercial application in April 2003. Then, the high-temperature Na-S batteries were rapidly extended to application for emergency power, combined emergency power and loading levelling, and electric transmission and distribution system support.

The first studies of Li ions as charge carriers for electrochemical energy storage took place in the 1970s. TiS_2 was first proposed for electrochemical lithium insertion and application in energy storage devices at room temperature. At nearly the same time, it was reported that TiS_2 could intercalate sodium ions in a highly reversible manner and could be used for electrochemical energy storage at ambient temperature. In 1980, $LiCoO_2$, a lithium-containing layered oxide, was developed by Goodenough as a positive electrode material for lithium storage, and it is still widely used as high energy positive electrode material in commercial lithium ion batteries even now. Meanwhile, the sodium containing layered oxides, Na_xCoO_2, were also reported as positive electrode for sodium ion storage. In the following 20 years, however, the studies of room-temperature sodium ion batteries were almost suspended, while the development of the lithium ion battery (LIB) proceeded ceaselessly from the

production of commercial lithium ion batteries by the Sony Co. in 1991. Three important developments played a vital role in the commercialization of lithium ion batteries: the discovery of the $LiCoO_2$ cathode by John Goodenough (1980), the discovery of the graphite anode by Rachid Yazami (1982), and the rechargeable lithium battery prototype produced by Asahi Chemical, Japan. Sony commercialized the lithium ion battery in 1991. Afterwards, research on lithium ion batteries became a hot topic.[57] The series of developments of secondary batteries is summarized in Figure 2.1.

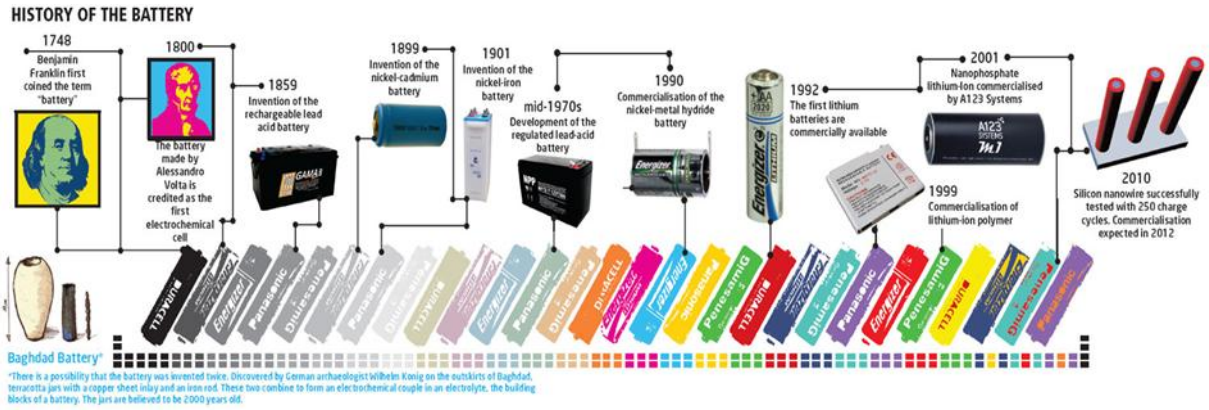

Figure 2.1. Schematic representation of battery development over the centuries.[57]

In 2000, investigations on sodium ion batteries (SIBs or NIBs) came back into researchers' view again. Stevens and Dahn reported that hard carbon can deliver a high reversible capacity of 300 mAh g^{-1} for sodium ion storage, close to that for lithium insertion into graphitic carbon, although its cycle life was not satisfactory for battery applications at that time. Hard carbon is now extensively investigated as a promising anode candidate for SIBs.[58] It was another important discovery for room-temperature sodium ion batteries that $NaFeO_2$ was reported to be electrochemically active for sodium ion insertion in 2009, based on the redox couple of Fe^{3+}/Fe^{4+}.[59] It is utilization of the Fe^{3+}/Fe^{4+} redox couple that is playing an important role in developing high-energy and cost-effective SIBs for the future. The studies of SIBs dramatically increased in recent year after 2010, which can be demonstrated from the number of publication on SIBs, as shown in Figure 2.2.

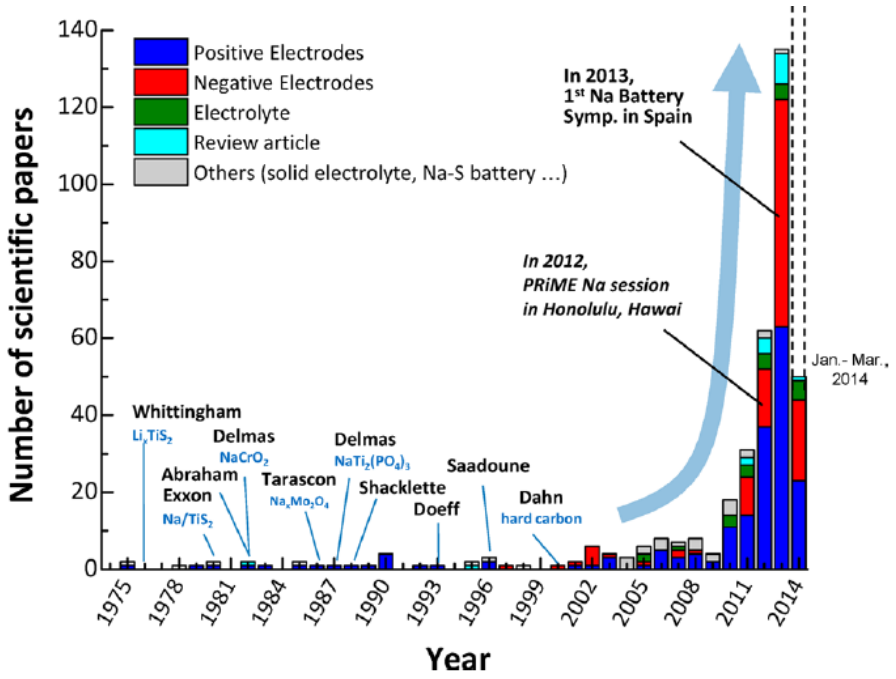

Figure 2.2. Numbers of publications related to sodium for energy storage devices that were published in the past three decades. (The number in 2014 is limited to the articles published from January to March.) [60]

The sodium ion batteries are a major topic of research, owing to the ever-increasing worldwide demand for large-scale batteries for energy storage systems. In terms of large-scale application, the lithium ion batteries are not suitable because their price is very high, resulting from the uneven distribution of lithium reserve around the world and increasing consumption. Sodium, however, is relatively cheap due to its abundant reserves in the Earth's crust, in comparison with lithium. Moreover, sodium is located below Li in the periodic table and possesses similar chemical and physical properties to Li in many aspects, as presented in Table 2.1. Sodium has a higher redox potential of -2.71V versus standard hydrogen electrode and lower gravimetric capacity of 1165 mAh g^{-1} compared with lithium (redox potential of -3.01V and gravimetric capacity of 3829 mAh g^{-1}, respectively). In addition, compared with the expensive copper used as current collector for Li-ion battery anodes, a cheap Al can be utilized as the current collector for the anode in Na-ion batteries because Al does not reaction with Na, which can bring about 8 % cost reduction. A slight cost reduction is also expected to be achieved by replacing Li salts with Na salts in the electrolyte. Figure 2.3 displays the comparison of the manufacturing costs for Li-ion batteries and Na-ion batteries, assuming that they deliver the same energy density. It demonstrates that Na-ion batteries are probably about 10 % less expensive in total cost than commercial Li ion batteries, Up to now, the

electrodes investigated for sodium ion batteries have shown lower energy density than lithium ion batteries. Even so, as secondary batteries are applied in the large-scale energy storage systems, compared with the low cost, the question of whether the batteries have high energy density becomes less crucial. Therefore, sodium ion batteries are considered as a promising candidate for application in large-scale energy storage systems.[61-75]

Table 2.1 Sodium versus Lithium characteristics.[44]

Category	**Lithium**	**Sodium**
Cation radius	0.76	1.06
Atomic weight (g mol^{-1})	6.9	23
Eo (vs. Li/Li^+, V)	0	0.3
Cost, carbonates	$5000/ton	$150/ton
Capacity (mAh g^{-1}), metal	3829	1165
Coordination preference	Octahedral and tetrahedral	Octahedral and prismatic

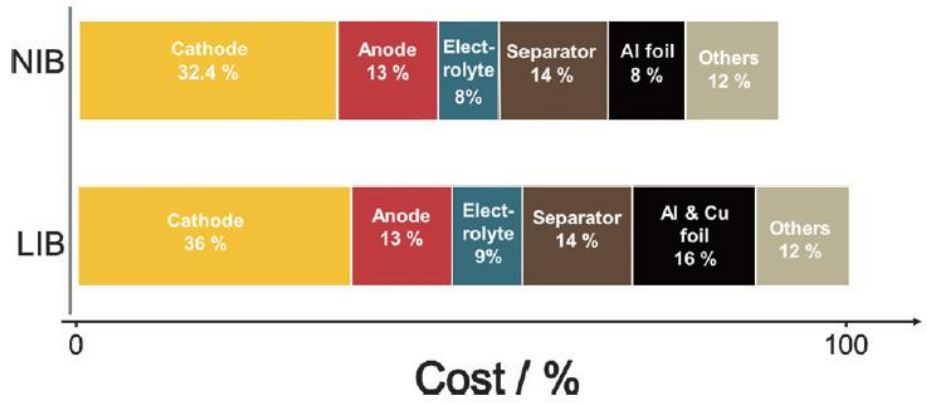

Figure 2.3. comparison of the manufacturing costs for Li-ion batteries and Na-ion batteries.[76]

2.2 Working principle of sodium ion batteries

The configuration of sodium ion batteries is similar to that of lithium ion batteries, including the anode (negative electrode), the cathode (positive electrode), the electrolyte with sodium salt, and the separator. The fundamental working principles of sodium ion batteries are shown in Figure 2.4. When the battery cell is discharged, the electrons are released from the anode, causing the oxidative chemical reactions there, and transferred through the external circuit to the cathode, where the reductive chemical reactions occur. During the process of charging, the active pathways of electrons are reversed. Na^+ functions as the charge carrier which

shuttle from anode to cathode. The electrolyte has high ionic conductivity and low electrical conductivity, acting as an insulator for the electrons and playing the role of transport medium between the cathode and anode for the alkali ions. The separator is a physical barrier located between the cathode and anode to prevent direct contact but allow the ions to freely shuttle through it.

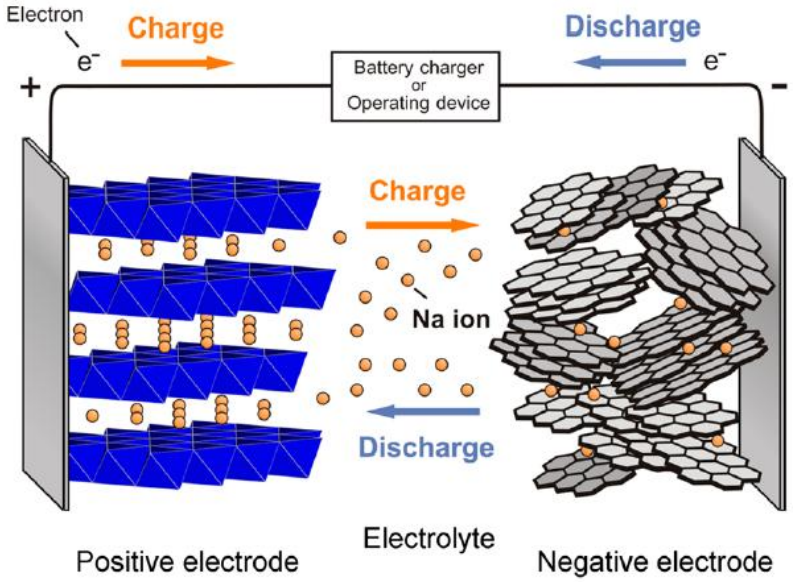

Figure 2.4. Schematic illustration of Na-ion batteries[60]

2.3 Fundamental concepts of sodium ion batteries

2.3.1 Active materials

The materials which can take part in chemical reactions in the battery and generate electrical current at the same time are called “active materials”.

2.3.2. Cathode

The cathode is the positively charged terminal of a storage battery that supplies current.

2.3.3 Anode

The anode is the negatively charged terminal of a storage battery that supplies current.

2.3.4 Binder

Generally speaking, the binder is an organic material which conglutinates the active materials and the conductive agent (*e.g.*, carbon black) on the metal current collector.

Currently, the common binders can be divided into two kinds - organic and water based binders, according to whether their solvents are organic.

(1) Organic-based binder, such as polyvinylidene difluoride (PVDF), which has been successfully applied in commercial lithium ion batteries. The significant advantage of

PVDF is its large anodic-cathodic stability widow at room temperature (0 − 5 V vs. Li^+/Li, 0−4.7 V vs. Na^+/Na). This binder also has some shortcomings, however, such as, hard decomposition and lack of environmental friendliness caused by its solvent (N-methyl-2-pyrrolidone (NMP)).

(2) Water-based binder. The most important advantage of this kind of binder is its cheaper cost and greater environmental friendliness. The binders of this kind that are commonly used are carboxymethyl cellulose,[77-90] alginate,[79] poly(acrylic acid),[78,90] polyvinyl alcohol,[86,91,92] etc.

2.3.5 Electrolyte

The electrolyte is a transport medium between the cathode and anode, which ensures that alkali ions are effectively transported. It also possesses the feature of electronic insulation. The electrolyte has an important influence on the electrochemical performance and safety of the battery.

2.3.6 Separator

The separator is an insulated and porous polymer or inorganic composite membrane which is placed between the cathode and anode. In liquid electrolyte batteries, it plays the crucial role of preventing direct contact between the cathode and anode while allowing the ions to freely shuttle through it. Its properties significantly determine the performance and safety of the battery, even though the separator itself participates in no electrochemical reactions.

2.3.7 Voltage

(1) Open circuit voltage (OCV)

Open circuit voltage (abbreviated as OCV or V_{OC}) is the difference in electrical potential between the cathode and anode of a battery when there is no current flow transferred through the cell.

(2) Working Voltage

The working voltage of the cell is the difference in electrical potential that is measured when there is current flowing through the circuit. It is determined by the following equation:

$$V = V_{oc} - RI \quad (2.1),$$

Where R is the internal resistance of the battery cell and I is the working current in the circuit.

2.3.8 Capacity (Q)

Capacity (Q) is the total amount of charge which the electrode provides for participation in the redox reactions during the charge/discharge process of the cell. The capacity can be calculated by the following equation:

$$Q = \int_{t1}^{t2} I(t)dt = nzF \quad (2.2),$$

where *I(t)* is the current, *t* is the time, *n* is the number of the ions (mol), *z* is the valence of the ions, and *F* is the Faraday constant (96485 C mol^{-1}).

(1) Specific capacity

The specific capacity is the capacity calculated based on the per unit weight of the active material, per unit density of the active material, or per unit area of the active material. Correspondingly, it can be described in terms of gravimetric specific capacity (ampere hour per kilogram; Ah g^{-1}), volumetric specific capacity (ampere hour per liter; Ah L^{-1}), and superficial specific capacity (ampere hour per square meter; Ah m^{-2}).

(2) Specific charge and specific discharge capacity

The specific charge or discharge capacity (Q_c or Q_d, mAh g^{-1}) is the amount of charge transferred and is calculated based on per unit weight of the active material during the process of charging or discharging. The equation is listed as follows:

$$Q_c(or\ Q_d) = \frac{\int_{t1}^{t2} I(t)dt}{m} \quad (2.3)$$

Where *I(t)* is the current (A), *t* is the time (h), and *m* (g) is the mass of active materials.

(3) Theoretical specific capacity (Q_{TSC})

The theoretical specific capacity (Q_{TSC}, mAh g^{-1}) is the capacity calculated from the following equation:

$$Q_{TSC} = \frac{1000 \times F \times n}{M \times 3600} \quad (2.4)$$

$$\text{or } Q_{TSC} = 26.8 \times \frac{n \times 1000}{M} \quad (2.5)$$

Where *n* is the number of moles of electrons participating in the electrochemical reaction, *F* is the Faraday constant (96485 C mol^{-1}), and *M* is the molar mass of the active materials.

(4) Irreversible capacity

Irreversible capacity is the difference between charge capacity (Q_c) and discharge capacity (Q_d) after each cycle, and is used to evaluate how much capacity is lost during each cycle.

For anode materials:

$$\text{Irreversible capacity} = Q_d - Q_c \quad (2.6)$$

For cathode materials:

$$\text{Irreversible capacity} = Q_c - Q_d \quad (2.7)$$

2.3.9 Capacity retention

The capacity retention is the ratio of charge or discharge capacity of a later cycle to a previous one.

Capacity retention = ($n^{th}Q_d/m^{th}Q_d$) × 100% or ($n^{th}Q_c/m^{th}Q_c$) × 100% ($n > m$) (2.8)

2.3.6 Coulombic efficiency (η)

The coulombic efficiency (η) is the ratio of the output of charge to the input of charge for a secondary battery, which can be expressed by the following equation

$$\eta = \frac{n_{th}Q_d}{n_{th}Q_c} \times 100\% \quad (2.9)$$

2.3.10 Discharging

Discharging is the operation in which the secondary battery outputs electrical energy to an external load.

2.3.11 Charging

Charging is the operation in which the secondary battery puts energy into the cell by forcing an electric current through it.

2.3.12 Rate capability

Rate capability, also called the C-rate, is generally used to evaluate the transfer speed of alkali ions when the battery is charged or discharged. 1 C means that the time for the battery to be completely charged or discharged is 1 h. 5 C means that the time for the battery to be completely charged or discharged is 0.2 h.

2.3.13 Charge-transfer resistance

Charge-transfer resistance (R_{ct}), as an important parameter of a battery, is used to quantitatively evaluate the speed of an electrochemical reaction on the electrode. Generally, when the charge-transfer resistance is larger, the electrochemical reaction is slower. The R_{ct} can be calculated from electrochemical impedance spectroscopy (EIS).

2.3.14 Specific energy density (*SED*)

Specific energy density (*SED*) is the amount of energy (Wh) stored in a given system per unit mass (m, kg) or volume (V, L), and can be calculated as follows:

$$SED(mass) = E \times Q \quad (2.10)$$

$$SED(volume) = \frac{E \times Q \times m}{V} \quad (2.11)$$

Where E is the voltage (V), Q is the specific capacity (Ah kg^{-1}), m is the weight of the cell (kg), and V is the volume of the cell (L).

2.3.15 Specific power density (*SPD*)

Specific power density (*SPD*) is used to characterize the ability of the battery to deliver power, and can be calculated as follows:

$$SPD(mass) = \frac{SED(mass)}{t} \quad (2.12)$$

$$SPD(volume) = \frac{SED(volume)}{t} \quad (2.13)$$

2.4 Current cathode materials for sodium ion batteries

For a full battery cell, the cathode plays a crucial role in both the electrochemical performance and the total cost of the advanced commercial SIBs needed to meet the demands of a large-scale energy storage system. It is a fact that the energy density and rate capability of a full cell are mainly limited by the theoretical capacity and thermodynamics of the cathode material in the present sodium ion battery technology. Moreover, it was reported that the cost of the cathode materials accounts for ~32% of the total cost of a battery,[76] more than twice that of the anode, in a typical SIB cell including cathode and anode electrodes, current collectors, electrolyte, and binders. Therefore, it is very important to develop promising cathode materials for the current SIB technology. Figure 2.5 shows the recent reported electrode materials for SIB. In the following text, I classify these current cathode materials into six groups that I will introduce in detail: Layered transition metal (TM) oxides, Phosphates, Pyrophosphates and mixed polyanions, Fluorides, Hexacyanoferrates, and Organic compounds.

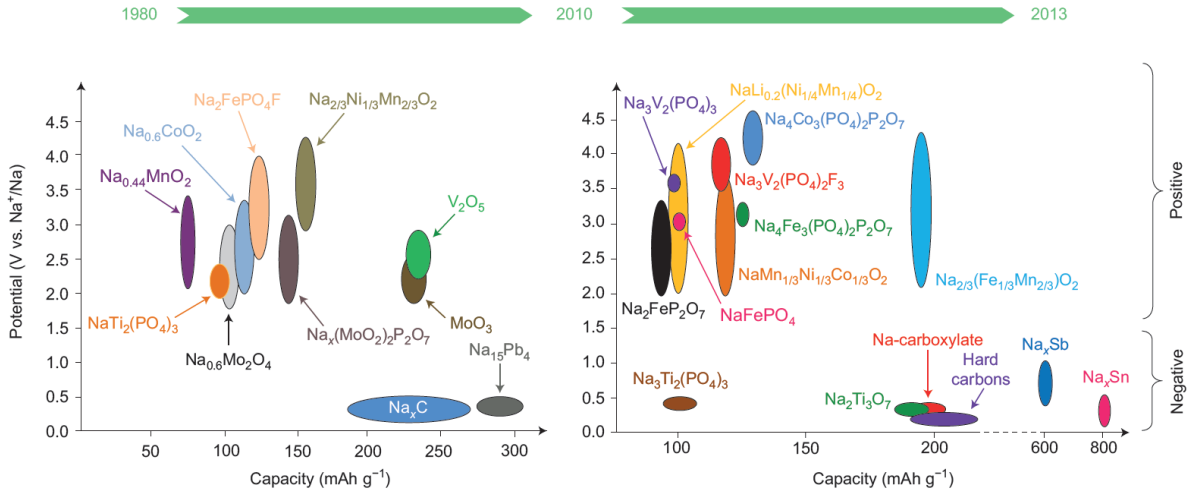

Figure 2.5. Recent reported electrode materials for sodium-based batteries. Voltage versus capacity for reported positive and negative electrode materials with plausible application in Na-ion cells within the past three decades and as studied during the past three years.[93]

2.4.1 Sodium transition metal (TM) oxides

2.4.1.1 Layered transition metal (TM) oxides

Delmas et al. proposed that the layered transition metal oxides are built by a stacking arrangement in which the alkali ions are stacked between layers which are constituted by sheets of edge-sharing MO_6 octahedra.[94] Accordingly, the sodium layered oxide compounds

(Na_xMO_2, M = transition metal) can be classified into two major groups: the O3 and P2 types (Figure 2.6(a) and (b)). The letter O or P refers to octahedral or prismatic sites occupied by alkali ions; the number 3 or 2 represents the number of transition metal layers in the repeated stacking unit perpendicular to the layering. O′3 and P′2 refer to the monoclinic distortion of O3 and P2 phase packing. The clear difference between the O3 and P2 type in the X-ray diffraction (XRD) patterns is shown in Figure 2.7.

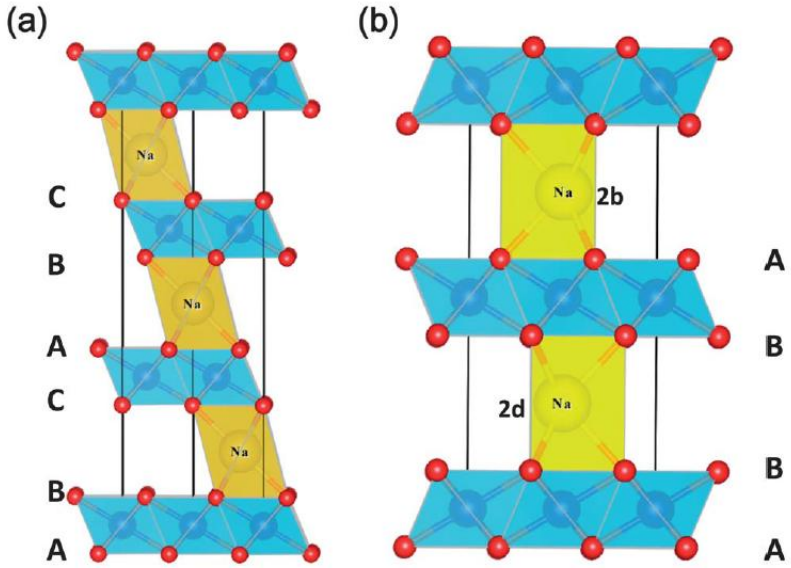

Figure 2.6. The stacking types of (a) O3 and (b) P2 phases in A_xMO_{2+y}. In particular, in the P2-structure, there are two different sites for Na ions. One occupies the 2d site sharing the edges with MO_6 octahedral whereas the other occupies the 2b site sharing two faces with the MO_6 octahedra.[95]

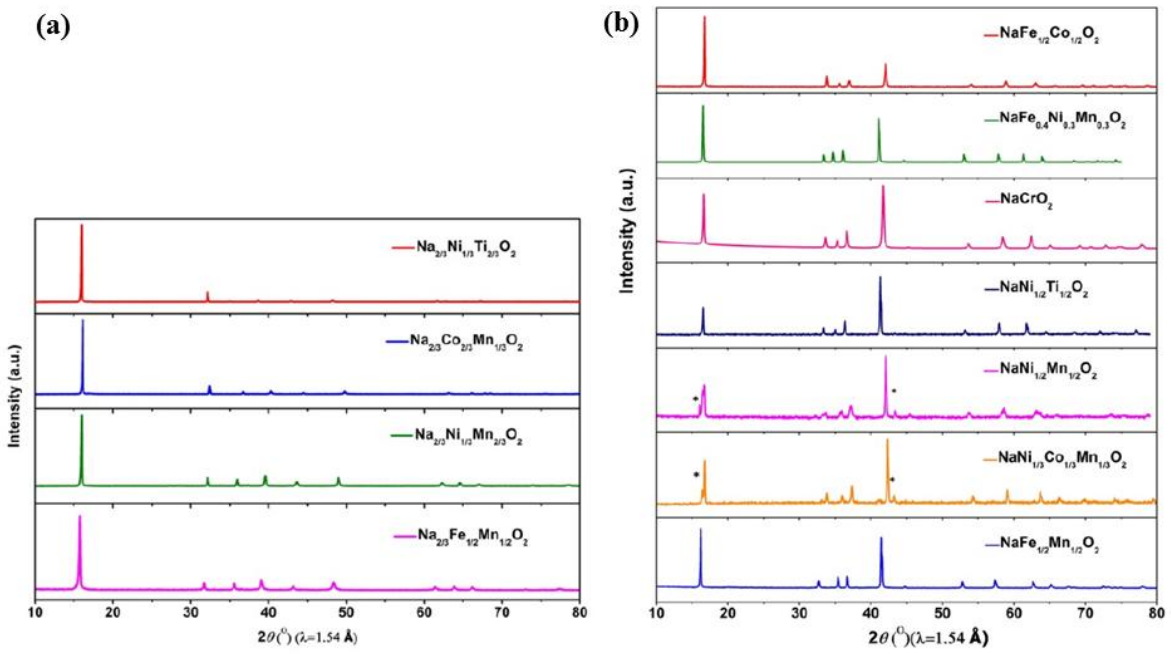

Figure 2.7. XRD patterns of the (a) O3-type and (b) P2-type $Na_xM_yO_2$.[96]

Recently, the layered transition metal (TM) oxides have been intensively investigated by the researchers due to their high energy density, above 500 Wh/kg.[97-99] Some issues, however, are blocking their practical application. O3-type Na_xMO_2 usually undergoes a complicated phase transition during the charge-discharge process, which results in a serious degradation in both the capacity and the cycle life.[100-105] For example, O3-type $NaCrO_2$ was charged in a Na half-cell, and the structural evolution was measured by the in-situ XRD. The in-situ XRD patterns and the structural evolution of the $NaCrO_2$ are shown in Figure 2.8. When 0.08Na is extracted from the initial O3 rhombohedral phase, a new phase began to form and grow. The rhombohedral (012) peak splits into two peaks, suggesting that the rhombohedral phase is making a transition to monoclinic phase. When 0.25Na is extracted from the pristine structure, the monoclinic phase $Na_{0.74}CrO_2$ became the dominant phase. With more Na extracted from the structure, a second new phase emerges and becomes the final phase when 0.48 Na is extracted. The peaks of the XRD pattern of the final phase are consistent with the $Na_{0.52}CrO_2$ phase (JCPDS no.38-1204), which is a P3-type structure.

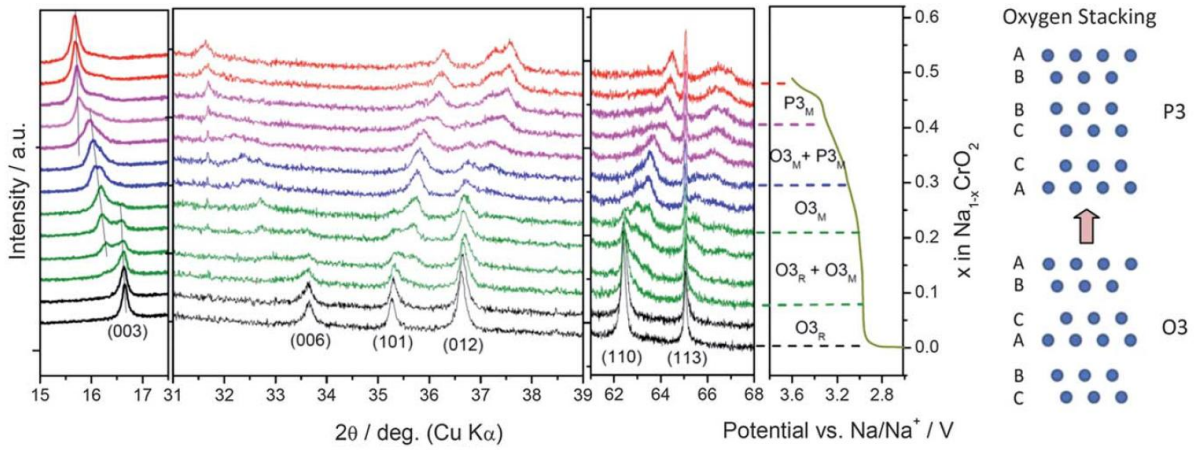

Figure 2.8. In situ X-ray diffraction patterns collected during the first charge (up to 3.6V at C/12 rate) or a $NaCrO_2$/Na cell (the 2θ angles are calculated to corresponding angles for =1.54Å for Cu-Kα from the real =0.7747 Å wavelength used for synchrotron XRD experiments).The corresponding voltage-composition profile is given on the right side of XRD patterns. Oxygen stacking of O3 and P3 structures is given on the extreme right.[102]

In addition, O3-type layered transition metal (TM) oxides are normally unstable under ambient atmosphere, because they can react with water, or water/CO_2 molecules can be inserted into alkali metal layer.[97,106-118] Subsequently, they need be stored under inert gases, adding to the costs. To improve the stability of the O3-type compound and the cycling performance, an effective strategy is to incorporate Co or Ni into the transition metal layer.[119-125] the elements Co and Ni are toxic, however. Moreover, due to the wide utilization of Ni and Co in lithium ion batteries, the cost of Ni and Co is increasing day by day. Therefore, it is better to avoid using Ni or Co in the cathode materials. Recently, Huang's group developed new air-stable Co/Ni-free O3-$Na_{0.9}[Cu_{0.22}Fe_{0.30}Mn_{0.48}]O_2$.[96] Figure 2.9 presents the electrochemical performance of the $Na_{0.9}[Cu_{0.22}Fe_{0.30}Mn_{0.48}]O_2$. As shown in Figure 2.9(a), $Na_{0.9}[Cu_{0.22}Fe_{0.30}Mn_{0.48}]O_2$ delivers about 100 mAh g^{-1} reversible capacity with an initial Coulombic efficiency of 90.4%. Moreover, it shows excellent cycling performance, with 97% capacity retention of its initial capacity after 100 cycles (Figure 2.9(b)). To evaluate the stability of $Na_{0.9}[Cu_{0.22}Fe_{0.30}Mn_{0.48}]O_2$ in air, its structure and the electrochemical performance were tested after the material was stored in air for one month to exclude the effects of CO_2. Figure 2.10 shows the XRD patterns and electrochemical performance of the O3-$Na_{0.9}[Cu_{0.22}Fe_{0.30}Mn_{0.48}]O_2$ stored in air for one month. As shown in Figure 2.10(a), it is clear that there was no change in the XRD pattern of $Na_{0.9}[Cu_{0.22}Fe_{0.30}Mn_{0.48}]O_2$ stored in air for one month compared with the as-prepared

$Na_{0.9}[Cu_{0.22}Fe_{0.30}Mn_{0.48}]O_2$. Moreover, the cycling performance of $Na_{0.9}[Cu_{0.22}Fe_{0.30}Mn_{0.48}]O_2$ remained stable after storage in air (Figure 2.10(d)). All the results demonstrate that $Na_{0.9}[Cu_{0.22}Fe_{0.30}Mn_{0.48}]O_2$ is very stable in air. Huang proposed two possible reasons for the stability improvement of $Na_{0.9}[Cu_{0.22}Fe_{0.30}Mn_{0.48}]O_2$. One is that the incorporation of Cu into layered oxides increases the average storage voltage, which avoids oxidation by water/oxygen/CO_2. The other one is that different surface structures and compositions can be formed to protect the bulk material from direct contact with air.

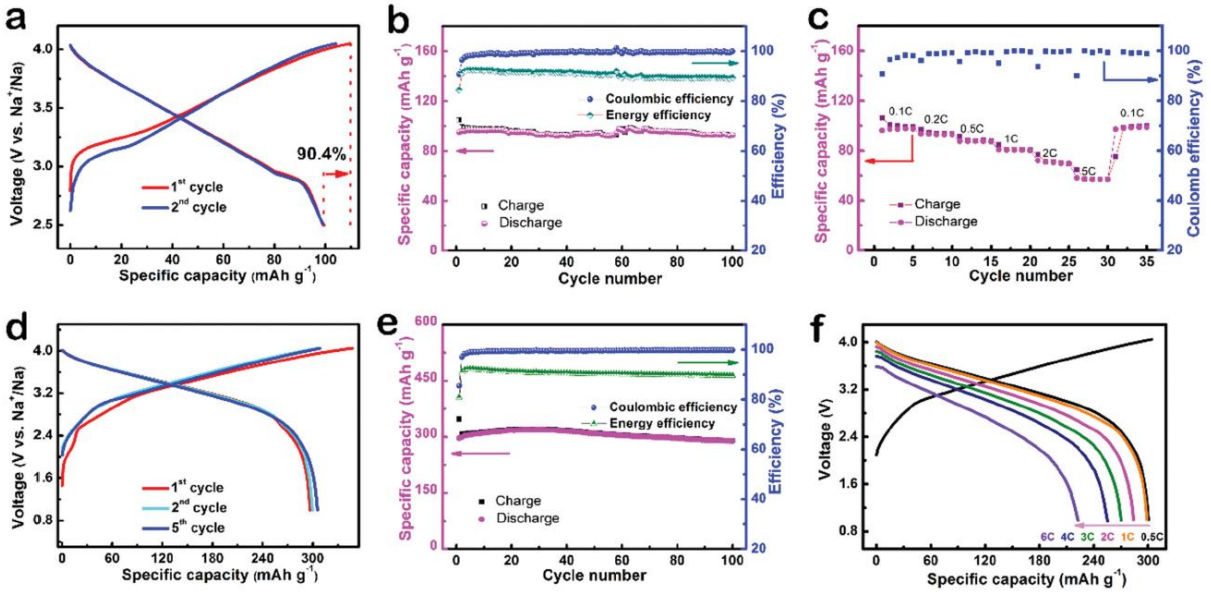

Figure 2.9. Na storage performance of the O3-$Na_{0.9}[Cu_{0.22}Fe_{0.30}Mn_{0.48}]O_2$ electrode (a–c). (a) The first and second galvanostatic charge and discharge curves of the $Na_{0.9}[Cu_{0.22}Fe_{0.30}Mn_{0.48}]O_2$ electrode cycled between 2.5 and 4.05 V at a current rate of 0.1C (10 mA g^{-1}). (b) Long-term cycling performance. The capacity, Coulombic efficiency, and energy conversion efficiency versus cycle number at a 0.1C rate. c) Rate capability. Capacity versus cycle number at various current rates from 0.1C to 5C. Na storage performance of the O3- $Na_{0.9}[Cu_{0.22}Fe_{0.30}Mn_{0.48}]O_2$//hard carbon full cells (d-f). (d) The first, second, and fifth charge and discharge curves of the full cell cycled between 1 and 4.05 V at a 0.5C rate. (e) Long-term cycling performance, the Coulombic efficiency, and the energy conversion efficiency versus cycle number at the 0.5C rate and (f) rate capability. Discharge curves of the full cell cycled at constant charge/discharge rates from 0.5C to 6C (one charge curve at 0.5C rate is also shown). The specific capacities were calculated based on the mass of cathode material in (a–c) and based on the mass of anode material in (d–f).[96]

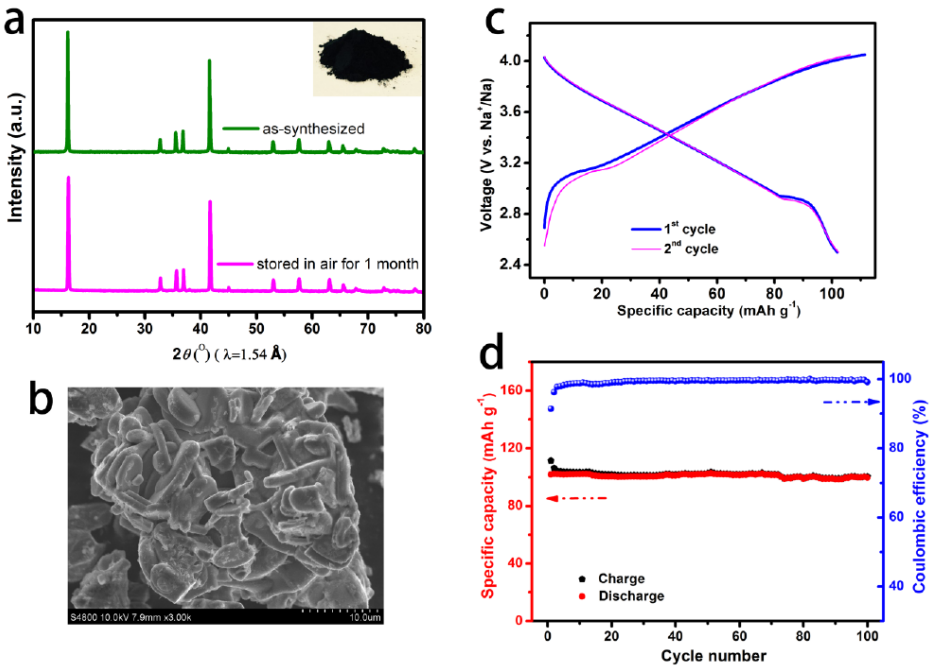

Figure 2.10. (a) The XRD patterns of as-synthesized O3- $Na_{0.9}[Cu_{0.22}Fe_{0.30}Mn_{0.48}]O_2$ and the sample stored in air for one month, the insert photograph is the $Na_{0.9}[Cu_{0.22}Fe_{0.30}Mn_{0.48}]O_2$ powder showing the black colour; (b) typical SEM image of the sample stored in air for one month; (c) the typical first and second charge/discharge curves of the sample stored in air for one month at the current rate of 0.1C and long cycling performance at 0.1C rate (d).[96]

In contrast to O3 compounds, the P2 compounds can keep the P2 structure over a wide range of Na content, suggesting that they rarely undergo a phase transition during the charge-discharge process.[98,99,126-128] Figure 2.11 shows the structural evolution of the P2-$Na_{0.67}[Mn_{0.65}Ni_{0.15}Fe_{0.2}]O_2$ during the first discharge process. Clearly, the initial P2 phase retains its structure over the wide range of voltage. When the $Na_{0.67}[Mn_{0.65}Ni_{0.15}Fe_{0.2}]O_2$ was discharged at low voltage of about 1.8 V, it was transformed from P2 phase into a distorted P2′ phase. A new uncharacterized high potential phase, denoted as "Z", appeared at high voltage (> 3.7 V). Moreover, Nazar suggested that this deleterious high voltage transition can be mitigated by substitution for Fe^{3+} by Ni^{2+}.[129] For example, when nickel atoms were incorporated into the transition metal layers of $Na_{0.35}Fe_{0.5}Mn_{0.5}O_2$ to form $Na_{0.29}Fe_{0.2}Mn_{0.65}Ni_{0.15}O_2$, the stability domain of the P2 structure was pushed to higher voltage-from 4 V to 4.1 V, as shown in Figure 2.12.

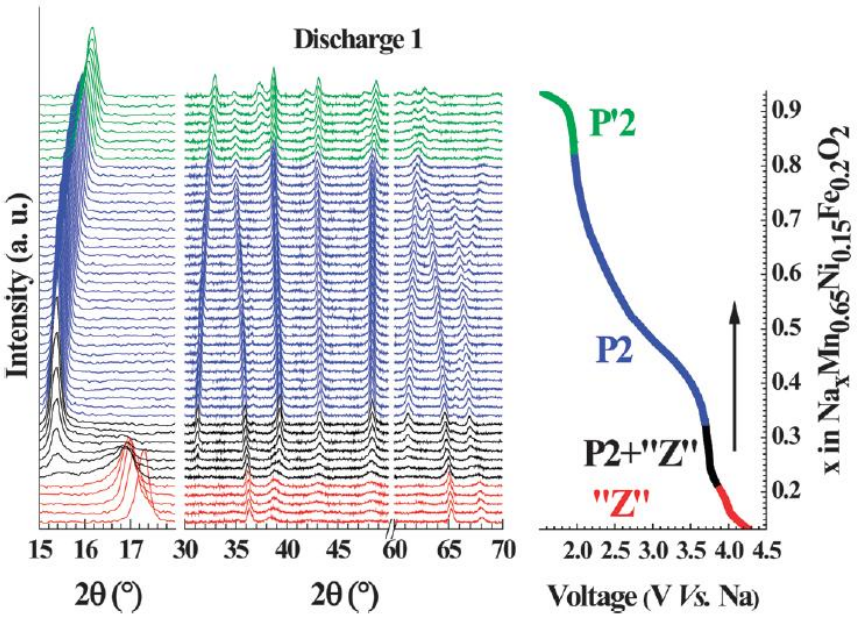

Figure 2.11. Operando XRD data recorded during galvanostatic cycling of $Na_{0.67}[Mn_{0.65}Ni_{0.15}Fe_{0.2}]O_2$ at a rate of C/20 (left) along with illustration of sodium content vs. voltage of the cell (right) or the first discharge. The races in the openrando XRD patterns are colour-coded with respect to the electrochemical profile on the right to reflect the structural composition if the cathode material.[129]

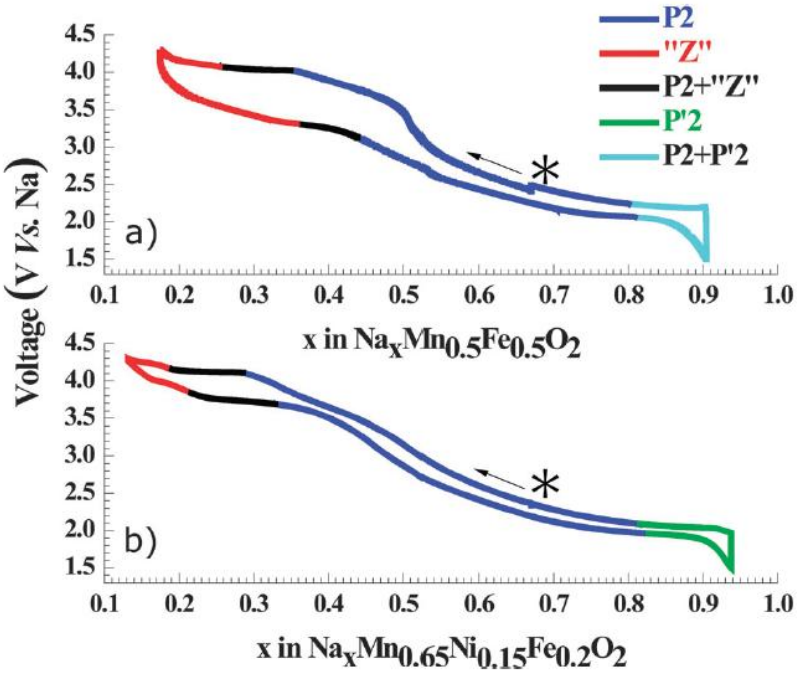

Figure 2.12. Phase evolution within: (a) $Na_{0.67}[Mn_{0.5}Fe_{0.5}]O_2$ and (b) $Na_{0.67}[Mn_{0.65}Ni_{0.15}Fe_{0.2}]O_2$ as a function of the sodium content during first cycle. The sign * shows the start point of cycling.[129]

2.4.1.2 tunnel-type transition metal oxides

Tunnel-structured Na_xMO_2 is an orthorhombic structure, as shown in Figure 2.13. It is built from octahedral units (MO_6) and square-pyramidal units (MO_5). The edge-sharing MO_5 sites are connected with one triple and two double octahedral chains at the vertexes, forming an S-shaped tunnel. This unique tunnel structure drives the sodium ions to mainly diffuse along the *c* direction. In contrast to most layered transition metal oxides, the tunnel-type transition metal oxides are extremely stable in air, resulting in their being studied widely. The representative tunnel-type compound is $Na_{0.44}MnO_2$, which was first proposed by Hagenmuller's group in 1971.[130] Recently, Huang's group developed a new tunnel-type $Na_{0.61}[Mn_{0.61-x}Fe_xTi_{0.39}]O_2$, which delivered the highest capacity of ~ 90 mAh g^{-1} among the tunnel-type oxides and exhibited a high storage voltage of 3.56 V due to the Fe^{3+}/Fe^{4+} redox couple.[131]

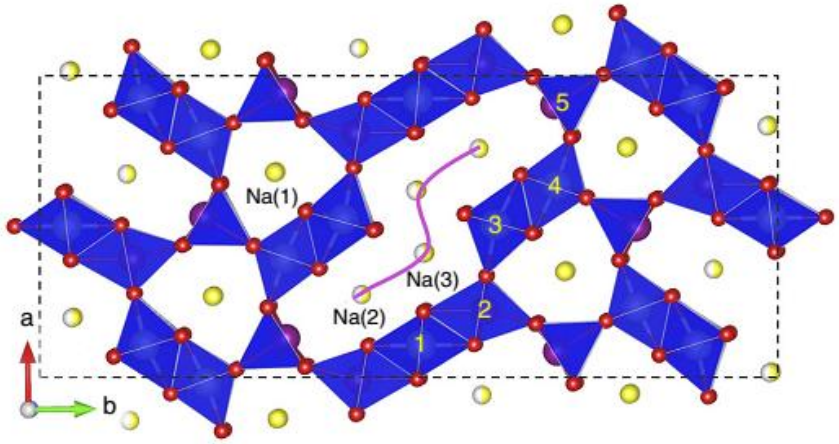

Figure 2.13. Structural pattern of tunnel oxides.[132]

2.4.2 Phosphates

The phosphates can be mainly classified into 4 groups: phosphates which contain a single phosphate group ($NaMPO_4$, M = transition metals), sodium superionic conductor (NASICON) type $Na_xM_2(PO_4)_3$, pyrophosphates and mixed polyanions ($Na_2MP_2O_7$ and $Na_4M_3(PO_4)_2P_2O_7$), and fluorophosphates. Figure 2.14 shows the structures of these phosphates.

2.4.2.1 Phosphate $NaMPO_4$

$NaFePO_4$ compound has two kinds of structures: the olivine structure and the thermodynamically stable maricite structure. Maricite NaFePO4 prepared by the normal route is electrochemically inactive, however, owing to the lack of cationic transport channels in the structure.[133] Nevertheless, it was reported that nanosized maricite $NaFePO_4$ with 50 nm

particle size can present superb electrochemical activity because the mobility of Na is enhanced through a structural transformation to the amorphous phase.[134] It delivered 142 mAh g^{-1} rechargeable capacity in the voltage range of 1.5-4.5 V and showed an impressive cycling performance with 95% capacity retention over 200 cycles.

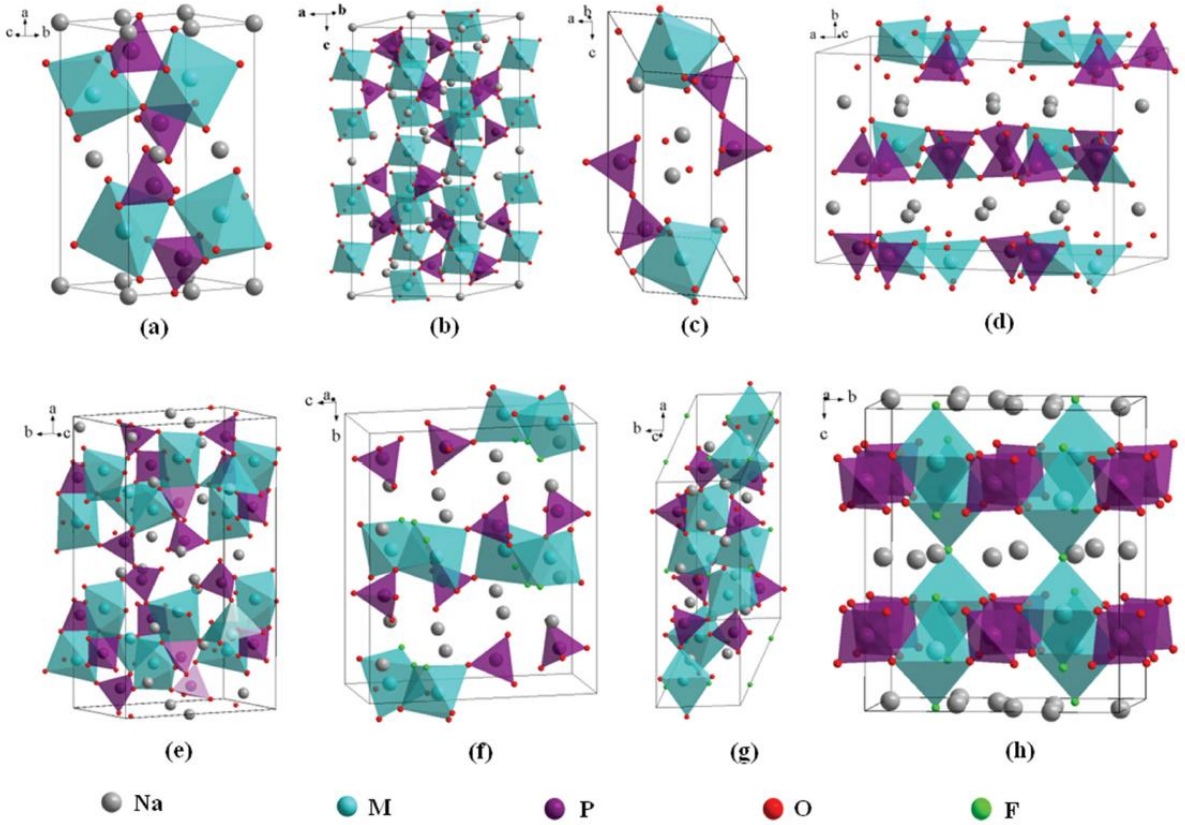

Figure 2.14. Crystal structures of (a) olivine $NaMPO_4$, (b) NASICON $Na_3V_2(PO_4)_3$, (c) triclinic $Na_2MP_2O_7$, (d) orthorhombic $Na_2MP_2O_7$, (e) orthorhombic $Na_4M_3(PO_4)_2P_2O_7$, (f) orthorhombic Na_2MPO_4F, (g) monoclinic Na_2MPO_4F, and (h) tetragonal $Na_3M_2(PO_4)_2F_3$ (M represents transition metals).[132]

2.4.2.2 NASICON $Na_3M_2(PO_4)_3$

NASICON type compounds were proposed as sodium ion solid electrolytes because of their high Na^+ ionic conductivity owing to their three-dimensional (3D) open framework. A typical representative NASICON material is $Na_3V_2(PO_4)_3$, which can exhibit both cathodic and anodic electrochemical properties.[135-140] The charge-discharge curves of $Na_3V_2(PO_4)_3$ used as both cathode and anode are shown in Figure 2.15. When it acts as cathode, two sodium ions can be extracted from the host with a theoretical capacity of 118 mAh g^{-1}, showing a potential plateau at 3.4 V. When $Na_3V_2(PO_4)_3$ is used as anode material, one sodium ion can be inserted into the host with a theoretical capacity of 59 mAh g^{-1}, exhibiting a potential plateau

at 1.6 V vs. Na^+/Na. Utilizing this unique feature, a symmetric battery using it as both cathode and anode can operate at a voltage of ~1.8 V. Moreover, this full cell showed superior rate capability due to the high Na^+ ionic conductivity of NASICON type compounds. Recently, Ji et al. used $Na_3V_2(PO_4)_3$ encapsulated inside nanoporous carbon as both cathode and anode material to fabricate an intercalation pseudocapacitor. This pseudocapacitor delivered a high power density exceeding 5.4 kW kg^{-1} and exhibited excellent cycle life, with 64.5% capacity retention over 10000 cycle at 1.17 A g^{-1}.[141]

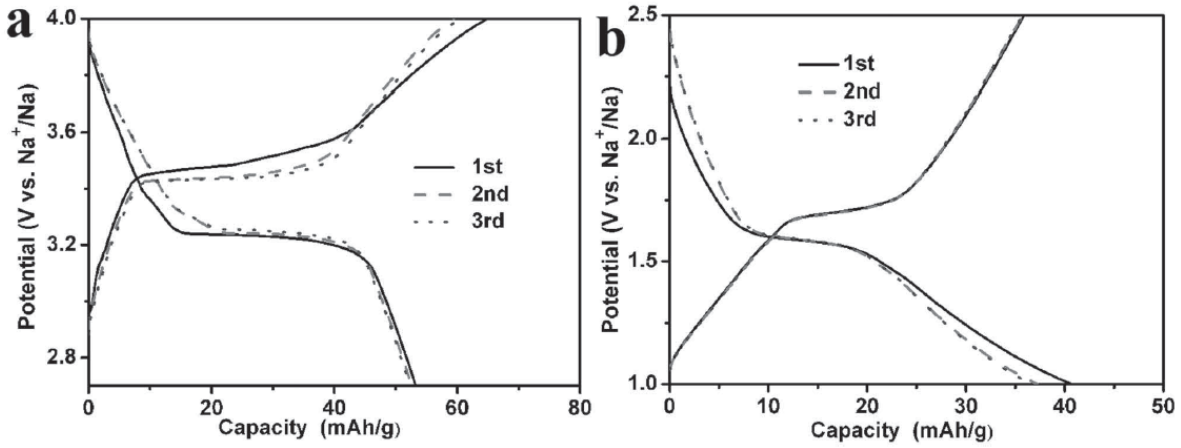

Figure 2.15. First-three sodiation/desodiation profiles at 1C current rate of the $Na_3V_2(PO_4)_3$ sample as (a) cathode and (b) anode.[141]

2.4.2.3 Pyrophosphates and mixed polyanions ($Na_2MP_2O_7$, $Na_4M_3(PO_4)_2P_2O_7$)

Pyrophosphate $Na_2MP_2O_7$ (M=Fe, Mn, Co) as a cathode material for sodium ion batteries has attracted more attention because it has a stable structure and good Na ion mobility. $Na_2MP_2O_7$ can grow into different structures depending on the type of transition metal and the synthesis conditions, including triclinic, orthorhombic, and tetragonal structure. For $Na_2FeP_2O_7$ and $Na_2CoP_2O_7$, the most thermodynamically stable structure is the triclinic phase, while for $Na_2CoP_2O_7$, the most accessible phase is the orthorhombic structure. Triclinic $Na_2FeP_2O_7$ was first reported as cathode for sodium ion batteries, delivering 83 mAh g^{-1} reversible capacity with a potential plateau at 3 V that is related to Fe^{3+}/Fe^{2+} redox couple.[142] The triclinic $Na_2MnP_2O_7$ shows a similar capacity of 80-90 mAh g^{-1} and an average potential of 3.7V.[143-146]

$Na_4M_3(PO_4)_2P_2O_7$ is a family which is consisted of mixed phosphate and pyrophosphate groups. As shown in Figure 2.14 (e), it is composed of a three-dimensional nework of [M3P2O13] finite layer parallel to the bc-plane.[147] $Na_4Fe_3(PO_4)_2P_2O_7$ is a typical mixed polyanion compound. It delivered capacity 110 mAh g^{-1} and showed an average voltage of

3.2V at the C/40 rate. Notably, the potential of Fe^{3+}/Fe^{2+} redox in the mixed polyanion compound is higher than that in phosphates and pyrophosphates.

Fluorophosphate is a new family which combines F^- ions with phosphates. Recently, there have been many papers reporting fluorophosphate as cathode for both Li- and Na-ion batteries.[63,148-157] Fluorophosphates can be divided into two main groups: Na_2MPO_4F and $Na_3(VO_x)_2(PO_4)_2F_{3-2x}$ ($0 \leq x \leq 1$). In terms of the Na_2MPO_4F family, Na_2FePO_4F and Na_2CoPO_4F are two main structures that need to be investigated. Recently, it was reported that carbon-coated Na_2FePO_4F delivered a reversible capacity of about 100 mAh g^{-1} and showed a potential plateau at 3.0 V vs. Na^+/Na.[158] Carbon-coated Na_2CoPO_4F also exhibited a similar capacity of 100 mAh g^{-1}, but its potential plateau is higher (4.3 V) than that of Na_2FePO_4F, so that it shows the highest energy density of more than 400 mWh g^{-1} in the Na_2MPO_4F family.[159,160] The framework of $Na_3V_2(PO_4)F_3$ consists of $[V_2O_8F_3]$ bi-octahedral and $[PO_4]$ tetrahedral units. It exhibits two potential plateaus at 3.7 V and 4.2 V, which are related to the two-step reaction of the V^{4+}/V^{3+} redox couple, respectively, when $Na_3V_2(PO_4)F_3$ is charged from 2.0 to 4.5 V. Moreover, the F in $Na_3V_2(PO_4)F_3$ can be replaced by oxygen to form $Na_3(VO_x)_2(PO_4)_2F_{3-2x}$ ($0 \leq x \leq 1$) family.

2.4.3 Sulfates

Sulfates belong to the family of polyanionic compounds, and there several sulfates have been developed as cathode candidates for sodium ion batteries, such as $Na_2Fe_2(SO_4)_3$ and $Na_2Fe(SO_4)_2{\cdot}2H_2O$. Recently, Goodenough's group prepared a new sulfate compound, $NaFe(SO_4)_2$.[161] It is a mineral with the eldfellite structure, and the detailed structure is shown in Figure 2.16. It is clear that the octahedral sites in the *ab* planes are occupied by Na^+ and Fe^{3+} ions. These planes are linked by (SO_4) polyanions that leave interplanar space for two-dimensional (2D) Na^+ ion diffusion. The theoretical specific capacity of $NaFe(SO_4)_2$ is 99 mAh g^{-1}, and it delivered a reversible capacity of 80 mAh g^{-1} at the 0.1 C rate. Moreover, it exhibited a potential plateau at 3.3 V vs Na^+/Na, related to the Fe^{3+}/Fe^{2+} redox couple.

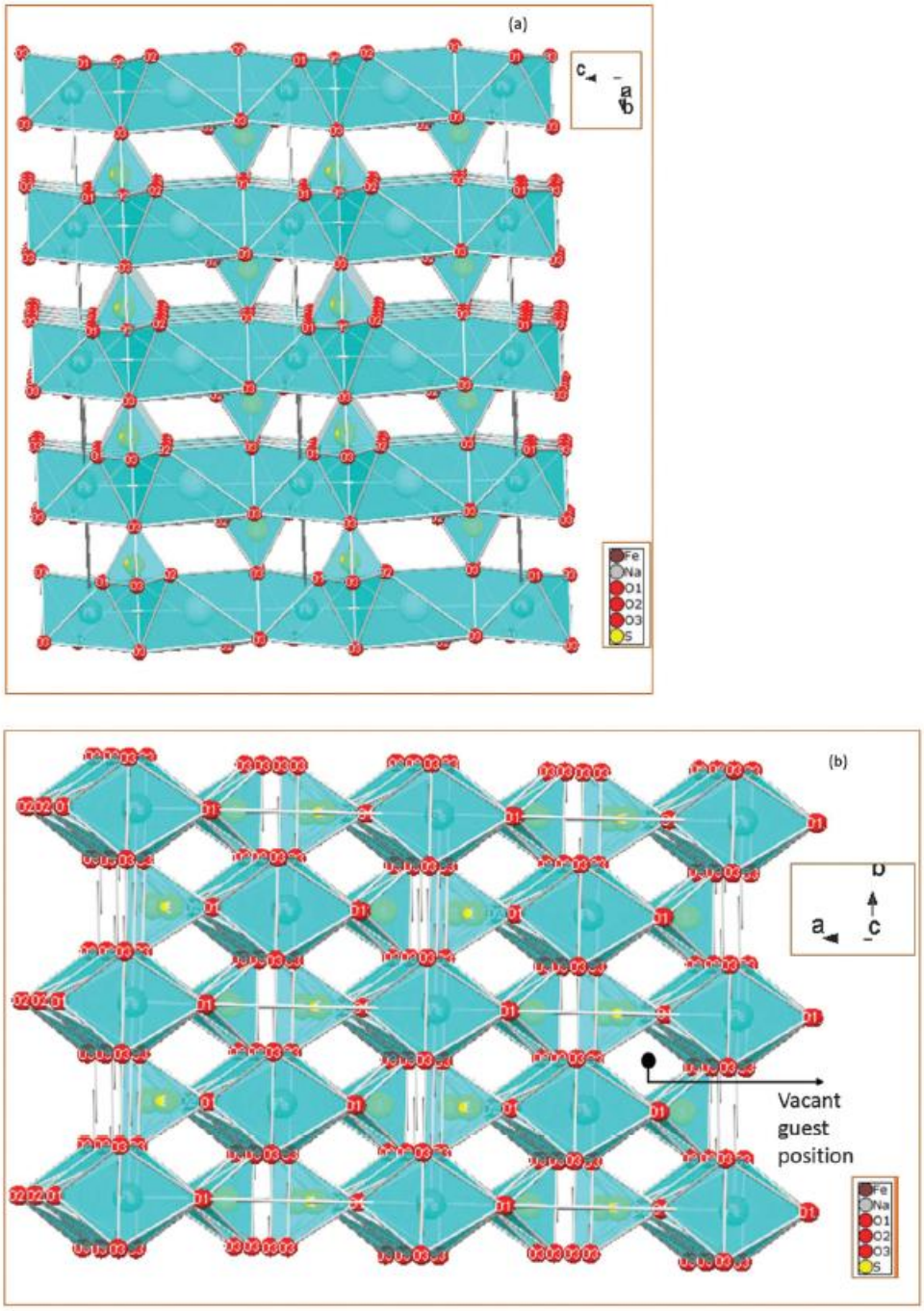

Figure2.16. Crystal structure of eldfellite, $NaFe(SO_4)_2$ (a) planner view and (b) vertical stacking.[161]

2.4.4 Fluorides

Fluoride cathode materials have attracted more attention in the field of lithium ion and sodium ion batteries in recent years, owing to their stable structure, high theoretical capacity, low cost, high safety, and low toxicity.[72,162-167] Fluorides have the ability to generate high electrochemical energy, resulting from their large electronegativity and the small

electrochemical equivalent of fluorine. Yamaki's group reported FeF_3 as cathode for sodium ion batteries, and it showed a discharge capacity of 100 mAh g^{-1}.[168] FeF_3 cannot be applied as cathode in commercial sodium ion batteries, however, because of the lack of sodium as a charge carrier. Therefore, Na-containing fluorides such as $NaFeF_3$ have been developed recently and are being intensively investigated.[72,167] Yamaki prepared two kinds of $NaFeF_3$ with different fluorine sources: NaF and $NaHF_2$.[72] The $NaFeF_3$ obtained from $NaHF_2$ exhibited better electrochemical performance than that obtained from NaF, delivering 130 mAh g^{-1} initial discharge capacity with 84.6% coulombic efficiency in the voltage range of 1.5-4.0 V, as shown in Figure 2.17.

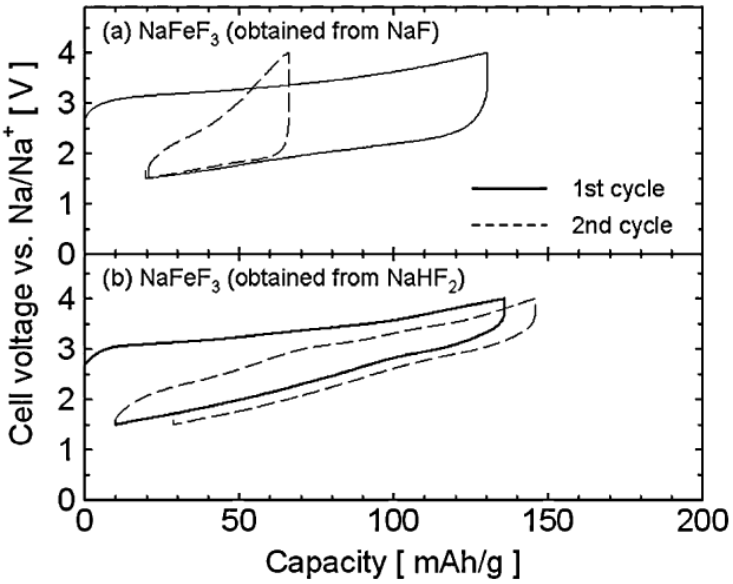

Figure 2.17. First and second charge and discharge curves of $NaFeF_3$ obtained from (a) NaF and (b) $NaHF_2$ at a rate of 0.076 mA cm^{-2} between 1.5 and 4.0V vs. Na^+/Na.[72]

2.4.5 Hexacyanoferrates

Prussian blue (PB) has the perovskite-type structure, A_2M^{II} $[T^{II}$ $(CN)_6]$ (A: alkali metal; M and T: transition metals), in which there are two redox reaction metals, as shown in Figure 2.18. Thus, the ideal electrochemical reaction is A_2M^{II} $[T^{II}$ $(CN)_6] \leftrightarrow 2A^+ + 2e^- + M^{III}[T^{III}$ $(CN)_6]$, which can achieve maximum ion storage ($2A^+$). Goodenough's group reported a series of $KMFe(CN)_6$ (M = Fe, Mn, Ni, Cu, Co, and Zn) compounds as cathode materials for sodium ion batteries.[169] Figure 2.19 shows the charge-discharge curves of $KMFe(CN)_6$ (M = Fe, Mn, Ni, Cu, Co and Zn) compounds in sodium ion batteries. A fatal flaw, however, is that $KMFe(CN)_6$ compounds do not have sodium ions, which hinders their application in sodium

ion batteries. Therefore, many $Na_xM[T(CN)_6]$ compounds are being investigated as cathode for sodium ion storage.[170-179]

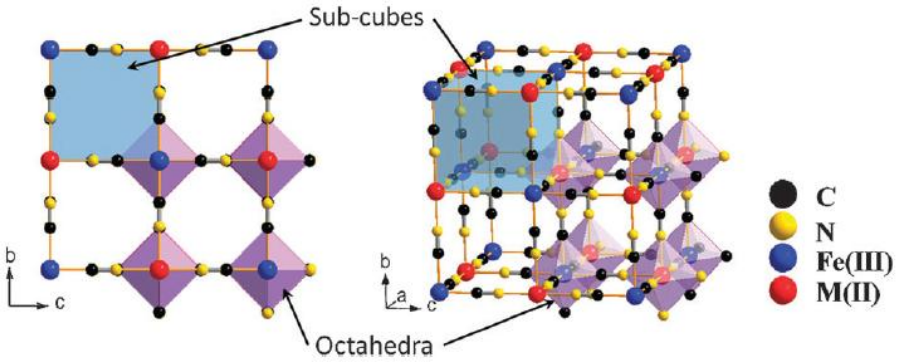

Figure 2.18. Framework of Prussian blue analogues.[169]

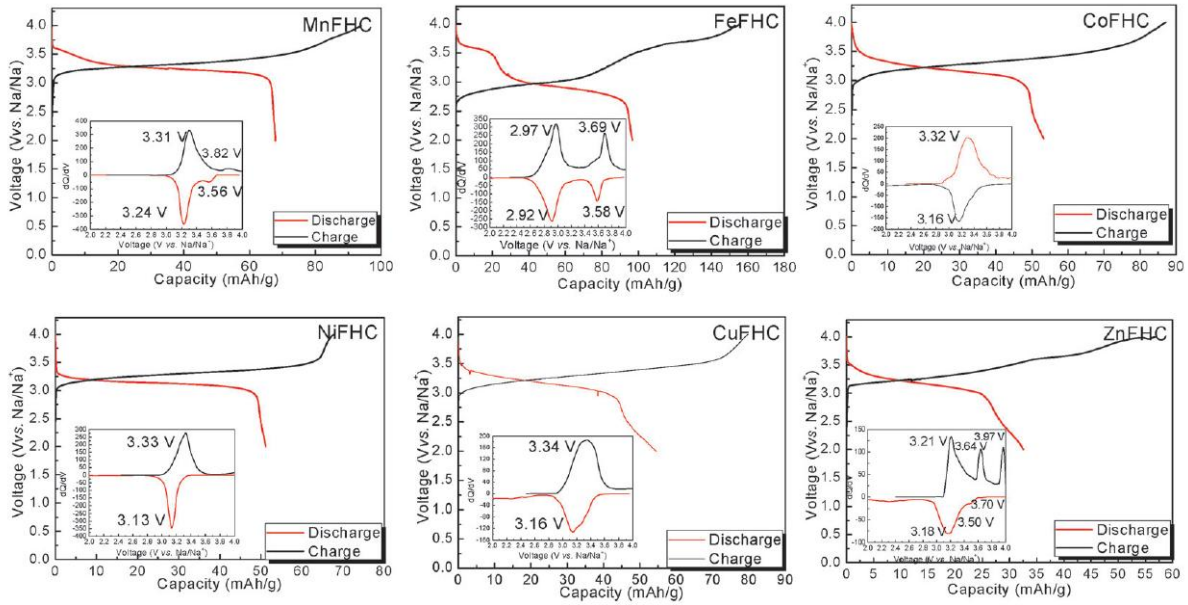

Figure 2.19. The charge-discharge curves of Prussian blue analogues $KMFe(CN)_6$-Na cells at the third cycle with a current of C/20. Insets show their corresponding chronoamperograms.[169]

The synthetic procedure for PB is in aqueous solution, however, so the general formula of PB as it is prepared is $A_xM[T(CN)_6]_{1-y}\square_y\ nH_2O$ ($0 < x < 2$, $y < 1$), where □ denotes a $[T(CN)_6]$ vacancy occupied by coordinating water.[180] The presence of vacancies and coordinating water will break down the bridging of the M-CN-T framework, resulting in a distorted lattice, which gives rise to lower efficiency and structural instability of the PB compound during the charge-discharge process.[181] Therefore, it is important to fabricate a PB framework with few vacancies. Recently, Guo's group reported that $Na_{0.61}Fe[Fe(CN)_6]_{0.94}\cdot\square_{0.06}$ with few vacancies had been prepared by a facile method and could be stably cycled over 150 cycles without

apparent capacity loss.[176] Goodenough's group removed the interstitial H_2O by drying as-prepared $Na_2MnFe(CN)_6$ in air/vacuum at 100 ℃ for 30 h. As a result, vacuum-dried $Na_2MnFe(CN)_6$ delivered a high capacity of 150 mAh g^{-1} with a potential plateau at 3.5 V. In addition, it showed excellent rate capability (120 mAh g^{-1} at 20 C) and superior cycling performance, with 75% capacity retention over 500 cycles.[182]

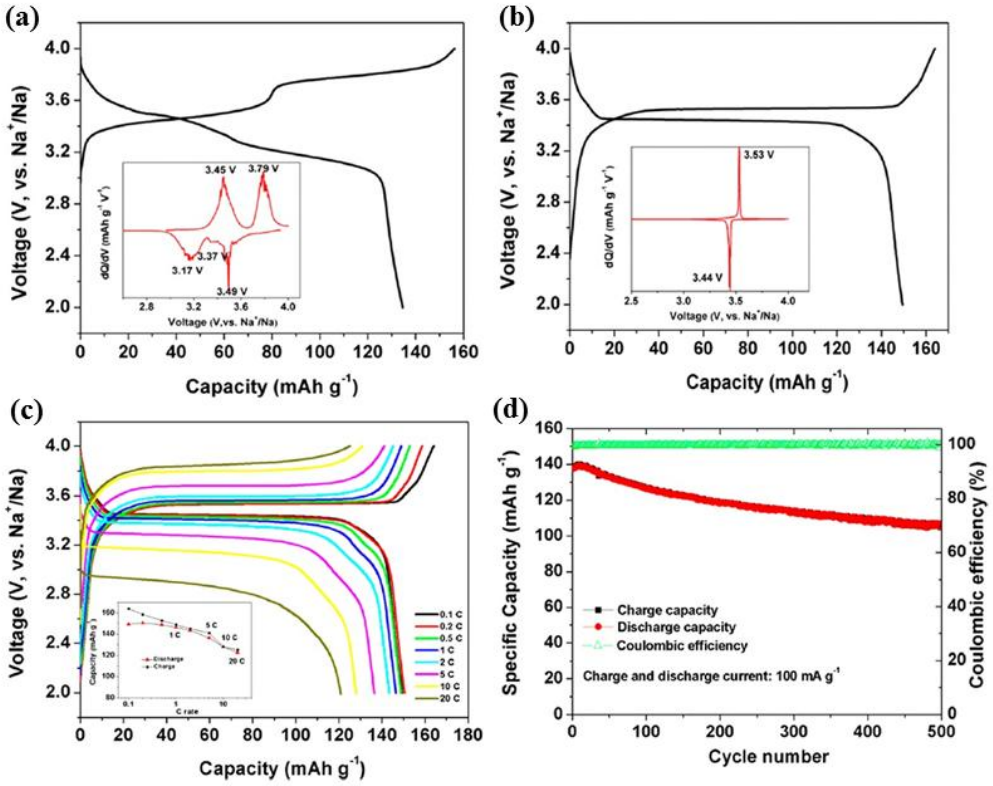

Figure 2.20. Galvanostatic initial charge and discharge profiles profiles of (a) air-dried and (b) vacuum-dried $Na_2MnFe(CN)_6$ at a current of 0.1C(15mA g^{-1}) in the voltage range of 2.0-4.0V. The derivative curves (dQ/dV) plotted as a function of V are shown as inserts. (c) Rate capability and (d) cycling performance of vacuum-dried $Na_2MnFe(CN)_6$.[182]

2.4.6 Organic compounds

Organic electrode materials have been intensively developed to construct green rechargeable batteries due to their environmental friendliness, low cost, and recyclability. Moreover, they can be synthesized from natural biomass by a process with low energy consumption.[183-187] Diverse organosulfur compounds, radical compounds, carbonyl compounds, and functional polymers have been studied as cathode materials for rechargeable batteries.[188-205] There is a problem limiting the development of organic electrodes, however, that they are easy to dissolve in organic liquid electrolytes. In addition, low thermal stability, particularly poor

electronic conductivity, and sluggish kinetics also hinder the application of organic electrodes, whether in Li- or Na-ion batteries. Figure 2.21 shows some representative organic cathode materials. These organic cathode materials can be classified into two groups: cation-insertion type and anion-insertion type.

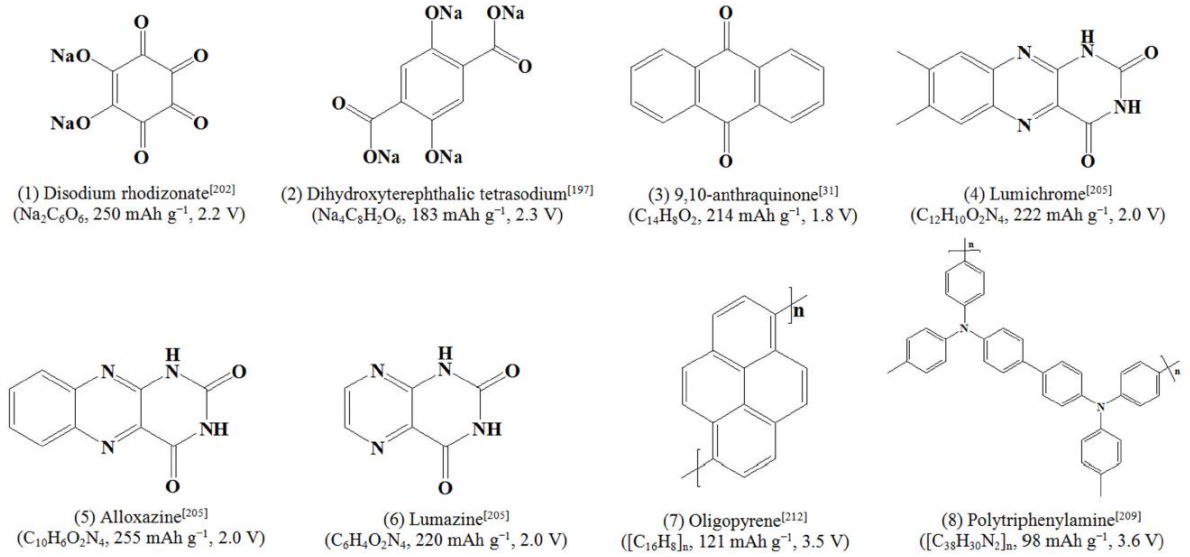

Figure 2.21. Representative organic cathode materials with high specific capacity or high operating potentials.[132]

2.5 Current anode materials for sodium ion batteries

The anode materials investigated for sodium ion batteries can be classified into four different groups: carbon-based materials, oxides and sulfides, alloy compounds, and organic compounds. Figure 2.22 shows the average voltage and energy density versus gravimetric capacity for various negative electrode materials for NIBs with sodiated $Na_{2/3}Ni_{1/3}Mn_{1/2}Ti_{1/6}O_2$ or $Na_{2/3}Fe_{1/2}Mn_{1/2}O_2$ as cathode. As shown in Figure 2.22 (a) and (b), when $Na_{2/3}Ni_{1/3}Mn_{1/2}Ti_{1/6}O_2$ is used as the cathode materials in the full cells, the average voltage and energy density for various anode materials for NIBs is higher than that for $Na_{2/3}Fe_{1/2}Mn_{1/2}O_2$. Notably, in all the recent anode candidates, phosphorus and phosphorus-based compounds show the relatively higher capacity and energy density for sodium ion storage.

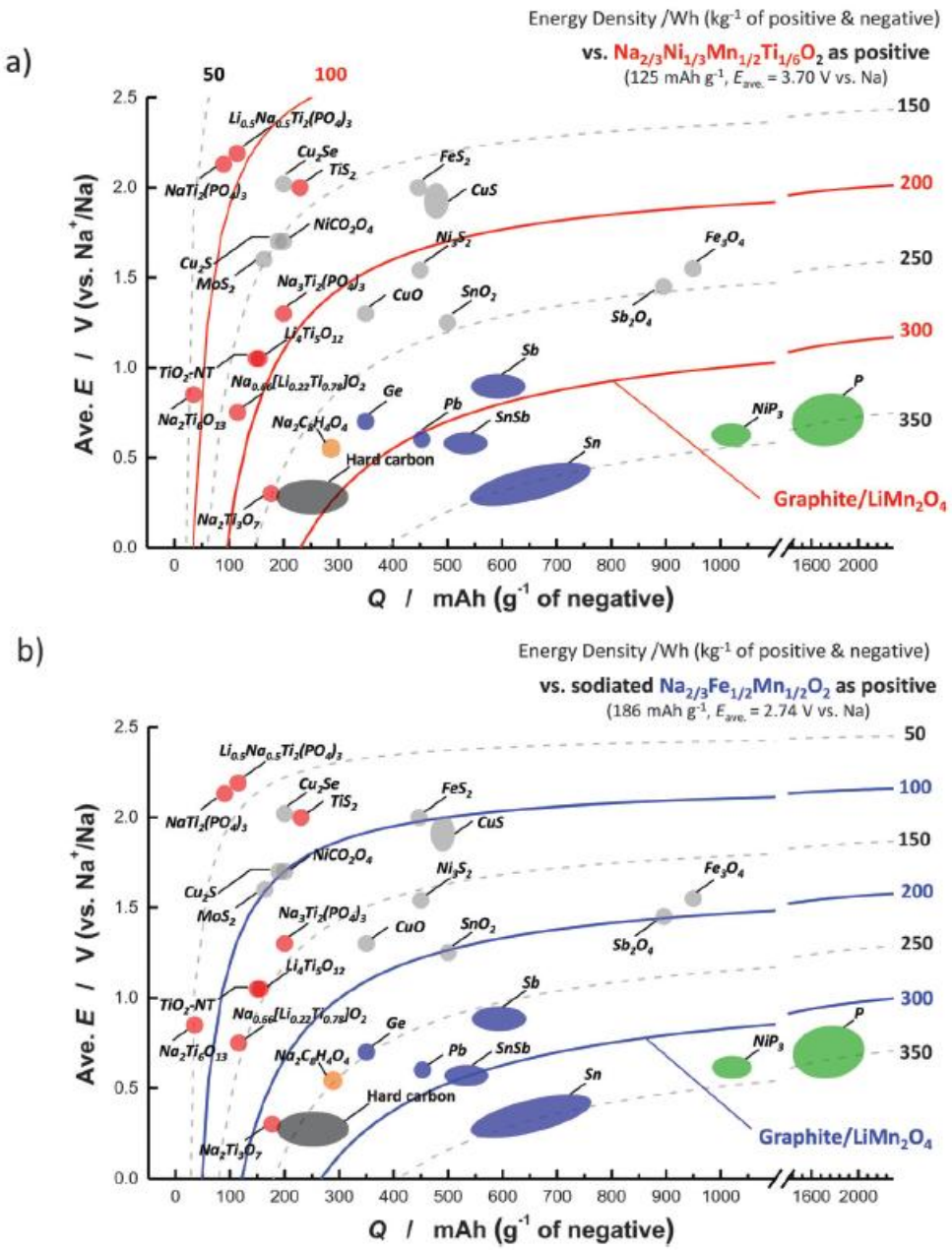

Figure. 2.22. Average voltage and energy density versus gravimetric capacity for various negative electrodes materials for NIBs: (a) sodiated as $Na_{2/3}Ni_{1/3}Mn_{1/2}Ti_{1/6}O_2$ as cathode; (b)$Na_{2/3}Fe_{1/2}Mn_{1/2}O_2$ as cathode. Gravimetric energy density (W h kg^{-1}), based on the weight of active materials in optimally balanced positive and negative electrodes, is calculated by the difference of average potential and reversible capacity of active materials examined in Na half cells according to previous reports. [206]

2.5.1 Carbon-based materials

Graphite is widely applied as anode material in commercial lithium ion batteries owing to its ability to reversibly form the intercalated compound LiC_6.[207] Nevertheless, there is no

intercalated NaC_6 compound that exists under moderate conditions, possibly due to the mismatch between the size of the Na^+ ion and the graphite structure.[208] Thus, in the past ten years, it is commonly recognized that graphite cannot be utilized as an anode candidate for sodium ion batteries. Recently, however, Adelhelm's group reported the opposite and showed that graphite can be used as anode material for sodium ion batteries.[209] They utilized the co-intercalation of both alkali ions and solvent to form a ternary graphite intercalation compound. The reaction can be described in Equation 2.14,

$$C_n + e^- + A^+ + ysolv \leftrightarrow A^+(solv)_y C_n^- \quad (2.14)$$

As a result, the graphite presented excellent cycle life with capacity of about 100 mAh g^{-1} over 1000 cycles and coulombic efficiency > 99.87% in sodium ion batteries (Figure 2.23).

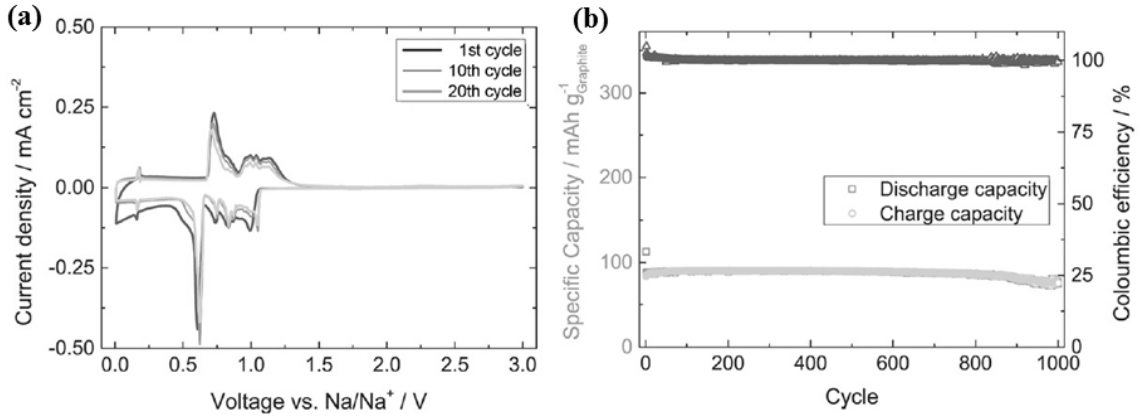

Figure 2.23. Cyclic voltammetry (a) and cycling performance and coulombic efficiency of the graphite in 1M NaOTf in diglyme over 1000 cycles at 0.1C.[209]

Hard carbon, as one type of amorphous carbon, shows promising electrochemical performance as anode for sodium ion batteries. Hard carbon with improved performance was reported in sodium ion batteries by Dahn's group, who synthesized it by paralysing glucose. It delivered a high capacity of about 320 mAh g^{-1}.[58] The sodium storage mechanism of hard carbon is also proposed by Dahn et al., in which Na^+ ion insertion into hard carbon takes place in two distinct structures. Correspondingly, there are two stages in the discharge curve, as shown in Figure 2.24. One is the sloping region ranging from 1 to 0.2 V, which is assigned to the insertion/deinsertion of the sodium ions in between parallel graphene layers in the turbostratic graphitic structure. The other stage is the potential plateau at 0.1 V, which corresponds to the sodium ion storage in the nanovoids of hard carbon.

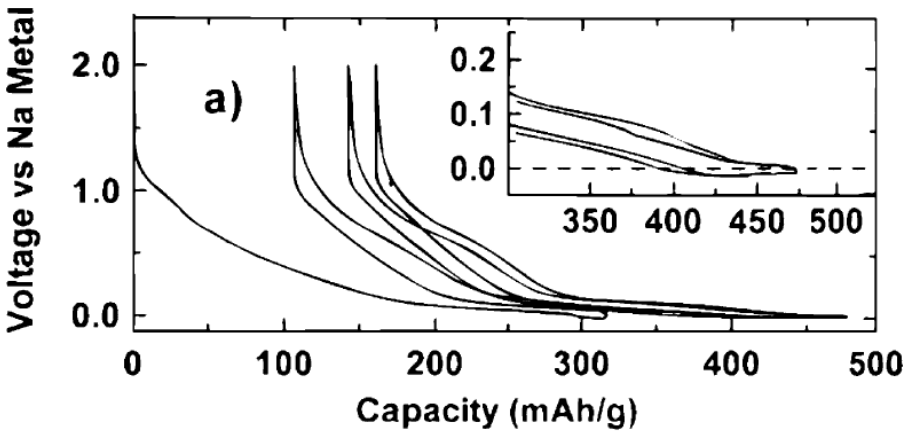

Figure 2.24. Sodiation/desodiation potential profiles for glucose-derived hard carbon formed by pyrolysis at 1000 ℃. The inset is an enlargement of the indicated region. [58]

In addition, other carbonaceous materials are also being intensively investigated, such as graphene, nanostructured carbon (carbon nanowires and nanospheres).[210-212] Our group reported that reduced graphene oxide can allow sodium ion insertion, showing a reversible capacity of 174 mAh g^{-1} at the 0.2 C rate and a superior rate capability as high as 93.3 mAh g^{-1}, even at 200 mA g^{-1}.[210] To improve the cyclability and capacity, some morphologies and structures of carbonaceous materials were studied, such as carbon nanospheres and nanowires. Liu et al. reported that the as-prepared nanospheres can deliver a reversible capacity of ~160 mAh g^{-1} at current density of 100 mA g^{-1} after 100 cycles.[211] The nanowires synthesized by Maier's group exhibited a ~200 mAh g^{-1} reversible capacity at 50 mA g^{-1} after 400 cycles.[212]

2.5.2 Metal oxides and sulphides

2.5.2.1 Metal oxides (MO_x)

In the recent years, many metal oxide materials have been tested as anodes for sodium ion batteries. According to the sodium storage mechanism, metal oxide electrodes can be classified into two groups: intercalation type and conversion type. Intercalation type metal oxides include TiO_2(B), $Na_2Ti_3O_7$, $Na_2Ti_6O_{13}$, $Na_4Ti_5O_{12}$, $Li_4Ti_5O_{12}$, and P2-$Na_{0.66}[Li_{0.22}Ti_{0.78}]O_2$.[213-221] Owing to the limited number of storage sites in these structures, the intercalation type metal oxides deliver reversible capacity of less than 300 mAh g^{-1}. In contrast, the conversion type metal oxides show high theoretical specific capacities (> 600 mAh g^{-1}). The conversion type metal oxides can be divided into two groups according to whether the metal in the oxides is active.

In the first group of conversion type metal oxides, such as Fe_3O_4, Fe_2O_3, CuO, $NiCo_2O_4$, and CoO, the metal M in the oxides is electrochemically inactive.[222-227] The sodiation/desodiation process can be described by the following equation,

$$MO_x + 2xNa^+ + 2xe^- \leftrightarrow xNa_2O + M \quad (2.15)$$

Most of this kind of metal oxide delivers low capacities of less than 400 mAh g^{-1}, in spite of the high theoretical capacities.

In the second group of conversion type metal oxides, such as SnO_2 and Sb_2O_4, the metal M in the oxides is electrochemically active. The mechanism for the reactions of these compounds during the charge-discharge process can be described by the following equations,

$$MO_x + 2xNa^+ + 2xe^- \leftrightarrow xNa_2O + M, \quad (2.16)$$

$$xNa_2O + M + yNa^+ + ye^- \leftrightarrow xNa_2O + Na_yM \quad (2.17)$$

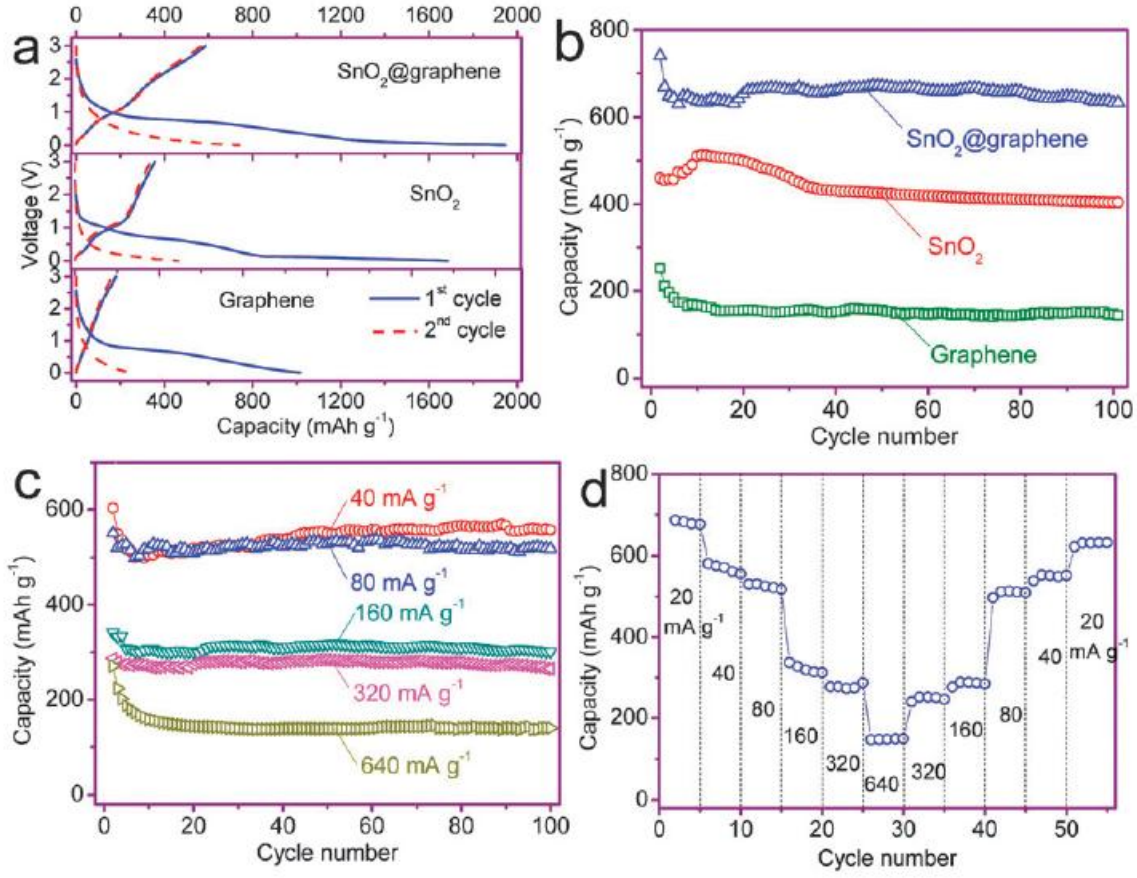

Figure 2.25. (a) 1st and 2nd cycles discharge and charge profiles of bare graphene, bare SnO2, and SnO2@graphene nanocomposites at 20 mA g^{-1} current density. (b) Cycling performance of bare graphene, bare SnO_2, and SnO_2@graphene nanocomposites at 20 mA g^{-1} current density. (c) Cycling performance of SnO_2@graphene nanocomposites at current

densities of 40, 80, 160, 320, and 640 mA g^{-1}. (d) Rate performance of SnO_2@graphene nanocomposites at varied current densities. (b–d) are recorded from the 2nd cycle.[228]

Due to the presence of active metal elements, most such oxides deliver high reversible capacities. SnO_2 is one of most investigated oxides with an active metal. Its theoretical capacity is 1368 mAh g^{-1}, based on the following sodiation reaction,[228]

$$31Na + 4SnO_2 \rightarrow Na_{15}S_4 + 8Na_2O \quad (2.18)$$

Nevertheless, the theoretical capacity is difficult to achieve for pure SnO_2 because of the huge volume changes and the poor electronic conductivity of SnO_2. To improve the electrochemical performance of SnO_2, the most effective strategy is to combine the SnO_2 with carbonaceous materials. Wang's group reported that SnO_2 incorporated in graphene nanosheets could deliver a high reversible capacity of 741 mAh g^{-1} at a current rate of 20 mA g^{-1}. It also showed good cycling performance with 638 mAh g^{-1} capacity remaining after 100 cycles, as shown in Figure 2.25.[228]

2.5.2.2 Sulphides

Metal sulphides, including FeS_2, Ni_3S_2, MoS_2, Sb_2S_3, have become an intensively studied family in recent years.[229-235] Layered structure MoS_2 has been widely researched as an anode material for sodium ion batteries. The storage mechanism of MoS_2 can be divided into two steps according to the sodiation voltage. When MoS_2 was discharged above 0.4 V, Na^+ was inserted into the layers, and the process can be described by Equation 2.19,[236]

$$MoS_2 + x\text{Na} \rightarrow Na_xMoS_2 \text{ (above 0.4 V, } x < 2) \quad (2.19)$$

When the MoS_2 was further discharged below 0.4 V, the conversion-type reaction takes place, as shown in Equation 2.20,[237]

$$Na_xMoS_2 + (4-x)\text{Na} = \text{Mo} + 2Na_2S \text{ (below 0.4 V)} \quad (2.20)$$

Chen et al. reported that MoS_2 nanoflowers showed a high discharge capacity of 350 mAh g^{-1} at 0.05 A g^{-1} and excellent rate capability, with 195 mAh g^{-1} at 10 A g^{-1}.[230] FeS_2 is another metal sulphide that was intensively investigated due to its non-toxicity, excellent reversibility, and the low cost of Fe.[235,238] Recently, Chen's group prepared FeS_2 microspheres that showed excellent cycling performance, with almost no degradation over 20000 cycles, as shown in Figure 2.26.[235]

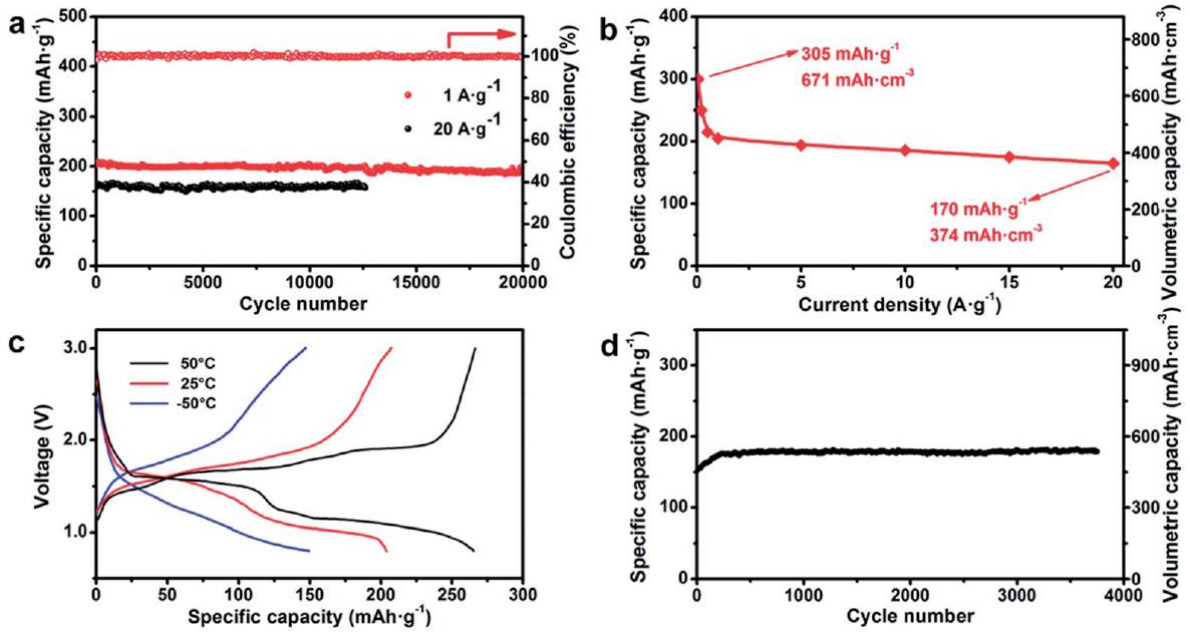

Figure 2.26. Electrochemical performances of Na/FeS_2 cells with optimized test parameters. (a) cyclic performance of FeS_2 microspheres, (b) rate capability of FeS_2 microspheres, (c) charge-discharge profiles of as-prepared FeS_2 at 1A g^{-1} at different temperatures, (d) cycling performance of a commercial bulk FeS_2 coin cell at a current density of 1A g^{-1}.[235]

2.5.3 Alloy materials

Most Group 14 and 15 elements have the ability to form binary alloy compounds with Na, including Sn, Sb, P, Ge, and Pb. Figure 2.27 presents the theoretical gravimetric and volumetric capacities of the Group 14 and 15 elements. The most significant feature of these alloy elements is that their theoretical capacities are very large because a single atom may combine with multiple Na atoms. Si and Ge can alloy with one Na^+ to form NaX-type alloy compounds. There is no report, however, on the electrochemical formation of NaSi in a Na cell so far. Sn and Pb have the ability to form $Na_{15}X_4$-type compounds, while P, Sb, and Bi can alloy with 3 Na^+ to form Na_3X-type compounds. P in particular has the highest theoretical capacity of 2600 mAh g^{-1} among these elements. Alloy anodes based on these elements, such as SnSb, $Sn_{4+x}P_3$, and SnGeSb, have also been investigated as anode materials for sodium ion batteries. In the following sections, we have chosen P, Sn, and Sb for detailed description.[74,239-242]

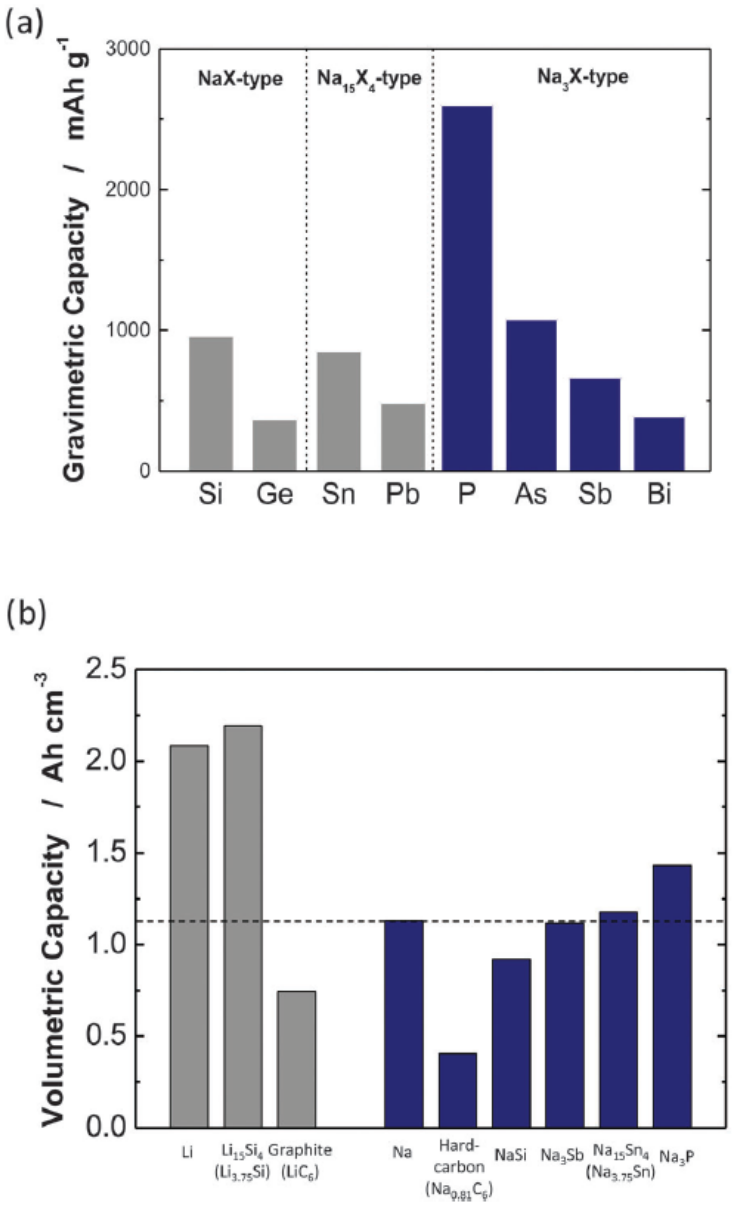

Figure. 2.27. (a) Theoretical gravimetric capacity estimated from phase diagrams for the group 14 and 15 elements. (b) Theoretical volumetric capacity of Si, Sn, Sb, and P electrodes in Na cells. Hard-carbon as a Na insertion material is also compared.[243]

2.5.3.1 Sn

Kumta et al. studied the alloying process for Sn in Na half-cells. Figure 2.28 shows the differential capacity plot (dQ/dV vs. V) in the first cycle for pure Sn. It is clear that there are three peaks appearing at 0.18 V, 0.081 V, and 0.033 V in the discharge process. This suggests that three phases are formed at 0.18 V, 0.081V, and 0.033V in the discharge process, denoted as X-I, X-Π, and X-ΙΙΙ, respectively. Based on the corresponding specific capacity of the respective phases related to the number of reacting sodium ions, the X-I, X-Π, and X-ΙΙΙ

phases are NaSn, Na_9Sn_4, and $Na_{15}Sn_4$, respectively.[244] Huang et al. used in-situ transmission electron microscopy to study the microstructural evolution and phase transformations of Sn nanoparticles during the sodiation process.[245]It was reported that the sodiation process for Sn passed through two steps: two-phase sodiation and single-phase sodiation. At first, Na^+ was converted to sodiated Sn particles through a two-phase mechanism to form a Na-poor, amorphous Na_xSn alloy ($x \approx 0.5$). Then, Sn was further sodiated via a single-phase mechanism to form some Na-rich amorphous phases and finally form the crystallized $Na_{15}Sn_4$ ($x = 3.75$). Figure 2.29 presents a schematic illustration of the structural evolution of Sn nanoparticles (NPs) during the sodiation.

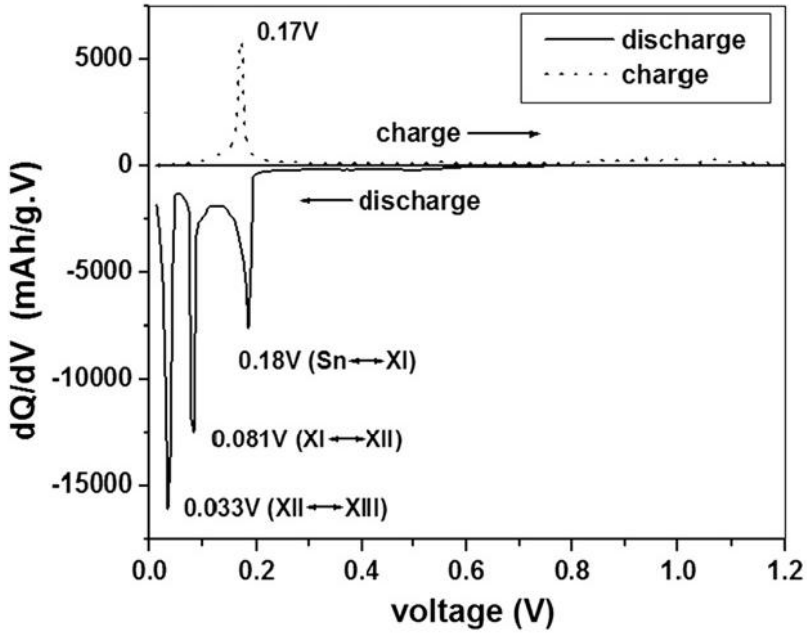

Figure 2.28. Differential capacity vs. cell potential curves of pure microcrystalline Sn obtained after 1st cycle at 50 mA g^{-1} in the potential window 0.01-1.2V.[244]

The big challenge for Sn application in sodium ion batteries is the huge volume change of 420% from the Sn transformation to $Na_{15}Sn_4$, which results in the poor cycling life of Sn. To improve the cycling performance of Sn, a few efforts have been made to prepare Sn/C composite. Hu's group synthesized a carbon/tin composite through depositing Sn thin film on wood fibers, which showed excellent cycling performance with a retained capacity of 145 mAh g^{-1} over 400 cycles at a current density of 85 mA g^{-1}.[246]

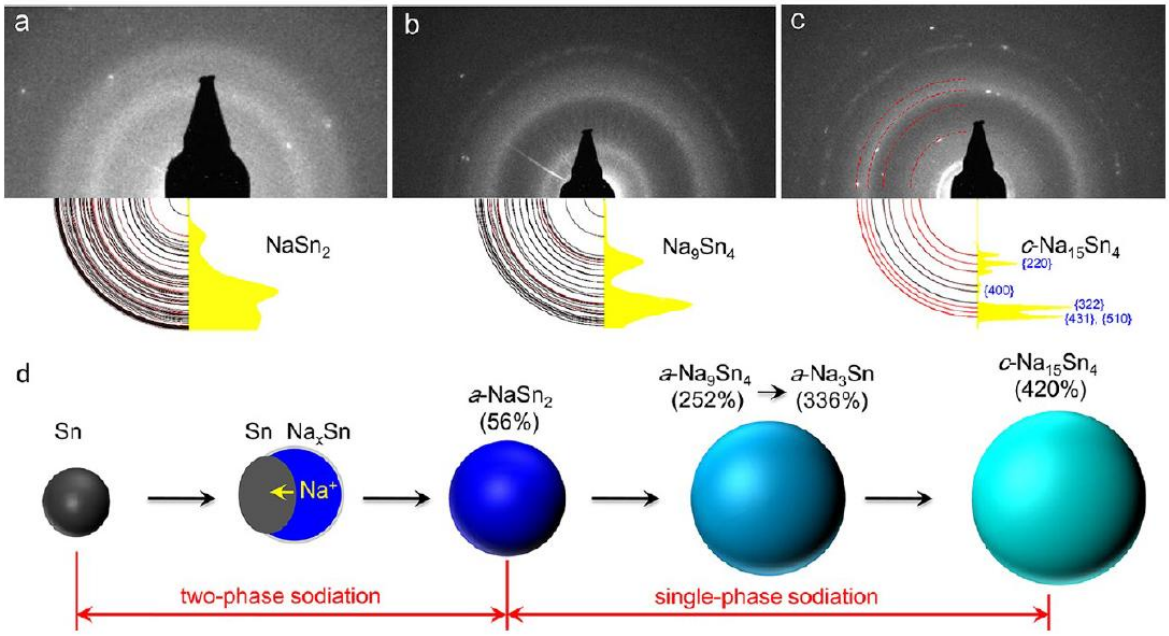

Figure 2.29. Three *a*-Na_xSn phases in the single-phase sodiation. (a) electron diffraction pattern (EDP) of the first *a*-Na_xSn phase, which was taken when the reaction front just swept the entire Sn NPs. The simulated EDP indicated that the composition of the first *a*-Na_xSn phase was close to the NaSn2 phase. (b) EDP of the second *a*-Na_xSn phase. The amorphous halos match the simulated *a*-Na_9Sn_4 phase. (c) EDP of the third *a*-Na_xSn phase, which was identified as *a*-Na_3Sn based on volumetric expansion. It is structurally close to the *c*-$Na_{15}Sn_4$ phase as tiny *c*-$Na_{15}Sn_4$ crystallites usually nucleate in this phase. (d) Schematic illustration of the structural evolution of Sn NPs during the sodiation.[245]

2.5.3.2 Sb

Monconduit et al. used in-situ XRD to explore the sodium storage mechanism of Sb. Figure 2.30 shows the XRD patterns of Sb cycled at the C/8 rate in the first two cycles. At first, Sb was sodiated with Na^+ to form an amorphous Na_xSb phase, which reaches its maximum sodium content at x = 1.5. With more Na^+ sodiation of Sb, the amorphous phase is converted into crystalline Na_3Sb phase. During the charge process, the crystalline Na_3Sb phase is first transformed into amorphous $Na_{1.5}Sb$ and then converted into Sb.[247] Also, like Sn, the huge volume changes of Sb (~390%) causes rapid capacity degradation. To improve its cycle life, some researchers milled Sb with a conducting carbon additive (Super P) to obtain good cycling performance with capacity retention of 94% over 100 cycles.[240,248] Recently, Yu's group prepared a novel Sb 3D nanostructure where the Sb nanoparticles were incorporated into a 3D reticular carbon network (denoted as Sb@3D RCN) by the electrostatic spray deposition technique.[249] Figure 2.31 shows the morphology of the Sb@3D RCN composite. It

is clear that the Sb nanoparticles were encapsulated in the reticular carbon matrix, which can effectively accommodate the large volume changes during the charge-discharge process. As a result, this 3D nanostructure presents excellent cycling performance with capacity of 224 mAh g^{-1} retained over 900 cycles at the 3 C rate (Figure 2.31(g)).

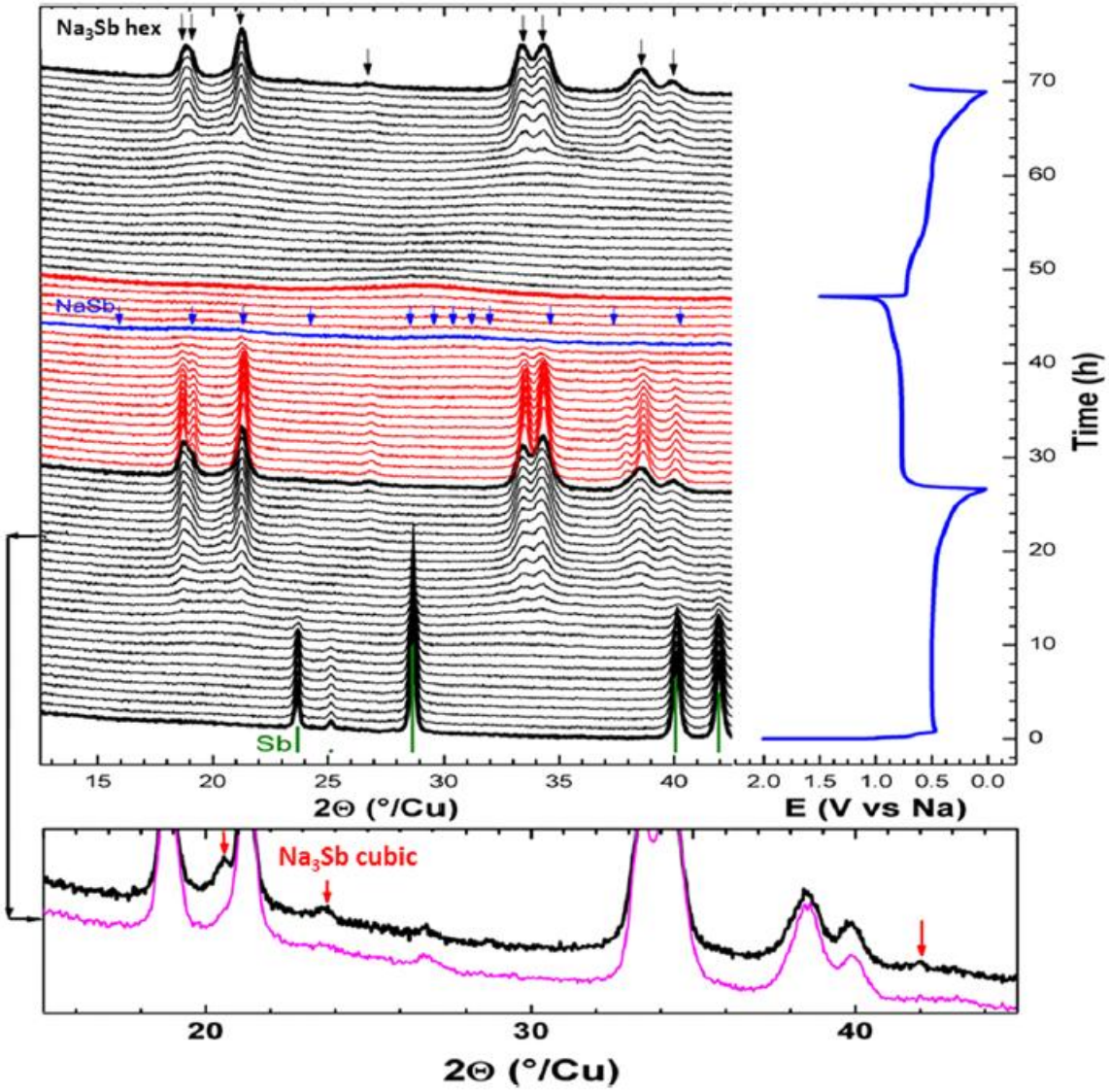

Figure 2.30. Operando evolution of the XRD pattern recorded at a C/8 rate (top left). The black and the red patterns are those recorded during the discharges and charge, respectively. The corresponding voltage profile (top right). A zoom illustrating the diffraction peaks from the cubic Na_3Sb (bottom). [247]

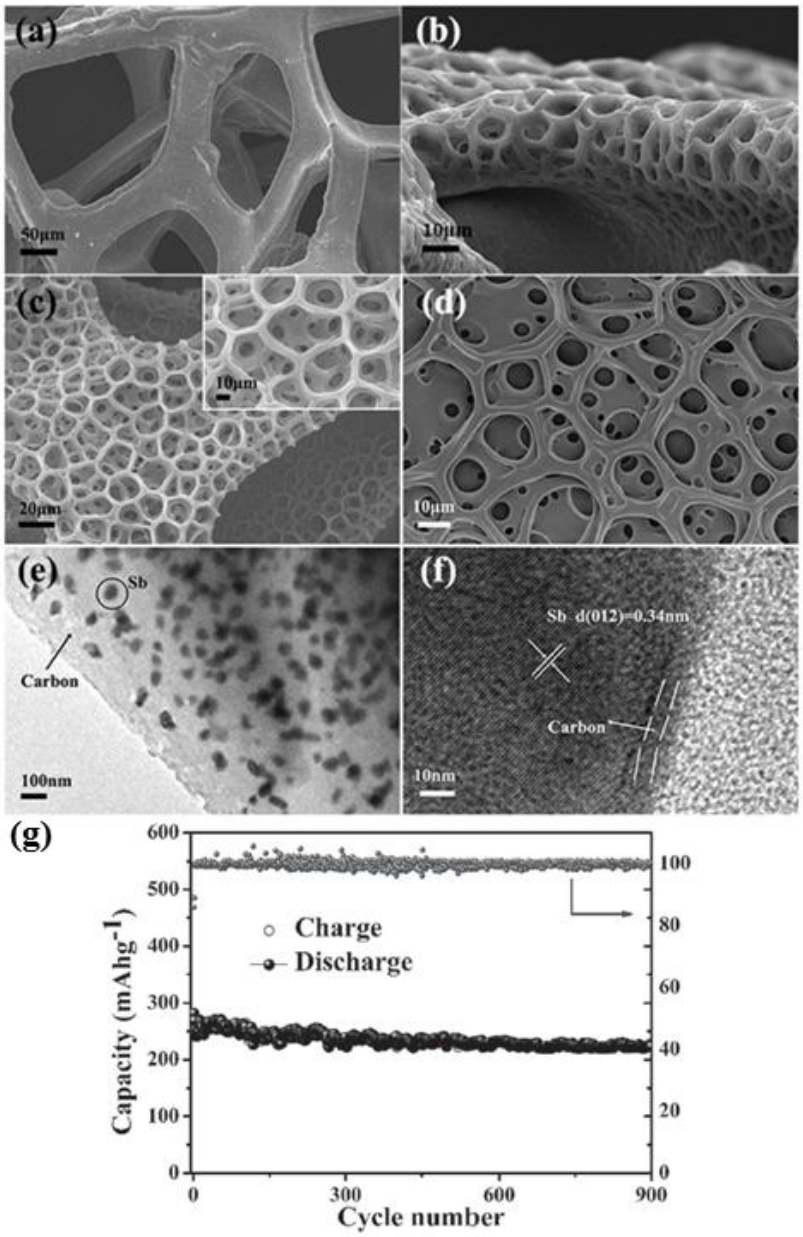

Figure 2.31. SEM images of (a) pure nickel-foam, (b) cross-section of the Sb@3D RCN film, (c) the Sb@3D RCN film and (inset) high-magnification image, (d) the obtained film after heat treatment at 600C. (e) TEM and (f) HRTEM images of the Sb@3D RCN, (g) cycling performance of Sb@3D RCN at 3C rate.[249]

2.5.3.3 P

Elemental phosphorus (P) is the most promising anode materials for SIBs with the highest theoretical capacity of 2596 mAh g^{-1}, because it can react with 3 Na^+ ions to form Na_3P phase. Phosphorus has three allotropes, white, black, and red. Among these allotropes, white phosphorus is not chemically stable, and synthesis of black phosphorus is not facile, as it needs an inert atmosphere under high pressure.[250,251] In comparison, red phosphorus is

commercially available with ease. For sodium ion storage, recently, Qian et al. and Kim et al. reported that an amorphous phosphorus composite with carbon that was obtained by high-energy mechanical milling could deliver a high capacity of 1764 mAh g^{-1} at the current density of 250 mA g^{-1} and 1890 mAh g^{-1} at the current density of 143 mA g^{-1}, respectively. [1,252] Moreover, the sodium storage mechanism of P was investigated through ex situ XRD by Kim et al.[252] It clearly shows that the red P is converted into Na_3P in the fully discharged state, as shown in Figure 2.32.

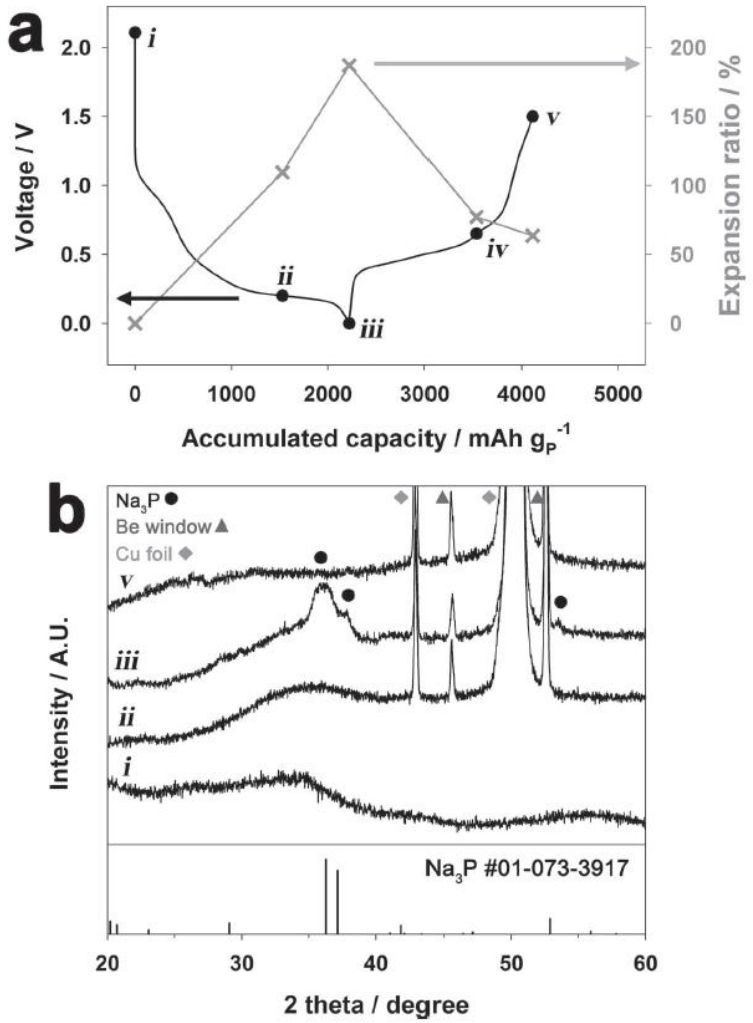

Figure 2.32. (a) Voltage profiles (black) of amorphous red P/C composite and the corresponding electrode thickness change (gray) during sodiation and desodiation. (b) ex situ XRD patterns of amorphous red P/C composite electrodes collected at various points as indicated in (a).[252]

2.5.4 Organic compounds

Organic compounds with C=O bonds can be used as anode materials due to the reaction between alkali ions and C=O bonds. Recently, disodium terephthalate ($Na_2C_8H_4O_4$) was reported as anode for sodium ion batteries because there are two C=O bonds in the compound. The molecular structure of $Na_2C_8H_4O_4$ and its Na insertion/deinsertion mechanism is shown in Figure 2.30(a). It showed 250 mAh g^{-1} reversible capacity with an average voltage of 0.45 V.[61]The electronic conductivity of $Na_2C_8H_4O_4$, however, is relatively poor. To improve its electronic conductivity, a large amount of carbon black was added when preparing the electrode slurry. Subsequently, the initial coulombic efficiency was very low, about 60%, as shown in Figure 2.30(b). This is possibly because a side reaction may take place between carbon black and the electrolyte. The coulombic efficiency and cycling stability of $Na_2C_8H_4O_4$ need improvement.

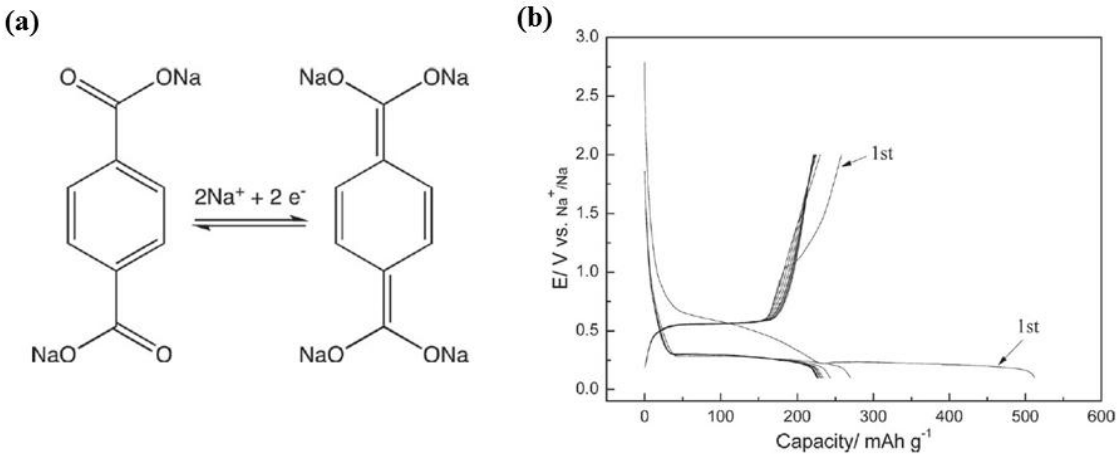

Figure 2.33. (a) Molecular structure of $Na_2C_8H_4O_4$ and its Na insertion/deinsertion mechanism, (b) charge-discharge curves of $Na_2C_8H_4O_4$/carbon black composite in the voltage range of 0.1-2V.[61]

2.6 Electrolyte

The electrolyte plays an indispensable role in batteries, providing alkali ion conduction and acting as a transport medium between the cathode and anode. Electrolytes are mainly composed of salts and solvents. In addition, to achieve a functional electrolyte, the third component, the additive, is added into the electrolyte. The most widely used additive is fluoroethylene carbonate (FEC), the function of which is to modify the solid electrolyte interphase (SEI) film. The most commonly used sodium salts and solvents are listed in Table 2 and Table 3, respectively.

Table 2.2 Basic properties of the most commonly used Na-salts for sodium ion batteries electrolytes.[253]

Salt	Anion chemical structure	M_w[g mol^{-1}]	T_m[℃](Li-salt)	σ[mS cm^{-1}][a](Li-salt)
$NaClO_4$	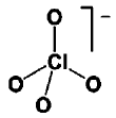	122.4	468 (236)	6.4 (6.5)
$NaBF_4$	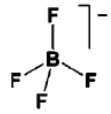	109.8	384 (293)	(3.4)
$NaPF_6$	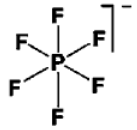	167.9	300 (200)	7.98 (5.8)
NaTf	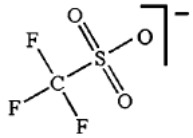	172.1	248 (>300)	(1.7)
NaTFSI	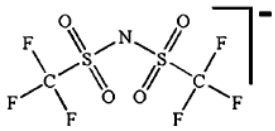	303.1	257 (234)	6.2 (5.1)
NaFSI	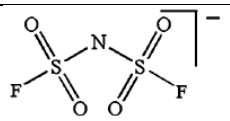	203.3	118 (130)	

Table 2.3 Solvents commonly used. T_m, T_b, T_f, η, ε and AN/DN stand for the melting point, the boiling point, the flash point, the viscosity, the dielectric constant and the acceptor and donor numbers, respectively.[253]

solvent	Tm (°C)	Tb(°C)	Tf (°C)	η (cP) 25 °C	ε 25 °C	AN (DN)
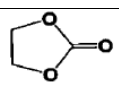 **Ethylene carbonate (EC)**	36.4	248	160	1.9 (40 °C)	89.78	(16.4)

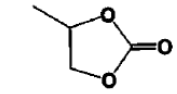 **Propylene carbonate (PC)**	-48.8	242	132	2.53	64.92	18.3(15.1)
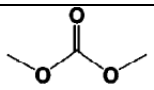 **Dimethyl-carbonate (DMC)**	4.6	91	18	0.59	3.107	
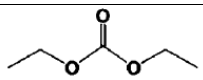 **Diethyl carbonate (DEC)**	-74.3	126	31	0.75	2.805	(16.0)
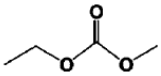 **Ethylmethyl carbonate (EMC)**	-53	110		0.65	2.958	
 **Dimethoxyethane (DME)**	-58	84	0	0.46	7.18	10.9(18.6)
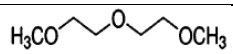 **Diethyleneglycol dimethylether (Diglyme)**	-64	162	57	1.06	7.4	9.9(19.2)
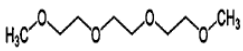 **Triethylene glycol dimethyl ether (Triglyme)**	-46	216	111	3.39	7.53	10.5(14)

Chapter 3. Experimental methods

Figure 3.1 shows the experimental procedures in this doctoral work. Initially, P/carbon composites (P/CNT and P/graphene nanoplates, denoted as P/GnPs), active metal phosphide ($Sn_{4+x}P_3$), and inactive metal phosphide (CoP and FeP) by the facile and large-scale ball-milling method; and synthesized $Na_{1.72}MnFe(CN)_6$ and $Na_{1.56}FeFe(CN)_6$ by large-scale co-precipitation. Then, these materials are characterized by a series of techniques, such as, X-ray diffraction (XRD), scanning electron microscopy (SEM), transmission electron microscopy (TEM), X-ray photoelectron spectroscopy (XPS), Raman and Mössbauer spectroscopy, etc. Finally, there materials were used to prepare electrodes to measure their electrochemical performance.

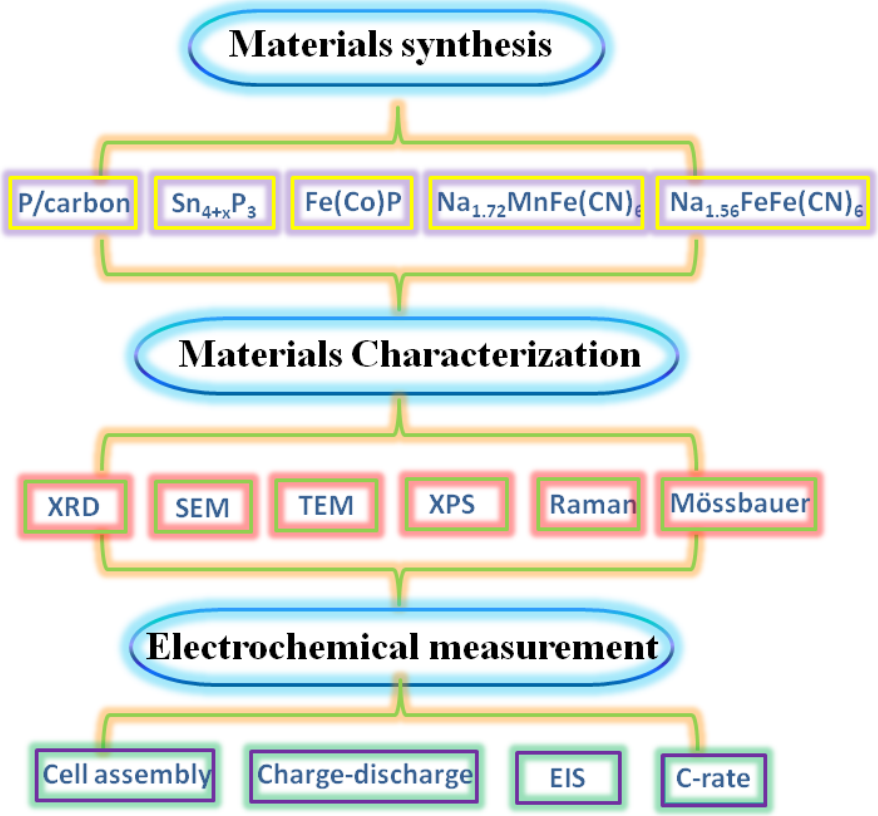

Figure 3.1. The outline of my experimental procedures.

3.1 Chemicals and materials

The chemicals and materials used in this doctoral work are summarized in Table 3.1.

Table 3.1 Chemicals and materials used in this work.

Materials/Chemicals	Formula	Purity (%)	Supplier

Carboxymethyl cellulose (CMC)	$C_8H_{16}NaO_8$	N/A	Sigma Aldrich
Polyacrylic acid (PAA)	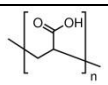	N/A	Sigma Aldrich
Polyvinylidene difluoride (PVDF)	$(CH_2CF_2)_n$	N/A	Sigma Aldrich
1-methyl-2-pyrrolidinone (NMP)	C_5H_9NO	99.5	Sigma Aldrich
Copper foil	Cu	N/A	China
Carbon black	C	Super P	Timcal Belgium
CR2032 type coin cells	N/A	N/A	China
Diethyl carbonate (DEC)	$C_5H_{10}O_3$	99^+	Sigma Aldrich
Ethylene carbonate	$C_3H_4O_3$	99	Sigma Aldrich
Graphite	C	N/A	Sigma Aldrich
Sodium metal	Na	99.9	Sigma Aldrich
Sodium perchlorate	$NaClO_4$	98^+	Sigma Aldrich
Fluoroethylene carbonate	FEC	99	Sigma Aldrich
Multi-wall carbon nanotube	C	CNT	Sigma Aldrich
Iron powder	Fe	97^+	Sigma Aldrich
Tin powder	Sn	99^+	Sigma Aldrich
Cobalt powder	Co	99.95	Sigma Aldrich
Pure ethanol	C_2H_5OH	99.95	Sigma Aldrich
Pyrrole		98	Sigma Aldrich
Sodium chloride	NaCl	99^+	
Hydrochloric acid	HCl	N/A	Sigma Aldrich
Sodium ferrocyanide decahydrate	$Na_4Fe(CN)_6 \cdot 10H_2O$	99^+	Sigma Aldrich
Poly(vinylpyrrolidone) (PVP)	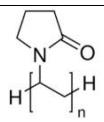	N/A	Sigma Aldrich

sodium citrate	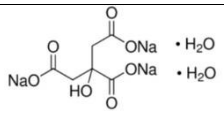	N/A	Sigma Aldrich
manganese acetate tetrahydrate	$Mn(CH_3COO)_2 \cdot 4H_2O$	99^+	Sigma Aldrich
Dimethyl carbonate	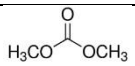	99^+	Sigma Aldrich
Iron (III) chloride	$FeCl_3$	97^+	Sigma Aldrich

3.2 Materials preparation

3.2.1 Ball milling method

A ball mill is a type of grinder used to grind and blend materials for use in mineral dressing processes. Ball mills are used extensively to produce alloys from powders. A ball mill works on the principle of impact, as the balls drop from near the top of the shell. There are some requirements for the grinding media (ball and jar): (1) Size: the grinding media particles are required to be larger than the largest pieces of material which are to be ground. It is noted that the particle size of the final product is more smaller if the smaller the media particles. (2) Density: The grinding media is required to be denser than the ground material. Otherwise, the grinding media will float on top of the ground material resulting in loosing the grinding function. (3) Hardness: The grinding media is required to have proper hardeness so that it can be durable enough to grind the material rather than it wears down due to its toughness. (4) Composition: The specifice requirements depends on different grinding applications.

The ball-milling method has unique advantages, making it a common method used for SIBs: the cost of the installation, power, and grinding medium is low; it is suitable for both batch and continuous operation, and similarly, it is suitable for open as well as closed circuit grinding and is applicable for materials with all degrees of hardness. The ball-milling machine used in this doctoral work is a Fritsch Pulverisette 7, shown in Figure 3.2.

Figure 3.2. The ball-milling machine.

3.2.2 Co-precipitation method

Co-precipitation (CPT) is a normal chemiscal method which product the precipation by mixing soluble solution under the specific conditions employed. In application of lithium ion batteries and sodium ion batteries, co-precipitaion is a commonly used synthesis method because it is facile, scalable and low energy consumption. In this doctoral work, co-precipitation is used to prepare the Prussian-blue analogues.

3.2.3 Polymerization

Polymerization is a chemical process in which the monomer molecules react together to form polymer chains or three-dimensional networks. Most photopolymerization reactions are chain-growth polymerizations, which are triggered by the absorption of visible or ultraviolet light. The light may be absorbed either directly by the reactant monomer (direct photopolymerization) or else by a photosensitizer, which absorbs the light and then transfers energy to the monomer. Generally, synthesizing the polymer requires two steps. One is to disperse the monomer precursors and catalyst into the solvent at the required temperature. The second step is to add the oxidant into the monomer precursor. In this doctoral work, we use polymerization of pyrrole to form polypyrole (PPy) on the surface of Prussian blue particles.

3.3 Physical and chemical characterization techniques

3.3.1 X-ray diffraction

X-ray diffraction (XRD) is a basic technique to identify the atomic and molecular structure of a crystal. The principle of XRD is illustraetd in Figure 3.3. When X-rays comes up with the crystals, it will be scattered by each set of lattice planes at a unique angle. This phenomenon

is called as elastic scattering. The patterns of the scattering X-ray waves have the characteristic relations with the give crystal materials, which can be determined by Bragg's law:

$2d\sin\theta = n\lambda$ (3.1).

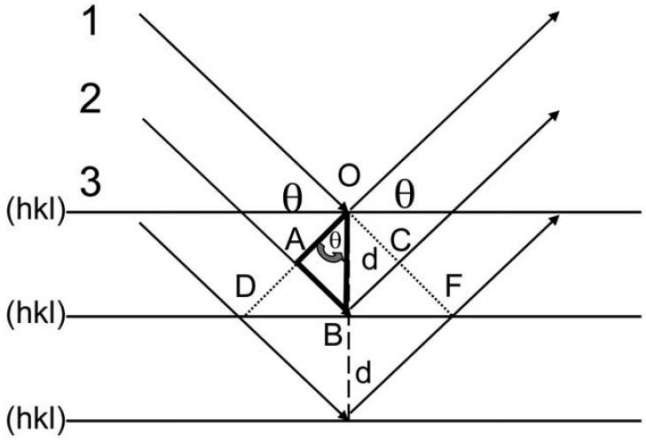

Figure 3. Bragg's law can be derived from the geometrical relation between the interplanar spacing d and the diffraction angle θ.[254]

Here d is the spacing between crystal planes in the given materials, θ is the incident angle, n is an integer, and λ is the wavelength of the incident X-ray beam. Thus, X-ray powder diffraction is most widely used for the identification of unknown crystalline materials. Determination of unknown solids is critical to studies in geology, environmental science, materials science, engineering and biology. Moreover, through Rietveld refinement, XRD can determine the crystal structure and unit cell dimensions, and measure the sample purity.

3.3.2 Synchrotron XRD

In Synchrotron Radiation X-Ray Powder Diffraction (SR-XRPD), X-rays generated by a synchrotron facility is at least 5 orders of magnitude more intense than the best X-ray laboratory source. In comparison with laboratory XRD, synchrotron XRD (SXRD) has some significant advantages: (1) High photon wavelength resolution; (2) Tunable photon energy, ideal for acquiring fluorescence-free XRD data and better diffraction peaks separation; (3) Angular (FWHM) resolution better than 0.01 °2θ; (4) d-spacing resolution better than 0.35 Å; (5) Ultra-fast data ciollection (millisecond scale); (6) Very high counting statistics (millions of counts) in a few seconds. In this doctoral work, SXRD measurements were carried out at the Australian Synchrotron Powder Diffraction Beamline.

3.3.3 Scanning electron microscopy equipped with energy dispersive spectroscopy

A scanning electron microscope (SEM) is a type of electron microscope which scans the sample with a high-energy beam of electrons to produce images of it. The electrons interact with atoms in the sample, producing various signals, including secondary electrons (SE), back-scattered electrons (BSE), characteristic X-rays, specimen currents under illumination, and transmitted electrons. Through these signals, we can detect and collect information on the morphology, composition, and other properties of the sample surface, such as electrical conductivity. In the mode of secondary electron imaging (SEI), the high-resolution images of a sample surface can be obtained to observe details under 1 nm in size.

Usually, SEM is equipped with some other detectors which have other analytical capabilities, for example, energy-dispersive X-ray spectroscopy (EDS, EDX, or XEDS). EDS is an analytical technique which is used to detect the elemental analysis or chemical characteristics of a sample. Its characterization capabilities rely on an interaction between some source of X-ray excitation and the sample, because each element has a unique atomic structure, allowing a unique set of peaks on its X-ray spectrum. In my doctoral work, the morphology, elemental analysis, and elemental mapping of the samples were detected by field emission scanning electron microscopy (FESEM; JEOL JSM-7500FA).

3.3.4 Transmission electron microscopy

Transmission electron microscopy (TEM) is a microscopy technique where a electron beam is transmitted through an ultra-thin sample, interacting with the sample when it passes through. TEM can be used to observe morphology, crystal structure, and electronic structure. Its selected area electron diffraction (SAED) capability can be used to identify crystal structures and examine crystal defects. Scanning transmission electron microscope (STEM) is a modified TEM by adding a system which rasters the beam across the sample to form the image. In this doctoral work, TEM of the samples was carried out using transmission electron microscopy (TEM, JEOL 2011, 200 keV) and scanning transmission electron microscope (STEM, JEOL ARM200F).

3.3.5 X-ray photoelectron spectroscopy

X-ray photoelectron spectroscopy (XPS) is a surface-sensitive technique to test the surface chemistry of a material in its as-received state or after some treatment. XPS usually test: (1) What elements and the quantity of those elements exist within sample surface. (2) The chemical state of identified elements. (3) The binding energy of the electronic states. (4) The density of electronic states. In this doctoral work, X-ray photoelectron spectroscopy (XPS)

was conducted using a SPECS PHOIBOS 100 Analyser installed in a high-vacuum chamber with base pressure below 10^{-8} mbar. X-ray excitation was provided by Al Kα radiation with photon energy hv = 1486.6 eV at the high voltage of 12 kV and power of 120 W. The XPS binding energy spectra were collected at the pass energy of 20 eV in the fixed analyser transmission mode. Analysis of the XPS data was carried out using the commercial CasaXPS 2.3.15 software package. All the spectra were calibrated by C 1s = 284.6 eV.

3.3.6 Raman spectroscopy

Raman spectroscopy is commonly used in chemistry to provide a fingerprint by which molecules can be identified. It can observe vibrational, rotational, and other low-frequency modes in a system. For instance, the vibrational frequencies of SiO, Si_2O_2, and Si_3O_3 were identified and assigned on the basis of normal coordinate analyses using infrared and Raman spectra.[255]The fingerprint region of organic molecules is in the (wavenumber) range of 500-2000 cm^{-1}. Another way that the technique is used is to study changes in chemical bonding, such as when a substrate is added to an enzyme. In this work, Raman spectra were collected using a JOBIN Yvon Horiba Raman 57 Spectrometer model HR800.

3.3.7 Fourier Transform Infrared Spectroscopy (FTIR)

Infrared spectroscopy (IR spectroscopy) is a common method based on absorption spectroscopy.It is used to collect an infrared region spectra of emission, absorption, and photoconductivity. In this doctoral work, a Nicolet Avatar 360 FTIR Fourier transform infrared spectrometer was used to collect FTIR spectrographs. The samples were mixed with KBr powder which acts as the background file, followed by placing the samples in a sample cup.

3.3.8 Mössbauer spectroscopy

Mössbauer spectroscopy is an analysis technique based on the Mössbauer effect to detect the magnetic properties and oxidation state of compounds. In this doctoral work, the ^{57}Fe Mössbauer spectra of the samples were detected at 300 K by using a ^{57}CoRh source and a standard constant-acceleration spectrometer. The spectrometer was calibrated at room temperature with α–ion foil.

3.3.9 Physical Properties Measurement System (PPMS)

The physical properties measurement system (PPMS) is an instrument that provides common analysis techniques in materials science, condensed matter physics, and analytical chemistry. It can measure the widest range of magnetic, thermal, and electrical properties of the analyte. In this doctoral work, the magnetic measurements were carried out using a 14 T physical

properties measurement system (PPMS), equipped with a vibrating sample magnetometer (VSM), over a wide temperature range from 5 K to 300 K in a 1000 Oe magnetic field.

3.3.10 Thermogravimetric analysis (TGA)

Thermogravimetric analysis (TGA) is a thermal analysis method to study the changes with temperature in the physical and chemical properties of materials. TGA analysis depends on a function of temperature or time. TGA is commonly used to test the composition of composites according to the weight loss or gain. In this doctoral work, TGA was carried out by using a SETARAM Thermogravimetric Analyzer (France) to measure the PPy content in the composite samples.

3.4 Electrochemical Measurements

3.4.1 Electrode preparation and battery assembly

Electrodes were prepared by mixing active materials, carbon black, and binder (carboxymethyl cellulose (CMC), polyvinylidene difluoride (PVDF), polyacrylic acid (PAA)) by weight ratio to form an electrode slurry, which then was coated on copper foil, followed by drying in a vacuum oven overnight at 80 ℃ for CMC and PAA binder or 120 ℃ for PVDF binder, and then pressing with a pressure of 30 MPa. The average loading mass for an electrode is 2 $mg \bullet cm^{-2}$. Then, the electrodes were assembled in 2032-type coin cells in an Ar-filled glove box. Sodium foil was cut by the doctor blade technique from sodium bulk stored in mineral oil, and it then was employed as both reference and counter electrode. A schematic illustration of the Na half-cell assembly is presented in Figure 3.4. The working electrode was first placed at the positive cap, and then 2 drops of electrolyte were dropped in. Then, the separator was placed on the top of working electrode followed by dropping an extra 2 drops of the electrolyte. The Na electrode, steel spacer, spring and positive cap were placed subsequently. Finally, the coin cell was sealed.

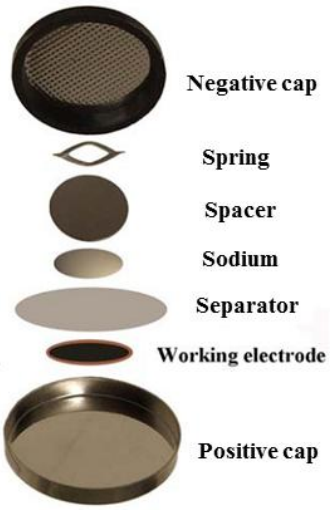

Figure 3.4. Schematic illustration of Na half-cell assembly.

3.4.2 Cyclic voltammetry

Cyclic voltammetry (CV) is an important electroanalytical technique that is commonly used to measure a variety of redox reactions. Thus, it can detect the electrochemical activity of electrode materials, and also can determine the stability of resultant products, reactions, and electron transfer kinetics, the presence of intermediates in redox reactions, and the reversibility of a redox reaction. In addition, CV can determine the reduction potential, the electron stoichiometry and the diffusion coefficient of a system. CV curves usually display a hysteresis in the absolute potential between the cathodic and anodic peaks due to the polarization of the electrode, which results from a combination of the diffusion rate and the intrinsic activation barrier obstructing the transfer electrons from an electrode to the sample. In a typical CV experiment, the potential of the cell is scanned at a specified scan rate, and then the response current is collected. In this doctoral work, the CV data were obtained on a Biologic VPM3 electrochemical workstation. All the CV testing is based on the two-electrode model, in which sodium foil (for SIBs) acts as the reference electrode and counter electrode.

3.4.3 Galvanostatic Charge-Discharge

Galvanostatic charge-discharge measurements are conducted in constant current density mode to test the capacity and cycling performance of the materials in a certain voltage window. This testing technique can also be used to estimate the rate capability of the electrode materials by using a variety of current densities. The charge or discharge capacity (Q) equals the total electron charge in the corresponding process and can be calculated from

the applied current and the total time. In this doctoral work, galvanostatic charge-discharge measurement was carried out with an automatic battery tester system (Land®, Wuhan, China).

3.4.4 Electrochemical impedance spectroscopy

Electrochemical impedance spectroscopy (EIS) is an important experimental measurement technique to test the inner resistance of a sodium-ion cell. EIS can determine the charge transfer resistance, double layer capacitance, and ohmic resistance of a cell. Normally, the impedance spectrum of a cell consists of a semicircle and a linear tail at high-frequency and low-frequency, respectively. The semicircle is attributed to the charge transfer resistance, reflecting the kinetic processes and the double layer capacitance. The linear tail relates to the diffusion of alkali ions into the bulk of the electrode materials from the electrolyte. Moreover, EIS can measure the alkali ion (Li^+, Na^+) diffusion and apparent energy activation of the electrode. In this doctoral thesis, EIS data were collected on a Biologic VPM3 electrochemical workstation.

Chapter 4. Simply Mixed Commercial Red Phosphorus and Carbon Nanotube Composite with Exceptionally Reversible Sodium-ion Storage

The commercially available red phosphorus with micro-size particle shows large initial specific capacity but cannot react with Na reversibly. A reversible sodium ion storage can be realized, when bulk commercial phosphorus particles were crushed into amorphous nanoparticles. Therefore, the question was raised here as to whether commercial red phosphorus with large particles can react reversibly with Na just via improving the electronic conductivity.

4.1 Introduction

Looking forward to the energy future of humanity, renewable energy will definitely the most sustainable way to solve many social and environmental problems. How to store the variable renewable energy in an efficient and cheap way would be a great challenge. The most promising energy storage systems should combine the features of relatively high energy density, good power capability, enviromental friendliness, and low cost.[256,257] Recently, sodium ion batteries (SIBs) have been given intense attention because they are the most promising alternative to lithium ion batteries for application in renewable power stations, owing to their low cost, their abundant natural resources, and the similar chemistry of sodium and lithium. In the last ten years, a large variety of host materials have been demonstrated as sodium ion storage cathodes, as summarized in recent review papers,[48,258] such as sodium transition metal oxidesand $MFe(CN)_6$ (M = Na, K).[169,174,175,259,260] In comparison, there have been few investigations on anode materials for SIBs. In the light of the successful experience with carbon anodes in lithium ion batteries (LIBs), carbonaceous materials, such as hard carbons,[58,261-264] carbon nanospheres and nanowires, and graphene, have been introduced as anode materials for SIBs.[210-212] Subsequently, Sn and Sb-based materials have been studied as anode for sodium ion batteries, as they have high reversible capacity, but their specific capacities are still relatively low (500 - 800 mAh g^{-1}).[70,247,265,266]

Elemental phosphorus (P) is an attractive anode material, which can give a high theoretical specific capacity of 2596 mAh g^{-1} to form Na_3P phase. Phosphorus has three allotropes, white, black, and red. Among these allotropes, white phosphorus is not chemically stable, and synthesis of black phosphorus is not facile, as it needs an inert atmosphere under high pressure.[250,251] In comparison, red phosphorus is commercially available with ease. For

sodium ion storage, recently, Qian et al. and Kim et al. reported that an amorphous phosphorus composite with carbon that was obtained by high-energy mechanical milling could deliver a high capacity of 1764 mAh g^{-1} at the current density of 250 mA g^{-1} and 1890 mAh g^{-1} at current density of 143 mA g^{-1}, respectively.[1,252] Based on their reports, the commercially available red phosphorus with micro-size particle shows large initial specific capacity but cannot react with Na reversibly. A reversible sodium ion storage can be realized, when bulk commercial phosphorus particles were crushed into amorphous nanoparticles, highly dispersing in a conductive carbon matrix, during the long and vigorous high-energy ball milling. Crystalline P can reversibly react with Li ions, however, via the electronic improvement of P by vaporization and condensation on mesoporous carbon.[267] The electronic modification was the main reason for the reversible de/insertion of Li ions into/out of crystalline red phosphorus. Therefore, the question was raised here as to whether commercial red phosphorus with large particles can react reversibly with Na just via improving the electronic conductivity.

Making carbon composite materials is one effective solution to improve conductivity in the battery field. Carbon nanotubes (CNTs) could be a promising candidate to serve as both the conductive network and the buffer to alleviate the stress from volume expansion, owing to its advantages of a unique network structure with low electrical resistivity and good mechanical properties, such as strength, stiffness, and resilience.[268-272] All the previous reports used different dedicated chemical or physical methode to prepare composite materials, which would also increase the cost of the materials. Herein, we kept the particle of commercial red phosphorus in micrometer size, simply mixed it with CNTs by hand grinding, to unexpectedly achieve highly reversible sodium storage in commercially available red phosphorus. The simplicity of the preparation method and the highly reversible sodium storage are likely to make a great impact in the reseach on sodium battery materials.

4.2 Experimental section

4.2.1 Materials preparation.

Crystalline red phosphorus/carbon nanotube (denoted as P/CNT) composite was prepared using a facile and simple method: hand grinding commercial red phosphorus (99%, Sigma Aldrich) with multi - wall carbon nanotubes (95%, Nanostructured & Amorphous Materials Inc.) in an agate mortar for 1 h. The composites mixed for 10, 20h were prepared by low-

energy ball milling. The weight ratio of red phosphorus to multi - wall carbon nanotubes was 7:3.

4.2.2 Structural and electrochemical characterizations.

The microstructure of the powders was characterized by Powder X-Ray diffraction (XRD; GBC MMA diffractometer) with Cu Kα radiation at a scan rate of 2° min^{-1}. The morphology of the samples was investigated by field emission scanning electron microscopy (FESEM; JEOL JSM-7500FA) and transmission electron microscopy (TEM, JEOL 2011, 200keV). Raman spectra were collected using a JOBIN Yvon Horiba Raman spectrometer model HR800, with a 10 mW helium/neon laser at 632.8 nm excitation in the range of 150 to 2000 cm^{-1}. X-ray photoelectron spectroscopy (XPS) was conducted using a SPECS PHOIBOS 100 Analyser installed in a high-vacuum chamber with the base pressure below 10–8 mbar, X-ray excitation was provided by Al Ka radiation with photon energy hν = 1486.6 eV at the high voltage of 12 kV and power of 120 W. The XPS binding energy spectra were recorded at the pass energy of 20 eV in the fixed analyser transmission mode. Analysis of the XPS data was carried out using the commercial CasaXPS 2.3.15 software package. All the spectrum were calibrated by C1s=284.6ev.

4.2.3 Electrochemical measurements

The electrochemical measurements of the phosphorus/multi-wall carbon nanotube as anode-active material were done using 2032 - type coin cells. The working electrode was prepared by coating slurry containing 70 wt% active materials, 10 wt% Super-P carbon black, and 20 wt% carboxymethyl cellulose (CMC) binder on a copper foil substrate. Then, the electrode film was dried in a vacuum oven at 80 ℃ overnight. The electrolyte used in this work was 1.0 mol L^{-1} $NaClO_4$ in an ethylene carbonate (EC) - diethyl carbonate (DEC) solution (1:1 v/v), with 5 wt% addition of fluoroethylene carbonate (FEC). All the cells were assembled in a glove box filled with argon and tested at room temperature. The galvanostatic charge/discharge testing was conducted on a Biologic VMP3 electrochemical workstation with a cut-off voltage range from 0 - 1.5 V (vs. Na/Na^+) at a constant reversal current of 143 mA g^{-1}.

4.3 Results and discussion

Figure 4.1 shows the Raman spectra and X-ray diffraction (XRD) patterns for commercial red phosphorus (P), carbon nanotubes (CNTs), and P/CNT composite. The XRD pattern of the commercial red P shows a sharp diffraction peak at 15 ° (Figure 4.1(a)), suggesting a

medium-range ordered structure.[273] The multiwall CNTs show two peaks at 26 ° and 44 °, respectively. After grinding red phosphorus with CNTs for 1 h, there is no new phase in the XRD pattern of the composite. The composite consists of commercial red phosphorus and carbon nanotubes (Figure 4.1(a)). The Raman spectra further demonstrate that the composite only exhibits peaks of red phosphorus and carbon nanotubes (Figure 1(b)). Three bands from 300 cm^{-1} to 500 cm^{-1} can be assigned to red phosphorus. The two peaks at 1324 cm^{-1} and 1571 cm^{-1} are the D-band and G-band of carbon nanotubes, respectively. Moreover, no shift in the D-band of the carbon nanotubes can be observed, indicating that there are no interactions between the P and the CNTs. XPS results further demonstrate this point (Figure 4.2). Hence, after grinding for 1 hour, the starting red phosphorus retains its pristine structure, showing that it is only physically mixed with the carbon nanotubes to form the P/CNT composite. Figure 4.3 shows the morphology of the P/CNT composite. The particle size of bulk commercial red phosphorus (Figure 4.3 (a)) was broken down to an average of 3 μm after grinding (Figure 4.3(c)). Moreover, the red phosphorus particles were wrapped up by the CNTs, which would be helpful for increasing the electronic conductivity of the red phosphorus (Figure 4.3(d, e,)).

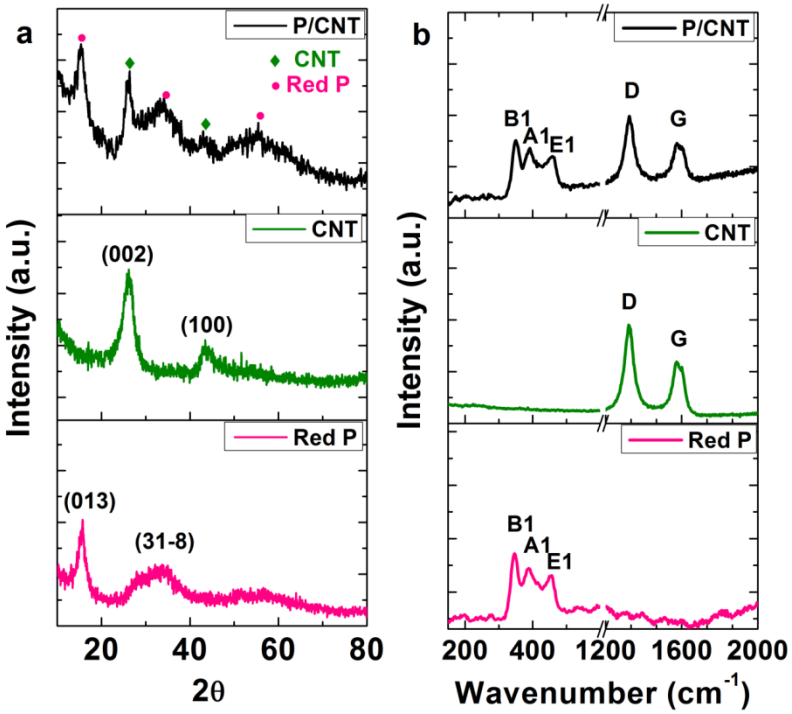

Figure 4.1. (a) XRD and (b) Raman spectra of the commercial red P, CNTs, and P/CNT composite.

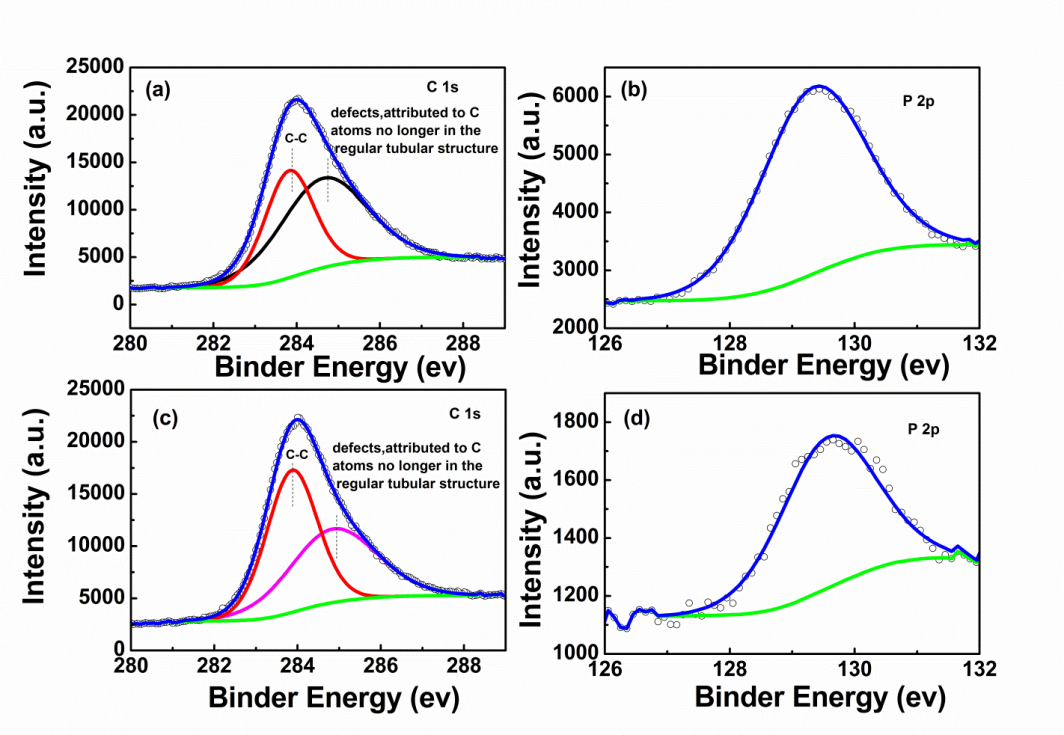

Figure 4.2. X-ray photoelectron spectroscopy of the (a) CNT, (b) phosphorus and (c, d) P / CNT composite ((c) C1s and (d) P 2p).

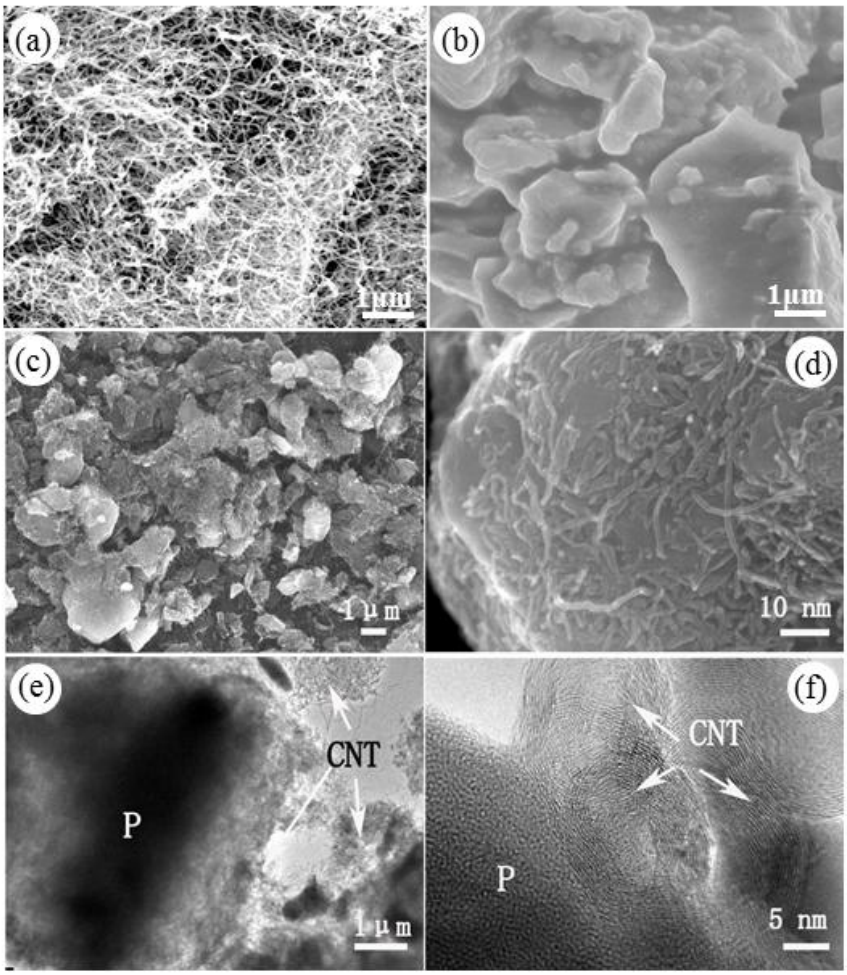

Figure 4.3. SEM images of the starting carbon nanotubes (a) and commercial P (b), and (c, d) images of P/CNT composite, (e,f) TEM images of P/CNT composite. (c, e) low and (d, f) high magnification.

Figure 4.4(c) presents the charge/discharge curves of the commercial P and P/CNT composite between 0 and 1.5 V at a current density of 143 mA g^{-1}. The commercial red phosphorus delivered an initial discharge capacity of ~1600 mAh g^{-1}. Its initial charge capacity was only 50 mAh g^{-1}, however, demonstrating its irreversible electrochemical performance. This result is similar to those reported in literature.[1,252] The pristine CNT also shows limited reversible capacity for sodium storage. It delivered ~300 mAh g^{-1} initial discharge capacity and ~40 mAh g^{-1} charge capacity in the first cycle (Figure 4.4(a)). Interestingly, when the commercial red phosphorus was mixed with the CNTs, it exhibited highly reversible charge/discharge capacity. The charge/discharge profiles of the P/CNT composite are similar to those of a reported amorphous red P/carbon black composite.[1]The initial discharge capacity of the P/CNT composite electrode was ~2210 mAh g^{-1}, which is about 40% larger than that of the

red P one, while the charge capacity was 1530 mAh g^{-1} in the first charge (Figure 4.4(c)). The specific capacity was calculated based on the weight of the phosphorus, because the contribution of the carbon nanotubes to the reversible capacity is negligible (only 40 mAh g^{-1}).

In order to clarify the reactions of the P/CNT composite in SIBs, the dQ/dV curves of red P and P/CNT composite are displayed in Figure 4.4(d) and (e). One small (~0.9 V) and two large (below 0.5 V) cathodic peaks can be seen in both samples. The peak position for red P is lower than for the P/CNT composite, which is due to the high resistance of the red P sample. The first small peak (Figure 4.4(e)) can be attributed to the decomposition of electrolyte in the formation of a solid-electrolyte interphase (SEI) layer on the surface of the active materials. The second cathodic peak located in the range of 0.2 - 0.35 V corresponds to the sodium ion insertion reaction to form the Na_xP compounds. The peak at around 0.1 V is ascribed to the formation of fully charged Na_3P phase.[252] In the reversed process, a very weak peak can be observed for the commercial red phosphorus (Figure 4.4(e)), demonstrating the irreversible desodiation process, while the P/CNT composite has one sharp peak and two small shoulder peaks, indicating a reversible sodiation/desodiation process. This phenomenon is possibly owing to the improvement of electronic conductivity after CNT addition.

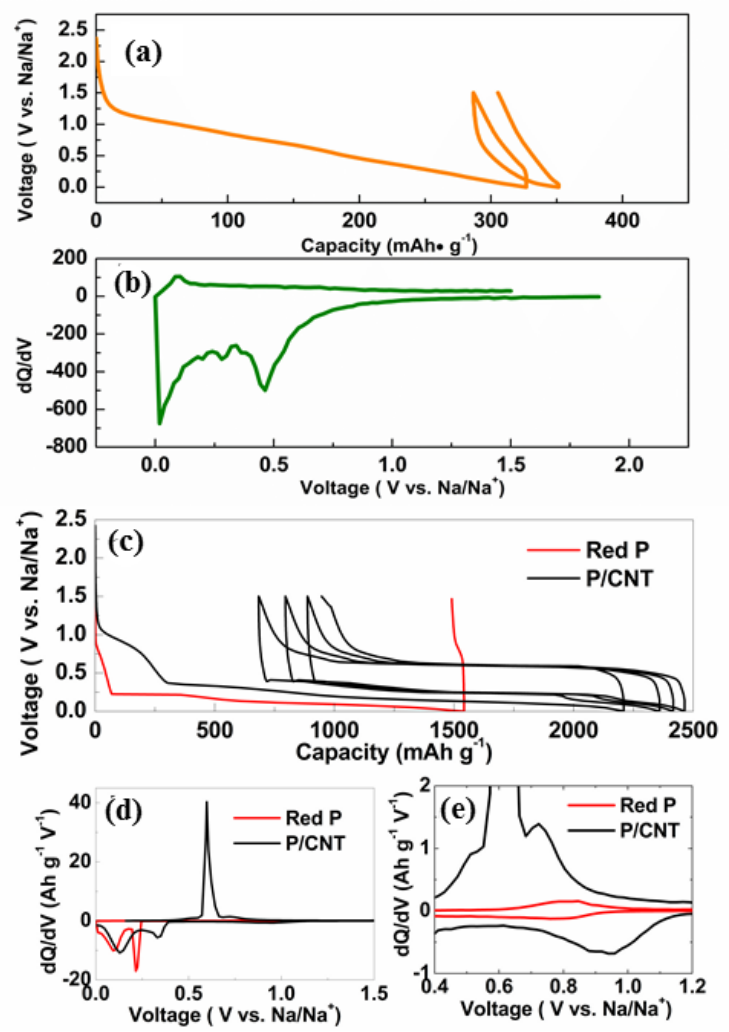

Figure 4.4. Initial charge-discharge curve (a) and (b) dQ/dV of CNTs. Charge-discharge curves (c) and dQ/dV ((d) and (e)) curves of red P and P/CNT composite at current density of 143 mA g^{-1} from 0 - 1.5 V; (d) is the enlargement of (f) from 0.4 to 1.2 V.

Electrochemical impedance spectroscopy (EIS) was conducted to further investigate the conductivity enhancement. Figure 4.5 shows the Nyquist plots of the P/CNT composite electrode compared with commercial P electrodes in the charged state at 0.65 V (vs. Na^+/Na). The impedance curves of both P/CNT and red P show two semicircles in the medium frequency and the low frequency regions, which could be assigned to the sodium ion diffusion through the solid electrolyte interphase (SEI) film (R_x) and the charge transfer resistance (R_{ct}), respectively. The R_{ct} is calculated using the equivalent circuit shown in the inset of Figure 4.5. The R_{ct} value of the commercial red P was 7500 Ω, but after the addition of CNTs, the R_{ct} value significantly decreased to 3900 Ω. This demonstrates that addition of

CNTs can significantly improve the conductivity of bulk commercial red P, delivering reversible charge/discharge capacity.

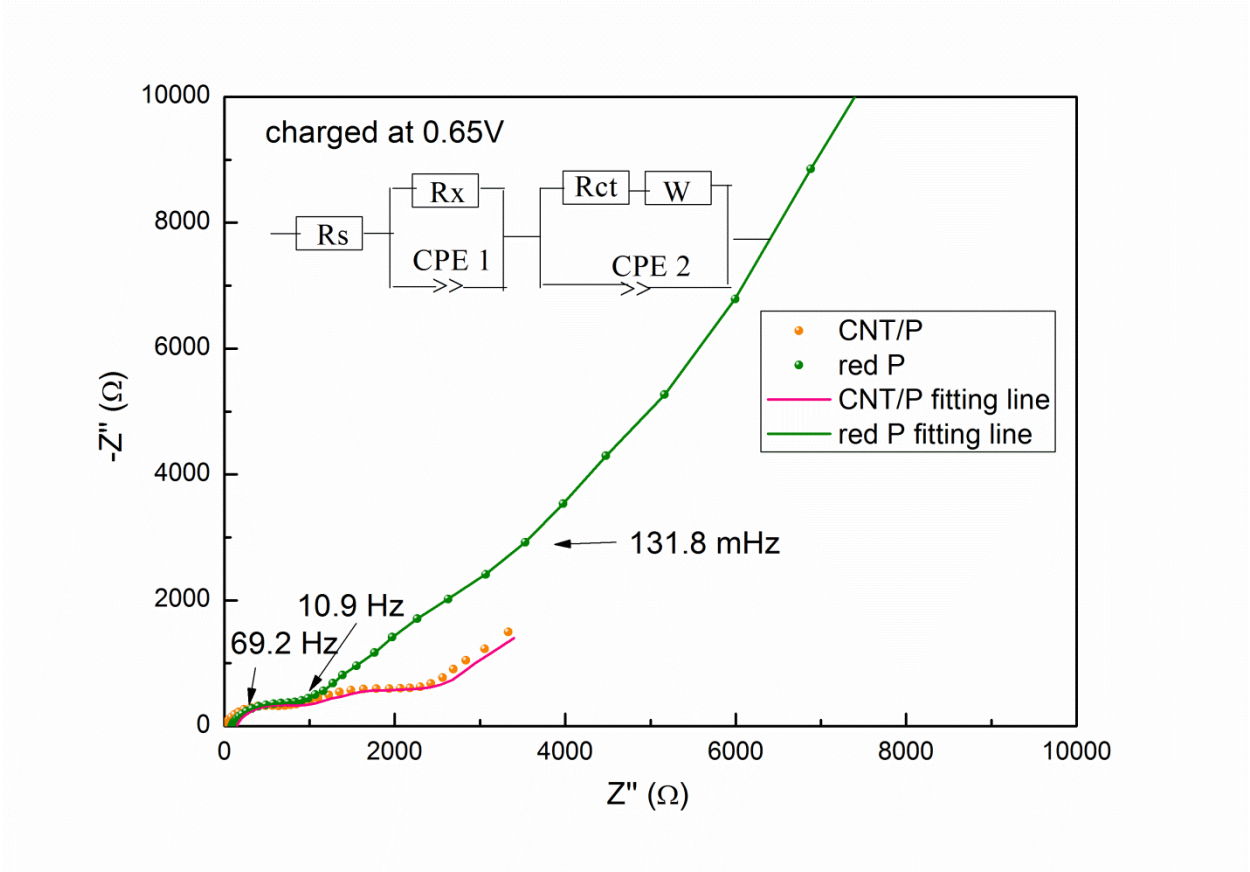

Figure 4.5. Electrochemical impedance spectrum of P/CNT compared with that of commercial red P in the charged state at 0.65 V in the first cycle. The inset shows the equivalent circuit used to interpret the data.

In order to further confirm the function of CNTs in the composite, P/carbon black (Super-P, CB) composite was prepared by hand grinding for 1 h, in which the weight percent of carbon black was also 30%. The cycling performance of P/CNT compared with P/carbon black is shown in Figure 4.6(a). When commercial red phosphorus was mixed with 30 wt.% carbon black, its initial discharge capacity (2200 mAh g^{-1}) was increased compared with the pristine red phosphorus (1530 mAh g^{-1}). Although the P/carbon black electrode could charge-discharge reversibly, the discharge capacity dropped dramatically, down to 770 mAh g^{-1} for the 2nd cycle and only 90 mAh g^{-1} for the 3rd cycle. In comparison with the P/carbon black composite, the reversible cycling performance of the P/CNT composite was much better. After 10 cycles, the discharge capacity was 1283.3 mAh g^{-1}, with 76.6 % reversible capacity retention.

In order to obtain good electrochemical performance, we optimized the weight ratio of carbon nanotubes to red phosphorus (see Figure 4.6(b, c)). From Figure 4.6(b), It is clear that the initial discharge capacity increased with the weight ratio of CNTs increasing from 10% to 50%, moreover, the cycle stability was also improved. However, when capacity was calculated on weight of composite, the composite with 30 wt.% CNTs performed more stable cycling performance (Figure 4.6(c)). It should be notice that the cycle stability of composite is not good enough, to achieve long cycle life, we should make further efforts in future, such as selecting appropriate binder which has both good cohesiveness and favorable mechanical properties, to get better stable electrochemical performance of commercial red phosphorus.

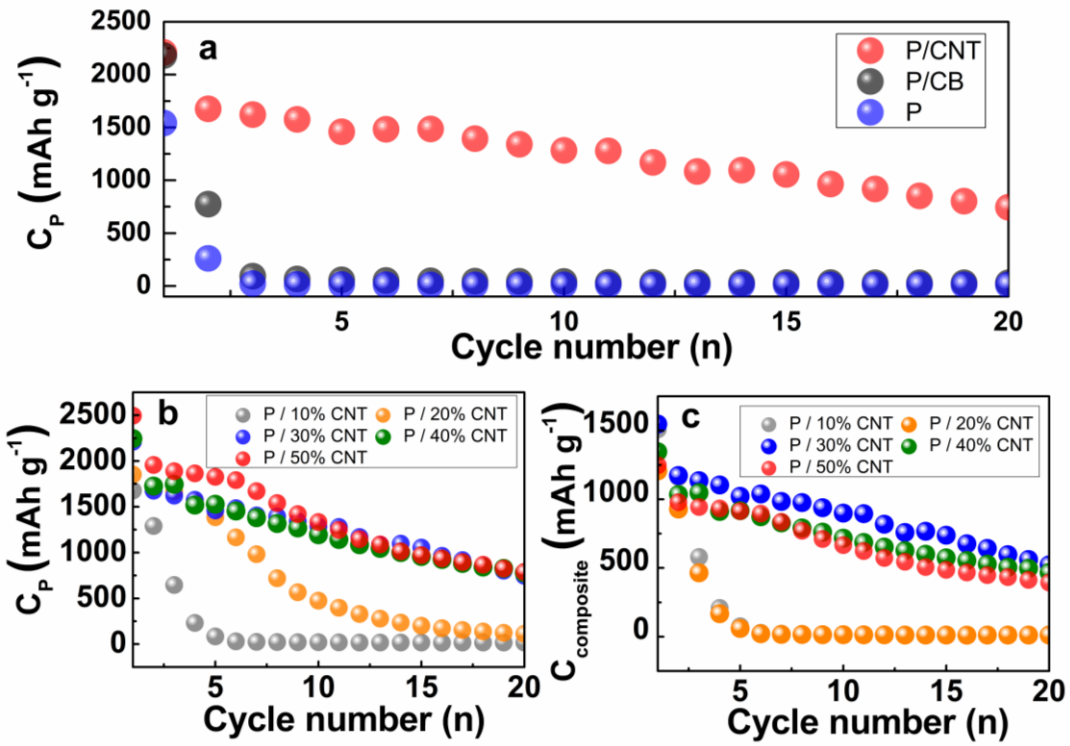

Figure 4.6. Cycling performance of P/CNT composite: (a) P/CNT composite compared with P/carbon black composite, (b) Capacity is calculated on weight of P and (c) P/CNT composites with different CNT content.

It is obvious that the commercial red phosphorus wrapped with CNTs can reversibly cycle better than when mixed with carbon black. The most likely reason would be that the CNTs could form a network structure and increase the buffer space between the P particles as shown in Figure 4.7. Since the volume expansion is around 491% during the phase transition from phosphorus to Na_3P after the initial discharge, CNTs, which have excellent mechanical properties, can effectively buffer enormous stresses and thus reduce the rate of bulk red

phosphorus pulverization. Also there are some reported papers make use of the CNT's network structure as a soft matrix to remit the stress from volume expansion of Si,[274] Sn,[272] SnO_2[275] and SnSb[276,277] in LIBs. For sodium ion batteries, recently, Wang and co-workers used CNT as a matrix and a conducting network to provide good contact between isolated SnO_2 particles and buffer the volume expansion of SnO_2 nanocrystals.[278] The network structure provides pathways for electron transport that promote good connections between the red phosphorous particles and reduce the influence of volume expansion on the connections not only between the red phosphorus particles, but also between red phosphorus and the current collector. This point was supported by the morphology of the P/carbon black (Figure 4.8) and P/CNT (Figure 4.9) composite electrodes before and after one cycle. It is apparent that the small carbon black particles didn't completely cover the big phosphorus particles, as shown in Figure 4.8(a). In contrast, the bulk red phosphorus particles were wrapped well by the CNT network in the P/CNT composite (Figure 4.9(a)). That is why the P/CNT composite electrode has better electronic conductivity than the P/carbon black composite electrode. After one cycle, there is a big change on the surface of the P/carbon black composite electrode. The fluffy morphology can be observed in Figure 4.8(b). It is due to both the formation of the SEI layer and huge volume change when sodium ions are inserted into and extracted from P, which induces strong stresses on the phosphorus particles and causes pulverization and rapid capacity fading (Figure 4.6). A similar phenomenon also can be observed when Li ions are inserted into and de-inserted from Si particles.[279] In contrast, the surface of the P/CNT composite electrode did not change much after 1 cycle, as shown in Figure 4.9(b). The red phosphorus particles cracked into small particles, but were still wrapped by the CNTs (Figure 4.9(c), which maintained the electronic connections among the red phosphorus particles. As a result, the P/CNT composite electrode could still be cycled beyond the first few cycles, with a relatively stable capacity (Figure 4.6).

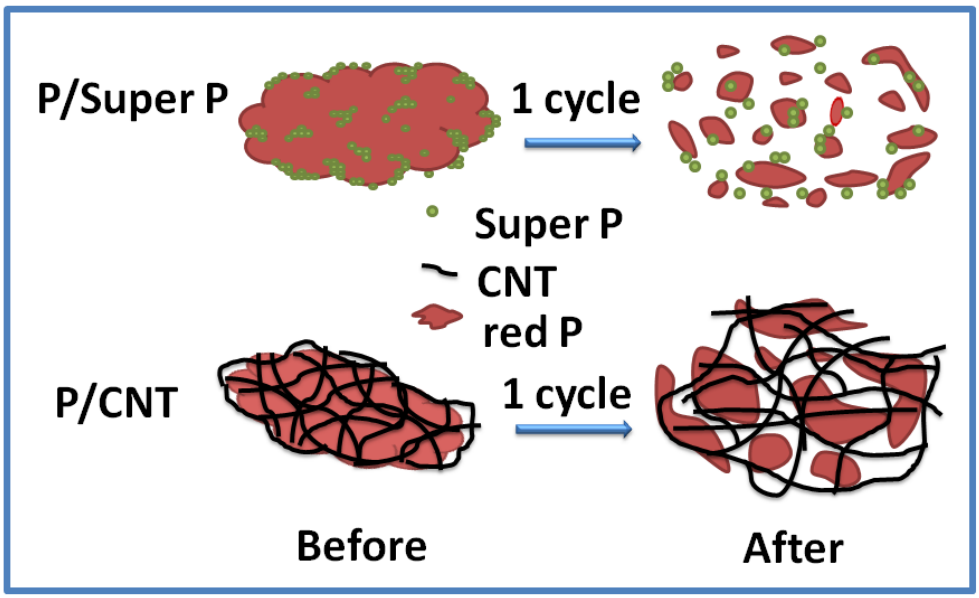

Figure 4.7. Proposed function of CNTs during the volume expansion.

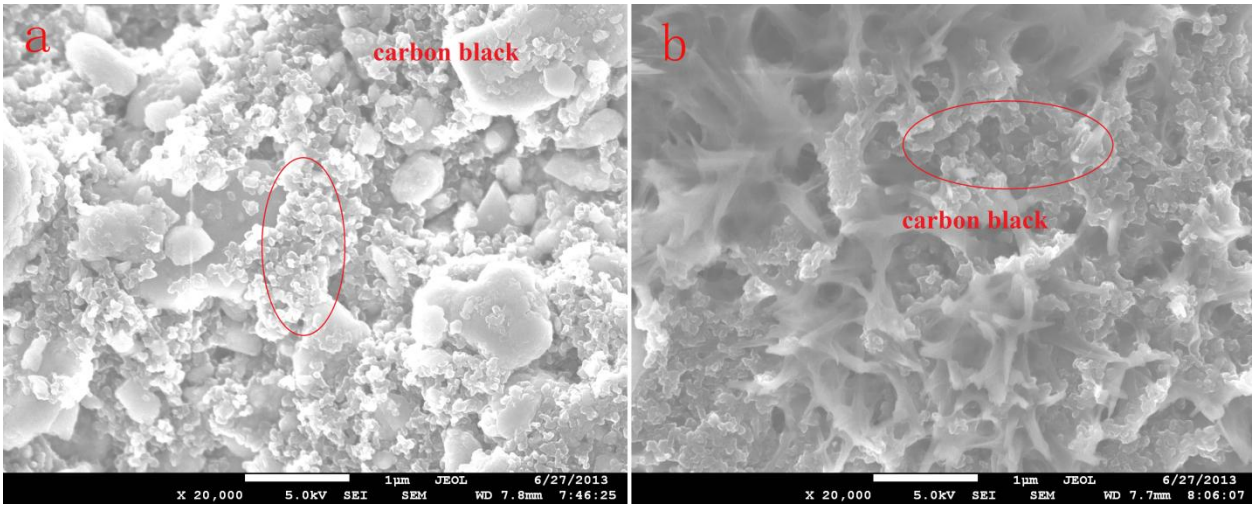

Figure 4.8. Morphology of the P/Super P composite electrode: (a) before and (b) after 1 cycle.

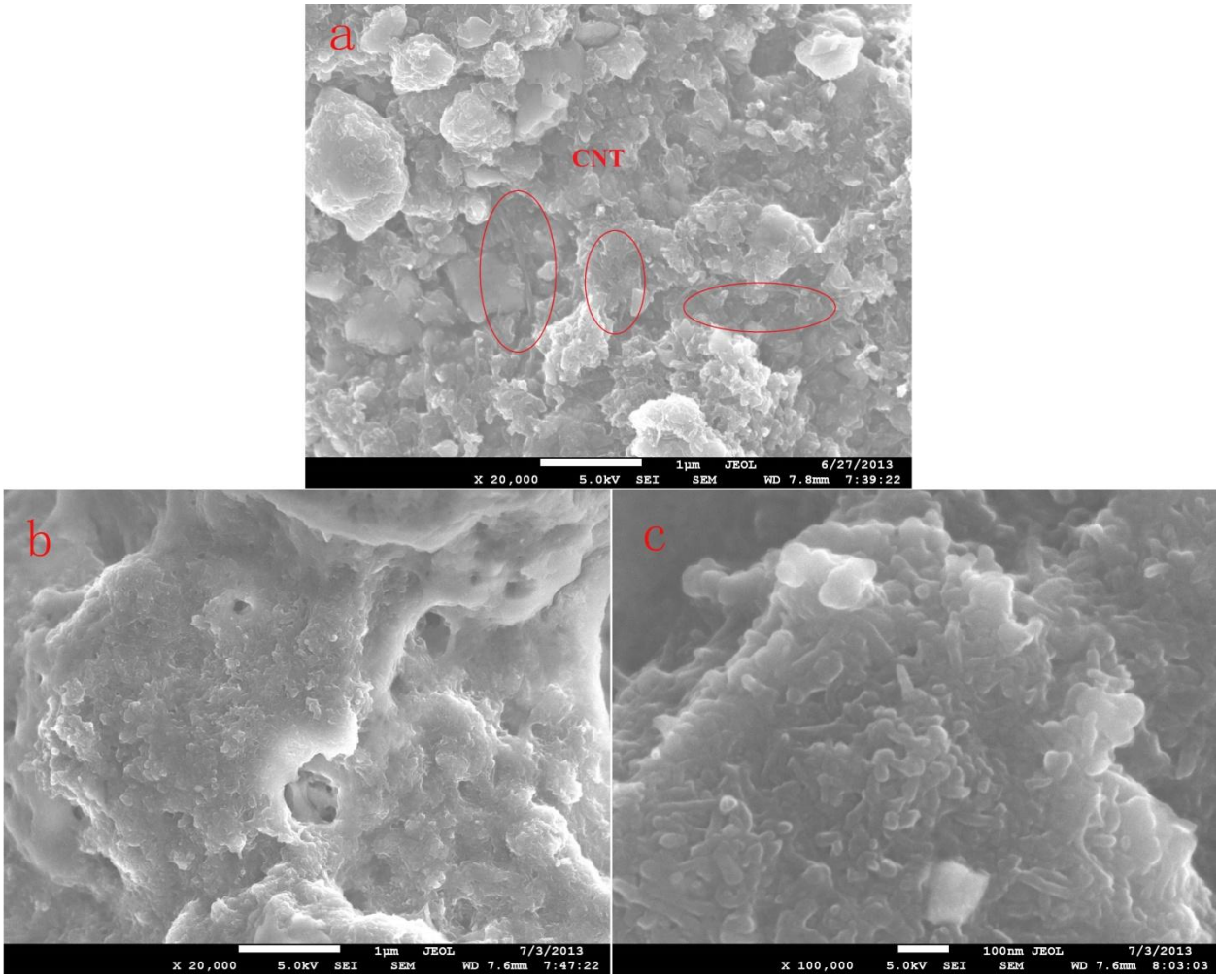

Figure 4.9. Morphology of the P/CNT composite electrode: (a) before and (b, c) after 1 cycle at different magnifications.

4.4 Conclusion

In summary, we prepared a P/CNT composite simply by hand grinding commercial red P with carbon nanotubes. The P/CNT composite can be cycled reversibly, with an initial discharge capacity of 2210 mAh g^{-1}, and 76.6 % of the initial reversible capacity still delivered after 10 cycles. CNTs play a crucial role in the reversibility of the commercial P/CNT composite. The network structure of the CNTs serves to effectively buffer the enormous stresses from the volume expansion of the P particles and reduce the rate of pulverization of particles. On the other hand, the CNT network provides pathways for electron transport, which is helpful for maintaining the connections not only between the red phosphorus particles, but also between the red phosphorus and the current collector. Our results suggest that the simply mixed commercial red phosphorus and CNTs would be a

promising candidate for the next generation anode material for sodium ion batteries with high capacity and low cost.

Chapter 5. Significantly enhance the cycling performance and rate capability for P/C composite via chemical bonding (P-C)

Although commercial red phosphorus can reversibly react with Na after improving the electronic conductivity by handing with CNT, the cycling performance was still unsatisfied. To further improve the cycling performance of P, P/C compsite in which the reduction of particle size and the carbon matrix covering the phosphorus are conductive to reducing the volume expansion and buffering the stress from the volume expansion, respectively. Moreover, the formation of P-C bonds between red phosphorus and graphene nanoplates brings the graphene nanoplates into close contact with the P particles, maintaining the electrical contact between the P particles and the graphene nanoplates, and consequently, stabilizing the structure of the composite to improve its cycling performance.

5.1 Introduction

Sodium ion batteries (SIBs), as a promising alternative to lithium ion batteries, which might well lead to a new era in energy storage systems, have attracted increasing attention, owing to the abundant sodium resources around the world and sodium's similar electrochemical (or physical) properties to lithium.[44,48,95,230,256-259,280] The big challenge for developing SIBs, however, is to search for an appropriate candidate with both a long lifetime and high capacity. In the case of cathode materials, massive improvement of cycle life has now been achieved. $Na_3V_2(PO_4)_3$ and acetylene carbon composite delivered 97.0 mAh g^{-1} capacity with retention of 96.4% over 200 cycles.[281] $Na_{1.25}V_3O_8$ nanowires presented excellent cycling performance with 95% and 92% capacity retention after 200 and 1000 cycles, respectively.[282] Our group developed Na-enriched $Na_{1+x}FeFe(CN)_6$ cathode material, showing superior capacity retention of 97% over 400 cycles.[283] In contrast, apart from carbon materials, anode materials seldom possess excellent cycling stability with more than 80% capacity retention after 200 cycles. For example, N-doped carbon showed 88.7% capacity retention over 200 cycles,[284] Carbon nanofibers synthesized by electrospinning exhibited excellent cycling stability, with 97.7% capacity retention over 200 cycles.[285] One of the biggest drawbacks of the carbon materials, however, is their low capacity (less than 300 mAh g^{-1}). In addition, Sn- and Sb-based materials, which can deliver 600 mAh g^{-1} capacity, based on their alloying mechanism, have recently demonstrated improved cycling performance.[62,286-288]

Among the anode candidates, red phosphorus has the highest theoretical capacity of ~2600 mAh g^{-1}, and it has been widely investigated since it was first reported as anode material for SIBs in 2013.[1,252,289] The poor electrical conductivity and huge volume expansion (490 %) of red phosphorus, however, give it poor practical capacity and cycling stability, which are obstructing its practical application. To overcome these problems, various carbon materials, such as Super P®,[1,252] multi-walled carbon nanotubes (MWCNT),[289] single-walled carbon nanotubes (SWCNT),[2] and graphene,[3] have been introduced to prepare red phosphorus and carbon (P/C) composites, where the carbon plays the roles of both improving the electric conductivity and buffering the volume expansion. Compared with commercial red phosphorus, the cycling performance of P/Super P and P/MWCNT composites was improved to some extent, however, the capacity still gradually deteriorated. Among these P/C composites, P/SWCNT and phosphorus/graphene (P/G) composites showed improved cycling performance.[2,3] P/SWCNT composite synthesized by the vaporization-condensation method showed excellent cycling stability with no capacity decay over 200 cycles at the current density of 500 mA g^{-1}.[2] There is a big potential safety hazard, however, if the tube is not well sealed, because of the white phosphorus generated during the preparation process at the temperature of 600 ℃, and moreover, the utilization of SWCNT can increase the cost. Song et al. reported that P/G composite prepared via simple ball milling delivered 1706 mAh g^{-1} capacity (on the basis of phosphorus weight) with 95% retention of the capacity in the second cycle for over 60 cycles.[3] Such good cycling performance is proposed to originate from the strong P-O-C chemical bonds between the graphene nanosheets and the phosphorus, which can stabilize the solid electrolyte interphase (SEI) to improve the cycling performance. The preparation of graphene requires tedious steps, however, such as the synthesis of graphite oxide (GO) and the reduction of GO. Moreover, the price of graphene is higher than that of natural graphite. Before, Jeon et al. reported the graphite can be exfoliated into graphene nanoplates during the ball milling process through the shear force.[290]Cui et al. demonstrated that the P-C bond can form during the ball-milling process to improve the contact between black phosphorus and carbon, giving the black phosphorus and carbon composite excellent electrochemical performance for lithium ion storage.[291]

Therefore, inspired by the reported functionality of the chemical P-C bond and the formation of graphene nanoplates from natural graphite during ball-milling process, we chose the cheap graphite as the carbon source to prepare our chemically bonded red phosphorus and graphene nanoplates (P/GnPs) composite as anode for sodium ion batteries through the simple and

productive ball-milling method. During the milling process, the bulk red phosphorus particles were milled into small nanoparticles and dispersed well into graphene nanoplates; such a reduction of particle size and the carbon matrix covering the phosphorus are conductive to reducing the volume expansion and buffering the stress from the volume expansion, respectively. Moreover, the formation of P-C bonds between red phosphorus and graphene nanoplates brings the graphene nanoplates into close contact with the P particles, maintaining the electrical contact between the P particles and the graphene nanoplates, and consequently, stabilizing the structure of the composite to improve its cycling performance. As a result, the P/GnPs composite exhibits superior cycling performance for sodium ion storage, with 92.5% capacity retention over 200 cycles at the high current density of 1000 mA g^{-1}. Additionally, it shows excellent rate capability, retaining 274 mAh g^{-1} capacity, even when discharged at the high current density of 10 A g^{-1}, corresponding to 27.6% retention of the capacity delivered at 100 mA g^{-1}.

5.2 Experimental

5.2.1 Synthesis of P/GnPs composite.

The red phosphorus (99%, Sigma Aldrich) and natural graphite were used as the raw materials without any further purifying treatment. The P/GnPs composite was prepared through a simple and productive ball - milling method. The weight ratio of red phosphorus to graphite was 7:3. Then, the materials were put into a jar and sealed in a glove box under argon gas, which was followed by milling for 40 h at a speed of 500 rpm. The resultant composite was denoted as P/GnPs - 500. To compare, the control sample was prepared under the same experimental conditions except the milling speed of 300 rpm, which is denoted as P/GnPs - 300.

5.2.2 Material Characterization

The microstructure of the powders was characterized by powder X-Ray diffraction (XRD; GBC MMA diffractometer) with Cu Kα radiation at a scan rate of 2° min^{-1}. The morphology of the samples was investigated by field emission scanning electron microscopy (FESEM; JEOL JSM-7500FA) and scanning transmission electron microscopy (STEM, JEOL ARM200F) in conjunction with energy - dispersive X-ray spectroscopy (EDS). Raman spectra were collected using a JOBIN Yvon Horiba Raman spectrometer model HR800, with excitation from a 10 mW helium/neon laser at 632.8 nm in the range of 150 to 2000 cm^{-1}. FTIR spectra were performed by a FTIR Prestige-21 (Shimadzu). X-ray photoelectron

spectroscopy (XPS) was conducted using a SPECS PHOIBOS 100 Analyser installed in a high-vacuum chamber with the base pressure below 10 - 8 mbar, with X-ray excitation provided by Al Ka radiation with photon energy hν = 1486.6 eV at the high voltage of 12 kV and power of 120 W. The XPS binding energy spectra were recorded at the pass energy of 20 eV in the fixed analyser transmission mode. Analysis of the XPS data was carried out using the commercial CasaXPS 2.3.15 software package. All the spectra were calibrated by C 1s = 284.6 eV.

5.2.3 Electrochemical test

The electrochemical measurements of the P/GnPs composite as anode material were conducted using 2032-type coin cells. The working electrode was prepared by coating aqueous slurry containing 70 wt% active materials, 15 wt% Super-P® carbon black, and 15 wt% carboxymethyl cellulose (CMC) binder on a copper foil substrate. Then, the electrode film was dried in a vacuum oven at 80 ℃ overnight and pressed at 10 MPa. The electrodes were punched into disks with loading of 1.5-2.0 mg cm^{-2}. The electrolyte used in this work was 1.0 mol L^{-1} $NaClO_4$ in an ethylene carbonate (EC) - diethyl carbonate (DEC) solution (1:1 v/v), with 5 wt% addition of fluoroethylene carbonate (FEC). All the cells were assembled in a glove box filled with argon and tested at room temperature. The galvanostatic charge/discharge testing was conducted on a Biologic VMP3 electrochemical workstation with a cut-off voltage range from 0 - 1.5 V (vs. Na/Na^+). The rate capability of the P/GnPs composite was also investigated at a variety of current densities from 50 mA g^{-1} to 10 A g^{-1} with a cut-off voltage range from 0 to 1.5 V (vs. Na/Na^+).

5.3 Results and discussion

The P/GnPs composite was prepared by a simple and productive ball-milling method. Commercial red phosphorus and natural graphite were used as the starting materials, in the weight ratio of 7:3, respectively, and then milled at 500 rpm for 40 h under argon atmosphere. The resultant composite was denoted as P/GnPs - 500. The morphologies of the red phosphorus and pristine graphite are shown in Figure 5.1. It is clear that the commercial red phosphorus is a micrometer-sized bulk and the pristine graphite is a layered bulk (Figure 5.1). After milling, these two bulk materials were broken down into nanoscale particles ~ 100 nm in size, as shown in Figure 5.2(a-b), however, the bulk pristine graphite cannot be observed in the SEM images. To clearly detect the morphology of pristine graphite in the P/GnPs - 500 composite, scanning transmission electron microscopy (STEM) was conducted. It is obvious

that the pristine graphite was exfoliated into nanoplatelets through the shear force during the milling process, and the small phosphorus particles were embedded in the graphene nanoplatelets (GnPs) (Figure 5.2(c)). Moreover, the selected area electron diffraction (SAED, inset of Figure 5.2(c)) pattern shows a diffuse ring, suggesting that the P/GnPs - 500 composite is amorphous. Energy-dispersive X-ray spectroscopy (EDS) mapping was carried out to further explore the structure of the P/GnPs - 500 composite, as shown in Figure 5.2(e-f). Significantly, the phosphorus was dispersed uniformly with the carbon, suggesting that the phosphorus and carbon were mixed uniformly and were in intimate contact.

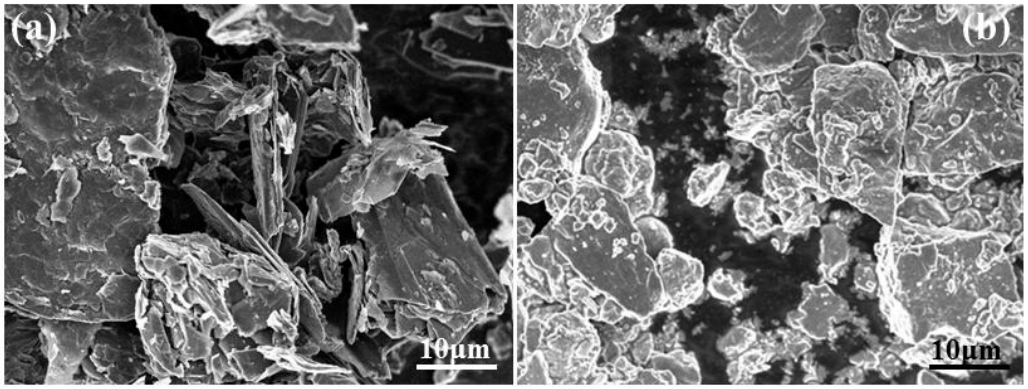

Figure 5.1. SEM images of (a) pristine graphite and (b) red phosphorus.

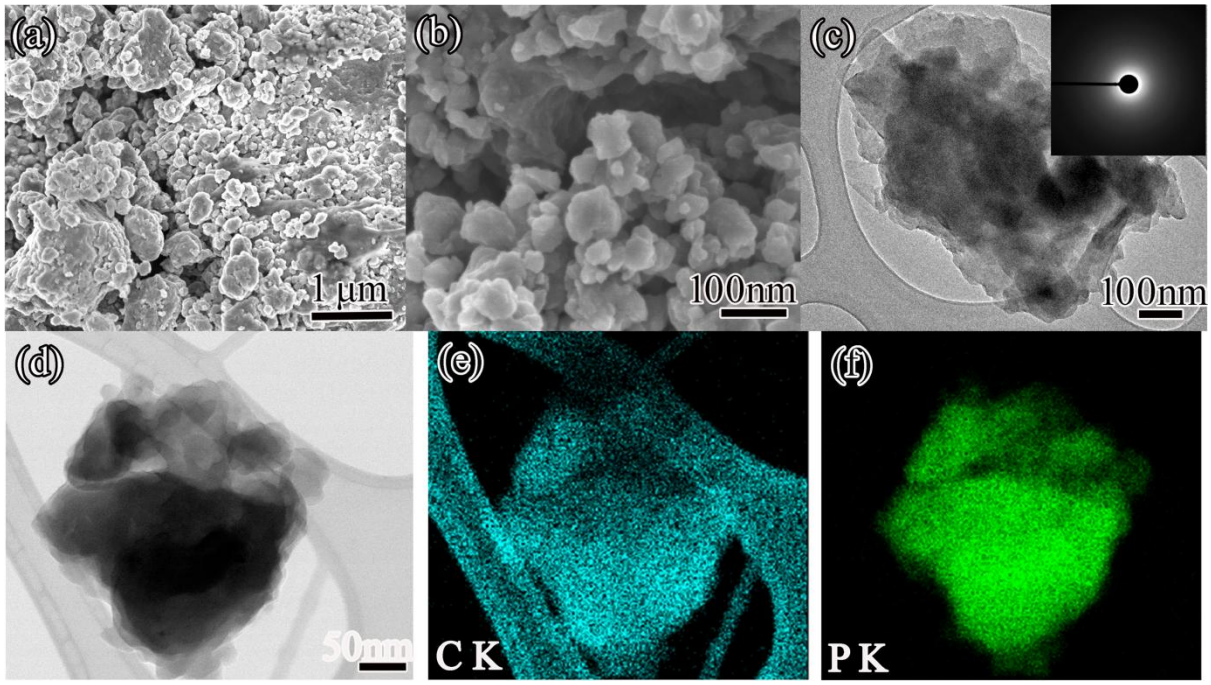

Figure. 5.2. Morphology of the P/GnPs composite: (a) low and (b) high magnification SEM images; (c) and (d) STEM images (inset of (c) is the corresponding SAED pattern); element mapping corresponding to (d) of (e) carbon and (f) phosphorus in the P/GnPs composite.

To further investigate the connections between the phosphorus particles and the graphene nanoplatelets, a variety of characterization techniques, including powder X-ray diffraction (XRD), Raman spectroscopy, and X-ray photoelectron spectroscopy (XPS), were implemented. Figure 5.3(a) shows the XRD patterns of the P/GnPs - 500 composite and its precursors. The XRD pattern of the commercial red phosphorus shows broad and low-intensity peaks at 2θ of 15.5° and 32.3°, respectively, obviously indicating its amorphous nature. In the XRD pattern of pristine graphite, there is a sharp diffraction peak at 26.5°, assigned to the (002) plane. After milling for 40 h, these diffraction peaks disappear, and no peak appears in the XRD pattern of P/GnPs composite. The XRD results demonstrate that the P/GnPs - 500 composite is amorphous, consistent with SAED pattern (inset of Figure 5.2(c)). Raman spectra were collected to further test the structure of P/GnPs - 500, as shown in Figure 5.3(b). Red phosphorus shows three bands from 300 cm^{-1} to 500 cm^{-1}, assigned to the P-P bonds. For the P/GnPs composite, these three bands were also observed, but their intensities were decreased, implying that some P-P bonds were broken up to generate the P-C bonds.[291] The spectrum of the pristine graphite shows a weak D band at 1327 cm^{-1} and a strong G band at 1572 cm^{-1}, corresponding to the breathing mode of aromatic rings and the E2g symmetrical bond stretching motion of pairs of C sp^2 atoms, respectively.[292] Compared with the pristine graphite, the intensity ratio of the D band to the G band (ID/IG) increased from 0.31 to 2.91 in the P/GnPs - 500 composite, implying that the carbon in the composite was partially amorphous. Notably, a right shift of the G band from 1572 cm^{-1} for pristine graphite to 1585 cm^{-1} was observed, demonstrating that the number of layers of pristine graphite in the P/GnPs - 500 composite was reduced due to the mechanical shear exfoliation of the graphene nanoplates.[292] XPS was carried out to detect the surface chemical composition of the P/GnPs - 500 composite, and the XPS results are shown in Figure 5.3(c, d). The C 1s peak is deconvoluted into four peaks at 283.4 eV, 284.6 eV, 285.3 eV and 288.3 eV (Figure 5.3(c)). The peaks at 284.6 eV and 285.3 eV are assigned to the sp2 and sp3 C-C bond, respectively, while the peak at 288.2 eV are assigned to the C=O bond from the carbon. The peak at 283.7 eV should be ascribed to the P-C bond, according to J. Sun et al.[291] The P 2p spectrum is fitted to two pairs of 2p1/2 and 2p3/2 doublets, as shown in Figure 5.3(d). One pair of 2p3/2 and 2p1/2 components at 129.7/130.6 eV corresponds to the P-P bond, while the other pair at 130.1/131.0 eV is assigned to the P-C bond, consistent with a previously reported result.26 In addition, there is a fitting peak that appears at 133.9 eV, which is ascribed to the P-O bond. The appearance of the C=O and P-O bonds is possibly due to the oxidization of milled

nanoparticles when the milling jars were opened. The XPS results demonstrate that P-C bonds are formed between red phosphorus and graphene nanoplate in the P/GnPs - 500 composite.

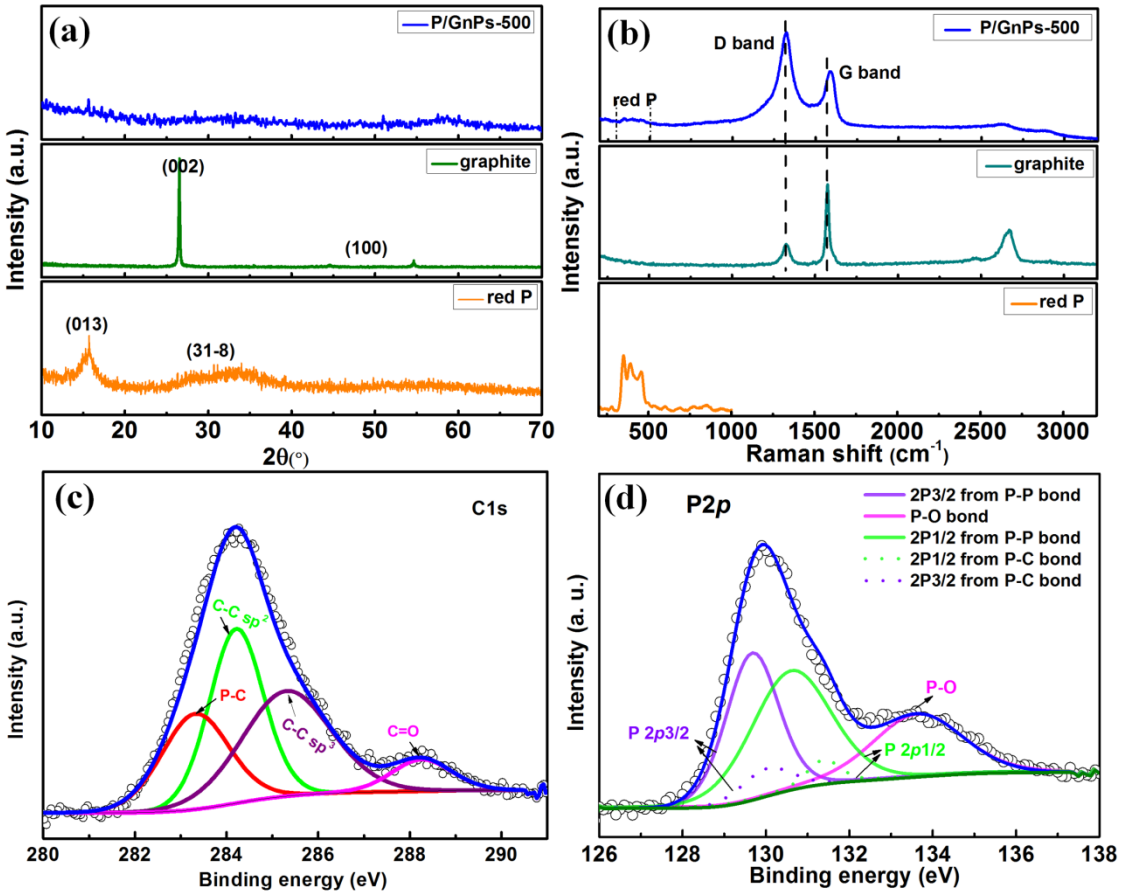

Figure. 5.3. Characterization of the P/GnPs - 500 composite and its precursors: (a) XRD patterns; (b) Raman spectra; (c) high resolution C 1s XPS spectrum and (d) P 2p XPS spectrum of P/GnPs - 500.

To investigate the effects of milling speed on the structure of P/GnPs composite, we prepared a control sample under the same experimental conditions as for P/GnPs - 500 except for using a milling speed of 300 rpm, with the sample denoted as P/GnPs - 300. XRD, SEM, XPS, transmission electron microscopy (TEM), and Raman spectroscopy were carried out to characterize the P/GnPs - 300, as shown in Figures 5.4-5.5. The XRD pattern shows that there is no new phase emerging in the P/GnPs - 300. The intensities of the peaks from carbon decreased after milling compared with the pristine graphite, demonstrating that the particle size of the carbon in the composite had been reduced (Figure 5.4 (a)). From the SEM image, it is clear that the particle size of the P/GnPs - 300 is about 100 nm. Moreover, the EDS mapping results indicate that the carbon and red P were mixed uniformly (Figure 5.4(b)). In

the TEM image of the P/GnPs - 300, there are some lattice fringes with spacing of ~ 0.34 nm, which were assigned to the gaps between the graphene layers in graphite (Figure 5.4(c)). It demonstrated that the extent of exfoliation of pristine graphite in P/GnPs – 300 is smaller than that of pristine graphite in the P/GnPs-500 (Figure 5.2(c)). Figure 5.4(d-e) shows the XPS spectra of P/GnPs – 300. The C 1s peak is deconvoluted into two peaks at 284.6 eV and 288.3 eV assigned to the C-C bond and C-O, respectively, (Figure 5.4(d)). The P 2p spectrum is fitted to a pair of 2p3/2 and 2p1/2 components at 129.7/130.6 eV corresponds to the P-P bond. Besides that, there is a fitting peak that appears at 133.9 eV ascribed to the P-O bond, as shown in Figure 5.4(e). To clearly observe the structural differences between the P/GnPs - 500 and P/GnPs - 300, Raman spectroscopy was conducted, and the results are presented in Figure 5.5(a). For both the P/GnPs - 500 and the P/GnPs - 300 composites, the intensity of the D-band from carbon is larger than that of the G-band, suggesting that the pristine graphite in the composites was partially amorphous after milling. In addition, compared with P/GnPs - 300, the G-band in the P/GnPs - 500 composite has left shifted from 1598 cm^{-1} to a lower wavenumber (1585 cm^{-1}). Considering the larger extent of exfoliation of pristine graphite in P/GnPs - 500, the G-band should shift to large wavenumber, compared with the P/GnPs -300. However, the actual tendency is reverse. This is due to the P-C bond formation in the P/GnPs - 500 composite through the π-p conjugation which makes the G-band shift left.[291] Therefore, the left shift of G-band is also evidence of the P-C bond formation in the P/GnPs - 500 composite. In addition, the FTIR spectra are also measured to test the P-C bond. The results show that there is an additional peak at 1006 cm^{-1} appearing in the FTIR spectrum of P/GnPs-500, compared with P/GnPs-300 (Figure 5.5(b)), suggesting a new bond forming in P/GnPs-500 composite. The formation of P-C bonds in the P/GnPs - 500 composite provides good contact between red phosphorus particles and graphene nanoplates, consequently improving the electronic conductivity of red phosphorus and promoting structural integrity during sodiation/desodiation processes.

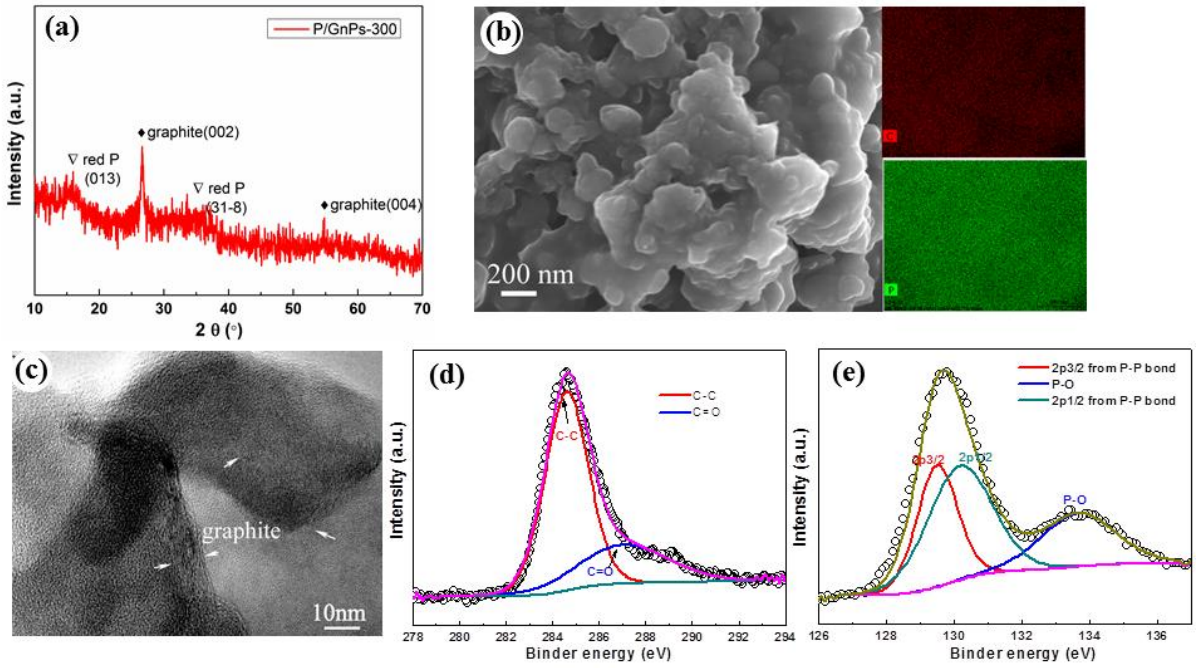

Figure 5.4. Characterization of the P/GnPs - 300 composite: (a)XRD pattern, (b)SEM image with corresponding EDS mapping, (c) TEM image, (d) C1s and (e) P 2p XPS spectra.

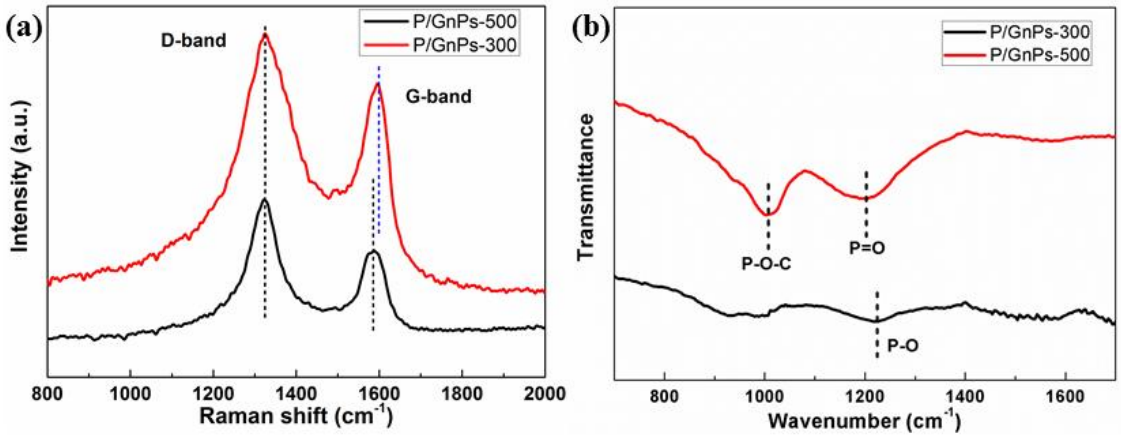

Figure 5.5. (a) Raman spectra and (b) FTIR spectra of P/GnPs of P/GnPs composites milled at different speeds.

To validate the function of the P-C bonds in the P/GnPs composites in the electrochemical performance, the P/GnPs composites were tested in sodium ion half cells in the voltage range of 0 - 1.5 V. Both the capacity and the current density were calculated on the basis of the overall weight of the P/GnPs composite. Figure 5.6(a) shows the charge-discharge curves of the P/GnPs - 500 and P/GnPs - 300 composites in the first two cycles at the current density of 100 mA g^{-1}. In the discharge curves of both the P/GnPs - 500 and the P/GnPs - 300 composites, there are three sloping regions at 1.5-0.5 V, 0.5-0.25 V, and 0.25-0 V, respectively, corresponding to the multistep reaction between P and sodium to form the final

Na_3P phase.[1-3,252,289] The P/GnPs - 300 delivered the discharge capacity of 1376 and 822 mAh g^{-1} in the first and second cycles, respectively. Compared with the P/GnPs - 300, the capacity delivered by the P/GnPs - 500 composite is higher, with 1471 mAh g^{-1} capacity in the first cycle and 1146 mAh g^{-1} in the second cycle. Additionally, the hysteresis (ΔE) between the discharge and charge potential plateaus was reduced from 0.34 V for P/GnPs - 300 to 0.22 V for P/GnPs - 500. The reduced hysteresis is similar to that of the reported black phosphorus and graphite composite, which was proposed as evidence of P-C bond formation and consequently, improved Coulombic efficiency resulting from the better connections between particles during the very large volume changes in the charge-discharge processes.[291]

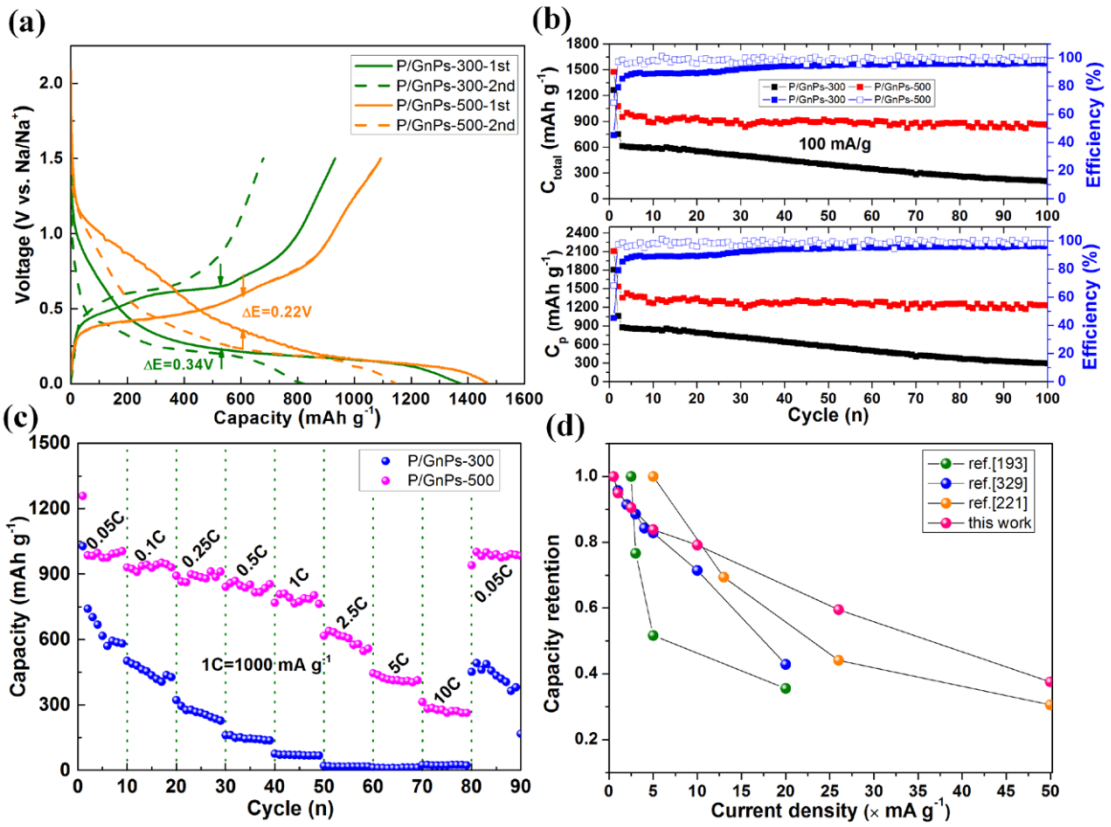

Figure 5.6. Electrochemical performances of the P/GnPs - 500 and P/GnPs - 300 composites. (a) Charge-discharge curves of the P/GnPs electrodes in the first two cycles between 0-1.5 V with current density of 100 mA g^{-1}, (b) cycling performances of the P/GnPs electrodes charged at current density of 100 mA g^{-1} (with Ctotal and Cp denoting the specific capacity calculated based on the weight of P/GnPs composite and based on the weight of phosphorus alone, respectively), (c) rate capability of the P/GnPs composites, and (d) comparison of P/GnPs - 500 with different reported phosphorus/carbon composites[1-3]for sodium ion storage.

Both the increased capacity and the reduced hysteresis for the P/GnPs - 500 composite demonstrate that it has better electronic conductivity than P/GnPs - 300. The electrochemical impedance measurements also confirm this point, and the results are shown in Figure 5.7. Before testing the impedance, the cells were run for 5 cycles and then charged at 0.6 V. The impedance curves of both P/GnPs - 500 and P/GnPs - 300 show two semicircles in the medium frequency and the low frequency regions, which could be assigned to the sodium ion diffusion through the solid electrolyte interphase (SEI) film (Rx) and the charge transfer resistance (Rct), respectively. The Rct was calculated using the equivalent circuit shown in Figure 5.7(a). Significantly, the Rct value of the P/GnPs - 500 composite (95 Ω) is very much smaller than that of the P/GnPs - 300 (147 Ω), demonstrating that the electronic conductivity of the P/GnPs - 500 composite is better than that of P/GnPs - 300.

Figure 5.6(b) shows the cycling performance of P/GnPs - 500 composite charged at the current density of 100 mA g^{-1}. For comparison, the P/GnPs - 300 electrode was also tested under the same experimental conditions, and its cycling performance is also shown in Figure 5.6(b). C_{total} and C_p denote the specific capacity calculated based on the weight of P/GnPs composite and based on the weight of the phosphorus alone, respectively. The P/GnPs - 300 presents a dramatic capacity decay of 4 mAh g^{-1} per cycle, with C_{total} of 205 mAh g^{-1} over 100 cycles. In contrast, the P/GnPs - 500 composite possessing P-C bonds showed superior cycling stability, with a capacity decay of 0.66 mAh g^{-1} per cycle. 864 mAh g^{-1} and 1234 mAh g^{-1} were retained for C_{total} and C_p over 100 cycles, respectively. Moreover, the Coulombic efficiency of the P/GnPs - 500 composite increased from 45% to 67%, compared with the P/GnPs - 300. Even when charged at the current density of 1 A g^{-1}, the P/GnPs - 500 electrode still demonstrated excellent cycling performance, with 92.5% retention of the capacity in the second cycle (649 mAh g^{-1}) over 200 cycles, as shown in Figure 5.8. Table 5.1 summarizes the electrochemical performances of phosphorus and carbon composites as anode materials for sodium ion batteries. Compared with the other red phosphorus and carbon (such as Super P, graphene, and SWCNT) composites reported, the cycling performance of our synthesized P/GnPs - 500 composite is superior for sodium ion storage. This is due to the P-C bond formation, leading to a better connection between the red phosphorus particles and the graphene nanoplates, which improves the cycling stability. The structural stability of the

Table 5.1 Summary of the electrochemical performances of phosphorus-carbon composites as anode materials for sodium ion batteries.

Carbon source	**Percentage of P**	**Voltage range**	**Mass loading (mg/cm)**	**1st capacity (based on composite)**	**Cycling performance (capacity based on composite)**	**Capacity decay (per cycle)**	**Reference**
Single-walled carbon nanotube	60%	0.001-2 V	0.7-1.2	670 mAh/g (at current density of 50 mA/g)	560 mAh/g over 200 cycles (current density of 500 mA/g)	0.2 mAh/g	2
graphene	70%	0-2 V	0.8-1.0	1454 mAh/g (at current density of 260 mA/g)	1194 mAh/g over 60 cycles(at current density of 260 mA/g)	1.3 mAh/g	291
Super P	70%	0-1.5 V	2.0-3.0	1323 mAh/g (at current density of 143 mA/g)	1230 mAh/g over 30 cycles(at current density of 143 mA/g)	3.1 mAh/g	252
Super P	70%	0-2 V	3.0	1235 mAh/g (at current density of 250 mA/g)	700 mAh/g over 140 cycles(at current density of 250 mA/g)	3.8 mAh/g	1
multi-walled carbon	70%	0-1.5 V	-	1547 mAh/g (at current	525 mAh/g over 20 cycles(at	32 mAh/g	289

nanotube				density of 143 mA/g)	current density of 143 mA/g)		
graphite	70%	0-1.5 V	1.5-2.0	1471 mAh/g (at current density of 100 mA/g)	667 mAh/g over 200 cycles(current density of 500 mA/g)	0.66 mAh/g	This work

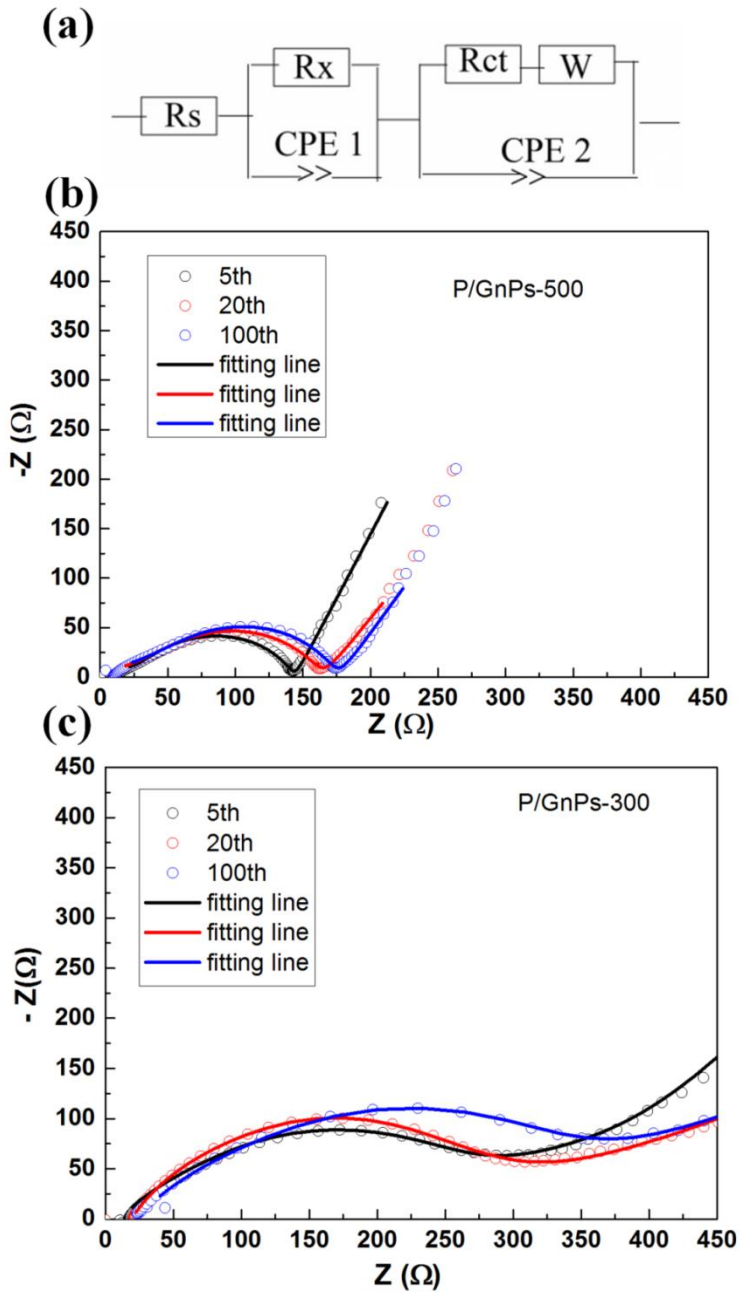

Figure 5.7. Electrochemical impedance spectra of P/GnPs – 500 (b) compared with P/GnPs -300 (c) in the charged state at 0.6 V in the 5th, 20th, and 100th cycles. (a) Equivalent circuit used to interpret the results.

Table 5.2 R_{ct} (Ω) and R_x (Ω) of the P/GnPs electrodes after different cycles.

	5^{th} cycle		20^{th} cycle		100^{th} cycle	
	R_x	R_{ct}	R_x	R_{ct}	R_x	R_{ct}
P/GnPs -500	49	95	70	96	79	106
P/GnPs -300	32	147	64	168	139	277

P/GnPs - 500 composite is also evidenced by the smaller impedance changes in the electrode during cycling, in comparison with the P/GnPs - 300 (Figure 5.7). Table 5.2 shows a comparison of Rct values calculated for the P/GnPs composites with and without P-C bonds. After 100 cycles, the Rct value of the P/GnPs - 500 composite increased a little, from 95 Ω to 106 Ω, while the Rct value of the P/GnPs - 300 composite changed from 147 Ω to 277 Ω. In order to calculate the contribution of red P to the capacity of the P/GnPs - 500 composite, we milled natural graphite for 40 h at 500 rpm. The electrochemical performance of the milled graphite is shown in Figure 5.9. The milled graphite delivered first discharge and charge capacities of 388 mAh g^{-1} and 168 mAh g^{-1}, respectively (Figure 5.9(a)). The huge irreversible capacity is due to the SEI formation on the surface of the milled graphite particles, resulting from the electrolyte decomposition. In the second cycle, the milled graphite delivered 186 mAh g^{-1} capacity. According to Equation 5.1, where 0.3 and 0.7 are the weight fractions of P and graphite in the composite, respectively, the capacity contributed by P is 1558 mAh g^{-1}.

$$0.7 * C_{Phosphorus} + 0.3 * C_{milled\ graphite} = C_{total} \quad (5.1)$$

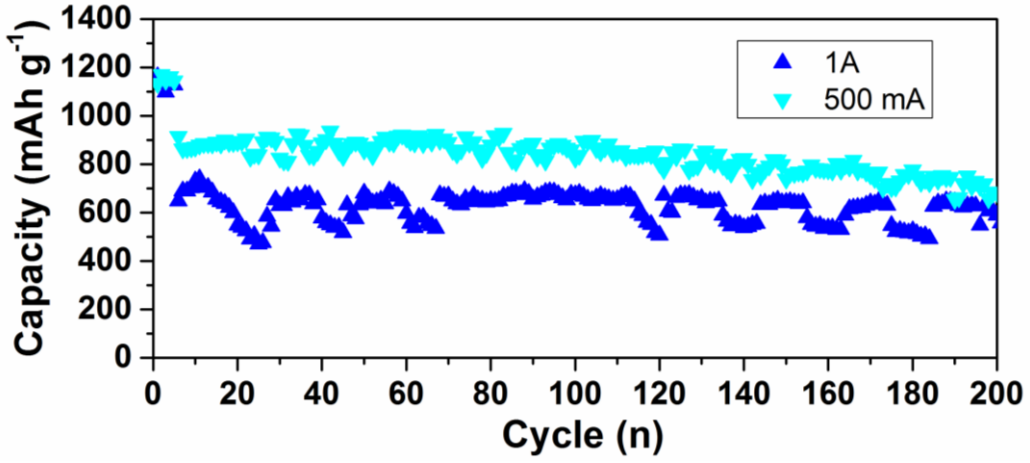

Figure 5.8. Cycling performance of the P/GnPs -500 composite electrode at the high current densities of 500 mA g^{-1} and 1 A g^{-1} (the current density is 100 mA g^{-1} in the first 5 cycles).

To further explore the structural stability of the P/GnPs composites, the morphologies of the P/GnPs - 500 and P/GnPs - 300 electrodes after 200 cycles were characterized by TEM. The cells were disassembled in an Ar-filled glove box. Figure 5.10(a) shows the morphology of the P/GnPs - 300 electrode after 200 cycles. It is clear that the particles of P/graphite - 300 are pulverized into isolated nanoparticles due to the huge volume changes in the P during cycling. The high resolution TEM image demonstrates that the size of the pulverized particles

was less than 5 nm, as shown in Figure 5.10(b). By contrast, the original morphology of the P/GnPs - 500 remains its primary morphology, and significant pulverization of particles cannot be observed (Figure 5.10(c, d)), suggesting that the structure of the P/GnPs - 500 is more stable than that of P/GnPs - 300. A schematic illustration of the structural evolution of P/GnPs - 500 and P/GnPs - 300 after cycling is shown in Figure 5.11. During the charge - discharge process, the red P particles undergo huge volume expansion and condensation (about 490 %), and concomitantly, enormous stresses emerge in the particles, leading to pulverization of the red phosphorus. As a result, some red P particles lose contact with both other red P particles and with the graphene nanoplates, so that the electrical conductivity is reduced. On the basis of our present investigation, the electrical conductivity plays an important role in the reversible capacity and cycling stability of red P.[289] Thus, for the P/GnPs - 300 composite, the loss of electrical contact in the active materials leads to capacity decay. In contrast, for the P/GnPs - 500 composite, the P-C bonds foster close connections between the P particles and the graphene nanoplates. Moreover, the P-C bond plays a role in restraining the expansion of P particles during the sodiation of P. Even if the P particles are pulverized during the cycling, the red P particles can maintain their contact with the graphene nanoplates, so that good electrical conductivity is retained. Therefore, the P/GnPs - 500 composite has excellent cycling stability.

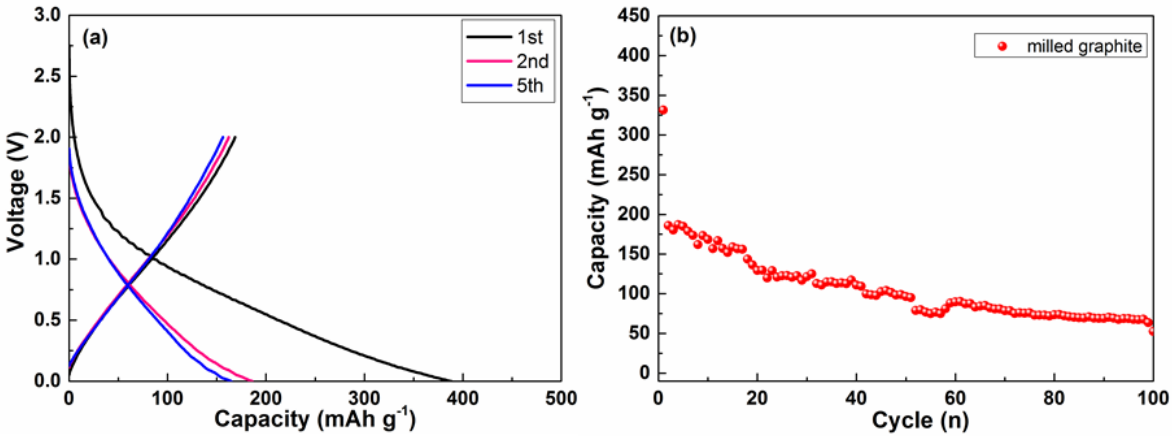

Figure 5.9. (a) Charge-discharge curves for selected cycles, and (b) cycling performance of the graphite milled for 40 h.

The rate capability of the P/GnPs - 500 composite was also investigated at a variety of current densities from 50 mA g^{-1} to 10 A g^{-1} with voltage range of 0-1.5V. As shown in Figure 5.6(c), the P/GnPs - 500 electrode delivered stable capacities of 990, 935, 888, 843, and 788 mAh g^{-1} at the current densities of 50, 100, 250, 500, and 1000 mA g^{-1}, respectively. Even at current

densities as high as 5 A g^{-1} and 10 A g^{-1}, the P/GnPs - 500 electrode still retained capacities of 413 mAh g^{-1} and 274 mAh g^{-1}, corresponding to capacity retention of 41.7% and 27.6%, respectively. Then, the current density was returned to the low value of 50 mA g^{-1}, and the capacity was restored to the previous value of 989 mAh g^{-1}, suggesting that the P/GnPs - 500 composite has excellent rate capability. By comparison, the capacity of the P/GnPs - 300 electrode dropped dramatically with increasing current density. With operation at the current density of 1000 mA g^{-1}, only 75 mAh g^{-1} was retained. On increasing the current density to 2.5 A g^{-1}, 5 A g^{-1}, and 10 A g^{-1}, the capacity delivered by the P/GnPs - 300 electrode was nearly zero. In addition, the rate capability of P/GnPs - 500 composite was further compared with other P/carbon composites previously reported. Figure 5.6(d) shows a comparison of the rate capability between other phosphorus/carbon (SWCNT, Super P®, and graphene) composites and P/GnPs - 500 composite for sodium ion storage. It can be clearly seen that the P/GnPs - 500 composite presents superior rate capability to other P/carbon composites. This is possibly due to the excellent conductivity of P/GnPs - 500 composite as a benefit of the P-C bond formation.

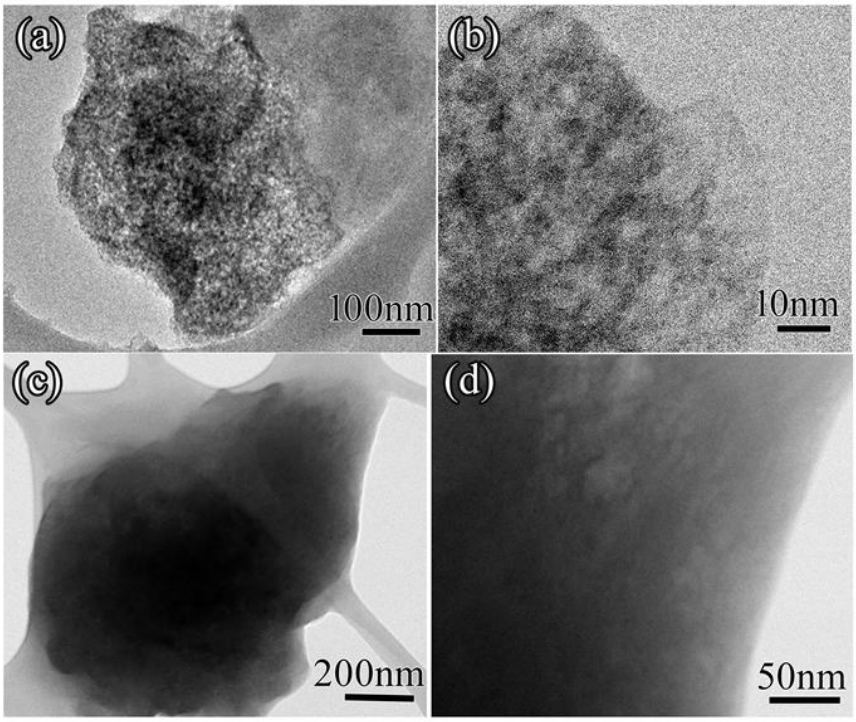

Figure 5.10. TEM images of (a, b) P/GnPs - 300 and (c, d) P/GnPs - 500 electrodes after 100 cycles.

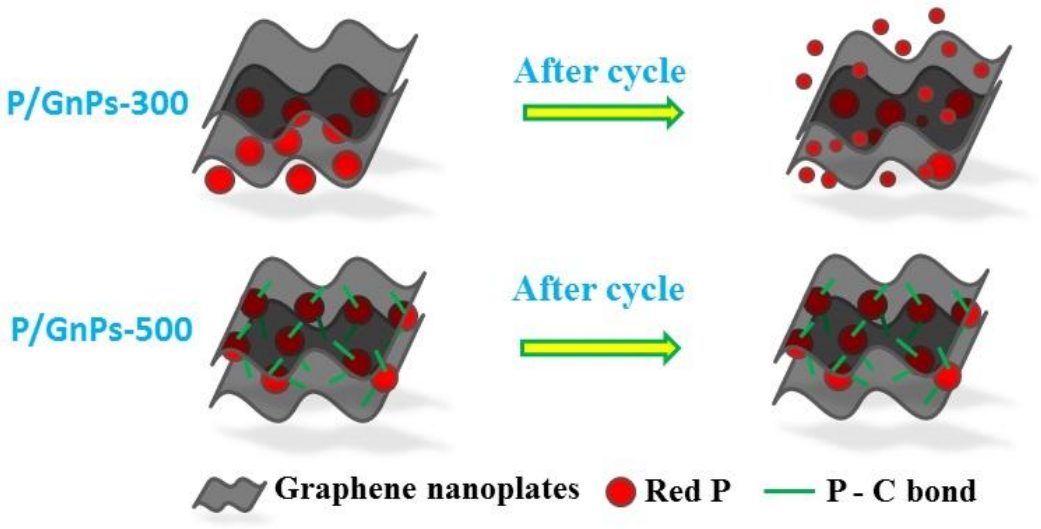

Figure 5.11. Schematic illustration of the structural evolution of P/GnPs - 500 and P/GnPs - 300 after cycle.

5.4 Conclusion

In summary, we prepared red phosphorus and graphene nanoplate composites by a facile and scalable ball milling method. The SEM and TEM images show that the pristine graphite was exfoliated into nanoplatelets through the shear forces during the milling process, and the small phosphorus particles were embedded in the graphene nanoplatelets. Moreover, the XPS results demonstrate the existence of P-C bonds formed between the red phosphorus particles and the graphene nanoplates in the P/GnPs - 500 composite. This unique morphology and strong chemical bonding is responsible for the stable structure of P/graphene nanoplate composite. During the sodiation of P, the P-C bond plays a role in restraining the expansion of P particles. Moreover, even if the P particles are pulverized during the cycling, the red P particles can remain in contact with the graphene nanoplates, so that good electric conductivity is retained. Therefore, the P/GnPs - 500 composite has excellent cycling stability and superior high rate capability, compare to that of the P/GnPs - 300 composite which does not have P-C bonds.

Chapter 6. $Sn_{4+x}P_3$ crystalline and amorphous composite as anode for sodium-ion batteries with low cost, high capacity, long life, and superior rate capability

Combined with carbonaceous materials, red phosphorus can realize the stable cycling performance, however, the introduction of large amount of carbon in the composite will decrease the energy density of the whole electrode. In order to prolong the cycling life of these anode candidates, preparing alloys with other elements is an effective solution. Herein, the as-obtained $Sn_{4+x}P_3$@(Sn+P) composite which contains two active elements (Sn and P) was investigated as anode for SIBs in half cells and showed high capacity, excellent cycling performance and rate capability.

6.1 Introduction

Effective usage of renewable energy sources such as solar and wind are the key to building a more sustainable society and reducing emissions of the main greenhouse gas (CO_2). Nowadays, the great challenge would be how to store renewable energy in a cheap and efficient way. That is to say, an energy storage system for renewable energy requires low cost, high power capability, relatively good energy density, and high safety.[256,257] Na-ion batteries (SIBs), which have been attracting more attention owing to their low cost, could potentially be the most promising candidate for stationary batteries.[48]

Since the Na ion (radius 0.95 Å) is about 55% larger than the Li ion (0.6 Å), this seriously limits the energy density and rate capability of SIBs. From the energy point of view, sodium can form alloys with Sn (847 mAh g^{-1}), Sb (664 mAh g^{-1}), Pb (484 mAh g^{-1}), and P (2596 mAh g^{-1}) that will deliver higher theoretical capacity as the anode in SIBs than non-graphitic carbons with reversible capacities of less than 300 mAh g^{-1}.[58,210-212,261,293] Sn and red P based materials show great potential due to the cheap and non-toxic nature of the raw materials. Komaba et al.[294,295] reported Sn electrodes with the high capacity of 500 mAh g^{-1} for 20 cycles. Zhu et al.[246] reported an electrodeposited Sn film on conductive wood fiber to acheive 150 mAh g^{-1} for 400 cycles. Qian et al.[1]and Kim et al.[252] reported that an amorphous phosphorus composite with carbon could deliver a high capacity of 1764 mAh g^{-1} at the current density of 250 mA g^{-1} and 1890 mAh g^{-1} at current density of 143 mA g^{-1}, respectively. Xiao et al.[239] reported SnSb/C alloy anode for Na-ion batteries with a capacity of 274 mAh g^{-1} at the high rate of 1000 mA g^{-1}. Liu et al.[296] reported that 3D Sn nanorod arrays composed of a carbon outer shell, a Sn intermediate layer and a metal inner core were fabricated by

combination of physical vapor deposition, radio frequency magnetron sputtering, and electroless deposition method via template route to achieve 405 mAh g^{-1} after 150 cycles. However, all the previous reports on Sn and P based materials involve the usage of large amounts (more than 30%) of carbon in the composite or using high-cost technique to show reasonably good electrochemical performance.[1,239,246,252,289,294,295] The large amount of carbon will significantly lower the volumetric energy density of the whole electrode and the high-cost technique will be hard for commercial application for cheap sodium ion battery. Furthermore, high rate capability is another challenge for SIBs, as SIBs have to accommodate the big current inputs and outputs that are used for stationary batteries. So far, the reported results show relatively poor rate capability up to the 2 C rate for Sn based anode materials.

Herein, we prepared a novel tin phosphide and amorphous Sn and P ($Sn_{4+x}P_3$@(Sn+P)) composite in large amounts by a simple low energy ball-milling method, which can meet the demand for large-scale applications. The as-obtained $Sn_{4+x}P_3$@(Sn+P) composite was investigated as anode for SIBs in half cells and showed high capacity and high rate capability, which offers a new alternative to carbonaceous anode materials in Na cells. In addition, improvement in its cycling stability was also achieved by including an additive to the electrolyte.

6.2 Experimental section

6.2.1 Preparation of the $Sn_{4+x}P_3$@(Sn+P).

The active $Sn_{4+x}P_3$@(Sn+P) powder was prepared by using red phosphorus and tin powder as the starting materials in the molar ratio of 3:5, respectively, for mechanochemical synthesis. The starting materials were put into a hardened steel vial with milling balls 2 mm in diameter. The weight ratio of milling balls to powder was 50:1. The vial was assembled in an argon-filled glove-box, and then mounted on the ball mill. The rotation speed of the mill was set to 300 rpm for 20 h. Sn_4P_3 was also prepared for comparison using the same procedure with red phosphorus and tin powder in the molar ratio of 3:4.

6.2.2 Characterization.

The crystalline structure of the active powder was characterized by powder X-ray diffraction (XRD) on a GBC MMA diffractometer with a Cu Kα source. The morphology of the sample was investigated by field emission scanning electron microscopy (FESEM; JEOL JSM-7500FA) and transmission electron microscopy (TEM, JEOL 2011, 200 keV). X-ray photoelectron spectroscopy (XPS) was conducted using a SPECS PHOIBOS 100 Analyser

installed in a high-vacuum chamber with base pressure below 10-8 mbar. X-ray excitation was provided by Al Kα radiation with photon energy hν = 1486.6 eV at the high voltage of 12 kV and power of 120 W. The XPS binding energy spectra were collected at the pass energy of 20 eV in the fixed analyser transmission mode. Analysis of the XPS data was carried out using the commercial CasaXPS 2.3.15 software package. All the spectra were calibrated by C 1s = 284.6 eV.

6.2.3 Electrochemical measurements

The $Sn_{4+x}P_3$@(Sn+P) electrodes were prepared by mixing 70% active materials, 10% carbon black, and 20% carboxymethyl cellulose (CMC)) binder by weight to form an electrode slurry, which then was coated on copper foil, followed by drying in a vacuum oven overnight at 80 ℃, and then pressing at 30 MPa. The sodium foil was cut by the doctor blade technique from a sodium bulk stored in mineral oil, which then was employed as both reference and counter electrode. The electrolyte was 1.0 mol/L NaClO4 in an ethylene carbonate (EC) - diethyl carbonate (DEC) solution (1:1 v/v), with or without 5 vol.% addition of fluoroethylene carbonate (FEC). The cells were assembled in a argon-filled glove box. The electrochemical performances were tested by a Land Test System in the voltage range of 0-1.5 V (vs. Na^+/Na).

6.3 Results and discussion

Figure 6.1(a) presents the X-ray diffraction (XRD) pattern of the $Sn_{4+x}P_3$@(Sn+P) powder. All the XRD peaks can be well indexed to the stoichiometric Sn_4P_3 phase (JCPDS, file no. 20-1294.) based on the hexagonal crystal system of *R-3m*, in good agreement with the XRD pattern reported previously.[297,298] This compound has a layered structure consisting of Sn layers and P layers packed alternately. The cell constants are a = 3.9935 Å and c = 35.4627 Å. No other impurity phases are observed. A broad background can be observed from 26 °to 32 °, which may be due to the presence of amorphous tin. The X-ray photoelectron spectroscopy (XPS) results show that the tin has two peaks: The main peak is located at 486.1 eV, with a peak area proportion of 83.62%, corresponding to Sn_4P_3 phase. The peak at 484.01 eV with peak area proportion of 26.38% is attributed to Sn Figure 6.1(b)). It is possible that the redundant tin exists in the amorphous state, so it was not detected in XRD. A scanning electron microscope (SEM) image of the as-prepared materials is shown in Figure 6.2(a). The morphology of the precursors, including the irregular oval shapes of commercial tin particles and the bulk size of commercial red phosphorus was not preserved after ball milling.

Microsized secondary $Sn_{4+x}P_3$ particles can be observed, which are composed of primary nanoparticles about 30-80 nm in size. Such a morphology is also an advantage for materials to be used in batteries, since the primary nanoparticles can facilitate the contact between the active materials and the electrolyte, and shorten the lithium diffusion length, while the secondary microsize particles can improve the electrode density to improve the volumetric energy density. A typical high resolution transmission electron microscope (HRTEM) image (Figure 6.2(b)) was taken from the edge of one particle. The lattice fringes are visible, with *d*-spacing of 0.29 nm, corresponding to the (107) plane of $Sn_{4+x}P_3$. The crystal size is about 30 nm, and there is an amorphous layer with thickness of 3 nm covering the surface of the particle. The selected area electron diffraction pattern (SAED, inset of Figure 6.2(b)) further confirms the coexistence of polycrystalline $Sn_{4+x}P_3$ with clear spotted diffraction rings and amorphous tin with diffusion rings. In order to further determine the composition of the anorphous layer, the high - resolution EDS was conducted by the probe-corrected JEOL ARM200F, as shown in Figure 6.3 and Table 6.1. The Sn/P ratio is 1.48 and 1.70 in the crystalline part, which are similar to that of Sn_4P_3. In comparison, the Sn/P ratio for spots at the amorphous adge increases, with the value of 2.9 and 3.7. It suggests that the amorphous layer is mainly consist of amorphous Sn and small amount of P. During ball milling, there are three kinds of powders in the jar, e.g. P, Sn, Sn_4P_3, which have different hardness. Sn_4P_3 as intermetallic compound has the highest hardness value, while the hardness value of P is smallest. Thus, Sn and P with the relatively smaller hardness value was milled into the smaller amorphous parcticles, covering over the surface of Sn_4P_3 to form the core-shell-like morphology of $Sn_{4+x}P_3$@(Sn+P).

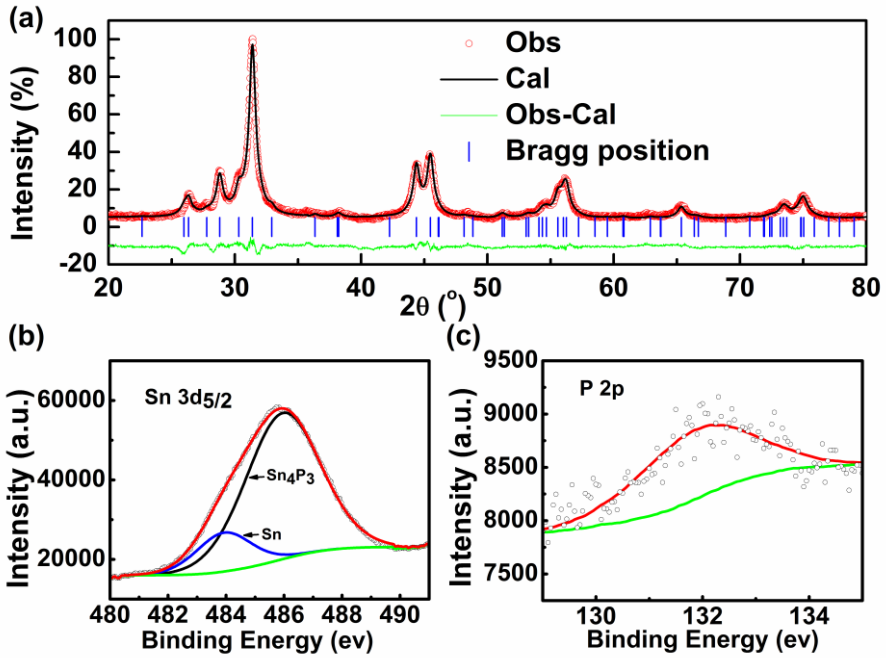

Figure 6.1. (a) Rietveld refinement XRD pattern of $Sn_{4+x}P_3$@(Sn+P) composite, and XPS analysis of $Sn_{4+x}P_3$@(Sn+P) powder for the elements (b) Sn and (c) P.

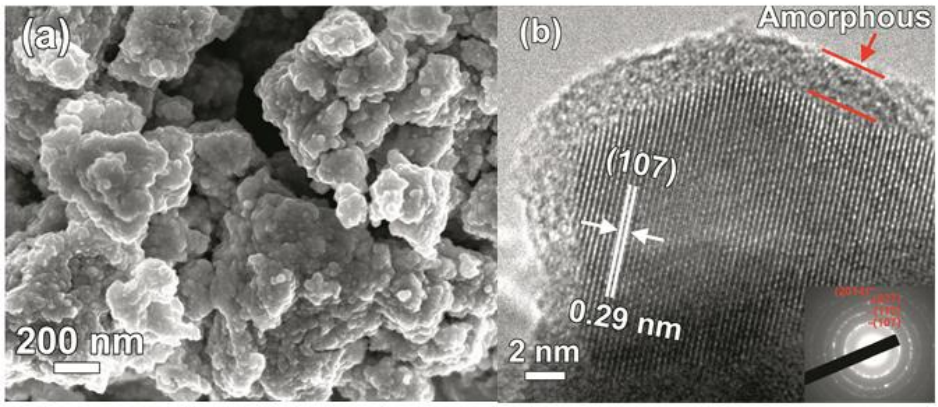

Figure 6.2. SEM (a) and HRTEM (b) images of $Sn_{4+x}P_3$@(Sn+P) composite. The inset in (b) is the corresponding SAED pattern.

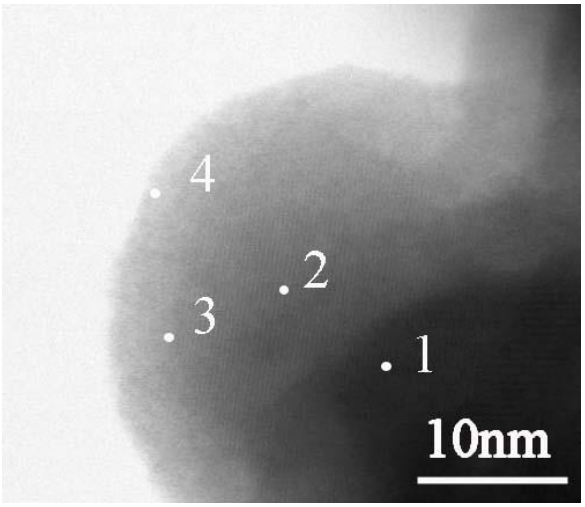

Figure 6.3. STEM image of the $Sn_{4+x}P_3$@(Sn+P) composite

Table 6.1 EDS results of the spots in both crystalline and amorphous layer.

Spot	Sn/P (at.%)
1	1.48
2	1.705
3	2.903
4	3.715

Figure 6.4 shows the charge and discharge curves of the $Sn_{4+x}P_3$@(Sn+P) electrode at current density of 100 mA g^{-1}. There were two potential plateaus in the discharge process: one was within the voltage range of 0.25 - 0.1 V and the other located at 0.1 - 0 V. Correspondly, there were two potential plateaus in the charge curve. The ex-situ XRD patterns of $Sn_{4+x}P_3$@(Sn+P) at different potentials during discharge and charge processes in the first cycle were used to try to determine the possible mechanism, as shown in the inset of Figure 6.4. Since the XRD patterns are amorphous during charge and discharge processes, it is very hard to study the mechanism in detail. The formation of small Sn peaks can be observed at point b, which may be due to the decomposition of $Sn_{4+x}P_3$. Based on the previous reports on P and Sn for Na storage, the possible reactions would be that $Sn_{4+x}P_3$ was transformed to Na_3P[1,252] and $Na_{15}Sn_4$,[299] respectively.

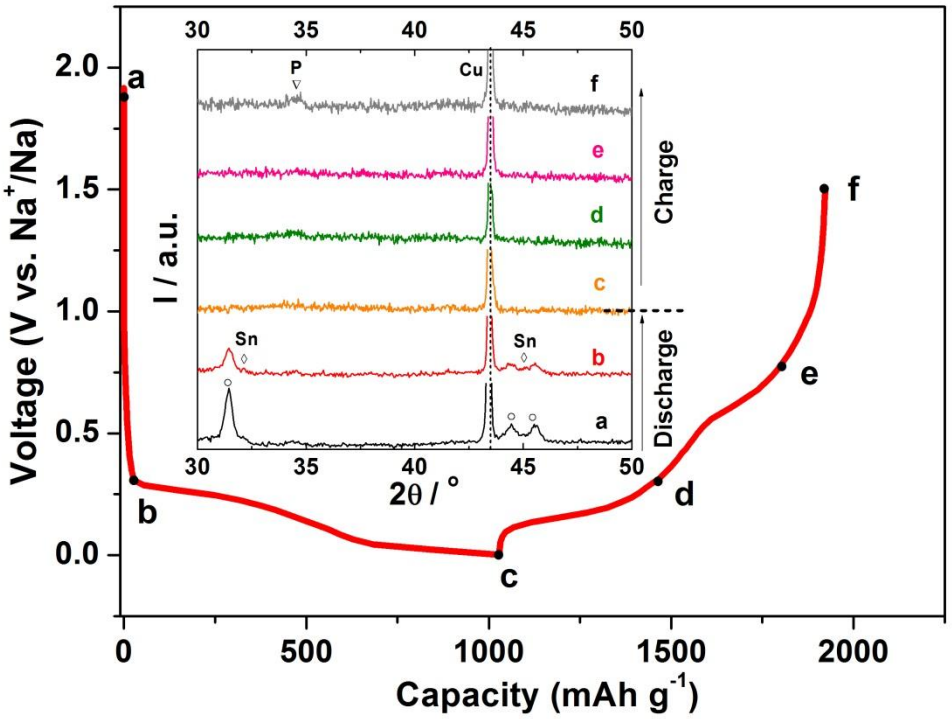

Figure 6.4. Charge and discharge curves of the $Sn_{4+x}P_3$@(Sn+P) composite electrode with CMC binder in 1 mol L^{-1} $NaClO_4$ in EC/DEC (1:1) at the current density of 100 mA/g. Inset presents ex-situ XRD patterns for the $Sn_{4+x}P_3$@(Sn+P) electrode collected at different potientials.

$$Sn_{4+x}P_3 + y\ Na \leftrightarrow Na_3P + Na_{15}Sn_4 \quad (6.1)$$

The theoretical specific capacity is 1080 mAh g^{-1}, based on the total conversion of $Sn_{4+x}P_3$@(Sn+P) to $Na_{15}Sn_4$ and Na_3P. Our result is approaching the theoretical capacity, with an initial discharge capacity of 1030 mAh g^{-1} and a reversible charge capacity of 892 mAh g^{-1}. A similar mechanism was also observed for Sn_4P_3 electrodes in lithium ion batteries (LIBs).[297,300]

Figure 6.5(a) presents the cycling performance of the $Sn_{4+x}P_3$@(Sn+P) electrodes with and without fluoroethylene carbonate (FEC) as additive in the electrolyte. A rapid fade in capacity was observed for the electrode without FEC as an additive, with discharge capacity of 50.4 mAh g^{-1} and capacity retention of 4.8% after 50 cycles. Komaba et al. have reported that FEC can improve the cycling stability.[294,295] Therefore, 5% volume fraction FEC was added into the electrolyte to improve the cycle life in our work. It is clearly seen that the $Sn_{4+x}P_3$@(Sn+P) electrode with 5 vol. % FEC exhibited relatively stable cycling performance.

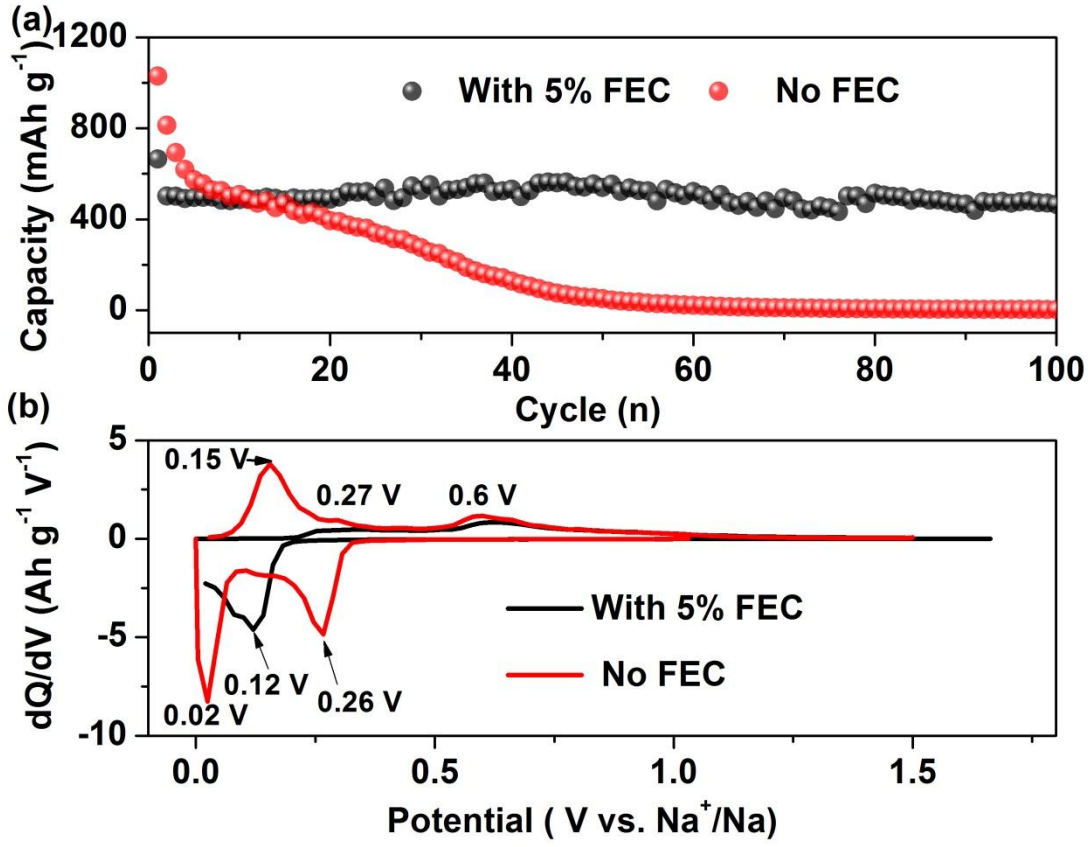

Figure 6.5. Cycle life (a) and differential capacity plots (dQ/dV) in the first cycle (b) of the $Sn_{4+x}P_3$@(Sn+P) composite electrode with and without FEC additive in 1 mol L^{-1} $NaClO_4$ in EC/DEC (1:1) at the current density of 100 mA g^{-1}.

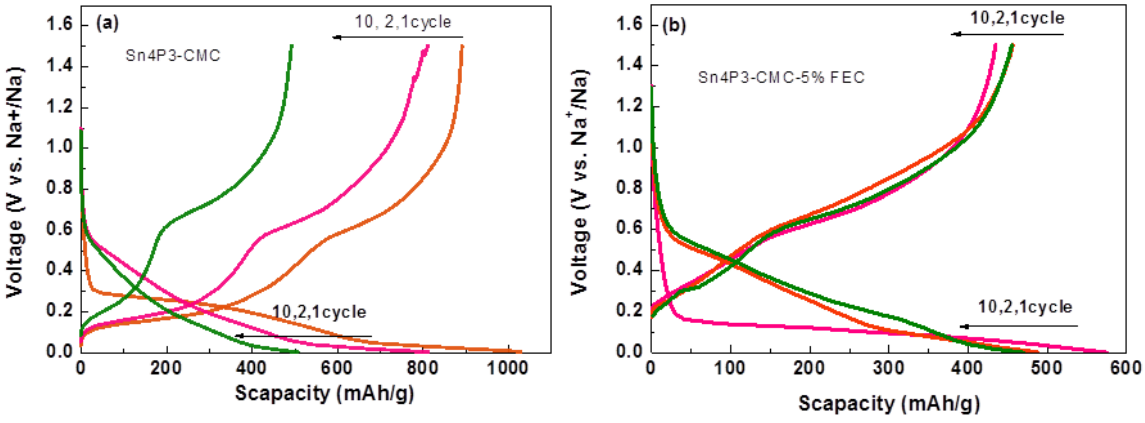

Figure 6.6. The charge/discharge curves of $Sn_{4+x}P_3$@(Sn+P) composite in the electrolyte (a) without and (b) with FEC additive .

After 100 cycles, the capacity still remained 465 mAh g^{-1}, with 72.1% and 92.6 % retention of the first (645 mAh g^{-1}) and second cycle (502 mAh g^{-1}) capacity, respectively. To the best

of our knowledge, this is the best electrochemical performance reported for tin-based anode in SIBs, with higher stable capacity and longer cycling life compared with the previously reported results.[1,228,239,244,246,252,278,294-296,301] The charge/discharge curves of $Sn_{4+x}P_3$@(Sn+P) in the electrolyte with FEC and withou FEC are shown in Figure 6.6. It is clear that the charge/discharge curves of $Sn_{4+x}P_3$@(Sn+P) with FEC electolyte additive overlapped well after 10 cycles, further suggesting cycling stability of $Sn_{4+x}P_3$@(Sn+P) has been improved significantly after adding FEC. This result clearly suggests that by using CMC as binder and the addition of 5 vol. % FEC to the electrolyte (1.0 mol/L $NaClO_4$ in an ethylene carbonate (EC) - diethyl carbonate (DEC) solution (1:1 v/v), $Sn_{4+x}P_3$@(Sn+P) can delivery highly stable cycling performance. It is noticed that the initial discharge capacity (645 mAh g^{-1}) for the electrode using FEC as additive was much lower than the one without FEC in the electrolyte. To investigate the low initial capacity of the electrode using FEC as additive, the differential capacity plots (dQ/dV) of the $Sn_{4+x}P_3$@(Sn+P) electrodes with and without FEC as additive are shown in Figure 6.5(b). Three cathodic peaks at around 0.26, 0.13, and 0.02 V are observed for the electrode with no addition of FEC. Correspondingly, there are three anodic peaks appearing at around 0.135, 0.27, and 0.58 V, respectively. In contrast, there are only two peaks in both the cathodic and anodic processes for the electrode using FEC as additive. The cathodic peak position was shifted from 0.26 to 0.12 V. The redox peaks at 0.02 V and 0.135 V are missing. This is probably due to the formation of a thick solid - electrolyte interphase (SEI) layer which has higher resistivity. Therefore, the capacity was only partially reversible. SEM images of the electrodes with and without FEC in the electrolyte are shown after one cycle in Figure 6.7. It is clearly seen that some microcracks have appeared in the $Sn_{4+x}P_3$@(Sn+P) electrode without FEC additive (Figure 6.7(a)), while after the addition of FEC, the $Sn_{4+x}P_3$@(Sn+P) electrode maintains its integrity (Figure 6.7(c)). This is because $Sn_{4+x}P_3$@(Sn+P) electrode suffers mechanical failure during alloying/de-alloying processes due to the large volume expansion (411.6%) occurring during alloying of Sn and P with Na to form Na_3P (391%) and $Na_{15}Sn_4$ (424%). As a result, there is a loss of electrical contact between the cracked and isolated $Sn_{4+x}P_3$@(Sn+P) particles in the electrode, resulting in capacity failure. Since the inital capacity of $Sn_{4+x}P_3$@(Sn+P) electrode with FEC in the electrolyte is only 62% of the capacity without using FEC, the volume expansion will be much smaller. Moreover, the FEC is decomposed to form a thicker SEI layer on the surface of the active materials and carbon black, as observed in Figure 6.7(d). This SEI layer can also maintain the integrity between the $Sn_{4+x}P_3$@(Sn+P) and carbon black particles and serve as a

buffer to relieve the stress from the volume expansion during the alloying/dealloying processes. This is the possible reason for the significant improvement in cycling stability of the $Sn_{4+x}P_3$@(Sn+P) electrode with FEC additive in the electrolyte. Figure 6.8 shows the morphology of the $Sn_{4+x}P_3$@(Sn+P) electrode charged at 2.0V after 50 cycles. The lattice fringes are visible, with *d*-spacing of 1.85nm, corresponding to the (106) plane of C, which is from the carbon black. Moreover, there are amorphous particles embedded into the amorphous layer (Figure 6.8(a)). In order to further determine the structure of the $Sn_{4+x}P_3$@(Sn+P) after cycling, STEM was tested and element mapping shows a compact SEI layer covered over the amorphous Sn and P particles (Figure 6.8(b)).

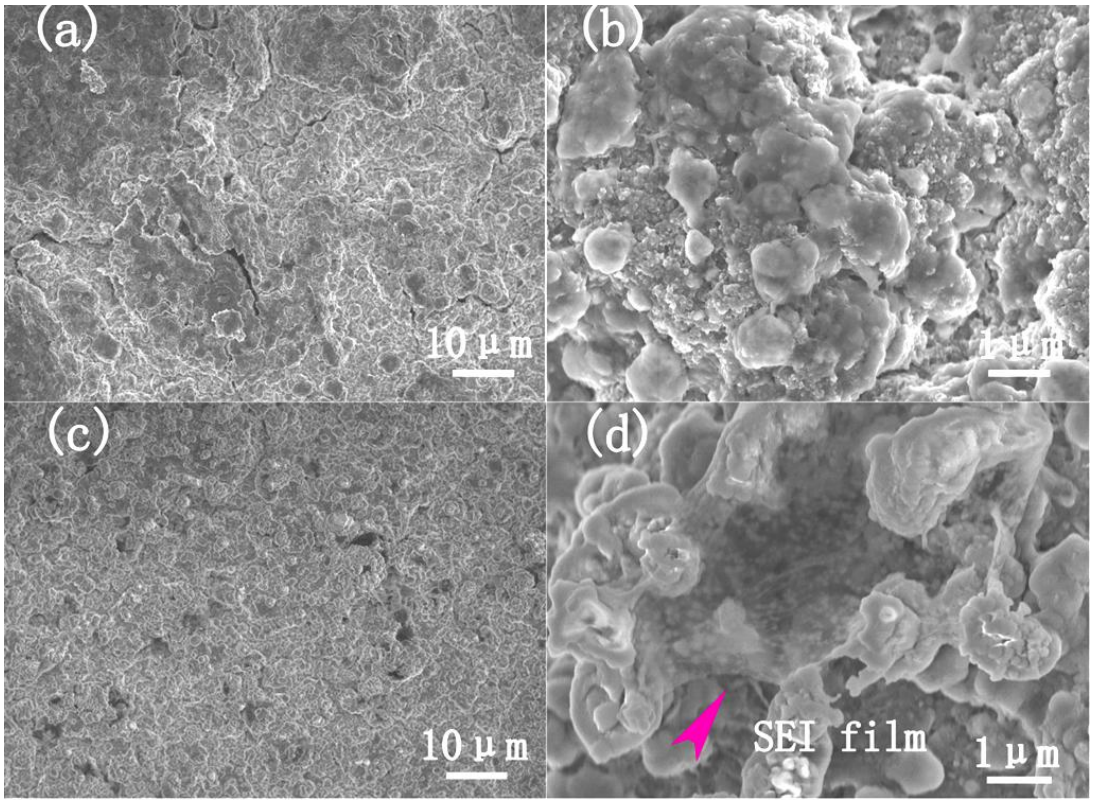

Figure 6.7. Morphology of the $Sn_{4+x}P_3$@(Sn+P) composite electrodes without (a, b) and with FEC (c, d) electrolyte additive after the first cycle: (a, c) low magnification; (b, d) high magnification.

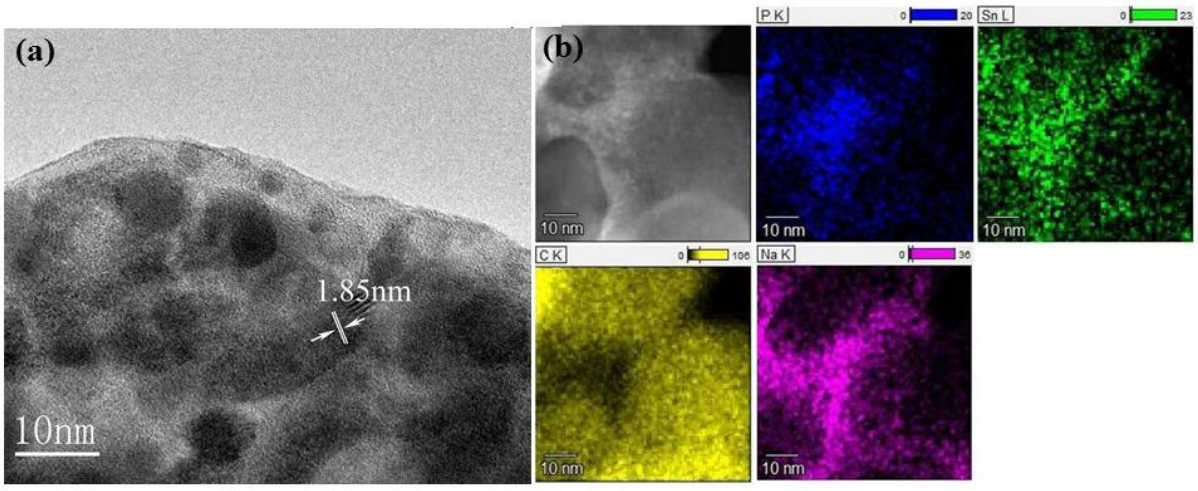

Figure 6.8. (a) TEM image and (b) high - resolution EDS of $Sn_{4+x}P_3$@(Sn+P) electrode after 50 cycles.

Figure 6.9 displays the rate capability of the $Sn_{4+x}P_3$@(Sn+P) electrode with 5 vol. % FEC additive in the electrolyte over the potential range of 0-1.5 V vs. Na^+/Na. The $Sn_{4+x}P_3$@(Sn+P) electrode exhibited excellent high rate cycling performance, as shown in Figure 6.9(a). The average discharge capacity is 543.2, 478.8, 423.3, 317.7, 245.2, 165.0, and 58.2 mAh g^{-1} at different current density of 0.2, 0.4, 1, 2, 4, 10, and 20 C (1 C = 500 mA g^{-1}), respectively. Finally, the rate performance of $Sn_{4+x}P_3$@(Sn+P) is compared with those of reported tin-based electrodes in composites with multiwalled carbon nanotubes (MWCNTs) and other forms of carbon for sodium storage (SnO_2@MWCNT composite,[278] SnO_2@graphene nanocomposites,[210,228] SnSb/C composite[239]), together with the best results for carbonaceous materials for SIBs (hollow carbon nanospheres,[211] carbon nanowires,[212] and reduced graphene oxide (RGO)[210]) (Figure 6.9(b)). It is obvious that the rate capability of the $Sn_{4+x}P_3$@(Sn+P) is better than those of the carbonaceous materials and is the best among the tin-based electrodes reported. This is probably due to the structure of the composite in which amorphous Sn can maintain electrical contact between $Sn_{4+x}P_3$ particles and small particle size (30-80 nm) can shorten the diffusion length of sodium ion. The characterization and electrochemical performance for Sn_4P_3 was shown in Figure 6.10 and Figure 6.11. The Sn_4P_3 without amorphous Sn coating confirmed by HRTEM (Figure 6.10(a)) and XPS results (Figure 6.10(b)) cannot cycle stably for more than 20 cycles even with 5% FEC additives in the electrolyte (Figure 6.11). This may be due to the fact that the amorphous Sn layer and FEC additive can work together to form a stable SEI layer. This shows the important role of

amorphous Sn in the composite. Further improvement of high rate capability could be achieved via making carbon composites and optimize the FEC contents.

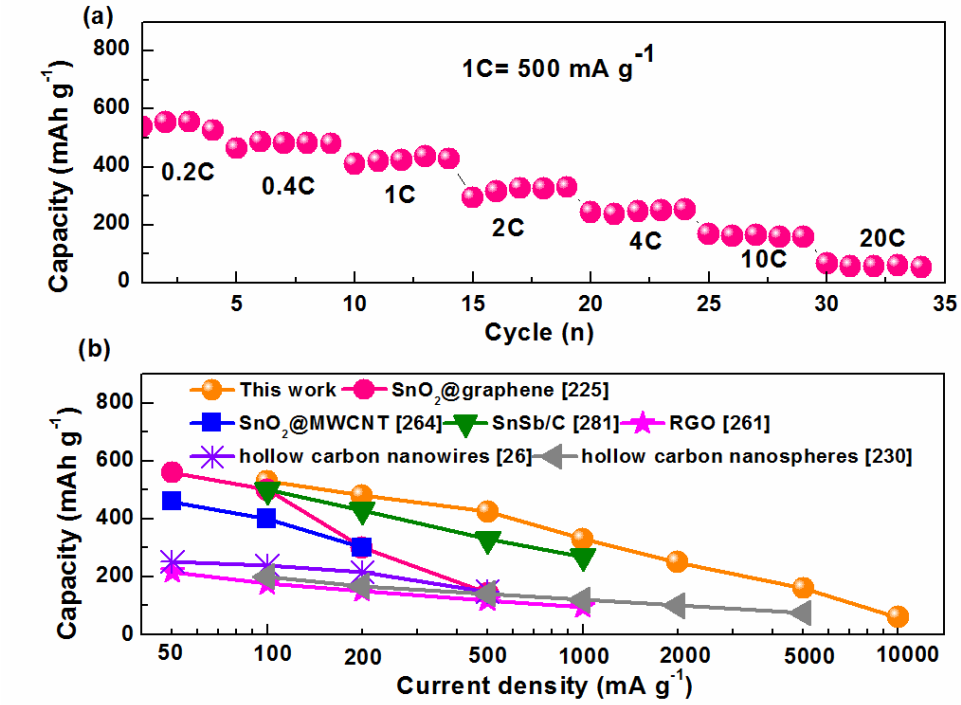

Figure 6.9. Rate capability of the $Sn_{4+x}P_3$@(Sn+P) composite electrode using CMC binder with 5% FEC additive in the electrolyte (a), and comparison of the rate capacity of $Sn_{4+x}P_3$@(Sn+P) with tin-based and carbonaceous materials [210-212,228,239,278](b).

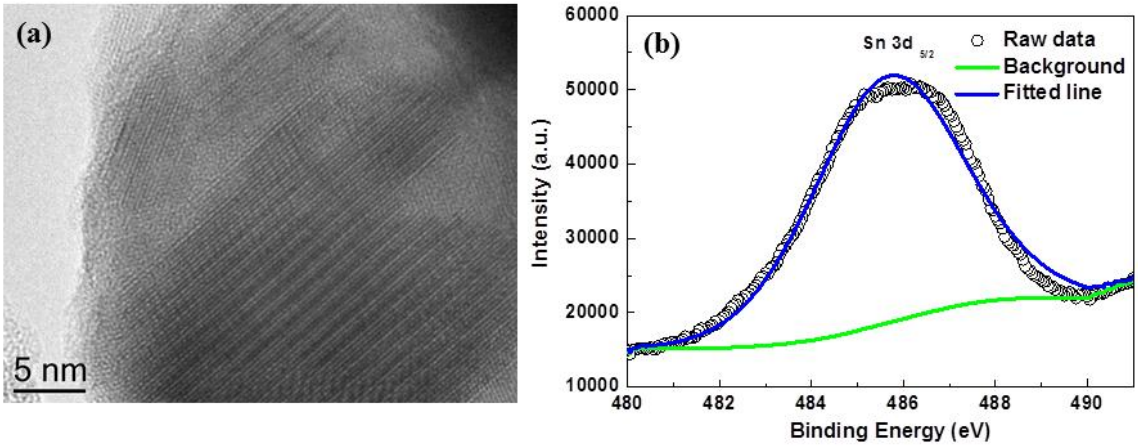

Figure 6.10. (a) HRTEM image and (b) Sn 3d XPS analysis of Sn_4P_3 sample.(The amorphous coating layer of Sn cannot be observed in Sn_4P_3 sample and the amorphous Sn peak was not observed in XPS).

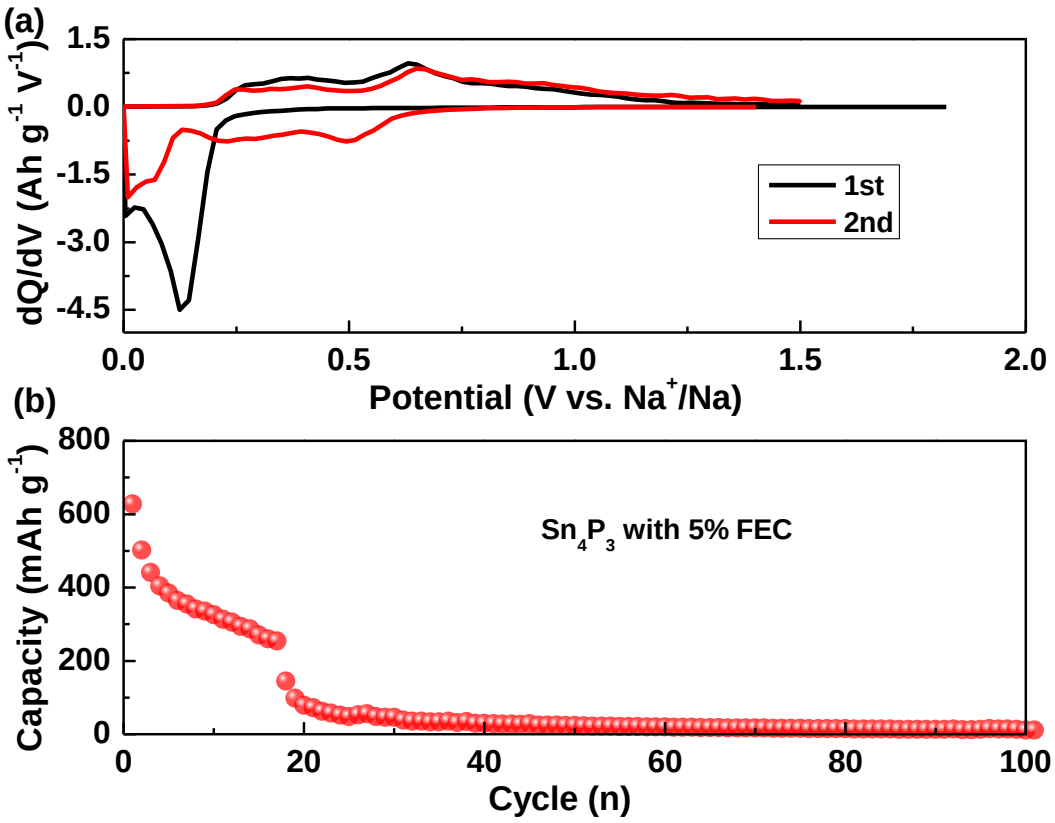

Figure 6.11. Differential capacity plots (dQ/dV) in the first 2 cycles (a) and cycle life (a) of the Sn_4P_3 electrode with 5% FEC additive in 1 mol L^{-1} $NaClO_4$ in EC/DEC (1:1) at the current density of 100 mA g^{-1}. The dQ/dV curves for Sn_4P_3 electrode shows similar shape as that of $Sn_{4+x}P_3$@Sn electrode. However, the cycling stability Sn_4P_3 electrode is much worse than $Sn_{4+x}P_3$@Sn electrode. This may be due to the fact that the amorphous Sn layer and FEC additive can work together to form a stable SEI layer.

6.4 Conclusion

In summary, we prepared $Sn_{4+x}P_3$@(Sn+P) composite in large quantities by direct low-speed ball milling of the P and Sn powders and studied its electrochemical performance as anode material for sodium ion batteries. The results demonstrated that the $Sn_{4+x}P_3$@(Sn+P) electrode using CMC binder delivered an initial discharge capacity of 1030 mAh g^{-1} and a reversible charge capacity of 892 mAh g^{-1}, at the current density of 100 mA g^{-1}. The addition of 5% FEC to the electrolyte can improve the cycling stability of the $Sn_{4+x}P_3$@(Sn+P) electrode, delivering a stable capacity of 465 mAh g^{-1}, with capacity retention of 92.6%, at the current density of 100 mA g^{-1} over 100 cycles. Moreover, the $Sn_{4+x}P_3$ electrode exhibited superior high rate capability, with a stable capacity of 165 mAh g^{-1} at the 10 C-rate (5000 mA g^{-1}). All the results indicate that $Sn_{4+x}P_3$@(Sn+P) would be a promising anode material

candidate for sodium ion batteries with low cost, long cycling stability, and relatively good rate capability.

Chapter 7. A new, productive MP (M=Fe,Co) anode material for sodium-ion batteries

$Sn_{4+x}P_3$ which is investigated in Chapter 6, notably, possesses two active elements, i.e., Sn and P, which both can alloy with Na. Therefore, Sn in the Sn_4P_3 compound makes contributions to both the total capacity and the volume change during the sodiation/desodiation. The question is whether the cycling performance of phosphide compound will be further improved through the substitution of Sn by inactive metals. Herein, we prepared iron phosphide (FeP) and cobalt phosphide (CoP) in large amounts by a simple ball-milling method. In this sample, the metal (Fe, Co) is inactive and acts as a conductive matrix to buffer the volume expansion.

7.1 Introduction

Recently, Na-ion batteries (SIBs) have been attracting more attention as the most promising candidate for stationary batteries due to their low cost, and the abundant supply and widespread reserves of Na mineral salts.[44,48,256-258,302,303] Since the Na ion (radius 0.95 Å) is about 55% larger than the Li ion (0.6 Å), however, the range of potential candidate materials is seriously limited. The main goal for sodium ion battery research is to search for a candidate material with long cycle life and high capacity. Carbonaceous materials have been widely investigated as the anode for sodium ion storage due to their good cycling performance, but their capacity is low (less than 300 mAh g^{-1}).[66,68,212,263,304] More recent reports show that some elements can alloy with sodium to deliver higher theoretical capacity as the anode in SIBs, such as Sn (847 mAh g^{-1}),[299] Sb (664 mAh g^{-1}),[248] and P (2596 mAh g^{-1}).[1,289] The fatal defect for these anode candidates, however, is their huge volume change during the sodiation/desodiation, resulting in pulverization of the electrode material accompanied by poor cycling performance.

Generally, there are three ways to overcome the poor cycling performance. The first is to synthesize nanosized materials.[288,313-315] It is very difficult, however, to use a chemical method to prepare nanosized P. In a previous report, even though the particles were nanosized, the cycling performance was still unstable, due to the poor electronic conductivity of P. Thus, this method to synthesize nanosized structures is not suitable for P. The second way is to coat a conductive and elastic layer on the surface of the active material to form a composite, which can not only improve the electronic conductivity, but also act as a buffer to absorb the stress from the volume expansion. Recently, some papers have reported P/carbon composites, such as P/Super P,[1,252] P/carbon nanotubes (CNTs),[289]P/graphene,[3]etc. The

results show that the cycling stability of P was improved dramatically. The third way is to prepare an alloy compound, which has been confirmed as an effective method to overcome the disadvantages resulting from huge volume expansion in both LIBs and SIBs.[18,233,239,306,316] Manthiram's group reported that MxSb (M = Cu, Fe, Ni) in a matrix of Al_2O_3-C had a better cycling performance than Sb in the same matrix of Al_2O_3-C for sodium-ion batteries.[305] Lin et al. reported that $Sn_{0.9}Cu_{0.1}$ as anode for SIBs had a stable capacity of 420 mAh g^{-1} for 100 cycles.[306] SnSb/C alloy anode for Na-ion batteries has been reported with a capacity retention of 80% after 50 cycles.[239] Recently, our group reported that $Sn_{4+x}P_3$@(Sn-P) composites as anodes for SIBs significantly extended the cycle life, with a stable capacity of 465 mAh g^{-1} and capacity retention of 92.6% over 100 cycles.[307] Kim et al. and Qian et al. also reported that Sn_4P_3 and Sn_4P_3/C can deliver the capacity of 718 mAh g^{-1} and 850 mAh g^{-1} at the current density of 100 mA g^{-1} and 50 mA g^{-1}, respectively.[242,308] Notably, Sn_4P_3 possesses two active elements, i.e., Sn and P, which both can alloy with Na. Therefore, Sn in the Sn_4P_3 compound makes contributions to both the total capacity and the volume change during the sodiation/desodiation. The reported specific capacity is still far below the theoretical capacity, however.

To fully utilize the capacity from P, herein, we prepared iron phosphide (FeP) and cobalt phosphide (CoP) in large amounts by a simple ball-milling method. In these sample, the metal (Fe, Co) is inactive and acts as a conductive matrix to buffer the volume expansion. The as-obtained FeP and CoP compoundS were investigated as anode in SIBs in half cells and showed high reversible capacity of more than 500 mAh g^{-1} and 700 mAh g^{-1}, respectively, which offers a new alternative to carbonaceous anode materials in Na cells.

7.2 Experimental Section

7.2.1 Synthesis of FeP phosphide

Fe (>99.5%, Sigma), Co (> 99.8%, Sigma) and red P (>99 %, Sigma) were used as the starting materials without further purifying. FeP and CoP was prepared by the simple ball-milling method using the corresponding stoichiometric molar ratio of the metal (Fe, Co) to P. The starting materials were put into a hardened steel vial with milling balls 2 mm in diameter. The weight ratio of milling balls to powder was 20:1. The vial was assembled in an argon-filled glove-box, and then mounted on the ball mill. The rotation speed of the mill was set to 300 rpm for 20 h.

7.2.2 Characterization

The crystalline structure of the active powder was characterized by powder X-ray diffraction (XRD) on a GBC MMA diffractometer with a Cu Kα source. The morphology of the sample was investigated by field emission scanning electron microscopy (FESEM; JEOL JSM-7500FA) and transmission electron microscopy (TEM, JEOL 2011, 200 keV). X-ray photoelectron spectroscopy (XPS) was conducted using a SPECS PHOIBOS 100 Analyser installed in a high-vacuum chamber with base pressure below 10-8 mbar. X-ray excitation was provided by Al Kα radiation with photon energy hν = 1486.6 eV at the high voltage of 12 kV and power of 120 W. Ex-situ XRD data were collected by powder X-ray diffraction (XRD) on a GBC MMA diffractometer with a Cu Kα source. The cell used for the data collection was charged at a current density of 100 mA g^{-1} between 0 V and 1.5 V.

7.2.3 Electrochemical measurements

The FeP and CoP electrodes were prepared by mixing 70% active materials, 10% carbon black, and 20% binder by weight to form an electrode slurry, which then was coated on copper foil, followed by drying in a vacuum oven overnight at 80 ℃, and then pressing at 30 MPa. The electrode was punched into a round area with 3 mg cm^{-2}. Three kinds of FeP electrodes were prepared by changing the binders: carboxymethyl cellulose (CMC)), Poly(vinylidene fluoride (PVDF), carboxymethyl cellulose (CMC))/Poly(acrylic acid) (PAA). The CoP electrodes were prepared using carboxymethyl cellulose (CMC) as binder. The sodium foil was cut by the doctor blade technique from a sodium bulk stored in mineral oil, which then was employed as both reference and counter electrode. The electrolyte was 1.0 mol/L $NaClO_4$ in an ethylene carbonate (EC) - diethyl carbonate (DEC) solution (1:1 v/v), with or without 5 vol.% addition of fluoroethylene carbonate (FEC). The cells were assembled in an argon-filled glove box. The electrochemical performances were tested by a Land Test System at current density of 50 mA g^{-1} in the voltage range of 0-1.5 V (vs. Na^+/Na).

7.3 Results and discussion

7.3.1 Investigation on FeP electrode for sodium ion battery

FeP was prepared by simple ball milling for 20 h using the corresponding stoichiometric molar ratio of the metal (Fe) to P. Figure 7.1(a) shows the XRD pattern of the FeP, which can be indexed to the orthorhombic phase with space group Pnma (JPCDS No. 65-2595, a = 5.187 Å, b = 3.095 Å, c = 5.793 Å). The as-prepared FeP showed broad peaks with low

intensity, suggesting that the particle size of the as-prepared sample after the ball milling is very small. The morphology of FeP was examined by field emission scanning electron microscopy (FE-SEM), as shown in Figure 7.1(b). The FE-SEM images of FeP show that the particle size is about 30-50 nm. Figure 7.1(c, d) shows a high resolution transmission electron microscope (HRTEM) image and the corresponding selected area electron diffraction (SAED) pattern, respectively, of the as-prepared FeP. As shown in Figure 7.1(c), small crystals 10-20 nm in size are embedded in the amorphous matrix. The d-spacings of these FeP nanoparticles are 0.273 nm and 0.237 nm, corresponding to the (011) and (201) planes, respectively. The SAED pattern of the as-prepared FeP presents the characteristics of polycrystalline rings (Figure 7.1(d)). X-ray photoelectron spectra (XPS) of the as-prepared FeP were collected and are shown in Figure 7.2. The binding energies for P2p at 129.3 eV and Fe 2p3/2 at 706.9 eV are ascribed to the FeP.[309]

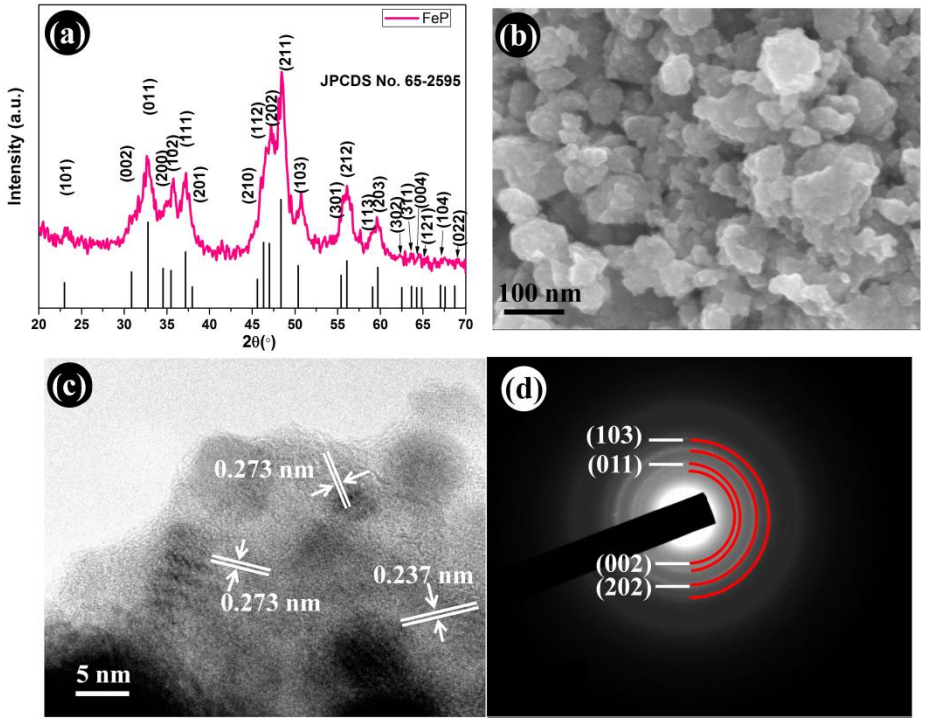

Figure 7.1. Characterization of FeP: (a) XRD pattern; (b) FE-SEM image; (c) high resolution TEM image; (d) the corresponding SAED pattern.

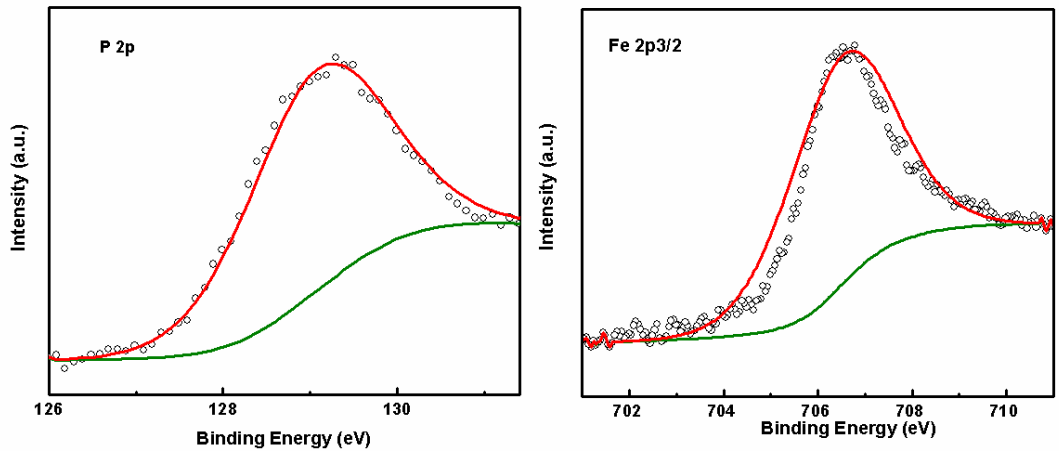

Figure 7.2. X-ray photoelectron spectroscopy (XPS) of the as-prepared FeP.

The electrochemical performance of the FeP electrode was tested at the current density of 50 mA g^{-1} within the voltage range of 0-1.5 V in the electrolyte of 1 M $NaClO_4$/ EC:DEC. The loading mass of each electrode tested in this work is about 3 mg cm^{-1}. Figure 7.3(a) presents the initial charge/discharge curve of FeP and the differential curves for the first two cycles (inset). As shown in Figure 7.3(a), the FeP electrode delivered the discharge and charge capacity of 764.7 and 460 mAh g^{-1}, respectively, in the initial cycle. There was one sloping plateau between 1.0 V and 0.4 V in the initial discharge curve, corresponding to the solid electrolyte interphase (SEI) formation due to the electrolyte decomposition.[1,211]This is the reason for the large irreversible capacity lost in the first cycle. To reveal the details of the electrochemical reactions of FeP, the differential capacity curves of the FeP in the first two cycles are plotted in the inset of Figure 7.3(a). It can be seen that two peaks around 0-0.3 V are observed in the second discharge process. Since no Na-Fe-P ternary phase exists, the possible sodium storage mechanism of FeP is not the intercalation reaction. Moreover, the peaks that appeared at 0-0.3 V in the dQ/dV curves are similar to those of P, which are assigned to Na_xP formation.

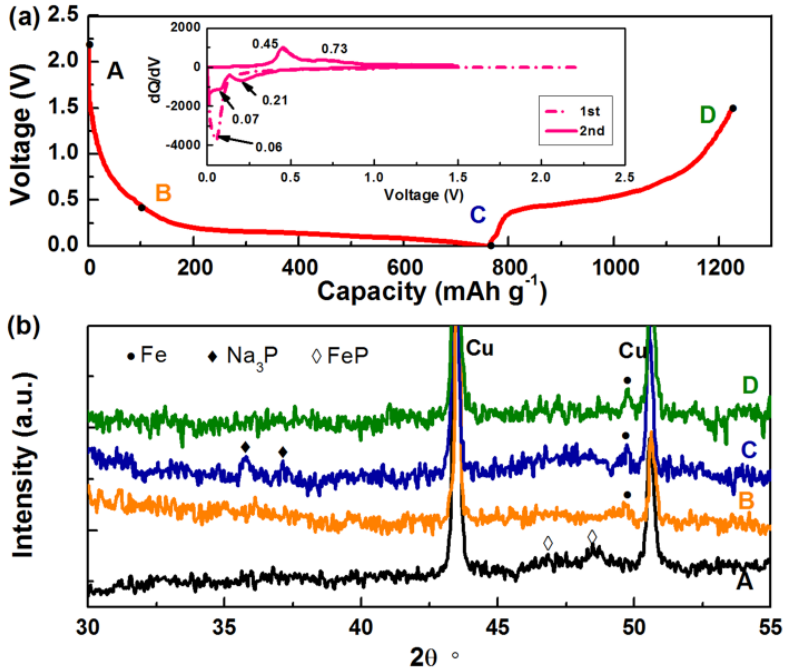

Figure 7.3. (a) Charge-discharge curve of FeP electrode and the differential curves for the first two cycles (inset). Point A is corresponding to the pristine state, Point B is corresponding to the discharged state at 0.4V, Point C and D are corresponding to the discharged state at 0V and charged state at 1.5V, respectively; (b) ex-situ XRD patterns of FeP tested at the current density of 50 mA g^{-1} in the first cycle at the points indicated on the curve in (a).

To reveal the sodium storage mechanism of FeP, ex-situ XRD, and transmission electron microscopy (TEM) have been used. Figure 7.3(b) shows the XRD patterns of the FeP electrodes charged at different states in the first cycle. When the FeP electrode is discharged at 0.4 V, the characteristic peak of Fe was observed in the XRD pattern, and the characteristic peaks of FeP disappeared (Figure 7.3(b)). This demonstrates that FeP decomposes to form the Fe during the electrochemical reduction process. Besides Fe, Na_3P was also detected in the XRD pattern when the FeP electrode was fully discharged at 0 V. Therefore, the sodium storage mechanism of FeP is described by the following equation

$$FeP + 3Na^+ + e^- \rightarrow Fe + Na_3P \quad (7.1).$$

Based on this mechanism, the theoretical capacity of FeP is about 924 mAh g^{-1}, which approaches the capacity of FeP delivered in the first cycle (764.7 mAh g^{-1}). However, the initial capacity is lower than the theoretical one, it is possible due to the polarization resulted from both the low electric conductivity of FeP and the SEI formation on the surface of electrode. During the charge process, the sodium is extracted from the Na3P to form P at the

end. Only the characteristic peak of Fe was observed, however, in the XRD pattern of the electrode charged at 1.5 V (the end of the charge process). This is possibly because the P that is finally formed is amorphous or the crystal size is very small, so that it cannot be detected by XRD. Therefore, the charge process of FeP for the sodium ion battery can be summarized as follows:

$$Na_3P + Fe \rightarrow P + Fe + 3Na^+ + 3e^- \quad (7.2).$$

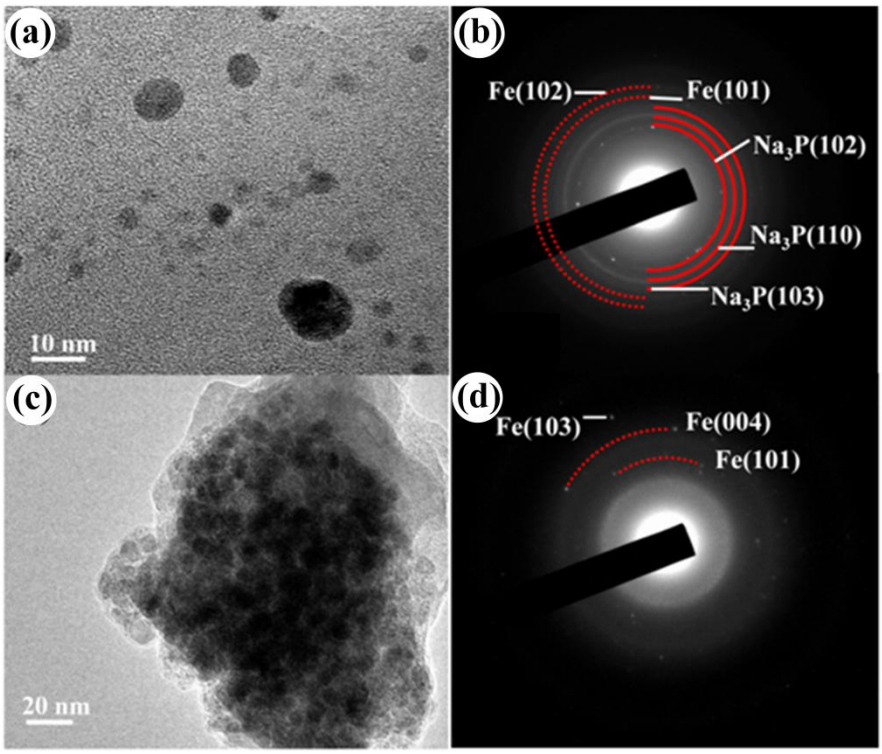

Figure 7.4. TEM images (a, c) and SAED patterns (b, d) of FeP electrode discharged at 0 V (a, b) and charged at 1.5 V (c, d).

To further confirm the storage mechanism of FeP, the structure and phase change of the FeP electrode were detected by transmission electron microscopy (TEM). Figure 7.4 shows the structures and the SAED patterns of the FeP electrodes charged at different states. When the FeP is fully reduced (Figure 7.4(a)), the morphology is completely changed compared to the as-prepared FeP in Figure 7.1(d). Small crystallized particles 5-10 nm in size can be seen in the amorphous matrix. Moreover, the SAED pattern reveals that two phases appear at the end of the discharging. One is Fe, and the other is Na_3P, as shown in Figure 7.4(b), which is consistent with the ex-situ XRD results. After fully charging, the FeP electrode has an amorphous character, as shown in Figure 7.4(c). The SAED pattern of the FeP electrode charged at 1.5 V shows the main amorphous diffusion rings with some diffraction spots. The

diffraction spots are indexed to Fe (Figure 7.4(d)). Therefore, combining the TEM results with the ex-situ XRD results, it is concluded that the sodium storage mechanism of FeP is through P reacting reaction with Na. In the FeP compound, the metal (Fe) is inactive and acts as a conductive matrix to buffer the huge volume expansion of P.

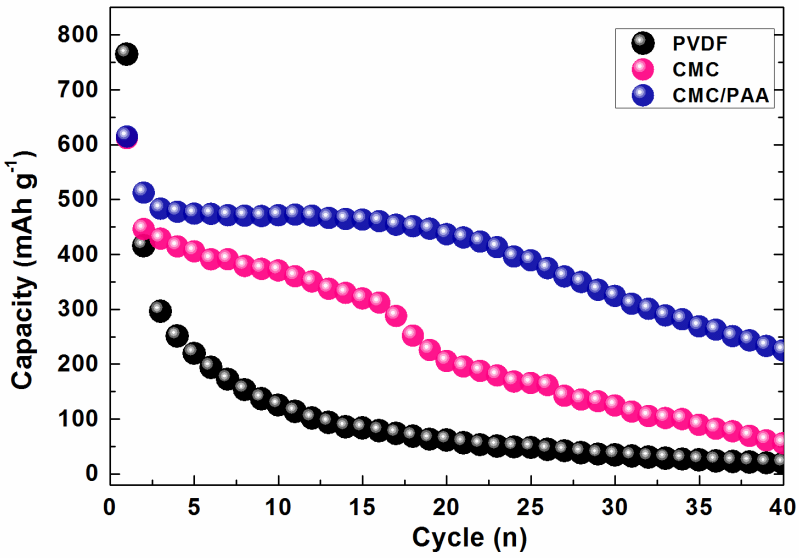

Figure 7.5. Cycling performance optimization of FeP electrodes prepared with different binders in the electrolyte of 1M $NaClO_4$/(EC: DEC).

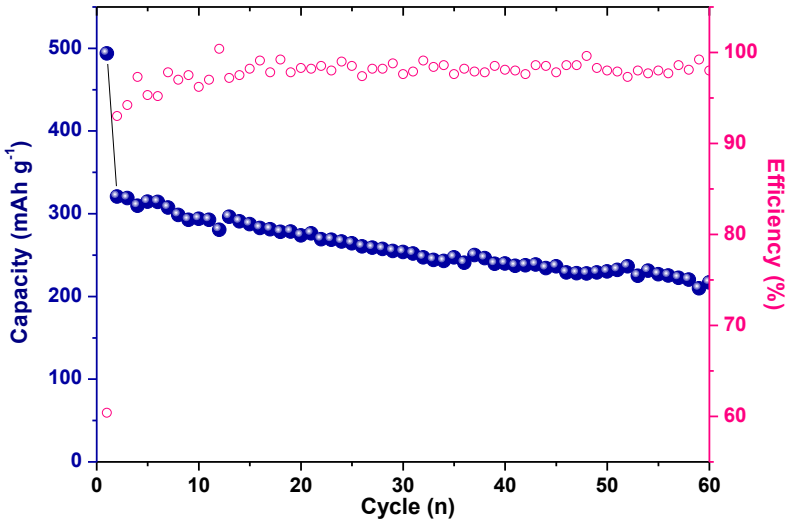

Figure 7.6. The cycling performance of FeP with CMC/PAA binder in the electrolyte of 1M $NaClO_4$/EC:DEC with 5% FEC additive.

In order to improve the electrochemical performance of FeP, optimization was conducted with three different binders (CMC, PVDF, CMC/PAA) and FEC electrolyte additive. The cycling performances of the FeP electrodes with different binders were tested at the current density of 50 mA g^{-1} in the voltage range of 0 - 1.5 V, as presented in Figure 7.5. It can be seen that the FeP electrode with PVDF binder presents serious capacity decay. After 5 cycles, the capacity decreased from about 765 mAh g^{-1} in the first cycle to 210 mAh g^{-1}. When CMC was used as the binder, the capacity degradation was improved. By using CMC and PAA in a combined binder, the cycle life of the FeP electrode was greatly extended. This is because CMC/PAA binder can form a cross-linked structure which has high tolerance for the internal mechanical stresses generated by the volume expansion.[310] The capacity of the FeP electrode with CMC/PAA binder still dropped after 20 cycles, however. In order to enhance the cycling performance of the FeP electrode, 5% FEC was added to the electrolyte. FEC is an effective additive to help a contact SEI film formation on the surface of the electrode, as reported by Komaba et al.[294,295] Clearly, after 5% FEC addition, the cycle life of the FeP electrode with CMC/PAA binder was prolonged significantly (Figure 7.6). Capacity of 321 mAh g^{-1} was retained after 60 cycles, which is 69 % retention of the capacity in the second cycle. SEM images of the electrodes after cycling for 5 cycles show some microcracks on the electrode without FEC additive, while the electrode remains intact with 5% FEC additive, confirming that FEC additive promotes stable SEI film formation on the surface of the electrode to improve the cycling performance (Figure 7.7 and Figure 7.8). At the same time, such thick and stable solid-electrolyte interphase (SEI) layer which has higher resistivity increases the resistance of the electrode.[307] Therefore, the capacity of the FeP electrode in the electrolyte with FEC was only partially reversible. In summary, the cycling performance of the FeP electrode was improved after choosing CMC/PAA as the binder and FEC as the electrolyte additive. The rate capability of FeP was tested at various current density and shown in Figure 7.10. When the current density increased from 50 mA g^{-1} to 500 mA g^{-1}, the capacity decreased from 420 mAh g^{-1} to 60 mAh g^{-1}, respectively.

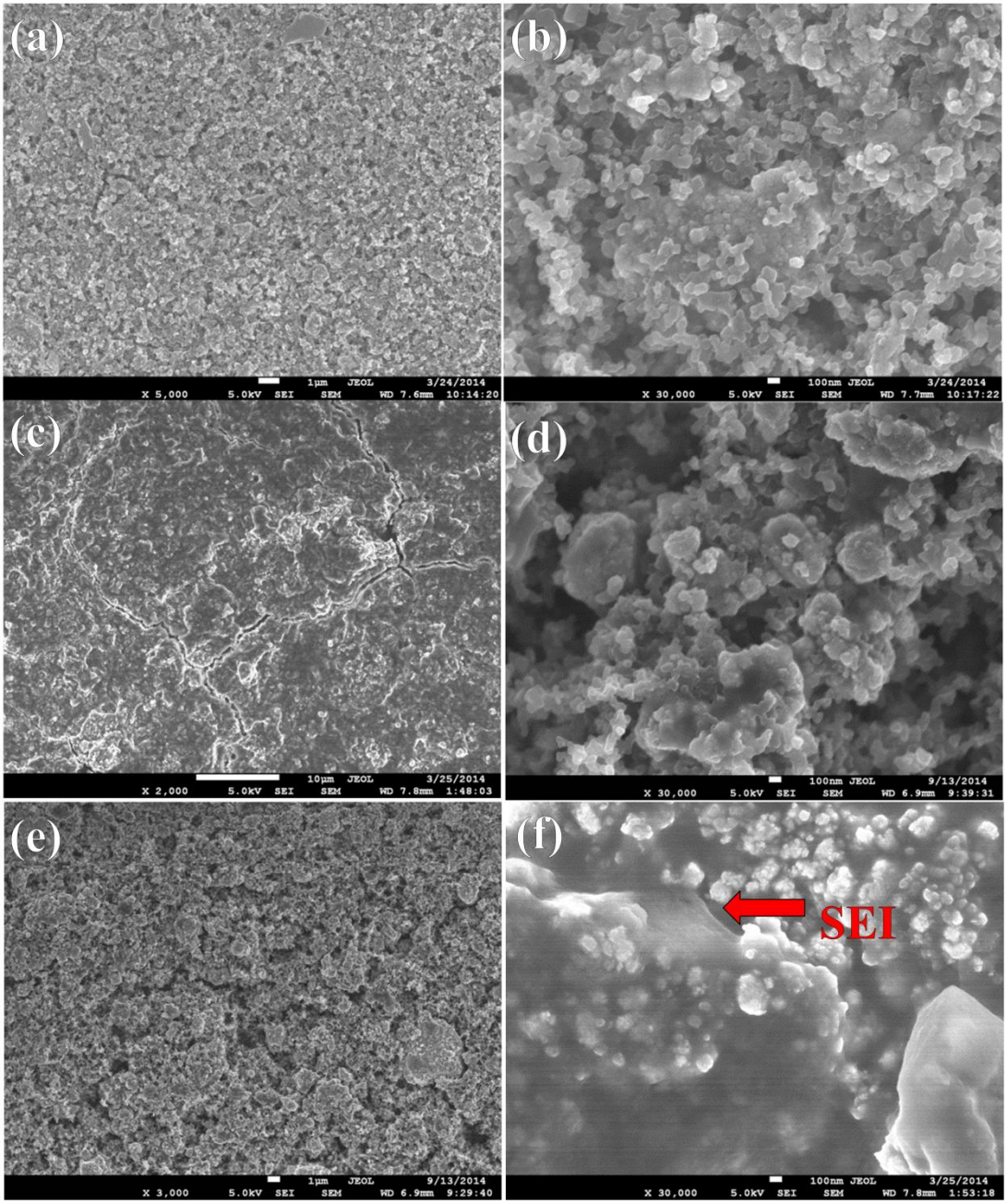

Figure 7.7. SEM images of FeP Electrodes with CMC/PAA binder (a, b) before and (c - f) after 5 cycles in the electrolyte (c, d) without FEC and (e, f) with FEC additive.

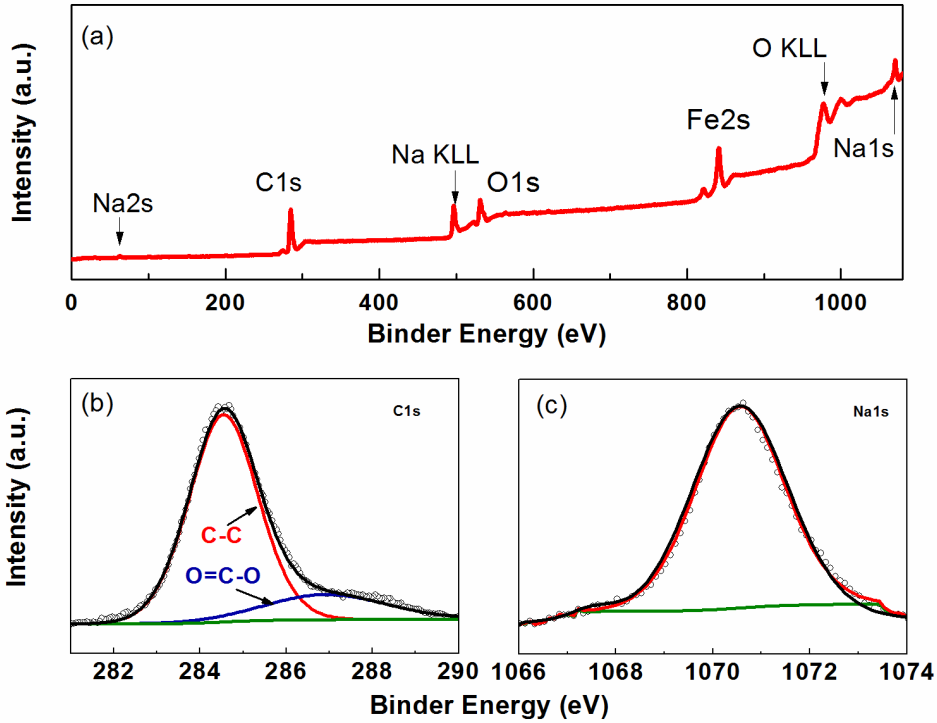

Figure 7.8. X-ray photoelectron spectroscopy (XPS) of the FeP electrode after 1 cycle in the electrolyte with FEC additive: (a) survey spectrum; (b) C1s; (c) Na1s.

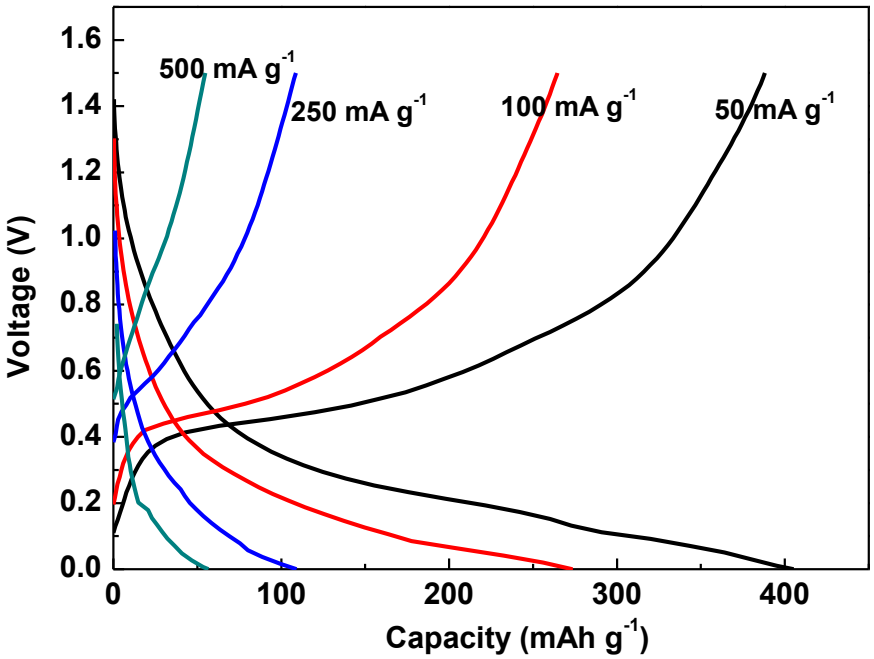

Figure 7.9. The rate capability of FeP tested at different current density.

7.3.2 Investigation on CoP electrode for sodium ion battery

The structure and morphology of CoP were characterized by X-ray diffraction (XRD), scanning electron microscopy (SEM), and transmission electron microscopy (TEM). Figure 8.1(a) shows the XRD pattern of the CoP. From the XRD pattern of the as-obtained CoP, the intensity of the CoP peaks is very low, and the peaks are very broad, indicating that the particle size is very small. The CoP phase was indexed to orthorhombic phase with Pnma space group (JPCDS No. 29-0497, a = 0.5077 nm, b = 0.3281 nm, c = 0.5587 nm). Moreover, the SEM and TEM images of CoP also demonstrate that the CoP particles are very small (Figure 8.1(b, c)). As shown in Figure 8.1(c), the morphology of the as-prepared CoP mainly presents amorphous characteristics, with small crystals 10-20 nm in size embedded in the amorphous matrix. The d-spacings of these CoP nanoparticles are 0.254 nm and 0.283 nm, assigned to the (200) and (011) planes, respectively. The selected area electron diffraction patterns (SAED) are indexed to the orthorhombic phase, and the diffraction rings correspond to the (020), (211), (200), (011), and (201) planes, as shown in Figure 8.1(d). It is worthy noticing that the as-prepared CoP is not sensitive to air, however, if it is kept under air for long time, it will be oxidized. Thus, it is kept in glove boxes. To detect the component of the amorphous part in the TEM image, energy-dispersive X-ray spectroscopy (EDS) mapping is carried out, and the results are shown in Figure 8.1(e). As shown in Figure 8.1(e), it is clear that the amorphous matrix mainly consists of amorphous P and small amount of Co.

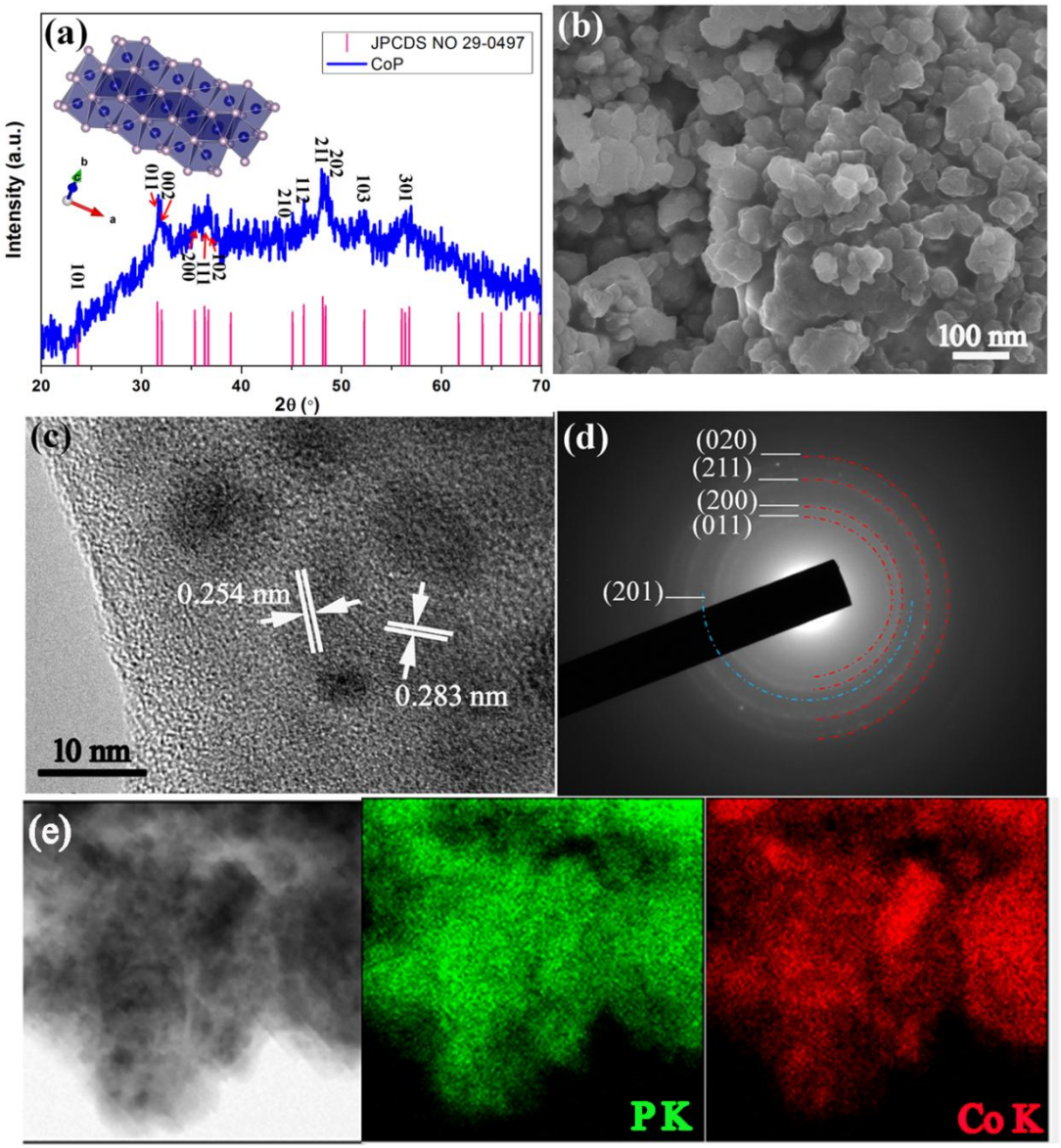

Figure 7.10. Characterization of CoP: (a) XRD pattern, (b) SEM image, (c) high resolution TEM image, (d) SAED pattern, (e) STEM image and corresponding EDS mapping.

The electrochemical performance of CoP as anode for sodium ion batteries was tested within the voltage window of 0-1.5 V. The electrolyte was 1 M $NaClO_4$ in a solution of EC:DEC = 1:1, (v/v). Figure 8.2(a) shows the charge/discharge curves of the CoP electrode at the current density of 100 mA g^{-1}. During the first discharge, the CoP electrode features one sloping profile in the voltage range of 1.0-0.5 V, which corresponds to the solid electrolyte interphase (SEI) film formation due to the electrolyte decomposition and the irreversible conversion reaction of CoP. Additionally, there is one obvious potential plateau at 0.05 V, which is similar to that of P assigned to the formation of Na_3P.[1,252,289] The charge-discharge curves of CoP in SIBs are similar to those of iron phosphide (FeP) in SIBs,[317] suggesting that they have

a similar storage mechanism, i.e., the P in the CoP is alloyed with Na to form Na_3P. The equation is listed as follows:

$$CoP + 3Na^+ + 3e^- \rightarrow Co + Na_3P \quad (7.3)$$

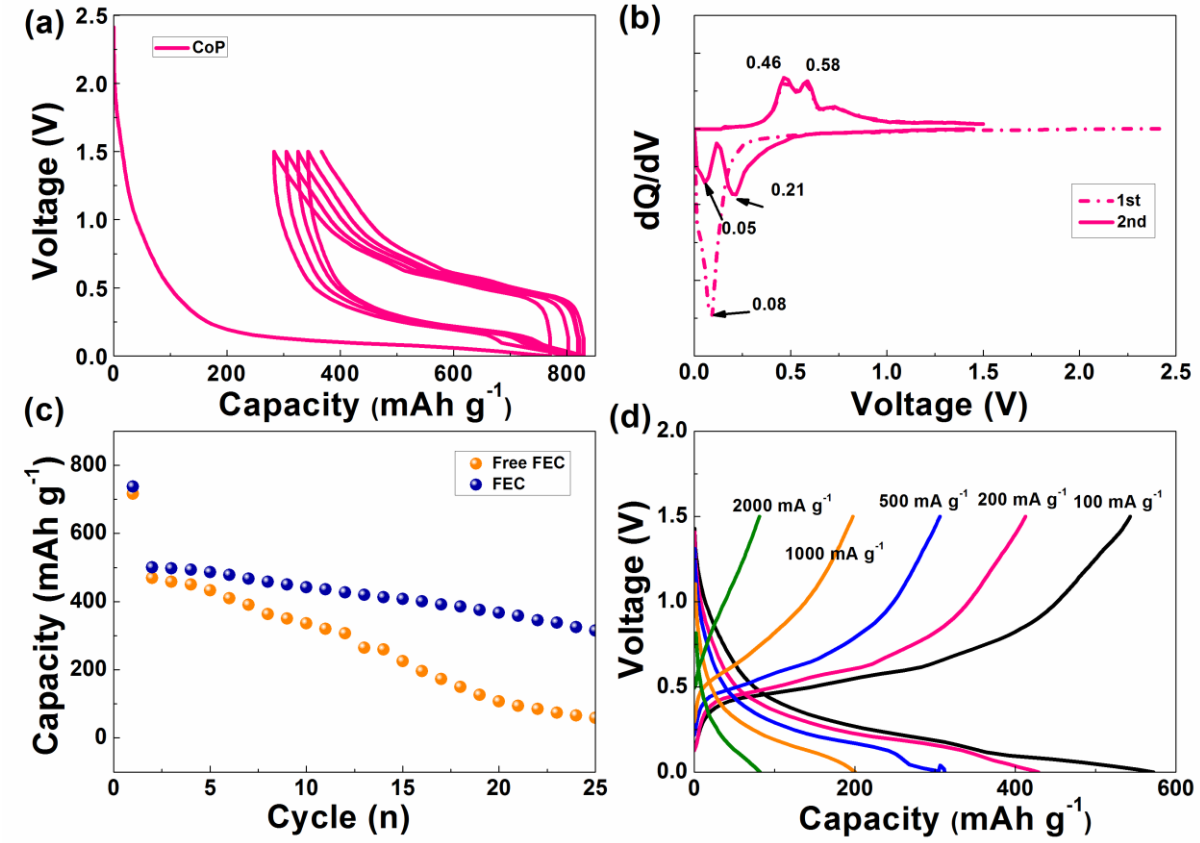

Figure 7.11. Electrochemical performance of CoP electrode in the voltage range of 0-1.5 V: (a) charge-discharge curves at the current density of 100 mA g^{-1}; (b) *dQ*/*dV* curves for the first 2 cycles; (c) cycling performance of charge capacity with and without FEC at the current density of 100 mA g^{-1}, and (d) rate capability of the CoP electrode with FEC additive.

Moreover, the CoP electrode delivered 770 mAh g^{-1} initial discharge capacity with 65.2% initial coulombic efficiency, which is close to the theoretical capacity of 893.3 mAh g^{-1} for Na_3P formation (Figure 8.2(a)). The reason for the lower than theoretical capacity is the pulverization caused by the low electronic conductivity of the SEI film. To clearly show the voltage plateau, the *dQ*/*dV* curves are plotted in Figure 8.2(b). It is clear that there are two couples represented by the reversible peaks at 0.05/0.46 V and 0.21/0.58 V in the second cycle *dQ*/*dV* curves, as shown in Figure 8.2(b). The peaks at 0.21/0.58 V are ascribed to the Na_xP (Na_2P, NaP and NaP_7) intermediate phase formation/decomposition, while the ones at 0.05/0.46 V correspond to the Na_3P formation/decomposition.[1]Thus, the sodium storage

mechanism of CoP anode can be explained as a reaction between Na and the P resulting from the decomposition of CoP.

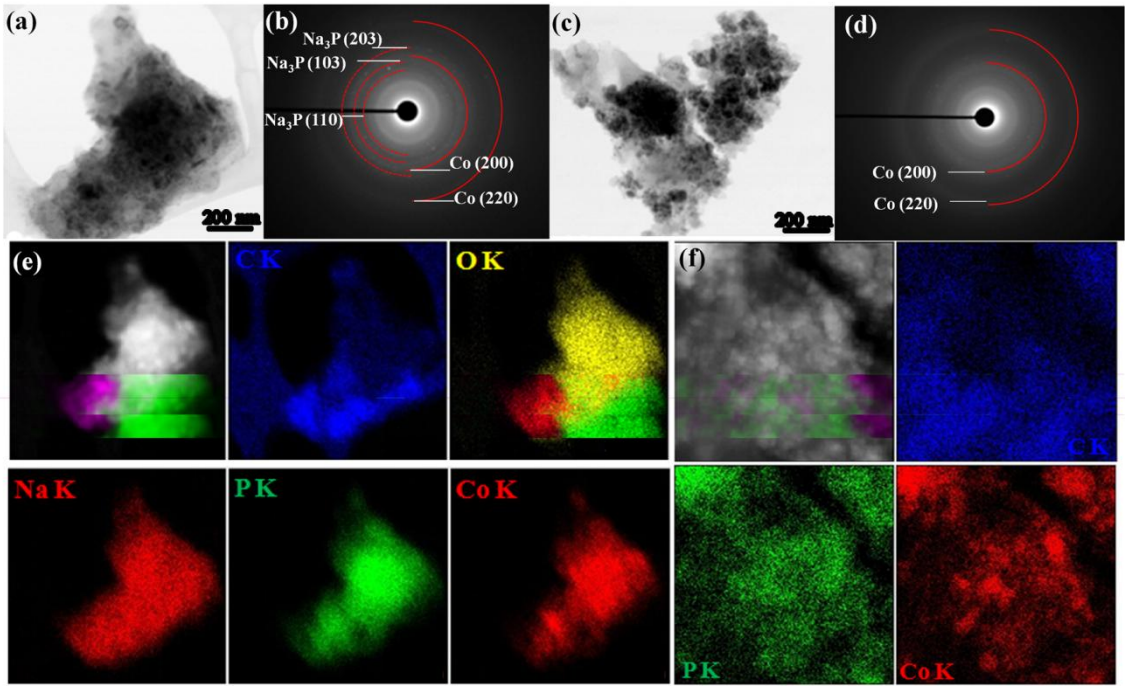

Figure 7.12. STEM characterization of the CoP electrodes charged or discharged to different states. (a), (b), and (e) are the image, corresponding SAED pattern, and EDS mapping of the electrode discharged to 0 V, respectively; (c), (d), and (f) are the image, corresponding SAED pattern, and EDS mapping of the electrode charged to 1.5 V, respectively.

Figure 8.2(c) shows the cycling performance of CoP electrodes in sodium ion batteries. In the second cycle, the CoP electrode delivered 470 mA h g^{-1} charge capacity, with 65.5% capacity retention. The low capacity retention is possibly due to irreversible electrolyte decomposition to form the SEI film during the first discharging process. Afterwards, the capacity of CoP electrode decayed dramatically in the following cycles. After 25 cycles, only 58 mA h g^{-1} charge capacity remained. There are two possible reasons for the dramatic capacity degradation of CoP electrode. One reason is that a stable SEI film is not easy to form for sodium anode because organic electrolytes tend to continuously erode the SEI layers.[44] The other reason is that the huge volume expansion when sodium ions are alloyed with P to form Na_3P (490% volume change) induces strong stresses on the particles and results in pulverization. To improve the cycling performance of CoP, 5 wt% of the film-forming additive fluoroethylene carbonate (FEC) was added into the electrolyte, which can help a compact and stable SEI film to form on the surface of the electrode.[312] Significantly, the cycling performance of CoP was improved with 5% FEC addition due to the stable SEI

formation, even though powder pulverization is not supressed (Figure 8.2(c)). After 25 cycles, the retained capacity was 315 mAh g^{-1}, which was 70% of the capacity in the second cycle. The rate capability of CoP was tested at various current densities, as shown in Figure 8.2(d). When the current density increased from 100 mA g^{-1} to 500 mA g^{-1}, the discharge capacity decreased from 570 to 310 mAh g^{-1}. The CoP electrode can deliver the discharge capacity of 200 and 80 mAh g^{-1}, even at as high a current density as 1 A g^{-1} and 2 A g^{-1}, respectively.

In order to explore the sodium storage mechanism of CoP, scanning transmission electron microscopy (STEM) was carried out to investigate the structural and phase changes of the CoP electrodes during the discharge-charge process. The electrodes that were examined were obtained by disassembling the cells in an Ar-filled glove box and washing them with DEC several times before testing. Figure 8.3(a) and (b) shows the morphology and SAED pattern of the CoP discharged to 0 V, respectively. When the CoP was fully discharged at 0 V, two phases appeared in the SAED pattern, assigned to Na_3P and Co metal (Figure 8.3(b)). Figure 8.3(e) shows the EDS element mapping of the CoP electrode discharged to 0 V. It is clear that the distribution of Co did not completely overlap that of P, suggesting the decomposition of CoP. Additionally, Na, C, and O were also observed from the EDS mapping. Since the electrode was washed several times before testing, the Na was not from the residual $NaClO_4$. On combining this evidence with the SAED pattern, it becomes clear that the Na is mainly from the Na_3P. In addition, the C, O, and a part of the Na come from the SEI film formation on the surface of the electrode during the first discharge process. At the end of charge, from the SAED pattern (Figure 8.3(d)), some diffraction rings from Co phase appeared, corresponding to the (200) and (220) crystal planes. Moreover, the morphology of the CoP electrode charged to 1.5 V shows some small particles embedded in the amorphous matrix, as shown in Figure 8.3(c). From the EDS mapping, the small particles are the Co dispersed in the amorphous P matrix (Figure 8.3(f)), demonstrating that the phases that exist after charging are Co and P.

In order to further demonstrate the sodium storage mechanism of CoP, XPS was conducted to detect the valence changes of CoP during the charge-discharge process. Figure 4 shows the XPS spectra of the CoP electrodes charged or discharged to different states. At the end of discharge, as shown in Figure 8.4(a), it is clearly seen that the peak of Co $2p_{3/2}$ has shifted from 780.1 eV to the lower binding energy of 778.6 eV, which is assigned to Co metal,[318] while the peak of P remains at the original position of 129.3 eV, suggesting that the element P keeps its reduced valence (Figure 8.4(b)). Therefore, it can be concluded that Na_3P and Co

are the constituents of the CoP electrode discharged to 0 V. When the electrode was charged to 1.5 V, the peak position of Co did not undergo any changes, while the peak of P shifted to the higher binding energy of 130.5 eV, which corresponds to elemental P. Thus, the constituents of the electrode charged to 1.5 V are Co and P, which is consistent with the STEM results. Additionally, a state change of the carbon on the electrode surface was also observed via the high-resolution spectra of C 1s, as shown in Figure 8.4(c). The C 1s peak of the pristine CoP electrode is fitted by two peaks at 284.6 eV and 285.6 eV, corresponding to the C-C and C-O-C bonds, respectively. The C-C band is associated with both the CMC binder and the carbon black in the electrode, while the C-O-C band is associated with the CMC binder. After discharging and charging, apart from the peak of the C-C band, the O-C=O peak at 288.4 eV was also observed. This bond is ascribed to the solid electrolyte interphase (SEI) layer on the surface of the CoP electrode. Thus, based on the XPS and STEM results, it is concluded that the sodium storage mechanism of CoP is based on the reaction between P and Na. The equation after the initial discharge is summarized as follows:

$$Na_3P + Co \leftrightarrow Co + P + 3Na^+ + 3e^- \quad (7.4)$$

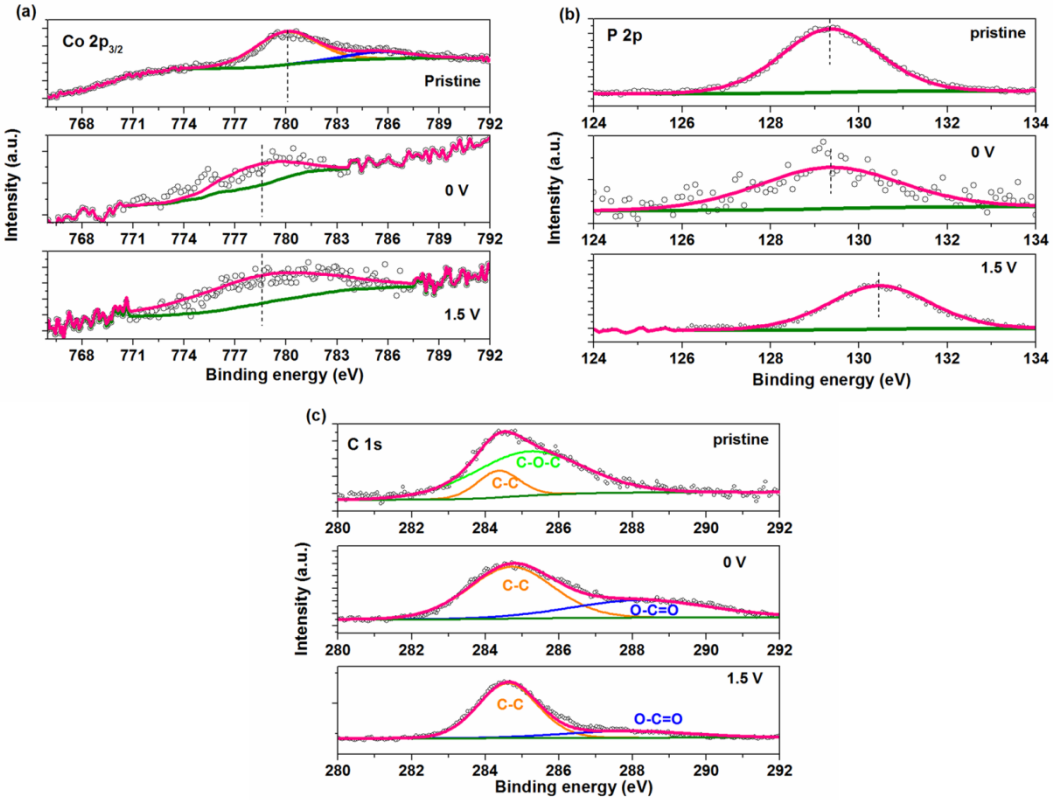

Figure 7.13. XPS spectra of the pristine CoP electrode, and the one discharged to 0 V and charged to 1.5V: (a) Co $2p_{3/2}$; (b) P 2p; (c) C 1s.

7.4 Conclusion

In summary, we prepared FeP and CoP in large quantities by direct low-speed ball milling of the P and Fe (Co) powders and studied its electrochemical performance as anode material for sodium ion batteries. The FeP and CoP electrode delivered a high capacity of 764.7 and 770 mAh g^{-1} in sodium ion batteries, respectively. In addition, improvement of its cycling stability was also achieved by selecting appropriate binders and an appropriate additive to the electrolyte. Moreover, a variety of techniques, including ex-situ XRD, XPS and transmission electron microscopy (TEM), was used to reveal that the sodium storage mechanism of FeP and CoP. It is concluded that the sodium storage mechanism of FeP and CoP involves the reaction of P with Na. All the results indicate that FeP and CoP would be a promising anode material candidate for sodium ion batteries with low cost and long cycling stability.

Chapter 8. Multifunctional conducing polymer coated $Na_{1+x}MnFe(CN)_6$ cathode for sodium-ion batteries with superior performance via a facile and one-step chemistry approach

As for the investigation on cathode for sodium storage, we choose the Prussian Blue analogues as the studied object. Rhombohedral $Na_{1.72}MnFe(CN)_6$ (denoted as NMHFC) prepared by Goodenough's group, delivered especially high performance compared to other analogues, including a reversible capacity as high as 134 mAh g^{-1}, with a higher average potential plateau of 3.55 V, contributing to high energy storage and making this compound a promising cathode material for rechargeable SIBs. Its short cycle life (just 30 cycles shown), however, and high potential polarization at high rates, due to the intrinsic poor electronic conductivity of NMHFC, need to be substantially improved for this material to be used commercially. Here, we utilize the intrinsic oxidation power of the NMHFC, without an external chemical oxidant, to form conducting polymers on the surfaces of NMHFC particles, resulting in improved electronic conductivity, which leads to increased rate capability.

8.1 Introduction

How to optimize the utilization of renewable energy sources (e.g. wind, solar) for a sustainable human future has become a global focus of attention. One of the most effective solutions is to use cost-effective and environmentally friendly rechargeable batteries to store renewable energy.[256,257]For these applications, lithium ion batteries (LIBs) are not the ideal options because lithium resources in the Earth's crust suffer from low abundance combined with rising prices. By comparison, sodium is abundant and low-cost, and it also has similar physical and chemical properties to Li. Therefore, sodium ion batteries (SIBs), as the most attractive choice, have been given more attention in recent years.[48,247,258,289]

Cathode materials play a decisive role in the final electrochemical performance of a full cell. Recently, a number of transition metal oxides,[98,126,259] phosphates,[319-322] and organic compounds[205,311,323] were reported as cathode host materials for sodium-ion storage. In particular, Prussian blue (PB) and its analogues ($KMFe(CN)_6$ or $Na_xMFe(CN)_6$, $0 \leq x < 2$, M = Fe, Mn, Ni, Zn, Cu, etc.) have attracted more attention due to their environmentally friendly nature, inexpensive constituents and superior electrochemical performance.[169,171,173,174,181,324] Rhombohedral $Na_{1.72}MnFe(CN)_6$ (denoted as NMHFC) prepared by Goodenough's group,[174]delivered especially high performance compared to other

analogues, including a reversible capacity as high as 134 mAh g^{-1}, with a higher average potential plateau of 3.55 V, contributing to high energy storage and making this compound a promising cathode material for rechargeable SIBs. Its short cycle life (just 30 cycles shown), however, and high potential polarization at high rates, due to the intrinsic poor electronic conductivity of NMHFC, need to be substantially improved for this material to be used commercially. Here, we utilize the intrinsic oxidation power of the NMHFC, without an external chemical oxidant, to form conducting polymers on the surfaces of NMHFC particles, resulting in improved electronic conductivity, which leads to increased rate capability. Simultaneously, perchlorate ions (ClO_4^-) and sodium ions (Na^+) are doped into the polymer chains and NMHFC crystals, respectively, during the polymerization**.** Perchlorate ions can act as a dopant to enhance the electronic conductivity of the polymer and function as redox-active sites to increase the capacity of the doped polymer. Additional sodium ion doping can improve the specific capacity by removing zeolitic water from crystal structure. In this way, the total capacity decrease resulting from the introduction of the conducting coating which has lower specific capacity than that of NMHFC crystals can be minimized. Compared with other coating methods, this method is facile, one-step, and energy-effective, especially because it does not need external oxidation as the driving force of the polymerization, eliminating the risks of residual oxidant or oxidant by-products.

8.2 Experimental Section

All the chemicals were purchased from Sigma Aldrich and used without further purification.

8.2.1 Synthesis of NMHFC

3 m mol manganese acetate was dissolved into 100 m L deionized water, denoted solution A. 1.5 m mol $Na_4Fe(CN)_6 \cdot 10H_2O$ and 4 m mol sodium citrate were dissolved into 100 m L deionized water, denoted solution B. Then, solution A was added dropwise into the solution B under magnetic stirring. The suspension was aged for several hours before centrifuging. The white precipitate was washed with deionized water for several times and then dried at 120 ℃ for 10 h.

8.2.2 Synthesis of NMHFC @ PPy

In a typical process, the above prepared NMHFC powder (100 mg) was dispersed in 40 m L of DMC solution (Dimethyl carbonate), irradiated by ultrasound for 1h. 24 mg $NaClO_4$ was added as dopant into NMHFC suspension. 45 μ L pyrrole which dissolved into 20 m L DMC solution, was slowly added to the previous DMC solution under magnetic stirring. The

polymerization was carried out in ice bath (at 0 - 5 ℃) for 6 h, and the nitrogen gas was blowed into the solution during the whole process. Then, NMHFC @ PPy powder was collected by centrifugation and washed with ethanol for several times. Finally, the NMHFC @ PPy powder was dried at 50 ℃ for 4 h under vacuum. For comparison, the pure PPy was synthesized in the similar method and the $FeCl_3$ was used as the oxidant instead of NMHFC.

8.2.3 Structural characterization

The microstructure of the NMHFC @ PPy powders was characterized by Powder X-Ray diffraction (XRD; GBC MMA diffractometer) with Cu K_α radiation at a scan rate of 2 °min^{-1}. The morphology of the samples was investigated by field emission scanning electron microscopy (FESEM; JEOL JSM-7500FA) equiped with energy-dispersive X-ray spectroscopy (EDS). Raman spectra were collected using a JOBIN Yvon Horiba Raman spectrometer model HR800, with a 10 mW helium/neon laser at 632.8 nm excitation in the range of 150 to 2000 cm^{-1}. X-ray photoelectron spectroscopy (XPS) was conducted using a SPECS PHOIBOS 100 Analyser installed in a high-vacuum chamber with the base pressure below 10^{-8} mbar, X-ray excitation was provided by Al Ka radiation with photon energy h_v = 1486.6 eV at the high voltage of 12 kV and power of 120 W. The XPS binding energy spectra were recorded at the pass energy of 20 eV in the fixed analyser transmission mode. Analysis of the XPS data was carried out using the commercial CasaXPS 2.3.15 software package. All the spectrum were calibrated by C1s=284.6ev. FTIR spectra were performed by a FTIR Prestige-21 (Shimadzu). The amount of PPy in the composites was determined using a Mettler - Toledo thermogravimetric analysis / differential scanning calorimetry (TGA / DSC) Stare System from 50-600 ℃ at 10 ℃ min^{-1} in Ar. The magnetic measurements were carried out using a 14 T physical properties measurement system (PPMS), equipped with a vibrating sample magnetometer (VSM), over a wide temperature range from 5 K to 300 K in a 1000 Oe magnetic field. In situ synchrotron XRD data were collected on the powder diffraction beamline at the Australian Synchrotron with a wavelength (λ) of 0.6888 Å, determined using the NIST LaB_6 660b standard reference material. Data were collected continuously in 30s acquisitions. The cell used for the data collection was charged at a current density of 50 mA g^{-1} between 2 V and 4.2 V.

8.2.4 Electrochemical characterization

NMHFC @ PPy electrodes were prepared by mixing 70% active materials, 20% carbon black and 10% carboxymethyl cellulose (CMC) used as binder by weight to form an electrode slurry, and then was coated on Aluminum foil, followed by being dried in a vacuum oven

overnight at 80 ℃, and then pressed with the pressure of 30 MPa. The active materials loading rate was ~7 mg cm^{-2}.The sodium foil was cut by the doctor blade technique from the sodium bulk stored in the mineral oil, and then was employed as both reference and counter electrode. A porous polypropylene film was used as the separator. The home-made electrolyte was 1.0 mol/L Sodium perchlorate ($NaClO_4$ ACS reagent 98.0%, Sigma-Aldrich) in a 1 : 1 (v/v) mixture of ethylene carbonate (EC, anhydrous 99%, Sigma-Aldrich) and diethyl carbonate (DEC, anhydrous 99+%, Sigma-Aldrich). The chemicals were used without further drying. The cells were assembled in an argon-filled glove box. The electrochemical performance were tested by a Land Test System in a voltage range of 2 ~ 4.2 V (vs. Na^+/Na). All of the capacities and energy density are calculated based on the mass of active materials including PPy and NMHFC.

8.3 Results and discussion

Before coating with conducting polymer, NMHFC was synthesized at room temperature. Briefly, 100 mL manganese acetate solution was added dropwise into 100 mL of $Na_4Fe(CN)_6$ and sodium citrate solution under vigorous magnetic stirring. Then, the white suspension was aged for 10 hours before centrifuging. The process of coating the conducting polymer on the surfaces of NMHFC particles is illustrated in Figure 8.1. The X-ray diffraction (XRD) pattern of the as-prepared NMHFC shows that it has a rhombohedral (space group *R-3m*) structure, which is the same as for the NMHFC previously reported,[174] as shown in Figure 9.2(a).

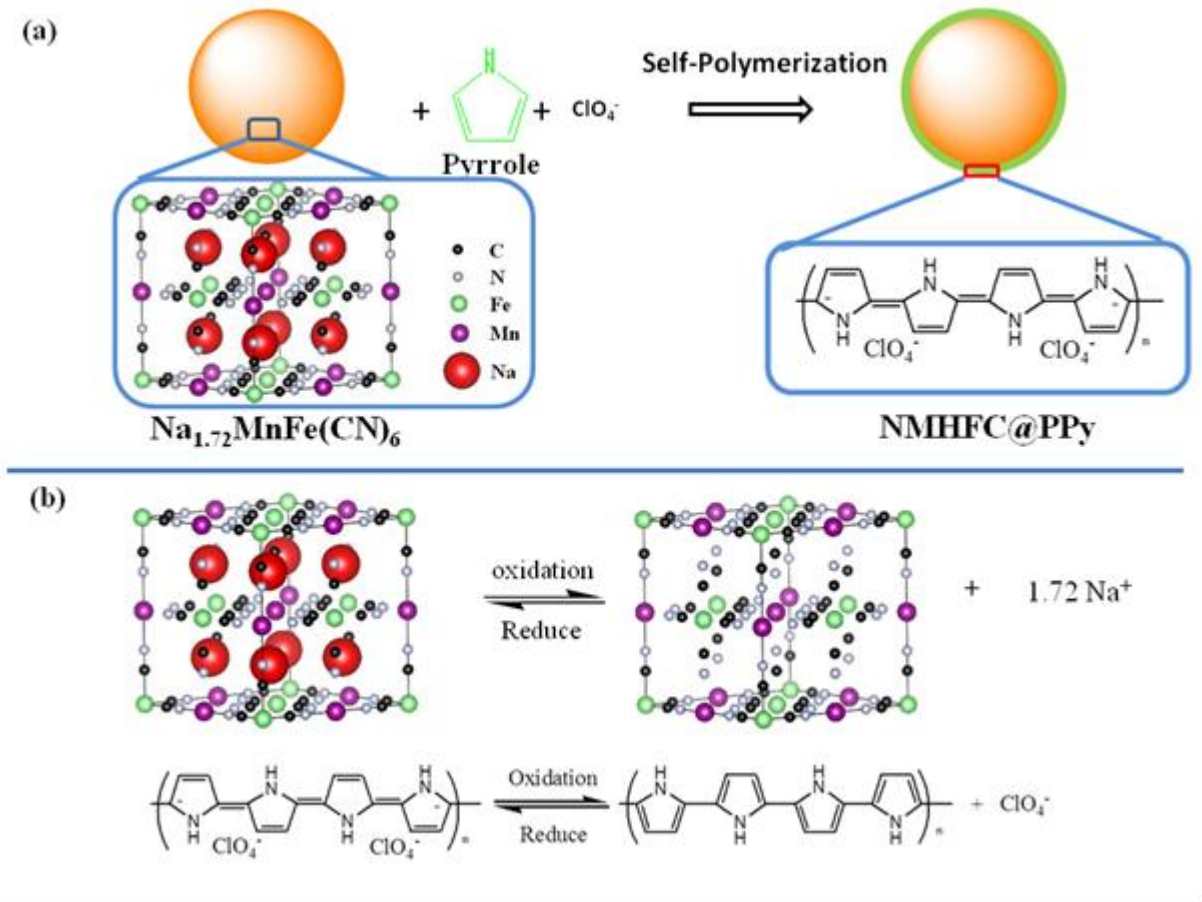

Figure 8.1. Schematic illustration of synthesis and sodium storage mechanism in NMHFC@PPy. (a) the polymerization reation between NMHFC particle and pyrrole; (b) the mechanism of electrochemical process. The high valence state of transition metal in the NMHFC leads to the oxidation of pyrrole, simultaneously, ClO_4^- as the dopant embedded into the chain, which is deposited on the solid surface as the conducting polymer ClO_4^- - doped PPy.

In this paper, pyrrole was chosen as the monomer of the conducting polymer, and $NaClO_4$ was chosen as the source of ClO_4^- dopant. The reason why we chose $NaClO_4$ is because $NaClO_4$ is the electrolyte salt in the sodium ion battery used here. Therefore, it will not introduce any impurities into the sodium ion battery system. In the meantime, the Na^+ can also insert itself into NMHFC to compensate for the charge imbalance that results from the reduction of Mn^{III}. The additional Na^+ is also good for improving the reversible capacity, as reported previously.[174] The obtained NMHFC particles coated with ClO_4^- doped conducting polypyrrole (PPy) are denoted as NMHFC@PPy. After coating, the XRD pattern of the NMHFC@PPy shows almost no change (Figure 8.2(a)), suggesting that the polymerization of pyrrole utilizing the intrinsic oxidation of NMHFC does not destroy its structure. This

could be related to the surface structure changes, which cannot be detected by XRD. Raman spectroscopy was carried out to determine the details of the formation of PPy on the surface of the NMHFC particles, as presented in Figure 8.2(b). It is obvious that after coating, four characteristic peaks of PPy appeared at 923, 1049.4, 1327.4, and 1614 cm^{-1}, demonstrating that the polymerization of pyrrole has occurred. For comparison, pure PPy was synthesized by a similar method, in which $FeCl_3$ is used as the oxidant, and the Raman spectrum of the pure PPy is shown in Figure 8.2(b). FTIR spectra of the NMHFC@PPy compared with the as-prepared NMHFC are shown in Figure 8.3. The difference in the IR spectra is the appearance of bands at 624.9 and 1238.3 cm^{-1} in the NMHFC@PPy sample, which are characteristic bands of PPy. Except for these IR features, all the other IR modes in the NMHFC@PPy sample are similar to those observed in the as-prepared NMHFC, suggesting that the PPy coating did not change the chemical structure of NMHFC. The energy-dispersive X-ray spectroscopy (EDS) results demonstrate that the elements Cl and O are present in the pure PPy, suggesting that ClO_4^- has been doped into the polymer chain (Figure 8.4(a)). Also, there are characteristic peaks of Cl and O that appear in the XPS spectra of pure PPy (Figure 8.5(a)), which is consistent with the EDS results. There is no peak for the elements Cl and O in the EDS spectra of NMHFC@PPy, probably due to lower content of PPy, which is difficult to detect (Figure 8.4(b)).

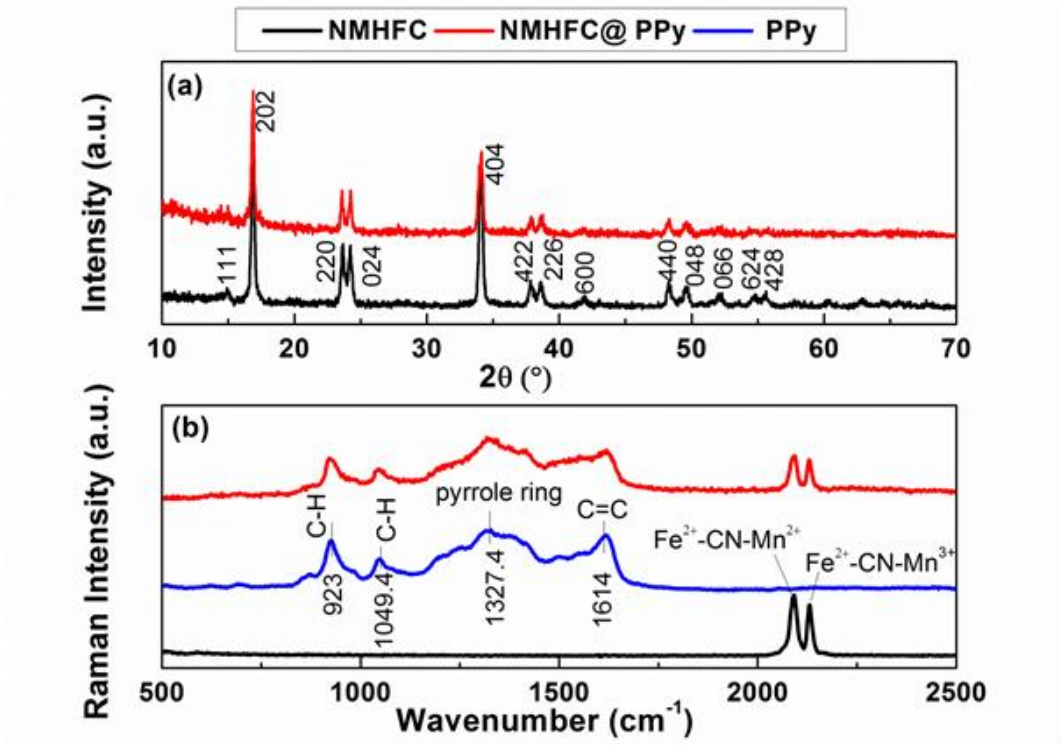

Figure 8.2. (a) XRD patterns and (b) Raman spectra of NMHFC particles before and after PPy coating.

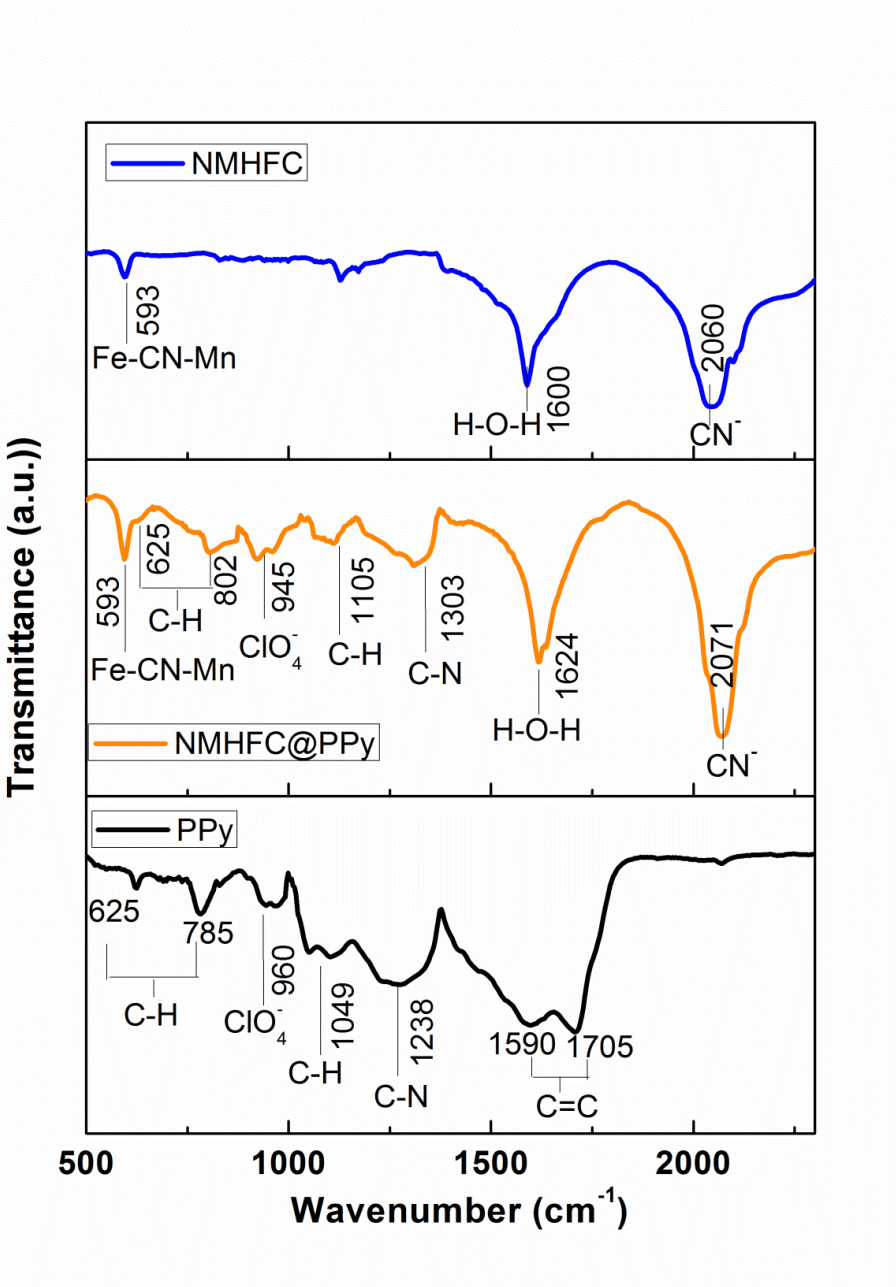

Figure 8.3. FT-IR spectra of PPy, NMHFC and NMHFC@Ppy

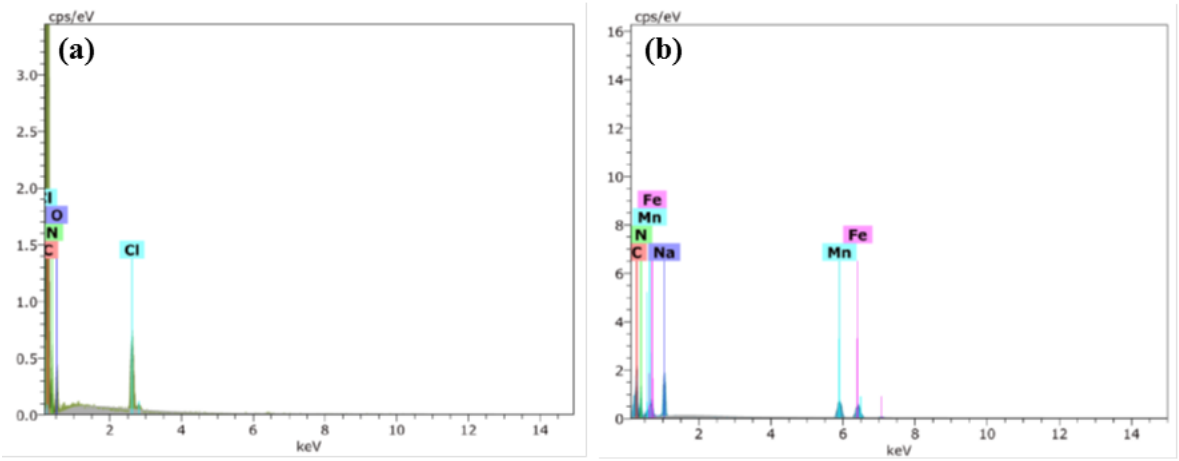

Figure 8.4. EDS elemental analysis of (a) pure PPy and (b) NMHFC@PPy

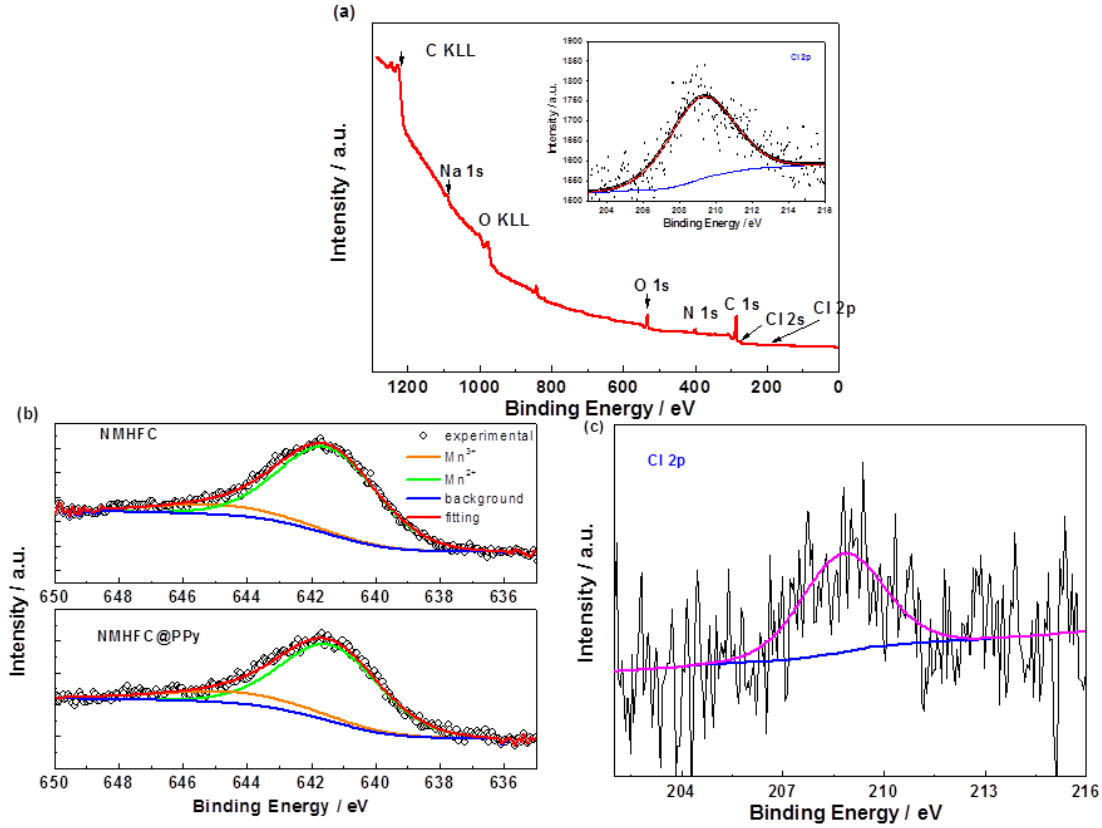

Figure 8.5. XPS analysis of (a) pure PPy, (b) Mn 2p3/2 of NMHFC@PPy compared with that of NMHFC, (c) Cl 2P of NMHFC@PPy.

The spin state is important for NMHFC because the potential for electrochemical reactions to occur is related to the spin state of the redox couples of Fe^{III}/Fe^{II} and Mn^{III}/Mn^{II}. In order to determine whether the spin state of Mn changes after PPy coating, we investigated the magnetic susceptibility of NMHFC@PPy versus temperature, as shown in Figure 8.6. Both

NMHFC and NMHFC@PPy show paramagnetic behavior from low temperature up to room temperature, and there is no phase transition that can be observed in this temperature range. The calculated effective magnetic moments (μ_{eff}) of NMHFC and NMHFC@PPy are 5.3 μ_B and 5.5 μ_B, respectively, which is smaller than what has been reported (5.8 μ_B),[174] suggesting that more Mn^{III} (S = 2) appears in NMHFC and NMHFC@PPy. Furthermore, the calculated μ_{eff} of NMHFC@PPy is slightly larger than that of NMHFC, demonstrating that a small amount of Mn^{III} has been reduced to Mn^{II} (S = 5/2). The change in the calculated effective magnetic moments is small, however, which indicates that the spin state of Mn only experienced a slight change after PPy coating because the amount of PPy was small. Moreover, XPS of Mn 2p3/2 also supports this point (Figure 8.5(b)).

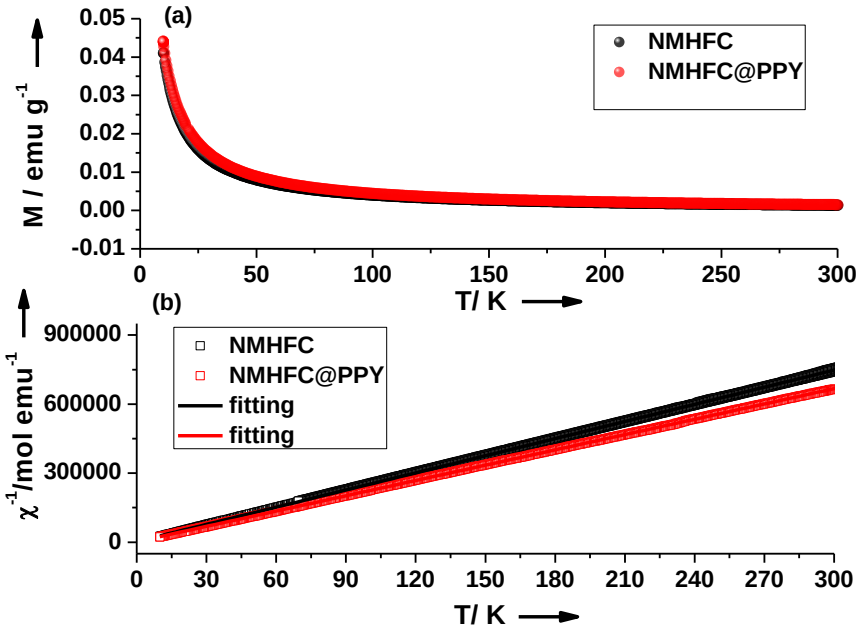

Figure 8.6. (a) The temperature dependence of the molar susceptibility and (b) inverse susceptibility versus temperature of NMHFC and NMHFC@Ppy (H=1000 Oe).

The morphology of NMHFC and NMHFC@PPy particles was detected by scanning electron microscope (SEM). The as-prepared NMHFC particles are irregular, with particle size of 200 - 500 nm (Figure 8.7(a)). After PPy coating, the morphology shows no significant change, but the surfaces of the particles become rough (Figure 8.7(b)).

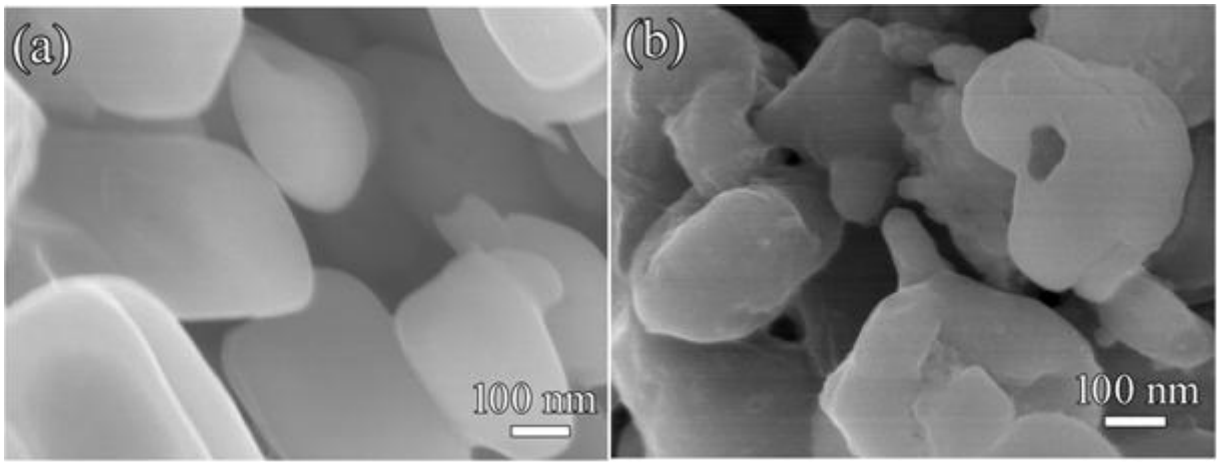

Figure 8.7. SEM image of NMHFC (a) and NMHFC@PPy particles (b).

The electrochemical results measured in coin cells are shown in Figure 8.8. The charge/discharge curves of the NMHFC and NMHFC@PPy electrodes in the first two cycles, conducted at the rate of 0.1 C (1C = 120 mA g^{-1}), are presented in Figure 8.8(a). The as-prepared NMHFC delivered 136.8 mA h g^{-1} initial capacity with coulombic efficiency of 52.2%. The low efficiency results from the irreversible removal of the water which occupied the large interstitial spaces in NMHFC structure during the initial charging process, which is a common problem in the PB analogues.[169] After coating with PPy, the initial capacity of the NMHFC@PPy electrodes is 124 mA h g^{-1} corresponding to an energy density of 428 Wh kg^{-1}, which is comparable to one of the most promising low-cost cathode materials for Li-ion battery, $LiMn_2O_4$, with an energy density of 450 Wh kg^{-1} (Figure 8.9). The coulombic efficiency is 72%, which is also a big increase compared with the as-prepared NMHFC. Moreover, the potential polarization of the charge/discharge becomes smaller (All of the capacities and energy density are calculated based on the mass of active materials including PPy and NMHFC). We tried to determine the PPy percent in the NMHFC@PPy composite by thermogravimetric analysis (TGA), but it is difficult to obtain an accurate value because the temperature of decomposition of PPy is close to that for evaporating the zeolitic water (Figure 8.10). The content of PPy in the composite is obtained by weighting the weights difference between NMHFC and NMHFC@PPy, which is about 4.44 wt%. However, the water content of NMHFC can be obtained from TGA results, which is about 14 wt% and is higher than that of the NMHFC reported by Wang et al (12 wt%). This is the possible reason for the lower initial coulombic efficiency than that reported. EDS results show that the molar Na:Fe:Mn ratio of NMHFC is 1.70:1:1 (Table 8.1). Coupled plasma analysis (ICP) is also carried out to detect the the molar Na:Fe:Mn ratio. Combined TGA results, EDS and ICP

results, the molecular formula for NMHFC is $Na_{1.7}MnFe(CN)_6 \cdot 2.38H_2O$. The d*Q*/d*V* curves of the NMHFC@PPy and NMHFC electrodes are shown in Figure 8.8(b). There were 3 redox peaks in the d*Q*/d*V* curves of the NMHFC@PPy and NMHFC electrodes, although NMHFC just has Fe^{III}/Fe^{II} and Mn^{III}/Mn^{II} as the two redox active couples. It was reported that the oxidation/reduction peak is related to the spin state of the transition metal in Prussian blue analogues.[181]

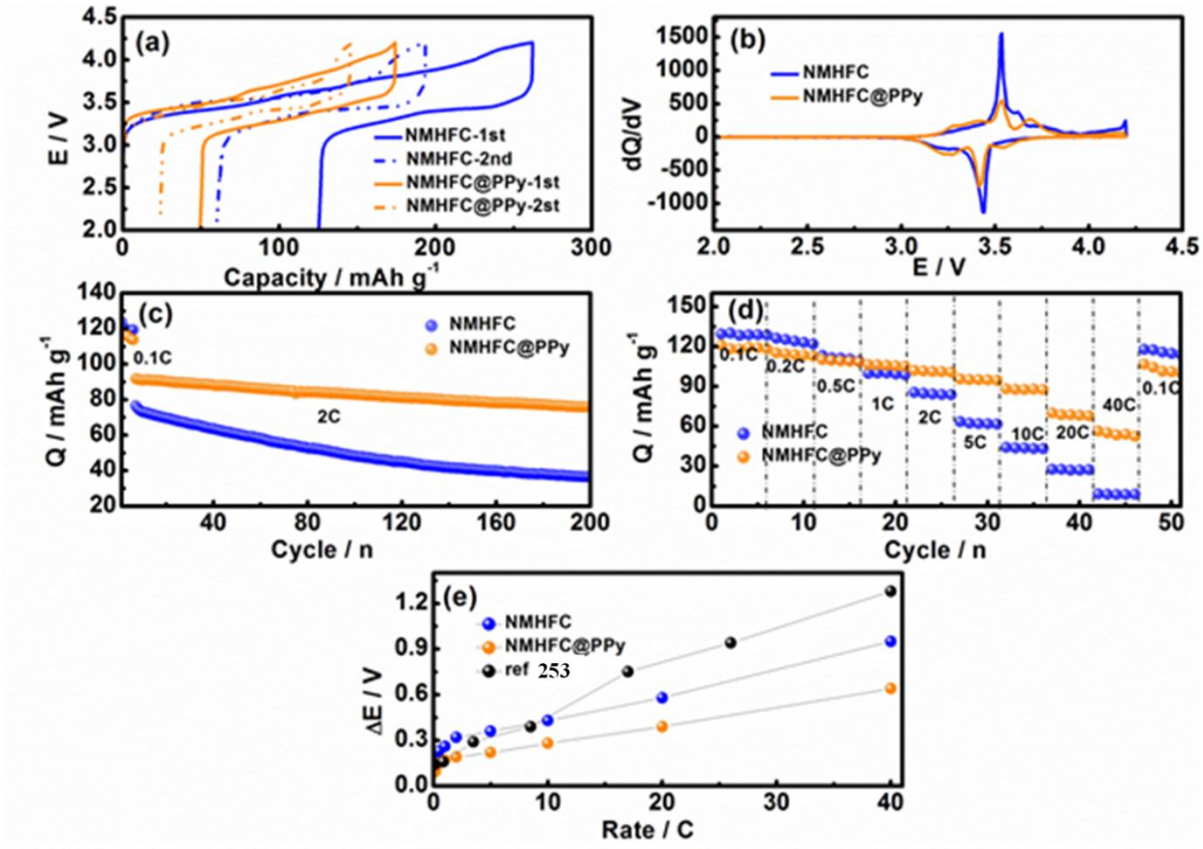

Figure 8.8. Electrochemical performance of NMHFC and NMHFC@PPy electrodes: (a) charge/discharge curves in the first 2 cycles at current density of 0.1 C; (b) d*Q*/d*V* curves in the first cycle; (c) cycling performance within a voltage window of 4.2 - 2.0 V at 2 C; (d) rate capability; and (e) potential polarization Δ*E* of the NMHFC and NMHFC@PPy electrodes compared with the one in reference.[174] (*Q* = capacity, *E* = Voltage, 1 C = 120 mA g^{-1}).

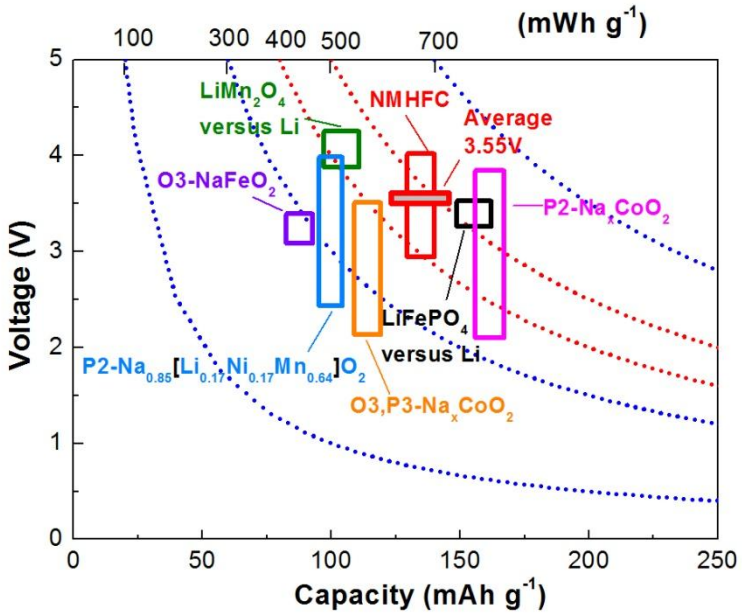

Figure 8.9. A comparison of reversible capacity and operating voltage ranges of the layered sodium insertion materials. The energy density was calculated on the basis of the voltage versus metallic sodium for simplicity. $LiFePO_4$ and $LiMn_2O_4$ are also shown for comparison based on the voltage versus Li metal.

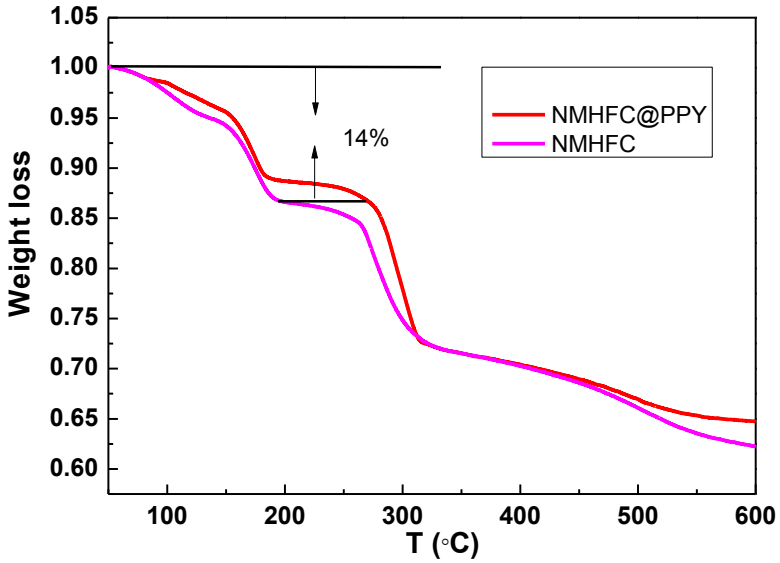

Figure 8.10. TGA curves of NMHFC and NMHFC@PPy measured from 50 to 600 ℃ at the 10 ℃ /min in Ar.

Table 8.1 The elements distribution of NMHFC from EDS.

	Na (at%)	Mn (at%)	Fe (at%)
Point 1	10.946	6.439	6.398
Point 2	10.233	6.134	6.074
Point 3	9.896	5.723	5.911
Average	10.358	6.099	6.128

Figure 8.8(c) shows the cycling performance of the NMHFC and NMHFC@PPy electrodes with a potential range from 2.0 to 4.2 V at the rate of 0.1 C in the first 6 cycles and then when the rate was increased to 2 C. As shown in Figure 8.8(c), the cycling performance of the as-prepared NMHFC is not satisfactory, after 100 cycles, as the retained capacity is only 44 mAh g^{-1}. In comparison, it is obvious that NMHFC@PPy shows better cycling stability, with 76 mAh g^{-1} capacity over 200 cycles (67% retention of the capacity in the 6^{th} cycle). To explore the reason for the capacity decay of NMHFC, the NMHFC and NMHFC@PPy cells were disassembled after 50 cycles. The entire separator in the NMHFC cell clearly became brown, while there were only some brown spots in the separator of the NMHFC@PPy cell (Figure 8.11(a-b)). Moreover, the EDS spectrum for the separator of the NMHFC cell shows the Mn peak, suggesting the dissolution of Mn in the electrolyte. On the contrary, the Mn peak was not detected in the EDS results for the separator in the NMHFC@PPy cell, indicating the reduced dissolution of Mn (Figure 8.11 (c-d)).

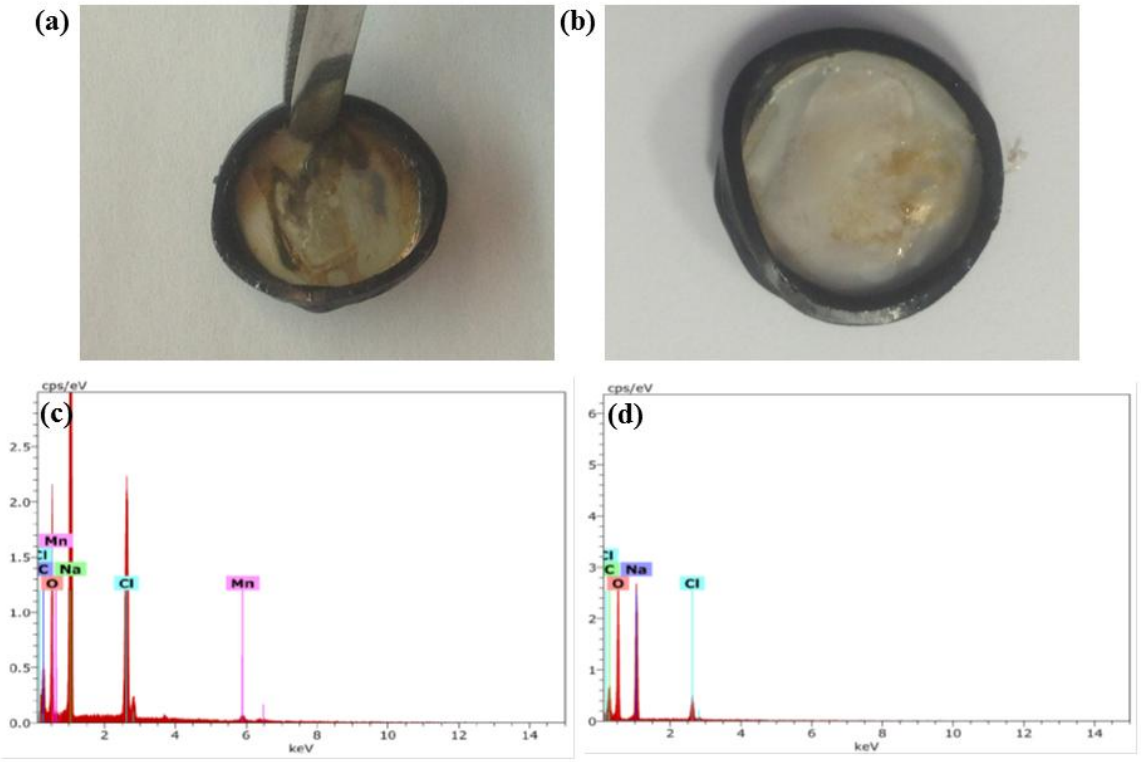

Figure 8.11. (a,b) photos and (c,d) EDS elemental analysis of the separator in the cells of (a,c) NMHFC and (b,d) NMHFC@PPy after cycling for 50 cycles.

In-situ Synchrotron XRD was carried out to explore the structural evolution of the NMHFC and NMHFC@PPy electrodes in the initial cycle. More detailed stacked plots of the diffraction patterns focused on the (202), (220), (024) and (404) reflections, presented in Figure 8.12. For NMHFC electrode, it is clear seen that the intensity of (202) peak decreased in the charging process and increase to the original state at the end of discharging. Meanwhile, the (202) peak shifted to the large angle during charging and shifted to the small angle during discharing, suggesting the space between the lattice place (202) underwent huge change from compression to expansion (Figure 8.12(a)). Such change can not be detected in Ex-situ XRD of NMHFC electrodes charged and discharged in different states in the first cycle, shown in Figure 8.13. The (220) and (024) two split peaks of rhombohedral phase have slowly begun to mix together during the charge/discharge process. At the end of discharging, there were no split peaks in the synchrotron XRD pattern (Figure 8.12(a)), indicating that the rhombohedral structured NMHFC had been transformed to cubic phase, in good agreement with a previous report.[174]In conclusion, the reason for the capacity drop in the NMHFC electrode is probably due to the dissolution of Mn in NMHFC and the rhombohedral-cubic phase transition. After PPy coating, it is significant that there is no big change on the diffraction patterns of (202),

(220), (024) and (404) reflections peaks during the charge/discharge process, demonstrating the structure of the NMHFC became stable (Figure 8.12(b)). A PPy coating on the surface of the NMHFC can retard the Mn dissolution by forming a protective layer and thus improve the cycling stability.

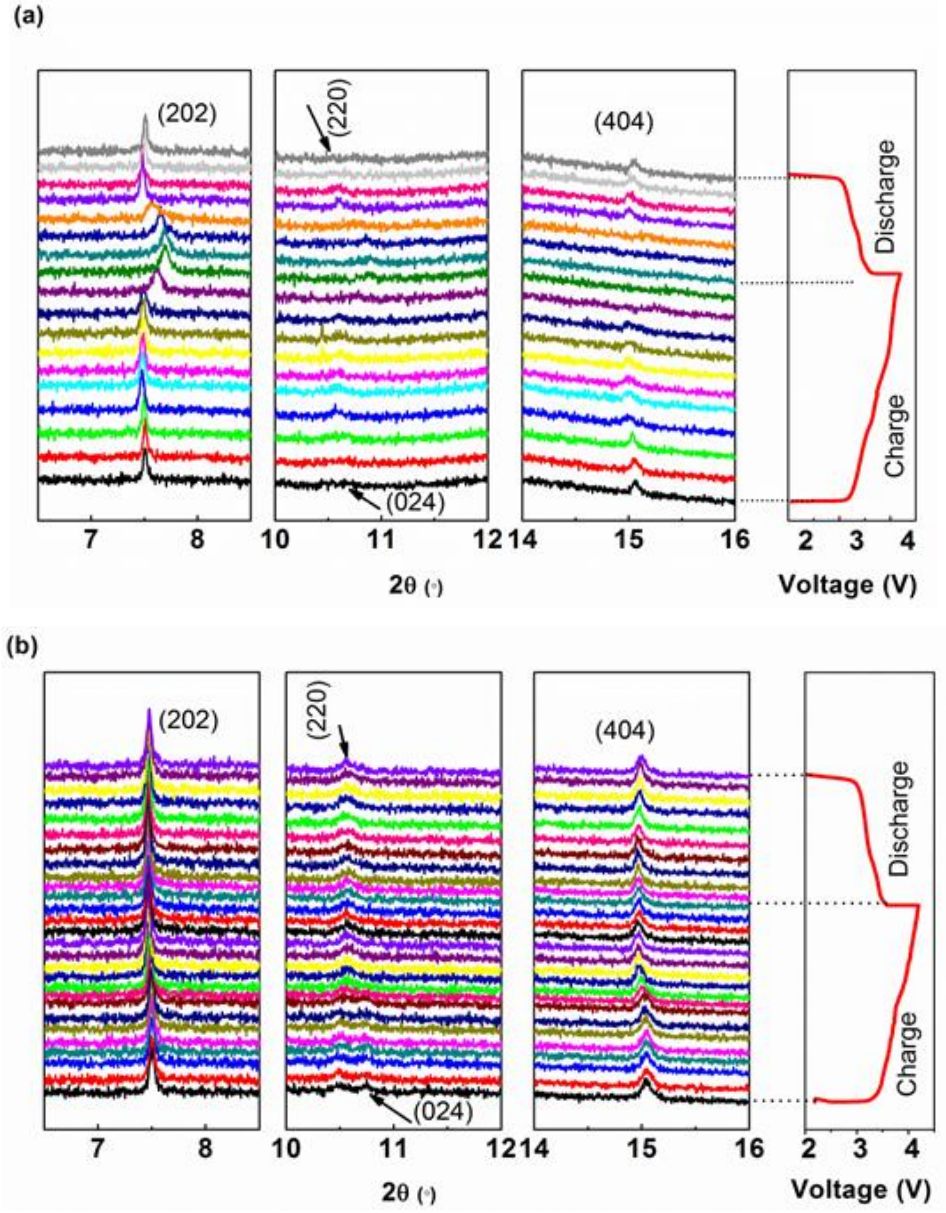

Figure 8.12. In situ Synchrotron XRD of (a) NMHFC and (b) NMHFC@PPy electrodes at current density of 50 mA g^{-1} in the voltage range of 2 - 4.2V in the first cycle (wavelength (λ) is 0.68917 Å).

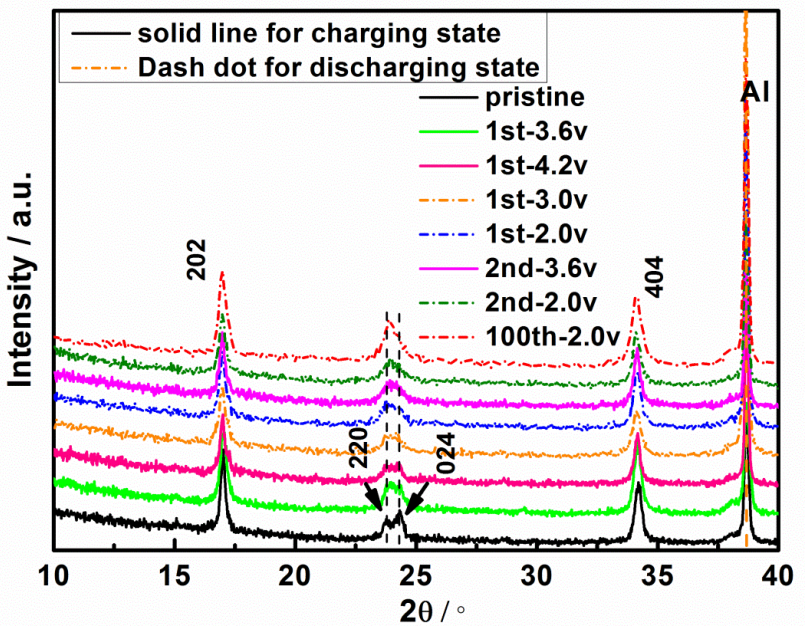

Figure 8.13. *Ex-situ* XRD patterns of NMHFC electrodes in different charged and discharged states in the 1st, 2nd, and 100th cycles. Solid lines denote the charging states and dashed-dotted lines denote the discharging states.

The rate capability of NMHFC@PPy is also greatly improved compared with that of NMHFC. Even at the high rates of 20 C and 40 C, the capacity of 68.8 and 55.6 mA h g^{-1} was still retained, respectively (Figure 8.8(d)). The superior rate capability of NMHFC@PPy benefits from the improvement of electronic conductivity after PPy coating. The electrochemical impedance spectra (EIS) further support this point: the resistance of NMHFC electrode significantly decreased from 600 to 160 Ω after coating with PPy (as shown in Figure 8.14. The apparent activation energies (E_a) for the sodium intercalation into particles and the diffusion apparent activation energy (E_{aD}) of NMHFC and NMHFC@PPy were calculated from the EIS spectra using a previously reported method to further investigate the electrode kinetics shown in Figure 8.16.[325,326] E_a of the NMHFC and NMHFC@PPy was calculated to be 19.2 and 18.9 kJ mol^{-1}, respectively. E_{aD} of the NMHFC and NMHFC@PPy was calculated to be 23.7 and 9.23 kJ mol^{-1}, respectively. It should be noted that the NMHFC@PPy electrode shows slightly smaller activation energy (E_a) and a much lower diffusion apparent activation energy (E_{aD}) than the NMHFC electrode, which is attributed to the superior rate capability of NMHFC@PPy compared to NMHFC. Additionally, it is clearly seen that the potential polarization in the charge/discharge curves is significantly weakened for the NMHFC@PPy electrode compared with the NMHFC electrode at different current density (Figure 8.16). For a clear demonstration of the polarization decay, the difference

between the potentials in the charge and discharge curves (ΔE) of the NMHFC@PPy electrode is compared with that for the as-prepared NMHFC in the present work and in a previous report, as shown in Figure 8.8(e). Obviously, the potential polarization of NMHFC@PPy was much smaller than that of the as-prepared NMHFC in our work and in the reported work.[174] Even at a high rate of 40 C, the value of Δ*E* was 0.64 V, while the reported as-prepared NMHFC showed a value as high as 1.3 V for the potential difference. The decrease in the polarization is attributed to the conductivity improvement of the NMHFC after PPy coating.

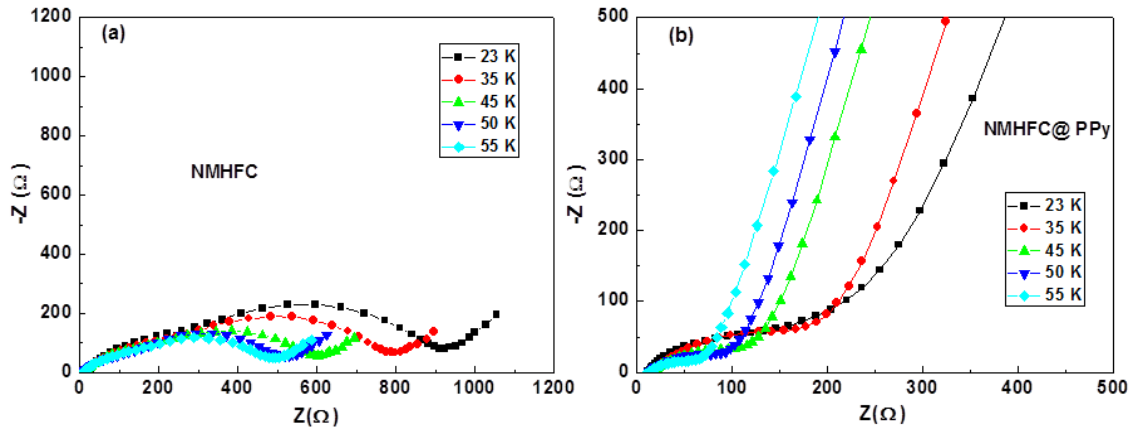

Figure 8.14. Nyquist plots of NMHFC (a) and NMHFC@PPy (b) electrodes at charged state of 3.6V at different temperatures.

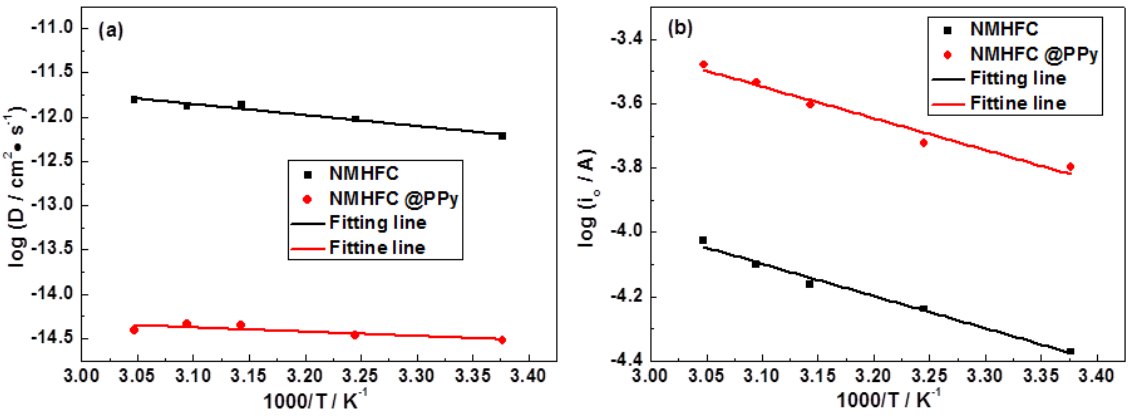

Figure 8.15. Log D (D is the diffusion coefficient) and (d) Arrhenius plots of log i_0 versus 1/T at the charged atate of 3.6V. The lines are the linear fitting results.

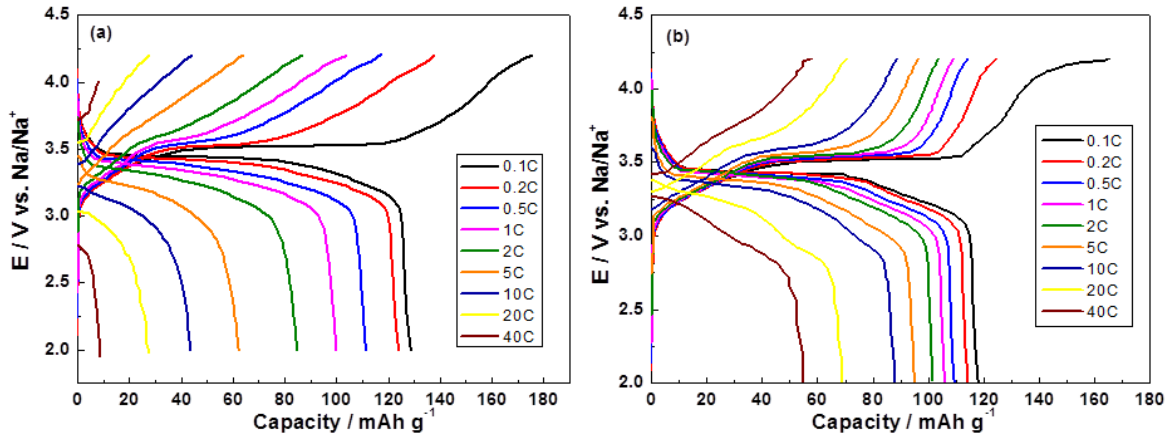

Figure 8.16. The charge/discharge curves of (a) NMHFC and (b) NMHFC@PPy at different rate.

In order to confirm the function of ClO_4^- doping on the PPy, we prepared the NMHFC@PPy composite without ClO_4^- doping, and the characterization is shown in Figure 8.17. Under the condition of absence of ClO_4^-, pyrrole can also polymerize to form PPy on the surface of NMHFC (Figure 8.17(a)), further demonstrating that Mn^{III} in the NMHFC is the driving force of the polymerization of pyrrole. Moreover, the XPS Cl2p spectra of NMHFC@Ppy show that the binding energy of Cl2p at 209.2 eV is assigned to that of NaClO4, suggesting $NaClO_4$ dese not serve as oxidant in the polymerization of pyrrole (Figure 8.5(c)). The capacity of this composite in the first and fifth cycles, however, is just 96.1 and 94 mA h g^{-1}, respectively, smaller than that of the composite with ClO_4^- doping on the PPy (Figure 8.17(b)). The results further demonstrate that the ClO_4^- dopant can act as a source of redox-active sites to reduce the total capacity loss due to the introduction of the conductive coating.

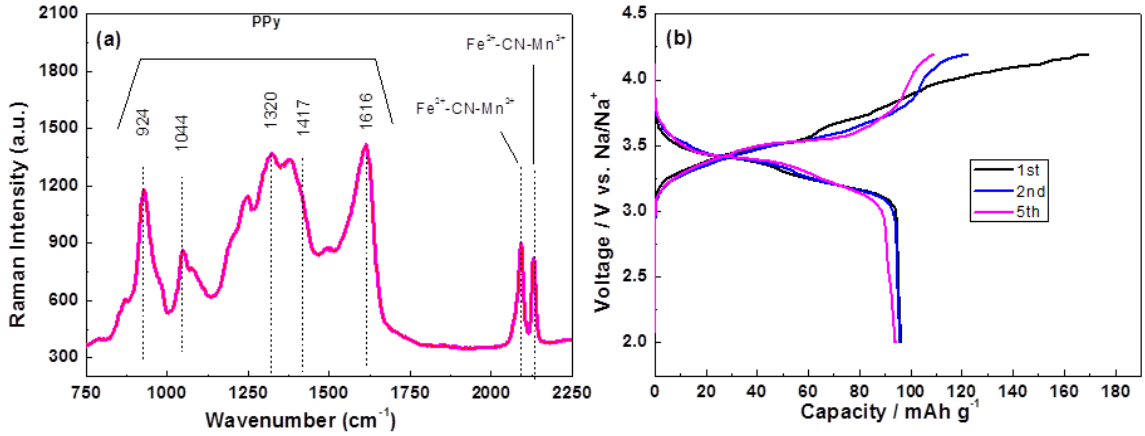

Figure 8.17. (a) Raman spectrum and (b) Charge/discharge curves of NMHFC@PPy without ClO_4^- doping.

8.4 Conclusions

In summary, a composite of NMHFC and PPy doped with ClO_4^- was prepared through a simple, energy-saving, and one-step soft chemistry method which utilizes the intrinsic oxidation of NMHFC to polymerize the pyrrole in the presence of ClO_4^-. PPy plays four important roles in the electrochemical performance of the NMHFC@PPy composite: (1) PPy as conducting polymer increases the electronic conductivity of NMHFC to enhance the rate capability. (2) PPy doped with ClO_4^- can offer redox sites to increase the capacity of the composite. (3) The PPy coating functions as a protective layer to reduce the dissolution of Mn in the NMHFC, improving the cycling performance. (4) The polymerization of PPy can lead to additional Na insertion into NMHFC due to the reduction of Mn^{III}, which is also good for improving reversible capacity. Therefore, the NMHFC@PPy composite could be the next-generation low-cost cathode material with excellent rate capability and good cycling performance, with capacity retention of 67% after 200 cycles.

Chapter 9. A facile method to synthesize Na-enriched $Na_{1+x}FeFe(CN)_6$ frameworks as cathode with superior electrochemical performance for sodium-ion batteries

To improve the cycling performance of Prussian blue, in Chapter 8, we provide a simple, energy-saving, and one-step soft chemistry method to prepare $Na_{1+x}MnFe(CN)_6$ and conductive polymer composite. Herein, we reported another stratage to improve the stability of Prussian blue by optimizing its structure. Na-enriched $Na_{1+x}FeFe(CN)_6$ synthesized by a facile one-step method, utilizing $Na_4Fe(CN)_6$ as the precursor in a saturated NaCl solution. In this method, more sodium ions enter into the framework, which not only can effectively reduce the amount of vacancies and coordinating water, but also can increase the amount of sodium ions per formula unit.

9.1 Introduction

Renewable energy sources, such as wind and sun, have attracted ever-growing attention due to exhaustion of fossil fuels and environmental concerns. Due to the intermittent nature of the renewable energy the utilization of these energy sources relies on the availability of large-scale energy storage systems (ESS).[257] In cases, lithium ion batteries (LIBs) are not suitable candidates because of the low abundance of lithium resources and high cost. In comparison, sodium is abundant and cheap, and also has similar physical and chemical properties to Lithium. Thus, more and more investigations on sodium ion batteries (SIBs) have been emerging in recent years.[48,258]

In a full cell, the cathode material determines the final charge-discharge capacity. Hence, it is crucial to develop a non-toxic, low-cost, high-capacity, stable cathode material for SIBs to ensure large-scale and long-term applications. Up to now, transition metal (M) oxides (Na_xMO_{2+y}),[98,126,259,327,328] phosphates,[319-322] fluorides,[168] and hexacyanoferrates[169,171,173,174] have been reported as cathode materials for SIBs. Few materials, however, can have both high capacity (> 100 mAh g^{-1}) and long cycle life simultaneously. Among these materials, iron hexacyanoferrate is a promising cathode material due to its low cost and non-toxicity. Yang's group reported that $FeFe(CN)_6$ had good cycling stability with a slight capacity decay from the initial 120 to 115 mAh g^{-1} after 150 cycles,[181] and Goodenough's group also suggested that $KFeFe(CN)_6$ exhibits excellent capacity retention of more than 99% after 30 cycles.[169] A fatal flaw, however, is that $FeFe(CN)_6$ and $KFeFe(CN)_6$ do not have sodium ions, which hinders their application in sodium ion batteries. Qian et al. ball milled $Na_4Fe(CN)_6$

with super P to obtain a $Na_4Fe(CN)_6$/C composite which displayed superior cycling stability, with a 88% capacity retention over 500 cycles at a current density of 9 mA g^{-1}, but its theoretical discharge capacity was only 87 mAh g^{-1} because it had just one redox site.[175] Yu et al. demonstrated that $NaFeFe(CN)_6$ can deliver a capacity as high as 118 mAh g^{-1} at 5 mA g^{-1} current density, however, after 20 cycles, the capacity retention was 85% of that in the 2nd cycle.[324] If we can prepare a material which combines the high capacity of $NaFeFe(CN)_6$ with the excellent cycling stability of $Na_4Fe(CN)_6$, it will represent a big improvement in the energy storage field.

Prussian blue (PB) has the perovskite-type structure, $A_2M^{II}[T^{II}(CN)_6]$ (A: alkali metal; M and T: transition metal), in which there are two redox reaction metals. Thus, the ideal electrochemical reaction is $A_2M^{II}[T^{II}(CN)_6] \leftrightarrow 2A^+ + 2e^- + M^{III}[T^{III}(CN)_6]$, which can achieve maximum ion storage ($2A^+$). The synthetic procedure for PB is in aqueous solution, however, so the general formula of PB as it is prepared is $A_xM[T(CN)_6]_{1-y}\square_y\, nH_2O$ ($0 < x < 2$, $y < 1$), where □ denotes a $[T(CN)_6]$ vacancy occupied by coordinating water.[180]The presence of vacancies and coordinating water will break down the bridging of the M-CN-T framework, resulting in a distorted lattice, which gives rise to lower efficiency and structural instability of the PB compound during the charge-discharge process.[181] Therefore, it is important to fabricate a PB framework with few vacancies. Recently, Guo's group reported that $Na_{0.61}Fe[Fe(CN)_6]_{0.94}\cdot\square_{0.06}$ with few vacancies had been prepared by a facile method and could be stably cycled over 150 cycles without apparent capacity loss.[176] There is a serious problem for this reported material, however, that the content of Na-ions per molecular formula unit is very low, and as a result, it must be initially discharged, which is not applicable for the sodium-ion full cell.

Here, we report Na-enriched $Na_{1+x}FeFe(CN)_6$ synthesized by a facile one-step method, utilizing $Na_4Fe(CN)_6$ as the precursor in a saturated NaCl solution. In this method, more sodium ions enter into the framework, which not only can effectively reduce the amount of vacancies and coordinating water, but also can increase the amount of sodium ions per formula unit. As a result, this not only can enhance the cycling stability and the efficiency due to the reduction in the amount of vacancies and crystal water, but also can improve the specific capacity, due to the benefit from more sodium ions entering into the framework.

9. 2 Experimental section

9.2.1. Synthesis of $Na_{1+x}Fe[Fe(CN)_6]$ cubes

All the chemicals were purchased from Sigma-Aldrich. In a typical procedure, different amounts of NaCl (0, 2, 7, and 21 g, and saturated) were dissolved into 100 mL HCl solutions (0, 0.34, 1.2, 3.6 and 6.16 M, respectively). Then, 581 mg $Na_4Fe(CN)_6 \cdot 10H_2O$ and 1 g poly(vinylpyrrolidone) (PVP, average molar weight of 40,000) were added into the NaCl solutions under magnetic stirring. After vigorous stirring for 1 h, a clear solution was obtained. Vials sealed with caps were placed in an electric oven and heated at 80 °C for 10 h. The products were collected by centrifugation at 7800 rpm speed for 5 min and washed in distilled water and ethanol several times. After drying, $Na_{1+x}Fe[Fe(CN)_6]$ cubes were obtained. The samples prepared in 0 M, 0.34 M, 1.2 M, 3.6 M and 6.16 M NaCl solutions, are denoted as PB-1, PB-2, PB-3, PB-4, and PB-5, respectively.

9.2.2.Characterization

The crystalline structure of the active powder and electrodes was characterized by powder X-ray diffraction (XRD) on a GBC MMA diffractometer with a Cu K_α source. The morphology of the sample was investigated by field emission scanning electron microscopy (FESEM; JEOL JSM-7500FA) and transmission electron microscopy (TEM). X-ray photoelectron spectroscopy (XPS) was conducted using a SPECS PHOIBOS 100 Analyser installed in a high-vacuum chamber with the base pressure below 10^{-8} mbar, and X-ray excitation was provided by Al Kα radiation with photon energy hν = 1486.6 eV at the high voltage of 12 kV and power of 120 W. Raman spectra were collected using a JOBIN Yvon Horiba Raman spectrometer model HR800, with a 10 mW helium/neon laser at 632.8 nm excitation in the range of 150 to 2000 cm^{-1}. The molar ratios of Na and Fe were measured by inductively coupled plasma (ICP) analysis (Elementar Vario EL CUBE). The amount of water in the samples was determined using a Mettler–Toledo thermogravimetric analysis / differential scanning calorimetry (TGA/DSC) STARe System from 50-600 ℃ ramped at 10 ℃ min^{-1} in Ar. ^{57}Fe Mössbauer spectra of the samples were detected at 300 K by using a standard constant-acceleration spectrometer and a ^{57}CoRh source, and the spectrometer was calibrated at room temperature with an α–ion foil. The magnetic measurements were carried out using a 14 T physical properties measurement system (PPMS), equipped with a vibrating sample magnetometer (VSM), over a wide temperature range from 5 K to 300 K in a 100 Oe magnetic field. The phases of PB-1, PB-3 and PB-5 were identified by synchrotron powder X-ray diffraction from the powder diffraction beamline at the Australian Synchrotron, with

wavelength of 0.7747Å. In situ synchrotron powder XRD data were collected on the powder diffraction beamline at the Australian Synchrotron with a wavelength (λ) of 0.6888Å, determined using the NIST LaB_6 660b standard reference material. Data were collected continuously in 30 s acquisitions. The cell used for the data collection was charged at a current density of 50 mA g^{-1}, and the cut-off was 2 - 4 V.

9.2.3.Electrochemical test

$Na_{1+x}Fe[Fe(CN)_6]$ electrodes were prepared by mixing 70% active materials, 20% carbon black, and 10% carboxymethyl cellulose (CMC) used as binder by weight to form an electrode slurry, which then was coated on aluminium foil, followed by drying in a vacuum oven overnight at 80 ℃, and then pressing with a pressure of 30 MPa. Sodium foil was cut by the doctor blade technique from sodium bulk stored in mineral oil, and it then was employed as both reference and counter electrode. The electrolyte was 1.0 mol/L $NaClO_4$ in an ethylene carbonate (EC) - diethyl carbonate (DEC) solution (1:1 v/v). The cells were assembled in an argon-filled glove box. The electrochemical performance were tested by a Land Test System in the voltage range of 2 - 4V (vs. Na^+/Na).

9.3 Results and discussion

To introduce more Na^+ into the framework, a series of $Na_{1+x}Fe[Fe(CN)_6]$ samples were prepared in different concentrations of NaCl solutions. The samples prepared in 0 M, 0.34 M, 1.2 M, 3.6 M, and 6.16 M NaCl solutions, are denoted as PB-1, PB-2, PB-3, PB-4, and PB-5, respectively. The lab X-ray powder diffraction (XRD) patterns of all samples show distinguish peaks, indicating that all synthesized samples are well crystallized phase (Figure 9.1). All main peaks can be indexed to a cubic (space group F*m-3m*) unit cell, which is close to reported pristine $Na_{1+x}Fe[Fe(CN)_6]$ structure in ICDD PDF-4 database (2014). With higher concentrations of NaCl solutions added in, the XRD patterns show a trend of peaks shift to smaller 2 theta angles. For example, the pristine $Na_{1+x}Fe[Fe(CN)_6]$ prepared without the addition of NaCl showed a (200) peak at 2θ about 17.46°. When 2 g NaCl was added into the solution (0.34 M), the (200) peak shifted to smaller angle, about 17.28°. Further increasing the amount of NaCl, the XRD peaks gradually shifted to even smaller diffraction angles, down to about 17.14° for PB-5 prepared in saturated NaCl solution, indicating that the spaces of the lattice planes had increased. Also, the energy dispersive spectroscopy (EDS) results show that the sodium content increased from 3.172 at% for PB-1 to 6.683 at% for PB-5 (Table 9.1). It is suggested that the increased concentration of sodium ions in the precursor solution resulted

for more Na^+ ions entry into the unit cell enlarged the interplanar distance, and increased lattice parameters of the PB phases. Scanning electron microscope (SEM) images show that $Na_{1+x}Fe[Fe(CN)_6]$ compound has a cubic morphology, and its particle size is about 0.5-3 μm, which is favourable for the improvement of tap density (Figure 9.2). It should be noted that the average particle size of $Na_{1+x}Fe[Fe(CN)_6]$ decreased with higher concentrations of sodium ions in the precursor solution (Figure 9.2). This result is also consistent with refined S-XRD data of crystalline size of 3696nm, 1097nm, 832nm for PB-1, PB-3, and PB-5, respectively. PB-1, PB-3, and PB-5 were selected as the main samples to investigate the structural evolution of the PB framework after more sodium was introduced into the framework.

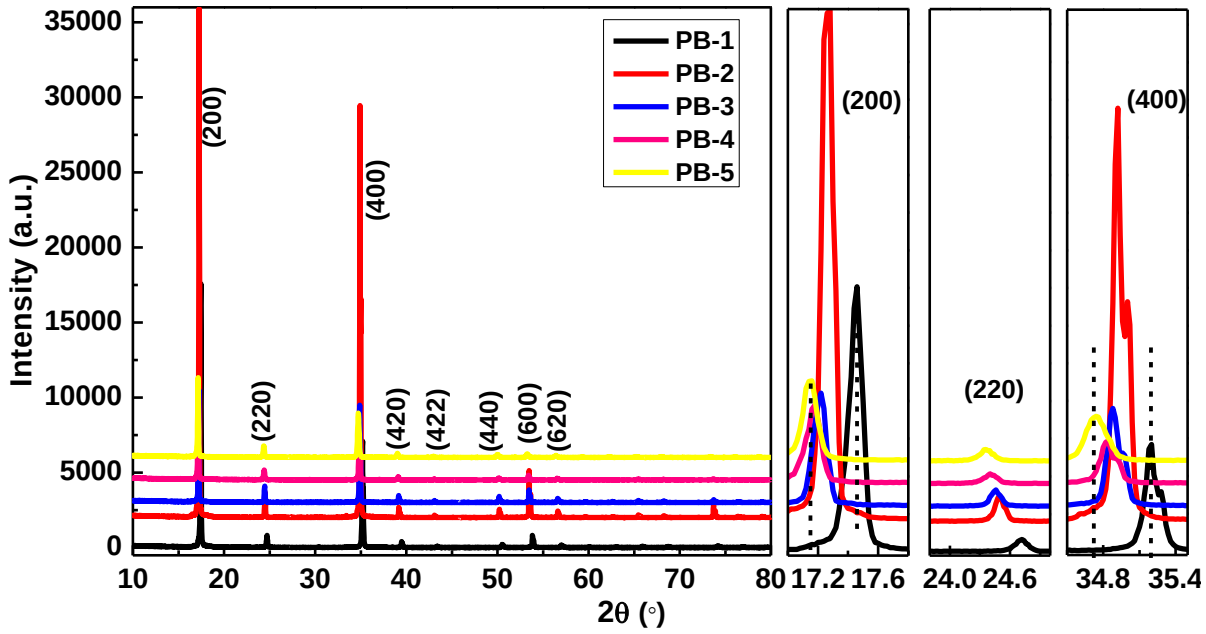

Figure 9.1. XRD patterns of the $Na_{1+x}Fe[Fe(CN)_6]$ powder samples.

Table 9.1 Sodium content in the $Na_{1+x}Fe[Fe(CN)_6]$ powders from the EDS results.

	Point 1 (error)	Point 2 (error)	Point 3 (error)	Point 4 (error)	Na (at%)
PB-1	3.0336 (0.0377)	2.1551 (0.0157)	3.4535 (0.0164)	4.0464 (0.0138)	3.1721
PB-2	4.4501 (0.0435)	4.7203 (0.0398)	4.5501 (0.0403)	4.4000 (0.0399)	4.5627
PB-3	5.6613 (0.0513)	4.6583 (0.0371)	5.2144 (0.0486)	5.5821 (0.0466)	5.2790

PB-4	5.9461	5.7521	5.6306	5.8553	5.7960
	(0.0580)	(0.0580)	(0.0572)	(0.0582)	
PB-5	6.5760	6.6608	6.6941	6.7997	6.6827
	(0.0463)	(0.0430)	(0.0408)	(0.0424)	

In order to further explore the structural evolution of the different $Na_{1+x}Fe[Fe(CN)_6]$ samples, synchrotron X-ray powder diffraction (S-XRD) experiment was conducted at room temperature on the Powder Diffraction Beamline at the Australian Synchrotron. The S-XRD data for PB-1, PB-3, and PB-5 were refined with GSASII software,[329] and the Rietveld refinement results are plotted in Figure 9.3(a). The changes in the crystal lattice caused by the introduction of more sodium ions into the PB framework can be clearly seen that the lattice parameter *a* increased from 10.3028 Å for PB-1, 10.3122(1) Å for PB-3 to 10.3304(1) Å for PB-5 sample, with 0.268% increased (Figure 9.3(b)). This demonstrates that more sodium ions could enter into the framework in PB-5, resulting in the expansion of crystal lattice of the $Na_{1+x}Fe[Fe(CN)_6]$ framework. The crystal structure of the $Na_{1+x}Fe[Fe(CN)_6]$ is shown in inset of Figure 9.3(b). Na atoms locate at *8c* position in the structure. Each Na atom is in the middle of void, which surrounded by eight Fe atoms forming a cubic lattice. The Na-Fe distance increased from 4.461 Å to 4.473 Å, in PB-1 to PB-5 phases. The occupation of the atoms in the $Na_{1+x}Fe[Fe(CN)_6]$ framework based on the refinement is listed in Table 9.2. Significantly, there were more sodium ions in the PB-5 framework by comparison with PB-1 and PB-3. Meanwhile, the amount of C≡N groups in the PB-5 framework increased, suggesting that the amount of vacancies decreased from PB-1 to PB-5. Moreover, the amount of O atoms, which come from the crystalline water, decreased gradually from the PB-1 to the PB-5 sample, demonstrating that the coordinating water in the crystal decreased with more sodium-ion occupation in the PB framework. Consequently, the structure of PB-5 sample forms one framework that is Na-enriched and has few vacancies, and it was synthesized by a facile one-step method, just utilizing $Na_4Fe(CN)_6$ as the precursor in a saturated NaCl solution. This method not only can effectively reduce the amount of vacancies and coordinating water, but also can increase the amount of sodium ions per formula unit.

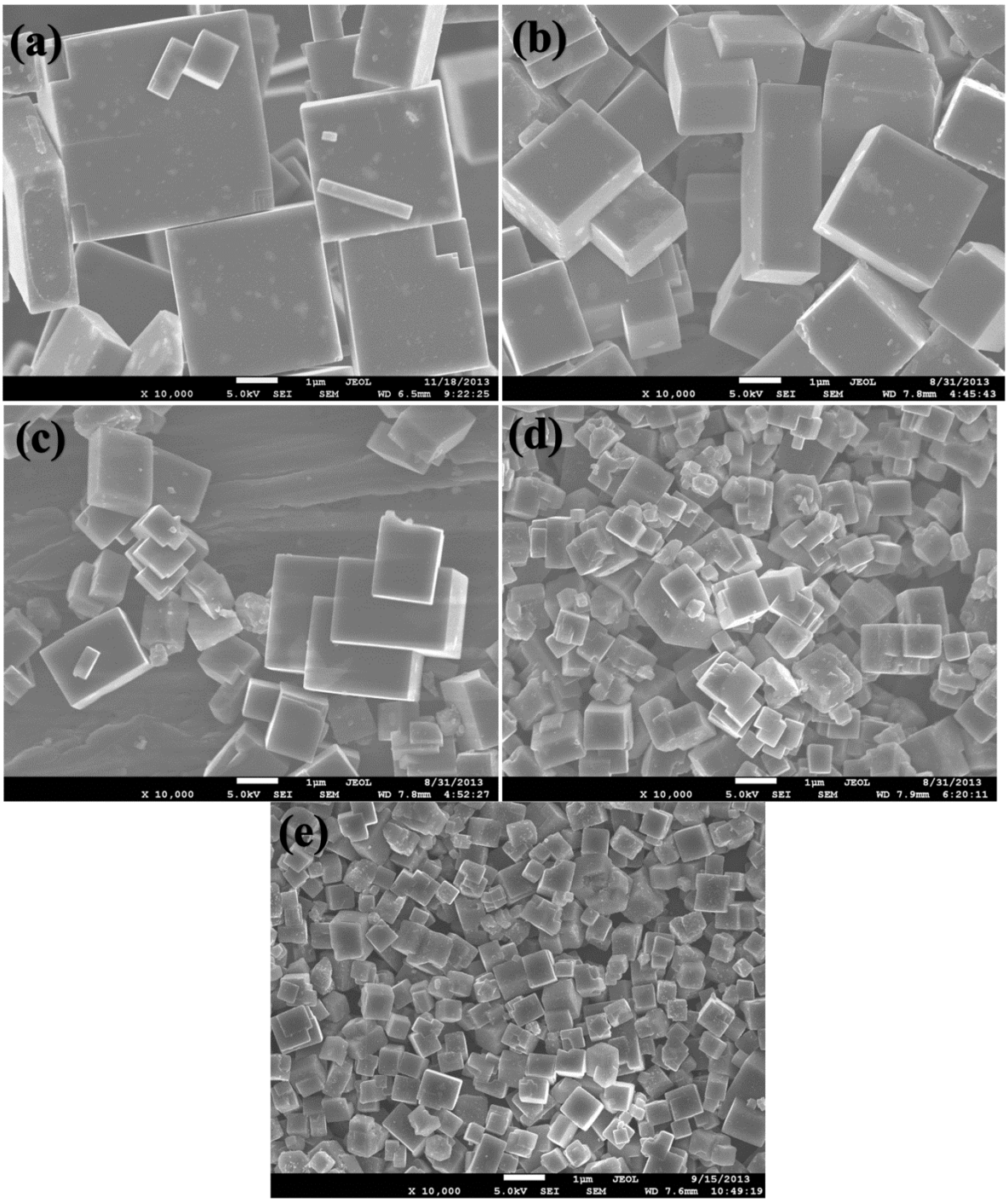

Figure 9.2. SEM images of $Na_{1+x}Fe[Fe(CN)_6]$ powders: (a) PB-1, (b) PB-2, (c) PB-3, (d) PB-4, (e) PB-5.

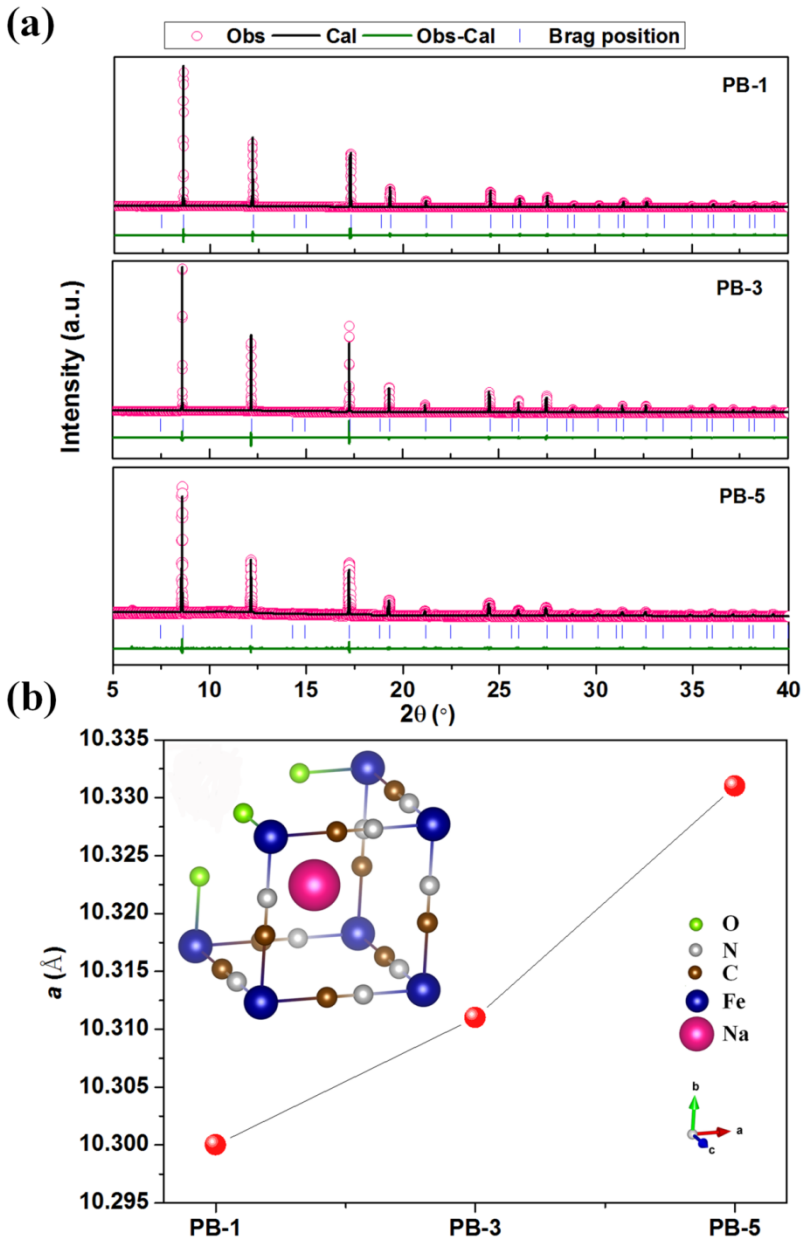

Figure 9.3. (a) Synchrotron XRD patterns of PB-1, PB-3, and PB-5, and their Rietveld refinements. (b) Lattice parameters changes of the $Na_{1+x}Fe[Fe(CN)_6]$ powders and the crystal structure of the $Na_{1+x}Fe[Fe(CN)_6]$ framework based on the S-XRD refinement inset. (The synchrotron X-ray powder diffraction was obtained from the Powder Diffraction Beamline at the Australian Synchrotron, with wavelength of 0.7747 Å.)

Table 9.2 The occupation of the atoms in the $Na_{1+x}Fe[Fe(CN)_6]$ framework.

	PB-1	PB-3	PB-5
Na	0.563	0.659	0.747
C	0.724	0.734	0.743
N	0.724	0.734	0.743
O	0.276	0.266	0.257

Figure 9.4(a) shows the Raman spectra of the $Na_{1+x}Fe[Fe(CN)_6]$ powders between 2000 and 2300 cm^{-1}. Three peaks at 2083.8, 2122.0 and 2139.4 cm^{-1} were observed from PB-1, PB-3 and PB-5. All these peaks can be assigned to the $(C\equiv N)^-$ group, reflecting the bonding of the $(C\equiv N)^-$ ion to the Fe ions in different valence states. The higher is the iron oxidation state, the more effective is the iron cation to $(C\equiv N)^-$ bonding.[330,331] Thus, the peak at 2139.4 cm^{-1} is assigned to the bonding of the $(C\equiv N)^-$ to Fe^{3+} ion. Clearly, with more sodium ion entry into the framework, the intensity of the peak at 2139.4 cm^{-1} decreased gradually, suggesting the amount of Fe^{3+} in the $Na_{1+x}Fe[Fe(CN)_6]$ decreased. Thermogravimetric analysis (TGA) was carried out in argon from 50 to 600 °C at a heating rate of 10 °C/min, to determine the water content in the $Na_{1+x}Fe[Fe(CN)_6]$ powders, as shown in Figure 9.4(b). It is clear that there is a considerable amount of water in the prepared compounds. A trace amount of water (lost at ~ 100 °C) was adsorbed on the particle surfaces, while much water was adsorbed in the vacancies (evaporating in the range of 200 - 350 °C). The water content of PB-1, PB-3, and PB-5 was 18.7, 17.2, and 15.5 wt %, respectively. The TGA results confirm that the introduction of more Na^+ into the $Na_{1+x}Fe[Fe(CN)_6]$ framework reduces the amount of crystal water in the unit cell. The molar Na : Fe ratios of the PB samples were detected by inductively coupled plasma (ICP). The molar ratios were calculated to be 0.633, 0.663, and 0.778 for PB-1, PB-3, and PB-5, respectively. Combined with the TGA results, the formulas for PB-1, PB-3, and PB-5 are $Na_{1.26}Fe[Fe(CN)_6]\cdot 3.8H_2O$, $Na_{1.33}Fe[Fe(CN)_6]\cdot 3.5H_2O$ and $Na_{1.56}Fe[Fe(CN)_6]\cdot 3.1H_2O$, respectively.

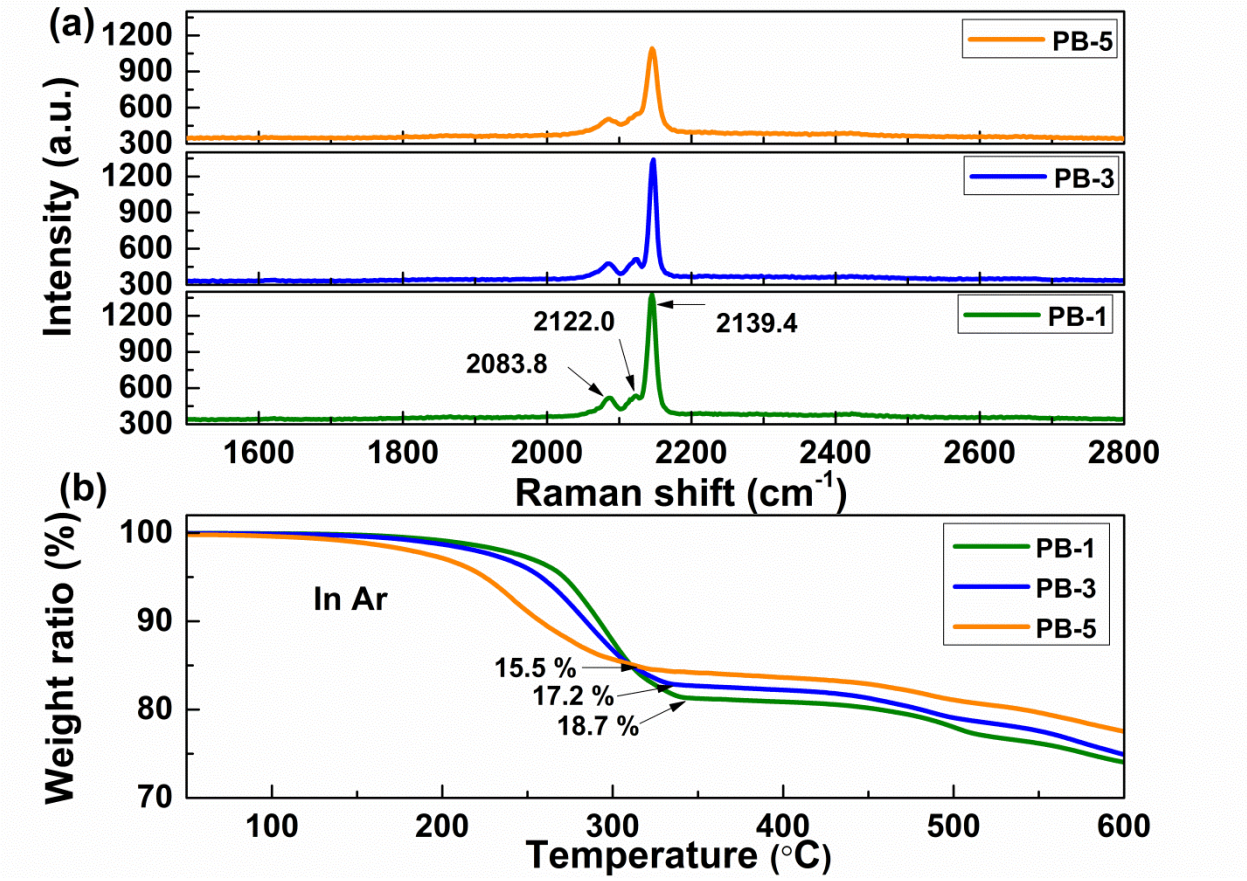

Figure 9.4. (a) Raman spectra and (b) TGA analysis of $Na_{1+x}Fe[Fe(CN)_6]$ powder samples.

In order to further determine the spin state of Fe in the as-prepared samples, Mössbauer spectroscopy was performed, and the results are shown in Figure 9.5. From the Mössbauer spectroscopy results, it is clearly seen that the $Na_{1+x}Fe[Fe(CN)_6]$ powder contains Fe^{2+} and Fe^{3+} ions. (The occupancy of Fe^{2+} and Fe^{3+} are listed in Table 9.3.) In the PB-1 sample, 82.7 % of the Fe was in the Fe^{3+} state. With increased sodium content in the $Na_{1+x}Fe[Fe(CN)_6]$, the amount of Fe^{3+} decreased, down to 62.1 % for PB-5, while the percentage of Fe^{2+} changed in the opposite way, increasing from 17.3 % for PB-1 to 37.9 % for PB-5. This trend is consistent with the Raman Spectra (Figure 9.4) and the X-ray photoelectron spectroscopy (XPS) results (Figure 9.6). Moreover, the decrease in Fe^{3+}, accompanied by the increase in Fe^{2+}, suggested that $[Fe(CN)_6]$ vacancy exists in the unit cell, and the formula of the as-prepared PB is $Na_{1+x}Fe^{III}[Fe^{II}(CN)_6]_{1-y}\square_y \cdot nH_2O$ ($0 < x < 1$, $y < 1$). Otherwise, the ratio of Fe^{2+} to Fe^{3+} should remain 1:1. In other words, with more sodium ion entering into the crystal structure, the ratio of Fe^{2+} to Fe^{3+} becomes closer to 1 (41.8 % : 58.2 % = 0.718), suggesting that amount of $[Fe(CN)_6]$ vacancy becomes less at the same time, while the amount of coordinating water occupying the vacancy becomes less (as seen from the TGA results in

Figure 9.4(b)), which indicates the better ordering in the lattice. Thus, it is concluded that PB prepared in saturated NaCl solution have an increased content of sodium and reduced amounts of vacancy and coordinating water in the formula for Prussian blue. This is beneficial for the improvement of both the capacity and the structural stability of the PB compound during charge-discharge processes.

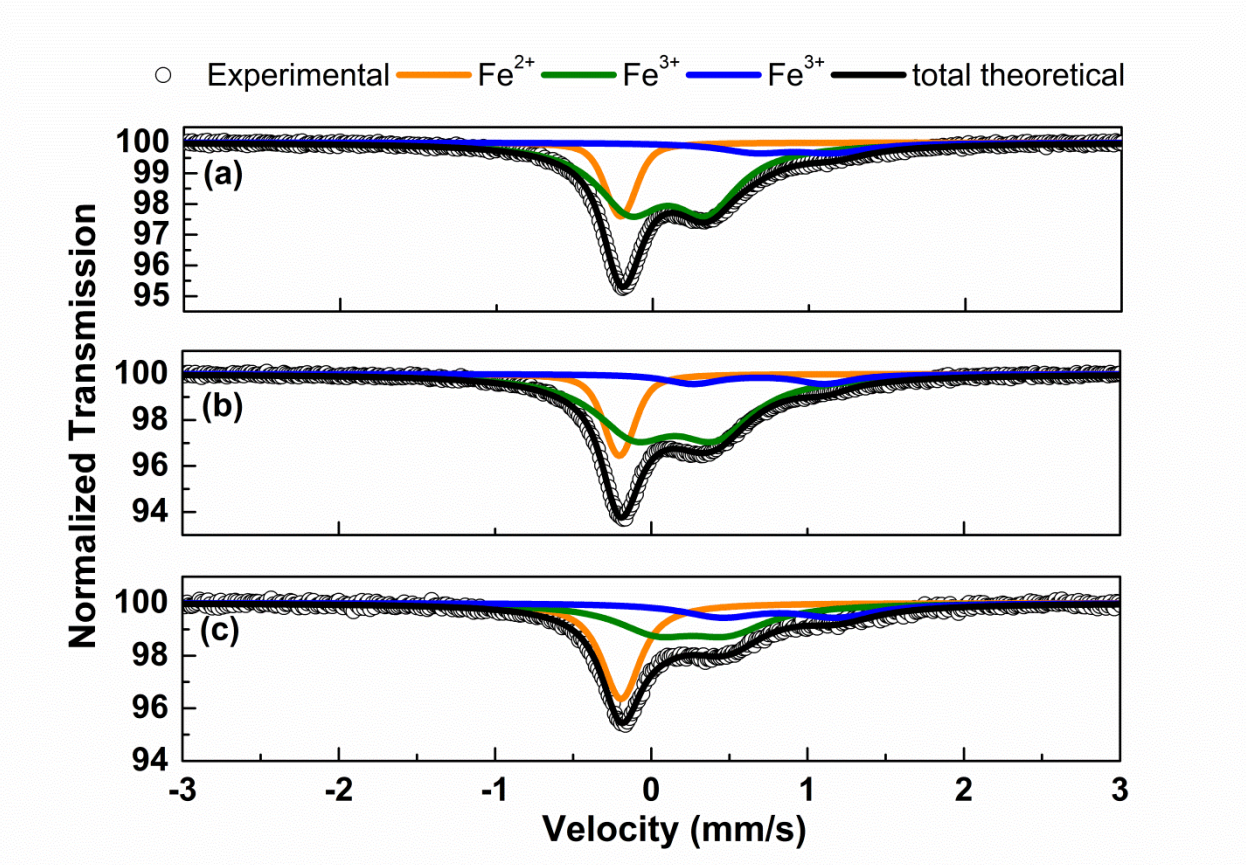

Figure 9.5. Mössbauer spectra of (a) PB-1, (b) PB-3, and (c) PB-5 samples.

Table 9.3 Valence state distribution of Fe in the $Na_{1+x}Fe[Fe(CN)_6]$ powders based on analysis of the Mössbauer spectra.

sample	Fe^{2+}	Fe^{3+}
PB-1	0.173	0.827
PB-3	0.193	0.807
PB-5	0.379	0.621

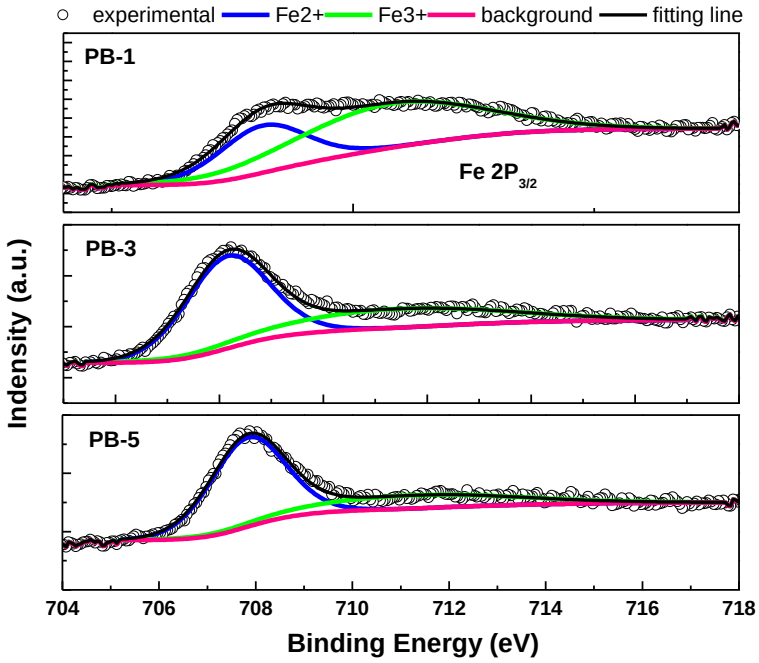

Figure 9.6. XPS results of the $Na_{1+x}Fe[Fe(CN)_6]$ powders.

To promote electron beam penetration into the particles, the micro sized $Na_{1+x}Fe[Fe(CN)_6]$ samples (~2 μm) were crushed into small pieces in a mortar before working on transmission electron microscopy (TEM). The selected area electron diffraction (SAED) patterns show that the $Na_{1+x}Fe[Fe(CN)_6]$ particles were single crystalline with face-centred-cubic structure (insets of Figure 9.7). It is difficult, however, to observe the lattice fringes in high resolution TEM (HRTEM) of $Na_{1+x}Fe[Fe(CN)_6]$ particles because the unstable structure will be changed under higher voltage (Figure 9.7).

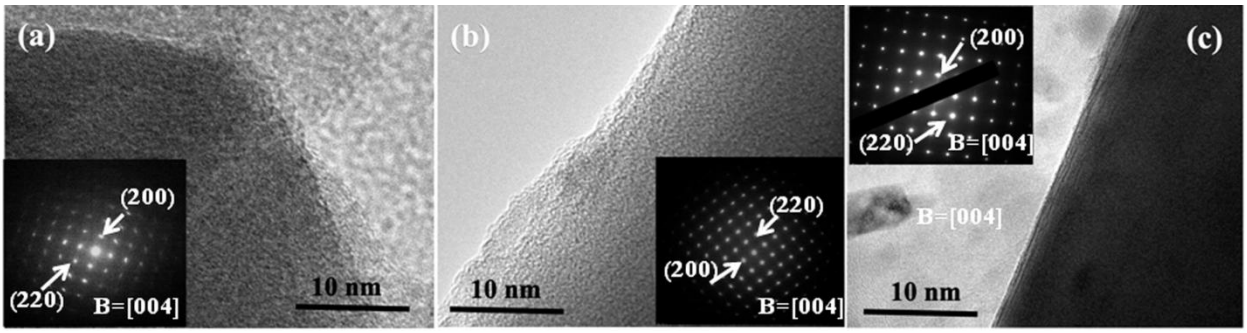

Figure 9.7. TEM images and SAED patterns (insets) of (a) PB-1, (b) PB-3, and (c) PB-5.

Figure 9.8(a) shows the charge-discharge curves of $Na_{1+x}Fe[Fe(CN)_6]$ powders between 2.0 - 4.0 V at the current density of 20 mA g^{-1}. The PB-1 sample can deliver 86.5 mAh g^{-1} discharge capacity, but by comparison, the PB-3 and PB-5 samples can deliver larger capacity, 90.8 and 103.6 mAh g^{-1}, respectively. Moreover, the potential hysteresis (ΔE)

between the charge and discharge curves is reduced for the PB-3 and PB-5 samples. There were two redox couples in the dQ/dV curve of PB-1 (Figure 9.8(b)), with the strong one located at 2.98/2.92 V and a small one at 3.74/3.42 V, which is similar to the cyclic voltammetry (CV) curves of $FeFe(CN)_6$.[181] It is likely that the different coordination sites of Fe ions in the $Na_{1+x}Fe[Fe(CN)_6]$ give rise to these two pairs of peaks in the dQ/dV curve. Thus, the peaks at 2.98/2.92 V are attributed to the high-spin Fe^{II}/Fe^{III} couple coordinated with $(C\equiv N)^-$ by N atoms, and the ones at 3.74/3.42 V are assigned to the low-spin Fe^{II}/Fe^{III} couple bonding to the C atoms of the $(C\equiv N)^-$.[169] In the subsequent cycles, the shapes and areas of the dQ/dV curve in the 50th cycle overlapped well with the second cycle one, demonstrating the reversible and stable Na insertion/deinsertion reactions of the $Na_{1+x}Fe[Fe(CN)_6]$. Interestingly, for the PB-3 and PB-5 samples, an extra two pairs of peaks appeared in the dQ/dV curves at 3.06/3.04 V and 3.34/3.3 V, respectively (Figure 9.8(c, d)). This is the reason for the extra capacity of the PB-3 and PB-5 samples compared with the PB-1 sample, which is related to the spin states of Fe^{II} and Fe^{III}.

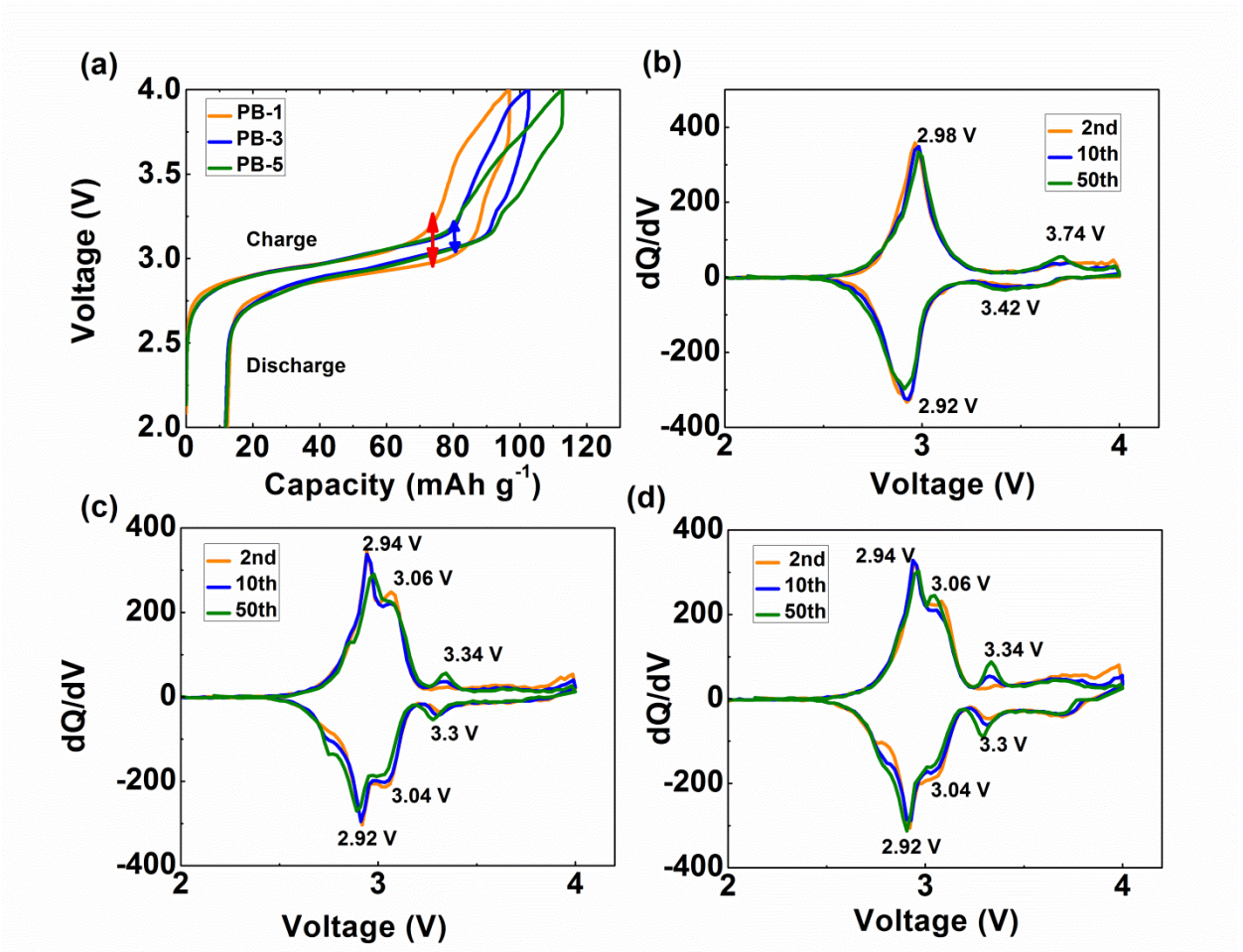

Figure 9.8. (a) Charge - discharge curves of $Na_{1+x}Fe[Fe(CN)_6]$ powders at current density of 20 mA g^{-1}; (b), (c), and (d) are dQ/dV curves of PB-1, PB-3, and PB-5, respectively.

To identify the spin states of Fe^{II} and Fe^{III} in the $Na_{1+x}Fe[Fe(CN)_6]$, the dependence of the magnetic susceptibility (χ) of the $Na_{1+x}Fe[Fe(CN)_6]$ powders on temperature was obtained, as shown in Figure 9.9. All the $Na_{1+x}Fe[Fe(CN)_6]$ powders show paramagnetic behavior from low temperature, and there is no phase transition observed in this temperature range (Figure 9.9(a)). The calculated effective magnetic moments (μ_{eff}) of PB-1, PB-3, and PB-5 are 4.45 μ_B, 4.2 μ_B, and 4.0 μ_B per formula unit, respectively. Moreover, the effective magnetic moments for the low-spin (S = 1/2) and high-spin (S = 5/2) states of Fe^{III} are 1.73 and 5.9 μ_B, respectively, while those for the low-spin (S = 0) and high-spin (S = 2) states of Fe^{II} are 0 and 4.89 μ_B, respectively. In our present state of knowledge, it is just concluded from combining the calculated effective magnetic moments (μ_{eff}) with the dQ/dV curves that the Fe^{II} and Fe^{III} in the PB-3 and PB-5 have four different spin states. It is difficult to determine, however, what the two extra redox couples that appear in PB-3 and PB-5 samples should be assigned to.

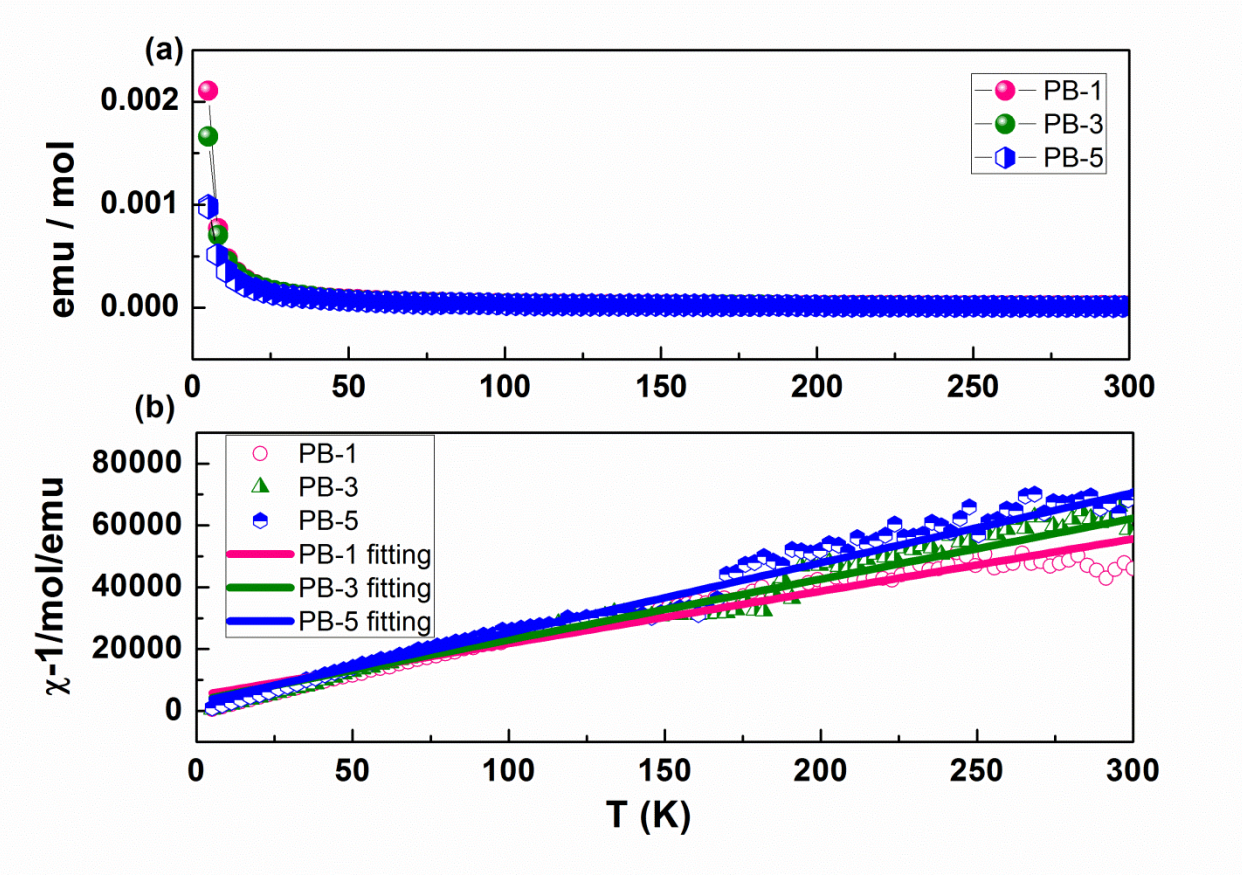

Figure 9.9. (a)Temperature dependence of the magnetic susceptibility of the $Na_{1+x}Fe[Fe(CN)_6]$ powders and (b) inverse susceptibilities corrected for the temperature-independent contribution and their fit to the Curie-Weiss law.

To investigate the structural evolution during Na-ion insertion/extraction processes, *in-situ* synchrotron pXRD was carried out on the Powder Diffraction Beam line at the Australian Synchrotron with a wavelength (λ) of 0.6888 Å. Figure 9.10 shows the *in-situ* pXRD patterns of the PB-5 cathode material during the first cycle within the voltage range of 2.0 - 4.0 V. From the image plots of the diffraction patterns for (200), (220), and (400), it is clear that the intensities of the (200) and (400) plane Bragg reflections decreased during charging, and the process was observed to be reversible during discharging (Figure 9.10(a)). The decrease/increase of the intensities during the charging/discharging suggests that the sodium ions were extracted from and inserted into the structure of PB-5 reversibly. Additionally, the positions of the (200), (220), and (400) peaks shifted towards larger 2θ values during the charge process and could not be restored during the discharging process, indicating the contraction of the unit cell during sodium-ion insertion/extraction into the PB-5 framework. This decrease in the unit cell volume can explain why the discharge capacity of PB-5 is smaller than the capacity during the charge process. Moreover, some appreciable positive intensities within the 7.55° to 7.7° and 15.2° to 15.43° 2θ ranges indicate the existence of a phase with lattice parameters that deviate from those of PB-5 ($Na_{1.56}Fe[Fe(CN)_6]\cdot 3.1H_2O$). This phenomenon can be clearly observed in the close individual diffraction patterns of the (200) and (400) reflections stacked against the voltage profile (Figure 9.10(b)). At the onset of the charge, the peaks of the (200) and (400) reflections show symmetrical profiles, and then the reflections start to broaden asymmetrically toward higher angles. Finally, the peaks of the (200) and (400) reflections split into two peaks at the end of the charging process. The changes of lattice parameter *a* during the first cycle is plotted in Figure 9.11. This is due to the phase transition that takes place from sodium-rich $Na_{1.56}Fe[Fe(CN)_6]\cdot 3.1H_2O$ ($Na_{1.56}$) to sodium-poor $Na_\delta Fe[Fe(CN)_6]\cdot nH_2O$ (Na_δ) during the charging process, which is also observed in $LiFePO_4$.[332]During the discharge process, with the sodium insertion into the framework, the peaks of the (200) and (400) reflections begin to narrow into symmetrical peaks and shift to smaller angle. Since the sodium composition cannot be restored to the original $Na_{1.56}Fe[Fe(CN)_6]\cdot 3.1H_2O$ at the end of the discharging process ($Na_{1.56-x}Fe[Fe(CN)_6]\cdot 3.1\text{-}yH_2O$ ($Na_{1.56-x}$)), the (200) and (400) peaks didn't shift back to their pristine positions. The valence state change of Fe in the PB-5 electrode during cycling was tested by

the Mössbauer spectra, shown in Figure 9.12, which also support this point. When the PB-5 electrode was fully charged at 4.0 V, the percentage of Fe^{2+} decreased from 37.9% to 28.7%. While the percentage of Fe^{2+} cannot restore to the original state, just 30.5% at the end of discharging process (Table 9.4). This also confirms that the sodium content of the PB-5 electrode at the end of the discharging process is lower than that of the original $Na_{1.56}Fe[Fe(CN)_6]\cdot 3.1H_2O$, in good agreement with the *in-situ* S-XRD observation. This irreversible structure change could also attribute to the removal of coordinating water in the Na-enriched phase.

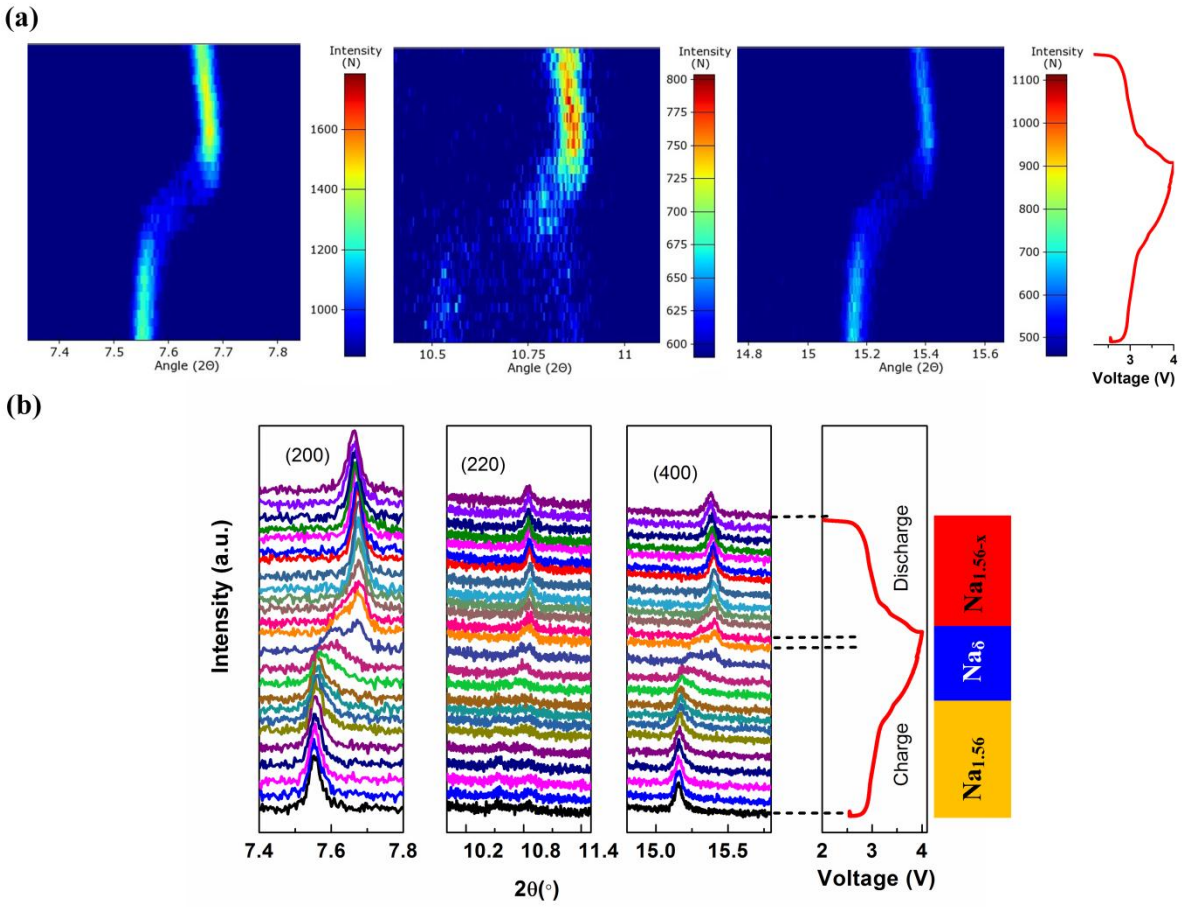

Figure 9.10. *In-situ* synchrotron pXRD patterns of PB-5 during the first charge and discharge at current density of 50 mA g^{-1}; (a) Image plots of diffraction patterns for the (200), (220), and (400) reflections during the first cycle. (b) Individual diffraction patterns of the (200), (220), and (400) reflections stacked against the voltage profile. (wavelength (λ) of 0.6888 Å, determined using the NIST LaB_6 660b standard reference material.)

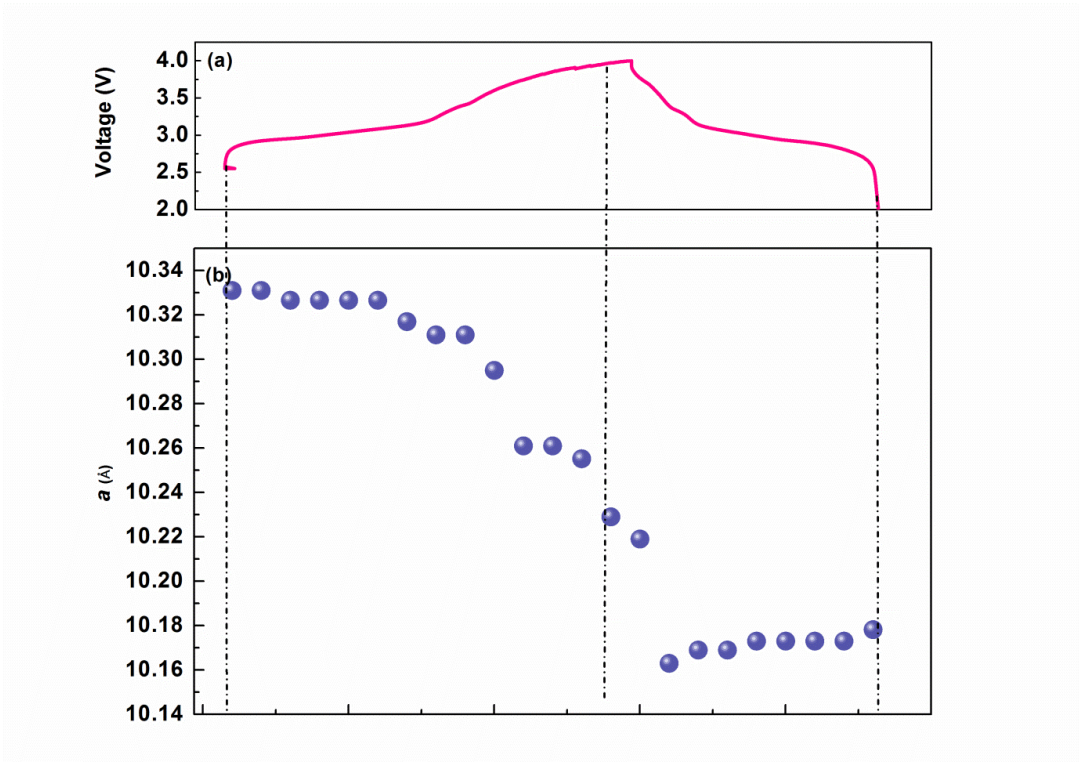

Figure 9.11. (b) The changes of lattice parameter *a* during (a) the first charge-discharge process.

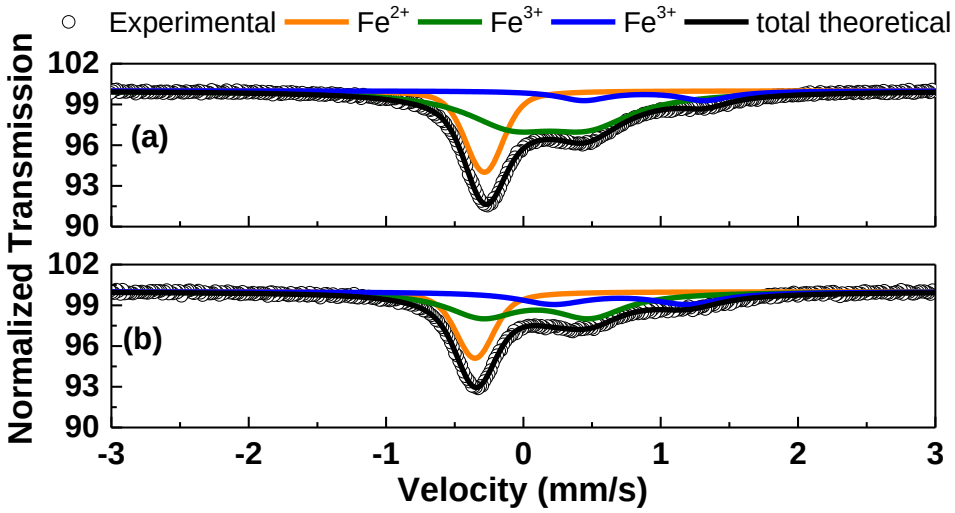

Figure 9.12. Mössbauer spectra of the PB-5 electrode charged at 4.0V (a) and discharged at 2.0V (b).

Table 9.4 Valence state distribution of Fe in the PB-5 electrode charged at different states based on analysis of the Mössbauer spectra.

sample	Fe^{2+}	Fe^{3+}
PB-5 charged at 4.0V	0.287	0.713
PB-5 discharged at 2.0V	0.305	0.695

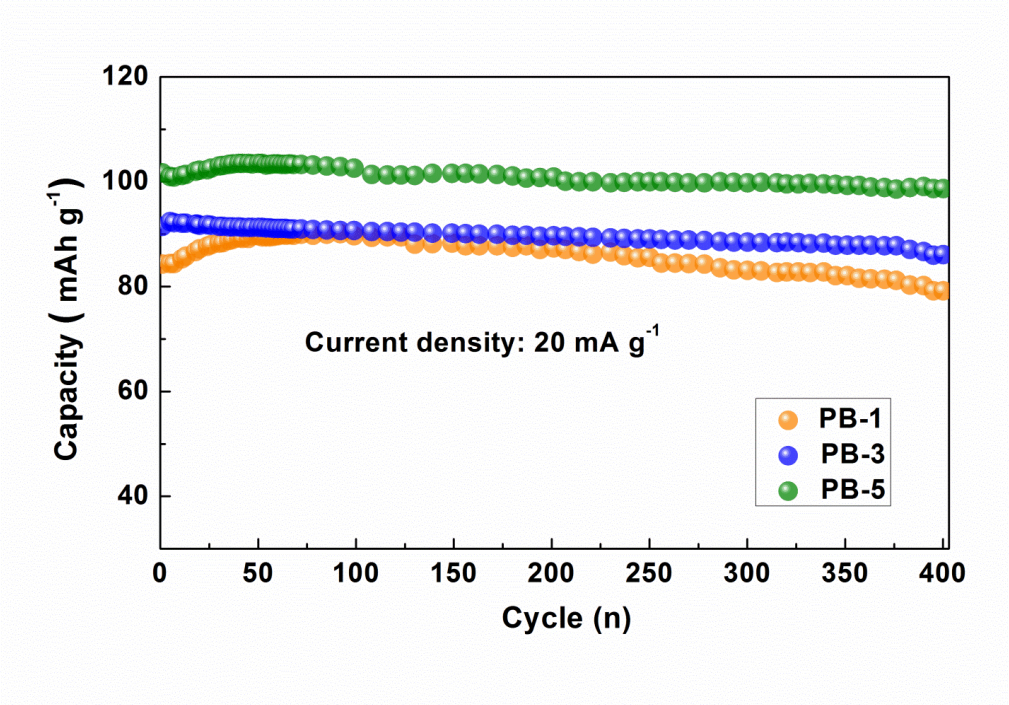

Figure 9.13. Cycling performance of $Na_{1+x}Fe[Fe(CN)_6]$ electrodes.

Figure 9.13 shows the cycling performance of the $Na_{1+x}Fe[Fe(CN)_6]$ cathodes between 4.0 - 2.0 V at the current density of 20 mA g^{-1}. It is clear that the cycling stability of the $Na_{1+x}Fe[Fe(CN)_6]$ is excellent; after 400 cycles, there was a slight capacity decay. The PB-5 sample, which had the most sodium ion content and the least vacancy in its framework, delivered a larger capacity of 103 mAh g^{-1}, compared with the PB-1 sample with capacity of 89.5 mAh g^{-1}. After 400 cycles, the capacity of PB-5 was still 97% of the initial capacity, while the capacity retention of PB-1 was 91%, which was also higher compared with other cathode materials for sodium-ion batteries.[98,126,168,169,171,173,174,259,319-322,327,328] This demonstrates that the reduction of the vacancies and coordinating water in the $Na_{1+x}Fe[Fe(CN)_6]$ framework results in structural stability of the PB compound, which gives rise to a higher capacity and greater cycling stability during the charge-discharge processes. The discharge-charge curves with cycles of the $Na_{1+x}Fe[Fe(CN)_6]$ cathode are plotted in

Figure 9.14. To clearly explore the reason for the greater cycling stability of $Na_{1+x}Fe[Fe(CN)_6]$ cathode, the impedance spectra of $Na_{1+x}Fe[Fe(CN)_6]$ cathode before and after cycles were tested and shown in Figure 9.15. The impedance curves of $Na_{1+x}Fe[Fe(CN)_6]$ electrodes show two semicircles in the medium frequency and the low frequency regions, which could be assigned to the sodium ion diffusion through the solid electrolyte interphase (SEI) film (R_x) and the charge transfer resistance (R_{ct}), respectively. The R_{ct} is calculated using the equivalent circuit shown in Figure 9.15(a). The R_{ct} values of the PB-1, PB-3 and PB-5 after 5 cycles are 680 Ω, 468 Ω and 411 Ω, respectively. Clearly, after 30 cycles, the resistance of $Na_{1+x}Fe[Fe(CN)_6]$ electrodes changed a little, suggesting the $Na_{1+x}Fe[Fe(CN)_6]$ framework could maintain a stable structure.

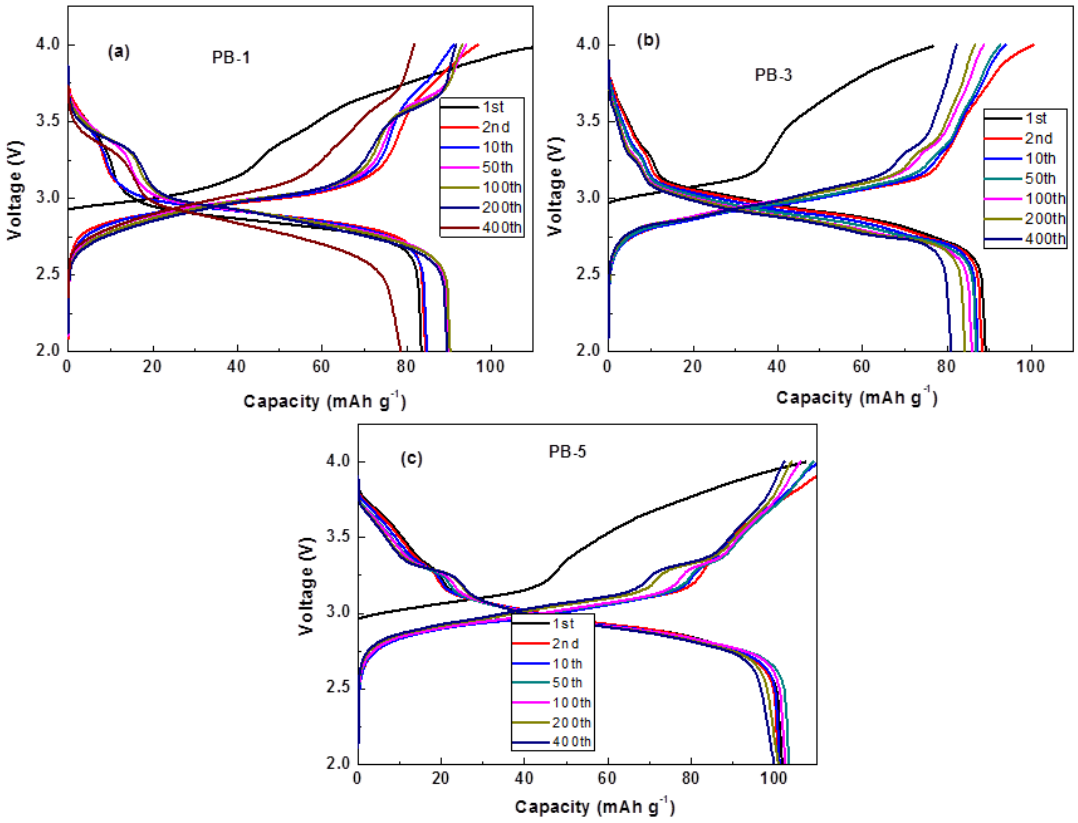

Figure 9.14. The discharge-charge curves with cycles of $Na_{1+x}Fe[Fe(CN)_6]$ cathode: (a) PB-1; (b) PB-3 and (c) PB-5.

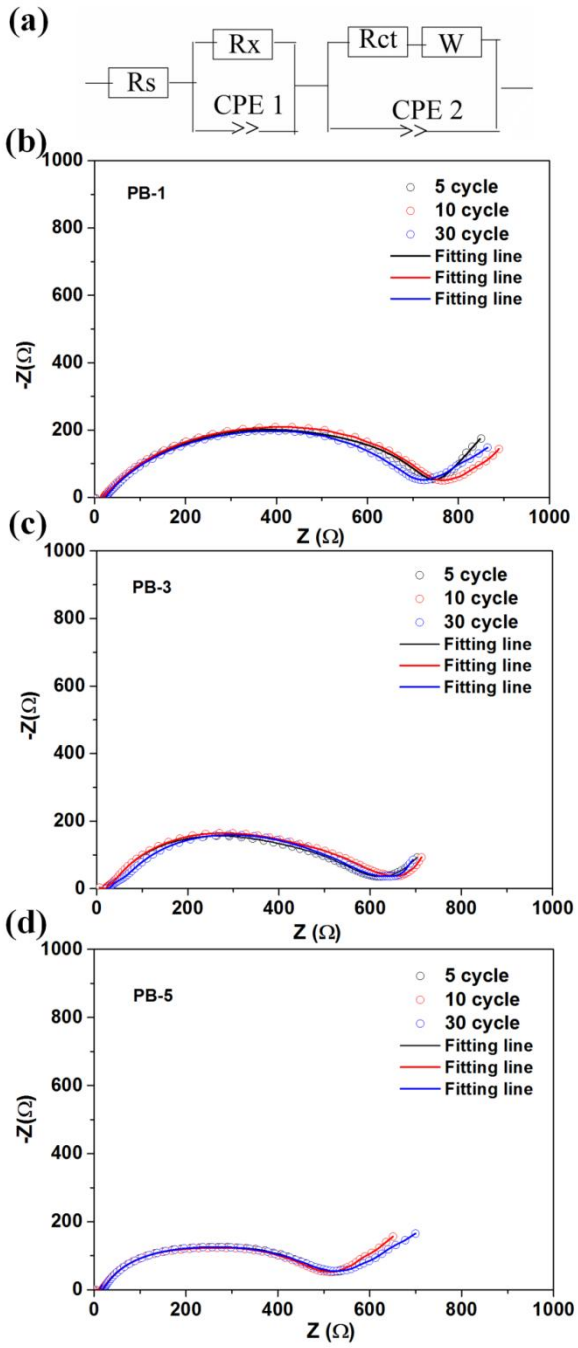

Figure 9.15. The impendence of spectra of $Na_{1+x}Fe[Fe(CN)_6]$ after cycles: (a) the equivalent circuit; (b) PB-1; (c) PB-3 and (d) PB-5.

The rate capability of the $Na_{1+x}Fe[Fe(CN)_6]$ cathode was also tested at various current densities from 5 mA g^{-1} (0.05 C) to 100 mA g^{-1} (1 C), as shown in Figure 9.16. At the current densities of 5, 10, 25, and 100 mA g^{-1}, the PB-5 sample delivered higher capacity than the PB-1 and PB-3 samples. In further work, a composite of the PB-5 sample with carbon can

be prepared to improve the rate capability, yielding a cathode which possesses high capacity, stable cycling performance, and high rate capability for sodium ion storage.

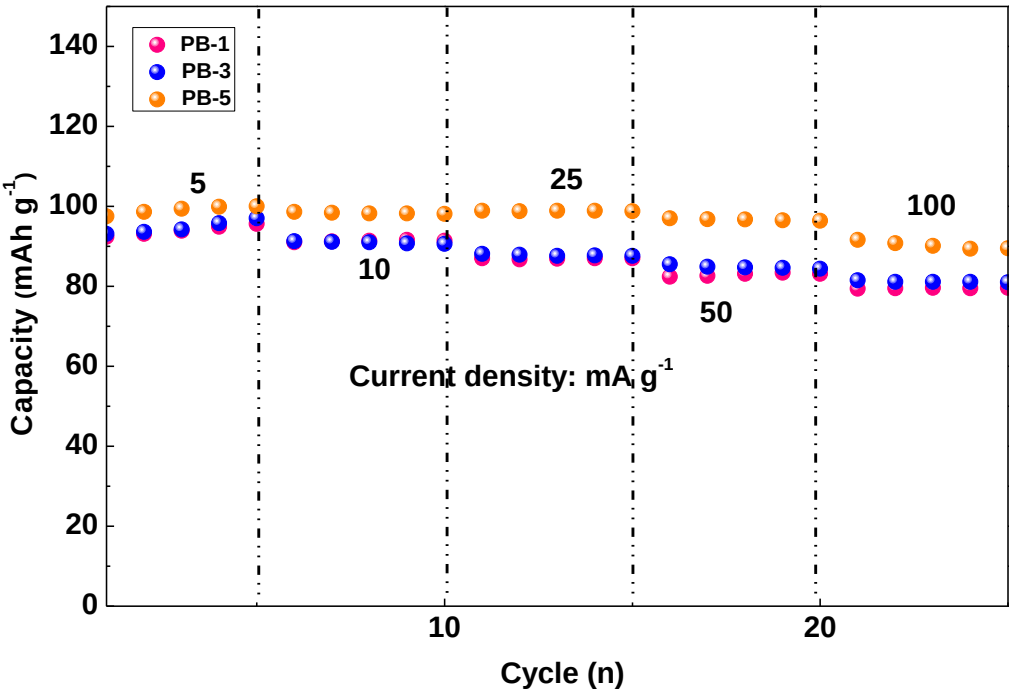

Figure 9.16. Rate capability of $Na_{1+x}Fe[Fe(CN)_6]$ powder electrodes.

10.4 Conclusion

In summary, Na-enriched $Na_{1+x}Fe[Fe(CN)_6]$ was prepared through a facile and one-step method using $Na_4Fe(CN)_6$ as the precursor in highly concentrated NaCl solutions. With increasing sodium ions entering into the framework, the amount of vacancies and coordinating water in the $Na_{1+x}Fe[Fe(CN)_6]$ decreased, resulting in enhanced structural stability. Thus, the Na-enriched $Na_{1+x}Fe[Fe(CN)_6]$ showed a superior cycling performance with excellent capacity retention of 97% over 400 cycles. The simple synthesis method, superior cycling stability with a high capacity of more than 100 mAh g^{-1}, and cost-effectiveness make the Na-enriched $Na_{1+x}Fe[Fe(CN)_6]$ a promising cathode for sodium-ion batteries.

Chapter 10 General conclusions and outlook

10.1 General conclusions

This doctoral work investigates some promising electrode materials for SIBs -phosphorus-based anode and Prussian blue analogue cathode material, aiming for high specific capacity and long cycling life. Through the simple and potentially large-scale ball milling method, the phosphorus and carbon composites and various phosphide compounds were synthesized as anode materials for SIBs. Through the facile chemical method, multifunctional PPy-coated $Na_{1.72}MnFe(CN)_6$ nanocomposite and Na-rich $Na_{1+x}FeFe(CN)_6$ with optimized structure were prepared as cathode materials for SIBs. Both the anode and the cathode composites combined with conductive carbon showed good cycling performance and excellent rate capability, due to highly enhanced electron or sodium ion transport within the electrode and buffering of the volume expansion by the carbon coating layer to extend the cycling life. The structurally optimized Prussian blue cathode showed improved electrochemical performance owing to its stable framework with a decreased amount of vacancies and coordinating water, and an increase in the amount of sodium ions per formula unit.

10.1.1 P-based anode materials

P/CNT composite was prepared by simply hand grinding commercial red P with carbon nanotubes. The P/CNT composite can be cycled reversibly, with an initial discharge capacity of 2210 mAh g^{-1}, and 76.6 % of the initial reversible capacity is still delivered after 10 cycles. CNTs play a crucial role in the reversibility of the commercial P/CNT composite. The network structure of the CNTs serves to effectively buffer the enormous stresses from the volume expansion of the P particles and reduces the rate of pulverization of particles. On the other hand, the CNT network provides pathways for electron transport, which is helpful for maintaining the connections not only between the red phosphorus particles, but also between the red phosphorus and the current collector. Our results suggest that the simply mixed commercial red phosphorus and CNTs would be a promising candidate for the next-generation anode material for sodium ion batteries with high capacity and low cost.

Red phosphorus and graphite composite was prepared by a facile and scalable ball-milling method. The SEM and TEM images show that the graphite was exfoliated into nanoplatelets through the shear forces during the milling process, and the small phosphorus particles were embedded in the graphite nanoplatelets. Moreover, the XPS results demonstrate the existence

of P-C bonds formed between the red phosphorus particles and the graphite nanoplates in the P/GnPs - 500 composite. This unique morphology and strong chemical bonding are responsible for the stable structure of the P/graphite composite. During the sodiation of P, the P-C bond plays a role in restraining the expansion of P particles. Moreover, even if the P particles are pulverized during the cycling, the red P particles can remain in contact with the graphite nanoplates, so that good electrical conductivity is retained. Therefore, the P/GnPs - 500 composite has excellent cycling stability (864 mAh g^{-1} over 100 cycles) and superior high rate capability, compared to that of the P/GnPs - 300 composite which does not have P-C bonds.

$Sn_{4+x}P_3$@(Sn+P) composite was synthesized in large quantities by direct low-speed ball milling of the P and Sn powders, and its electrochemical performance was studied as anode material for sodium ion batteries. The results demonstrated that the $Sn_{4+x}P_3$@(Sn+P) electrode using CMC binder delivered an initial discharge capacity of 1030 mAh g^{-1} and a reversible charge capacity of 892 mAh g^{-1}, at the current density of 100 mA g^{-1}. The addition of 5% FEC to the electrolyte can improve the cycling stability of the $Sn_{4+x}P_3$@(Sn+P) electrode, delivering a stable capacity of 465 mAh g^{-1}, with capacity retention of 92.6%, at the current density of 100 mA g^{-1} over 100 cycles. Moreover, the $Sn_{4+x}P_3$ electrode exhibited superior high rate capability, with a stable capacity of 165 mAh g^{-1} at the 10 C-rate (5000 mA g^{-1}). All the results indicate that $Sn_{4+x}P_3$@(Sn+P) would be a promising anode material candidate for sodium ion batteries with low cost, long cycling stability, and relatively good rate capability.

FeP and CoP were prepared in large quantities by direct low-speed ball milling of the P and Fe (Co) powders, and their electrochemical performances as anode materials for sodium ion batteries were studied. The FeP electrode delivered a high capacity of 764.7 mAh g^{-1} in sodium ion batteries. In addition, improvement of its cycling stability was also achieved by selecting appropriate binders and an appropriate additive to the electrolyte. CoP can deliver a large initial capacity of 770 mAh g^{-1}, and it shows lower voltage polarization. Moreover, a variety of techniques, including *ex-situ* XRD, *ex-situ* XPS, and TEM, were used to reveal the sodium storage mechanism of FeP and CoP. All the results indicate that FeP and CoP would be promising anode material candidates for sodium ion batteries with low cost and long cycling stability.

10.1.2 Prussian Blue cathode materials

A composite of NMHFC and PPy doped with ClO_4^- was prepared through a simple, energy-saving, and one-step soft chemistry method, which utilizes the intrinsic oxidation of NMHFC to polymerize the pyrrole in the presence of ClO_4^-. PPy plays four important roles in the electrochemical performance of the NMHFC@PPy composite: (1) PPy as conducting polymer increases the electronic conductivity of NMHFC to enhance the rate capability. (2) PPy doped with ClO_4^- can offer redox sites to increase the capacity of the composite. (3) The PPy coating functions as a protective layer to reduce the dissolution of Mn in the NMHFC, improving the cycling performance. (4) The polymerization of PPy can lead to additional Na insertion into NMHFC due to the reduction of Mn^{III}, which is also good for improving reversible capacity. Therefore, the NMHFC@PPy composite could be a next-generation low-cost cathode material with excellent rate capability and good cycling performance, with capacity retention of 67% after 200 cycles.

Na-enriched $Na_{1+x}Fe[Fe(CN)_6]$ was prepared through a facile and one-step method using $Na_4Fe(CN)_6$ as the precursor in highly concentrated NaCl solutions. With increasing sodium ions entering into the framework, the amount of vacancies and coordinating water in the $Na_{1+x}Fe[Fe(CN)_6]$ decreased, resulting in enhanced structural stability. Thus, the Na-enriched $Na_{1+x}Fe[Fe(CN)_6]$ showed superior cycling performance with excellent capacity retention of 97% over 400 cycles. The simple synthesis method, superior cycling stability with a high capacity of more than 100 mAh g^{-1}, and cost-effectiveness make the Na-enriched $Na_{1+x}Fe[Fe(CN)_6]$ a promising cathode for sodium-ion batteries.

10.2 Outlook

This doctoral work mainly focused on facile synthesis approaches to P-based anode materials and Prussian blue cathode materials, and on characterising their electrochemical performance in SIBs. The studied anode and cathode materials all possess outstanding advantages of non-toxicity, high specific capacity, and low-cost, making them promising electrode candidates for SIBs. The synthesis methods utilized in this doctoral work are just simple ball milling and co-precipitation. The morphologies of the materials prepared by these methods are not good. Furthermore, special morphologies (1D, 3D) of these electrode materials can be attained through using other approaches, such as the hydrothermal method, electrospinning, spray drying, etc.

To improve the cycling performance of electrode materials in SIBs, the main strategies used in this doctoral work was to form alloy compounds or composites with carbon. The

shortcoming of this strategy is that inactive carbon and metal materials are introduced, reducing the total specific capacity of the electrodes. Therefore, in future work, we should focus on optimizing the structure of Prussian blue cathode materials through doping with other transition metal elements.

In addition, researchers have been focusing most of their attention on the electrochemical performance of the electrode materials and trying their best to improve the electrochemical performance through various methods. Little attention, however, has been given to the safety properties of the electrode materials. It is worth noting that safety is a key parameter for commercial energy storage batteries. It is usual to evaluate the thermal stability of the materials to determine the safety of cells. Therefore, further research will give more attention to the safety issues related to the P-based and Prussian blue electrode materials through conducting accelerating-rate calorimeter (ARC) tests.

References

[1]. J. Qian, X. Wu, Y. Cao, X. Ai, H. Yang, Angewandte Chemie International Edition, 52 (2013) 4633-4636.

[2]. Y. Zhu, Y. Wen, X. Fan, T. Gao, F. Han, C. Luo, S. C. Liou, C. Wang, ACS Nano, 9 (2015) 3254-3264.

[3]. J. Song, Z. Yu, M. L. Gordin, S. Hu, R. Yi, D. Tang, T. Walter, M. Regula, D. Choi, X. Li, A. Manivannan, D. Wang, Nano Letters, 14 (2014) 6329-6335.

[4]. K. M. M. Kozlovsky Y., Biophysical Journal, 82 (2002) 882-895.

[5]. H. Chen, T. N. Cong, W. Yang, C. Tan, Y. Li, Y. Ding, Progress in Natural Science, 19 (2009) 291-312.

[6]. Z. Haihua, T. Bhattacharya, T. Duong, T. S. T. Siew, A. M. Khambadkone, Power Electronics, IEEE Transactions on, 26 (2011) 923-930.

[7]. A. Sari, K. Kaygusuz, Solar Energy, 71 (2001) 365-376.

[8]. L. Wei, G. Joos In Power Electronics Specialists Conference, 2008 PESC 2008 IEEE 2008, 1762-1768.

[9]. K. Yoshimoto, T. Nanahara, G. Koshimizu In Power Systems Conference and Exposition, 2006 PSCE 2006 IEEE PES 2006, 1244-1251.

[10]. K. C. Divya, J. Østergaard, Electric Power Systems Research, 79 (2009) 511-520.

[11]. P. F. Ribeiro, B. K. Johnson, M. L. Crow, A. Arsoy, Y. Liu, Proceedings of the IEEE, 89 (2001) 1744-1756.

[12]. M. Bragard, N. Soltau, S. Thomas, R. W. De Doncker, Power Electronics, IEEE Transactions on, 25 (2010) 3049-3056.

[13]. S. Teleke, M. E. Baran, S. Bhattacharya, A. Q. Huang, Energy Conversion, IEEE Transactions on, 25 (2010) 787-794.

[14]. L. Lu, X. Han, J. Li, J. Hua, M. Ouyang, Journal of Power Sources, 226 (2013) 272-288.

[15]. J. Y. Song, Y. Y. Wang, C. C. Wan, Journal of Power Sources, 77 (1999) 183-197.

[16]. S. S. Zhang, Journal of Power Sources, 162 (2006) 1379-1394.

[17]. C. de las Casas, W. Li, Journal of Power Sources, 208 (2012) 74-85.

[18]. W. J. Zhang, Journal of Power Sources, 196 (2011) 13-24.

[19]. V. Etacheri, R. Marom, R. Elazari, G. Salitra, D. Aurbach, Energy & Environmental Science, 4 (2011) 3243-3262.

[20]. D. Aurbach, Journal of Power Sources, 89 (2000) 206-218.

[21]. B. Scrosati, Electrochimica Acta, 45 (2000) 2461-2466.

[22]. J. M. Tarascon, M. Armand, Nature, 414 (2001) 359-367.

[23]. R. Malini, U. Uma, T. Sheela, M. Ganesan, N. G. Renganathan, Ionics, 15 (2009) 301-307.

[24]. Y. Wang, G. Cao, Advanced Materials, 20 (2008) 2251-2269.

[25]. D. Doerffel, S. A. Sharkh, Journal of Power Sources, 155 (2006) 395-400.

[26]. A. D. Robertson, A. R. West, A. G. Ritchie, Solid State Ionics, 104 (1997) 1-11.

[27]. D. K. Kim, P. Muralidharan, H. W. Lee, R. Ruffo, Y. Yang, C. K. Chan, H. Peng, R. A. Huggins, Y. Cui, Nano Letters, 8 (2008) 3948-3952.

[28]. J. W. Fergus, Journal of Power Sources, 195 (2010) 939-954.

[29]. J. Xu, H. R. Thomas, R. W. Francis, K. R. Lum, J. Wang, B. Liang, Journal of Power Sources, 177 (2008) 512-527.

[30]. A. Barré, B. Deguilhem, S. Grolleau, M. Gérard, F. Suard, D. Riu, Journal of Power Sources, 241 (2013) 680-689.

[31]. Z. S. Wu, W. Ren, L. Wen, L. Gao, J. Zhao, Z. Chen, G. Zhou, F. Li, H. M. Cheng, ACS Nano, 4 (2010) 3187-3194.

[32]. P. Verma, P. Maire, P. Novák, Electrochimica Acta, 55 (2010) 6332-6341.

[33]. E. Yoo, J. Kim, E. Hosono, H. S. Zhou, T. Kudo, I. Honma, Nano Letters, 8 (2008) 2277-2282.

[34]. G. Zhou, D. W. Wang, F. Li, L. Zhang, N. Li, Z. S. Wu, L. Wen, G. Q. Lu, H. M. Cheng, Chemistry of Materials, 22 (2010) 5306-5313.

[35]. S. S. Zhang, Journal of Power Sources, 164 (2007) 351-364.

[36]. G. Kucinskis, G. Bajars, J. Kleperis, Journal of Power Sources, 240 (2013) 66-79.

[37]. H. Wang, L. F. Cui, Y. Yang, H. Sanchez Casalongue, J. T. Robinson, Y. Liang, Y. Cui, H. Dai, Journal of the American Chemical Society, 132 (2010) 13978-13980.

[38]. J. Liu, H. Xia, D. Xue, L. Lu, Journal of the American Chemical Society, 131 (2009) 12086-12087.

[39]. J. K. Kim, Y. Kim, S. Park, H. Ko, Y. Kim, Energy & Environmental Science, (2015)

[40]. E. Yang, H. Ji, Y. Jung, The Journal of Physical Chemistry C, (2015)

[41]. J. Song, Z. Yu, M. L. Gordin, X. Li, H. Peng, D. Wang, ACS Nano, (2015)

[42]. Z. Yuan, L. Si, X. Zhu, Journal of Materials Chemistry A, (2015)

[43]. S. W. Kim, D. H. Seo, X. Ma, G. Ceder, K. Kang, Advanced Energy Materials, 2 (2012) 710-721.

[44]. M. D. Slater, D. Kim, E. Lee, C. S. Johnson, Advanced Functional Materials, 23 (2013) 947-958.

[45]. Y. Cao, L. Xiao, M. L. Sushko, W. Wang, B. Schwenzer, J. Xiao, Z. Nie, L. V. Saraf, Z. Yang, J. Liu, Nano Letters, 12 (2012) 3783-3787.

[46]. S. Komaba, N. Yabuuchi, T. Nakayama, A. Ogata, T. Ishikawa, I. Nakai, Inorganic Chemistry, 51 (2012) 6211-6220.

[47]. L. David, R. Bhandavat, G. Singh, ACS Nano, 8 (2014) 1759-1770.

[48]. S. P. Ong, V. L. Chevrier, G. Hautier, A. Jain, C. Moore, S. Kim, X. Ma, G. Ceder, Energy & Environmental Science, 4 (2011) 3680-3688.

[49]. S. Tepavcevic, H. Xiong, V. R. Stamenkovic, X. Zuo, M. Balasubramanian, V. B. Prakapenka, C. S. Johnson, T. Rajh, ACS Nano, 6 (2012) 530-538.

[50]. V. Palomares, P. Serras, I. Villaluenga, K. B. Hueso, J. Carretero-Gonzalez, T. Rojo, Energy & Environmental Science, 5 (2012) 5884-5901.

[51]. P. Barpanda, G. Liu, C. D. Ling, M. Tamaru, M. Avdeev, S.-C. Chung, Y. Yamada, A. Yamada, Chemistry of Materials, 25 (2013) 3480-3487.

[52]. P. R. Abel, Y. M. Lin, T. de Souza, C. Y. Chou, A. Gupta, J. B. Goodenough, G. S. Hwang, A. Heller, C. B. Mullins, The Journal of Physical Chemistry C, 117 (2013) 18885-18890.

[53]. Y. Shao, J. Xiao, W. Wang, M. Engelhard, X. Chen, Z. Nie, M. Gu, L. V. Saraf, G. Exarhos, J. G. Zhang, J. Liu, Nano Letters, 13 (2013) 3909-3914.

[54]. Y. U. Park, D. H. Seo, H. S. Kwon, B. Kim, J. Kim, H. Kim, I. Kim, H. I. Yoo, K. Kang, Journal of the American Chemical Society, 135 (2013) 13870-13878.

[55]. X. Han, Y. Liu, Z. Jia, Y. C. Chen, J. Wan, N. Weadock, K. J. Gaskell, T. Li, L. Hu, Nano Letters, 14 (2014) 139-147.

[56]. J. J. Ding, Y. N. Zhou, Q. Sun, X. Q. Yu, X. Q. Yang, Z. W. Fu, Electrochimica Acta, 87 (2013) 388-393.

[57]. History of Batteries: A Timeline, 2014, www.upsbatterycenter.com/blog/history-batteries-timeline.

[58]. J. R. D. D.A.Stevens, Journal of the Electrochemical Society, 147 (2000) 1271-1273.

[59]. K. Matsuki, K. Ozawa In *Lithium Ion Rechargeable Batteries*; Wiley-VCH Verlag GmbH & Co. KGaA: 2010, 1-9.

[60]. N. Yabuuchi, K. Kubota, M. Dahbi, S. Komaba, Chemical Reviews, 114 (2014) 11636-11682.

[61]. L. Zhao, J. Zhao, Y. S. Hu, H. Li, Z. Zhou, M. Armand, L. Chen, Advanced Energy Materials, 2 (2012) 962-965.

[62]. Y. Zhu, X. Han, Y. Xu, Y. Liu, S. Zheng, K. Xu, L. Hu, C. Wang, ACS Nano, 7 (2013) 6378-6386.

[63]. H. Zhuo, X. Wang, A. Tang, Z. Liu, S. Gamboa, P. J. Sebastian, Journal of Power Sources, 160 (2006) 698-703.

[64]. X. Wu, Y. Cao, X. Ai, J. Qian, H. Yang, Electrochemistry Communications, 31 (2013) 145-148.

[65]. B. Qu, C. Ma, G. Ji, C. Xu, J. Xu, Y. S. Meng, T. Wang, J. Y. Lee, Advanced Materials, 26 (2014) 3854-3859.

[66]. J. Ding, H. Wang, Z. Li, A. Kohandehghan, K. Cui, Z. Xu, B. Zahiri, X. Tan, E. M. Lotfabad, B. C. Olsen, D. Mitlin, ACS Nano, 7 (2013) 11004-11015.

[67]. Y. Cao, L. Xiao, W. Wang, D. Choi, Z. Nie, J. Yu, L. V. Saraf, Z. Yang, J. Liu, Advanced Materials, 23 (2011) 3155-3160.

[68]. S. Wenzel, T. Hara, J. Janek, P. Adelhelm, Energy & Environmental Science, 4 (2011) 3342-3345.

[69]. R. Alcántara, M. Jaraba, P. Lavela, J. L. Tirado, Chemistry of Materials, 14 (2002) 2847-2848.

[70]. Y. Xu, Y. Zhu, Y. Liu, C. Wang, Advanced Energy Materials, 3 (2013) 128-133.

[71]. H. Xiong, M. D. Slater, M. Balasubramanian, C. S. Johnson, T. Rajh, The Journal of Physical Chemistry Letters, 2 (2011) 2560-2565.

[72]. A. Kitajou, H. Komatsu, K. Chihara, I. D. Gocheva, S. Okada, J. Yamaki, Journal of Power Sources, 198 (2012) 389-392.

[73]. Z. Jian, L. Zhao, H. Pan, Y. S. Hu, H. Li, W. Chen, L. Chen, Electrochemistry Communications, 14 (2012) 86-89.

[74]. C. Luo, Y. Zhu, Y. Xu, Y. Liu, T. Gao, J. Wang, C. Wang, Journal of Power Sources, 250 (2014) 372-378.

[75]. J. F. Whitacre, A. Tevar, S. Sharma, Electrochemistry Communications, 12 (2010) 463-466.

[76]. Y. Kim, K. H. Ha, S. M. Oh, K. T. Lee, Chemistry, 20 (2014) 11980-11992.

[77]. H. Buqa, M. Holzapfel, F. Krumeich, C. Veit, P. Novak, Journal of Power Sources, 161 (2006) 617-622.

[78]. A. Magasinski, B. Zdyrko, I. Kovalenko, B. Hertzberg, R. Burtovyy, C. F. Huebner, T. F. Fuller, I. Luzinov, G. Yushin, Acs Applied Materials & Interfaces, 2 (2010) 3004-3010.

[79]. I. Kovalenko, B. Zdyrko, A. Magasinski, B. Hertzberg, Z. Milicev, R. Burtovyy, I. Luzinov, G. Yushin, Science, 334 (2011) 75-79.

[80]. J. S. Bridel, T. Azais, M. Morcrette, J. M. Tarascon, D. Larcher, Chemistry of Materials, 22 (2009) 1229-1241.

[81]. J. Li, R. Lewis, J. Dahn, Electrochemical and Solid-State Letters, 10 (2007) A17-A20.

[82]. J. S. Bridel, T. Aza ïs, M. Morcrette, J. M. Tarascon, D. Larcher, Chemistry of Materials, 22 (2010) 1229-1241.

[83]. J. Li, R. B. Lewis, J. R. Dahn, Electrochemical and Solid State Letters, 10 (2007) A17-A20.

[84]. Z. L. Wang, N. Dupre, A. C. Gaillot, B. Lestriez, J. F. Martin, L. Daniel, S. Patoux, D. Guyomard, Electrochimica Acta, 62 (2012) 77-83.

[85]. T. Li, J. Y. Yang, S. G. Lu, International Journal of Minerals Metallurgy and Materials, 19 (2012) 752-756.

[86]. S. Komaba, K. Shimomura, N. Yabuuchi, T. Ozeki, H. Yui, K. Konno, Journal of Physical Chemistry C, 115 (2011) 13487-13495.

[87]. B. R. Lee, E. S. Oh, Journal of Physical Chemistry C, 117 (2013) 4404-4409.

[88]. H. Buqa, M. Holzapfel, F. Krumeich, C. Veit, P. Nov åk, Journal of Power Sources, 161 (2006) 617-622.

[89]. C. C. Li, Y. W. Wang, Journal of Power Sources, 227 (2013) 204-210.

[90]. B. Koo, H. Kim, Y. Cho, K. T. Lee, N. S. Choi, J. Cho, Angewandte Chemie International Edition, 51 (2012) 8762-8767.

[91]. S. Rasanen, M. Karppinen, Thermochimica Acta, 547 (2012) 126-129.

[92]. H. K. Park, B. S. Kong, E. S. Oh, Electrochemistry Communications, 13 (2011) 1051-1053.

[93]. D. Larcher, J. M. Tarascon, Nature Chemistry, 7 (2014) 19-29.

[94]. F. C. Delmas. C., Hagenmuller P., Physica, 99B (1980) 81.

[95]. H. Pan, Y. S. Hu, L. Chen, Energy & Environmental Science, 6 (2013) 2338.

[96]. L. Mu, S. Xu, Y. Li, Y. S. Hu, H. Li, L. Chen, X. Huang, Advanced Materials, (2015) n/a-n/a.

[97]. X. Li, D. Wu, Y. N. Zhou, L. Liu, X. Q. Yang, G. Ceder, Electrochemistry Communications, 49 (2014) 51-54.

[98]. N. Yabuuchi, M. Kajiyama, J. Iwatate, H. Nishikawa, S. Hitomi, R. Okuyama, R. Usui, Y. Yamada, S. Komaba, Nature Materials, 11 (2012) 512-517.

[99]. I. Hasa, D. Buchholz, S. Passerini, B. Scrosati, J. Hassoun, Advanced Energy Materials, 4 (2014) 1400083.

[100]. M. H. Han, E. Gonzalo, M. Casas-Cabanas, T. Rojo, Journal of Power Sources, 258 (2014) 266-271.

[101]. S. Komaba, N. Yabuuchi, T. Nakayama, A. Ogata, T. Ishikawa, I. Nakai, Inorganic Chemistry, 51 (2012) 6211-6220.

[102]. Y. N. Zhou, J. J. Ding, K. W. Nam, X. Yu, S. M. Bak, E. Hu, J. Liu, J. Bai, H. Li, Z. W. Fu, X. Q. Yang, Journal of Materials Chemistry A, 1 (2013) 11130.

[103]. J. L. Yue, Y. N. Zhou, X. Yu, S. M. Bak, X. Q. Yang, Z. W. Fu, Chemical Communications, 51 (2015) 15712.

[104]. H. Liu, J. Xu, C. Ma, Y. S. Meng, Chemical Communications, 51 (2015) 4693-4696.

[105]. S. M. Oh, S. T. Myung, J. Y. Hwang, B. Scrosati, K. Amine, Y. K. Sun, Chemistry of Materials, 26 (2014) 6165-6171.

[106]. G. Herzog, P. Eichelmann-Daly, D. W. M. Arrigan, Electrochemistry Communications, 12 (2010) 335-337.

[107]. P. Vassilaras, X. Ma, X. Li, G. Ceder, Journal of the Electrochemical Society, 160 (2012) A207-A211.

[108]. X. Ma, H. Chen, G. Ceder, Journal of The Electrochemical Society, 158 (2011) A1307.

[109]. M. Guignard, C. Didier, J. Darriet, P. Bordet, E. Elkaim, C. Delmas, Nature Materials, 12 (2013) 74-80.

[110]. Z. Lu, J. R. Dahn, Journal of The Electrochemical Society, 148 (2001) A710.

[111]. D. Carlier, J. H. Cheng, R. Berthelot, M. Guignard, M. Yoncheva, R. Stoyanova, B. J. Hwang, C. Delmas, Dalton Transactions, 40 (2011) 9306-9312.

[112]. H. Yoshida, N. Yabuuchi, S. Komaba, Electrochemistry Communications, 34 (2013) 60-63.

[113]. D. Kim, E. Lee, M. Slater, W. Lu, S. Rood, C. S. Johnson, Electrochemistry Communications, 18 (2012) 66-69.

[114]. M. Sathiya, K. Hemalatha, K. Ramesha, J. M. Tarascon, A. S. Prakash, Chemistry of Materials, 24 (2012) 1846-1853.

[115]. H. Yu, S. Guo, Y. Zhu, M. Ishida, H. Zhou, Chemical Communications, 50 (2014) 457-459.

[116]. D. Kim, S. H. Kang, M. Slater, S. Rood, J. T. Vaughey, N. Karan, M. Balasubramanian, C. S. Johnson, Advanced Energy Materials, 1 (2011) 333-336.

[117]. N. Yabuuchi, M. Yano, H. Yoshida, S. Kuze, S. Komaba, Journal of the Electrochemical Society, 160 (2013) A3131-A3137.

[118]. D. Yuan, X. Hu, J. Qian, F. Pei, F. Wu, R. Mao, X. Ai, H. Yang, Y. Cao, Electrochimica Acta, 116 (2014) 300-305.

[119]. E. Lee, J. Lu, Y. Ren, X. Luo, X. Zhang, J. Wen, D. Miller, A. DeWahl, S. Hackney, B. Key, D. Kim, M. D. Slater, C. S. Johnson, Advanced Energy Materials, 4 (2014) 1400458.

[120]. Y. Lei, X. Li, L. Liu, G. Ceder, Chemistry of Materials, 26 (2014) 5288-5296.

[121]. J. Xu, D. H. Lee, R. J. Clément, X. Yu, M. Leskes, A. J. Pell, G. Pintacuda, X.-Q. Yang, C. P. Grey, Y. S. Meng, Chemistry of Materials, 26 (2014) 1260-1269.

[122]. X. Wang, M. Tamaru, M. Okubo, A. Yamada, The Journal of Physical Chemistry C, 117 (2013) 15545-15551.

[123]. D. Yuan, W. He, F. Pei, F. Wu, Y. Wu, J. Qian, Y. Cao, X. Ai, H. Yang, Journal of Materials Chemistry A, 1 (2013) 3895.

[124]. X. Sun, Y. Jin, C. Y. Zhang, J. W. Wen, Y. Shao, Y. Zang, C. H. Chen, J Materials Chemistry A, 2 (2014) 17268-17271.

[125]. R. Kataoka, T. Mukai, A. Yoshizawa, T. Sakai, Journal of the Electrochemical Society, 160 (2013) A933-A939.

[126]. D. Buchholz, A. Moretti, R. Kloepsch, S. Nowak, V. Siozios, M. Winter, S. Passerini, Chemistry of Materials, 25 (2013) 142-148.

[127]. S. Guo, P. Liu, Y. Sun, K. Zhu, J. Yi, M. Chen, M. Ishida, H. Zhou, Angewandte Chemie International Edition, 54 (2015) 1-6.

[128]. X. Xu, S. Ji, R. Gao, J. Liu, RSC Advances, 5 (2015) 51454-51460.

[129]. E. Talaie, V. Duffort, H. L. Smith, B. Fultz, L. F. Nazar, Energy & Environmental Science, 8 (2015) 2512-2523.

[130]. R. O. J. P. Parent, M. Devalett, C. Fouassie, P. Hagenmul, Journal of Solid State Chemistry, 3 (1971) 1.

[131]. S. Xu, Y. Wang, L. Ben, Y. Lyu, N. Song, Z. Yang, Y. Li, L. Mu, H. T. Yang, L. Gu, Y. S. Hu, H. Li, Z. H. Cheng, L. Chen, X. Huang, Advanced Energy Materials, (2015) 1501156.

[132]. Y. Wang, J. Liu, B. Lee, R. Qiao, Z, Yang, S. Xu, X. Yu, L. Gu, Y. Hu, W. Yang, K. Kang, H. Li, X. Yang, L. Chen, X. Huang, Nature Commication, 6 (2015), 6401.

[133]. K. Zaghib, J. Trottier, P. Hovington, F. Brochu, A. Guerfi, A. Mauger, C. M. Julien, Journal of Power Sources, 196 (2011) 9612-9617.

[134]. J. Kim, D. H. Seo, H. Kim, I. Park, J. K. Yoo, S. K. Jung, Y. U. Park, W. A. Goddard Iii, K. Kang, Energy & Environmental Science, 8 (2015) 540-545.

[135]. Z. Jian, Y. Sun, X. Ji, Chemical Communications, 51 (2015) 6381-6383.

[136]. Z. Jian, W. Han, Y. Liang, Y. Lan, Z. Fang, Y.-S. Hu, Y. Yao, Journal of Materials Chemistry A, 2 (2014) 20231-20236.

[137]. W. Duan, Z. Zhu, H. Li, Z. Hu, K. Zhang, F. Cheng, J. Chen, Journal of Materials Chemistry A, 2 (2014) 8668-8675.

[138]. J. Liu, K. Tang, K. Song, P. A. van Aken, Y. Yu, J. Maier, Nanoscale, 6 (2014) 5081-5086.

[139]. J. N. Chotard, G. Rousse, R. David, O. Mentré, M. Courty, C. Masquelier, Chemistry of Materials, 27 (2015) 5982-5987.

[140]. J. Mao, C. Luo, T. Gao, X. Fan, C. Wang, Journal of Materials Chemistry A, 3 (2015) 10378-10385.

[141]. Z. Jian, V. Raju, Z. Li, Z. Xing, Y. S. Hu, X. Ji, Advanced Functional Materials, 25 (2015) 5778-5785.

[142]. P. Barpanda, T. Ye, S. Nishimura, S. C. Chung, Y. Yamada, M. Okubo, H. Zhou, A. Yamada, Electrochemistry Communications, 24 (2012) 116-119.

[143]. P. Barpanda, T. Ye, M. Avdeev, S. C. Chung, A. Yamada, Journal of Materials Chemistry A, 1 (2013) 4194.

[144]. C. S. Park, H. Kim, R. A. Shakoor, E. Yang, S. Y. Lim, R. Kahraman, Y. Jung, J. W. Choi, Journal of the American Chemical Society, 135 (2013) 2787-2792.

[145]. J. M. Clark, P. Barpanda, A. Yamada, M. S. Islam, Journal of Materials Chemistry A, 2 (2014) 11807-11812.

[146]. P. Barpanda, T. Ye, M. Avdeev, S. C. Chung, A. Yamada, Journal of Materials Chemistry A, 1 (2013) 4194-4197.

[147]. C. P. F. Sanz, J.M. Rojo, C. Ruiz-Valero, Chemistry of Materials, 13 (2001) 1334-1340.

[148]. B. L. Ellis, W. R. M. Makahnouk, W. N. Rowan-Weetaluktuk, D. H. Ryan, L. F. Nazar, Chemistry of Materials, 22 (2010) 1059-1070.

[149]. R. Tripathi, S. M. Wood, M. S. Islam, L. F. Nazar, Energy & Environmental Science, 6 (2013) 2257.

[150]. X. Wu, J. Zheng, Z. Gong, Y. Yang, Journal of Materials Chemistry, 21 (2011) 18630.

[151]. R. A. Shakoor, D. H. Seo, H. Kim, Y. U. Park, J. Kim, S. W. Kim, H. Gwon, S. Lee, K. Kang, Journal of Materials Chemistry, 22 (2012) 20535.

[152]. Z. Liu, Y. Y. Hu, M. T. Dunstan, H. Huo, X. Hao, H. Zou, G. Zhong, Y. Yang, C. P. Grey, Chemistry of Materials, 26 (2014) 2513-2521.

[153]. M. Bianchini, F. Fauth, N. Brisset, F. Weill, E. Suard, C. Masquelier, L. Croguennec, Chemistry of Materials, 27 (2015) 3009-3020.

[154]. P. V. Serras P., Goni A., Muro I.G., Kubiak P., Lezama L., Rojo T., Journal of Materials Chemistry, 22 (2012) 22301.

[155]. N. Sharma, P. Serras, V. Palomares, H. E. A. Brand, J. Alonso, P. Kubiak, M. L. Fdez-Gubieda, T. Rojo, Chemistry of Materials, 26 (2014) 3391-3402.

[156]. J. Zhao, L. Mu, Y. Qi, Y. S. Hu, H. Liu, S. Dai, Chemical Communications, 51 (2015) 7160-7163.

[157]. Y. U. Park, D. H. Seo, H. S. Kwon, B. Kim, J. Kim, H. Kim, I. Kim, H. I. Yoo, K. Kang, Journal of the American Chemical Society, 135 (2013) 13870-13878.

[158]. Y. Kawabe, N. Yabuuchi, M. Kajiyama, N. Fukuhara, T. Inamasu, R. Okuyama, I. Nakai, S. Komaba, Electrochemistry Communications, 13 (2011) 1225-1228.

[159]. K. Kubota, K. Yokoh, N. Yabuuchi, S. Komaba, Electrochemistry, 82 (2014) 909-911.

[160]. H. Zou, S. Li, X. Wu, M. J. McDonald, Y. Yang, ECS Electrochemistry Letters, 4 (2015) A53-A55.

[161]. P. Singh, K. Shiva, H. Celio, J. B. Goodenough, Energy & Environmental Science, 8 (2015) 3000-3005.

[162]. C. Li, L. Gu, S. Tsukimoto, P. A. van Aken, J. Maier, Advaned Materials, 22 (2010) 3650-3654.

[163]. L. Li, F. Meng, S. Jin, Nano Letters, 12 (2012) 6030-6037.

[164]. S. W. Kim, D. H. Seo, H. Gwon, J. Kim, K. Kang, Advanced Materials, 22 (2010) 5260-5264.

[165]. F. Badway, F. Cosandey, N. Pereira, G. G. Amatucci, Journal of The Electrochemical Society, 150 (2003) A1318.

[166]. D. Ma, H. Wang, Y. Li, D. Xu, S. Yuan, X. Huang, X. Zhang, Y. Zhang, Nano Energy, 10 (2014) 295-304.

[167]. I. D. Gocheva, M. Nishijima, T. Doi, S. Okada, J. Yamaki, T. Nishida, Journal of Power Sources, 187 (2009) 247-252.

[168]. M. Nishijima, I. D. Gocheva, S. Okada, T. Doi, J. Yamaki, T. Nishida, Journal of Power Sources, 190 (2009) 558-562.

[169]. Y. Lu, L. Wang, J. Cheng, J. B. Goodenough, Chemical Communications, 48 (2012) 6544-6546.

[170]. C. D. Wessells, R. A. Huggins, Y. Cui, Nature Communications, 2 (2011) 550.

[171]. C. D. Wessells, S. V. Peddada, R. A. Huggins, Y. Cui, Nano Letters, 11 (2011) 5421-5425.

[172]. H. Lee, Y. I. Kim, J. K. Park, J. W. Choi, Chemical Communications, 48 (2012) 8416-8418.

[173]. T. Matsuda, M. Takachi, Y. Moritomo, Chemical Communications, 49 (2013) 2750-2752.

[174]. L. Wang, Y. Lu, J. Liu, M. Xu, J. Cheng, D. Zhang, J. B. Goodenough, Angewandte Chemie International Edition, 52 (2013) 1964-1967.

[175]. J. Qian, M. Zhou, Y. Cao, X. Ai, H. Yang, Advanced Energy Materials, 2 (2012) 410-414.

[176]. Y. You, X. L. Wu, Y. X. Yin, Y. G. Guo, Energy & Environmental Science, 7 (2014) 1643.

[177]. Y. Yue, A. J. Binder, B. Guo, Z. Zhang, Z. A. Qiao, C. Tian, S. Dai, Angewandte Chemie International Edition, 53 (2014) 3134-3137.

[178]. H. W. Lee, R. Y. Wang, M. Pasta, S. Woo Lee, N. Liu, Y. Cui, Nature Communications, 5 (2014) 5280.

[179]. Y. You, X. L. Wu, Y. X. Yin, Y. G. Guo, Journal of Materials Chemistry A, 1 (2013) 14061.

[180]. D. Asakura, M. Okubo, Y. Mizuno, T. Kudo, H. Zhou, K. Ikedo, T. Mizokawa, A. Okazawa, N. Kojima, The Journal of Physical Chemistry C, 116 (2012) 8364-8369.

[181]. X. Wu, W. Deng, J. Qian, Y. Cao, X. Ai, H. Yang, Journal of Materials Chemistry A, 1 (2013) 10130.

[182]. J. Song, L. Wang, Y. Lu, J. Liu, B. Guo, P. Xiao, J. J. Lee, X. Q. Yang, G. Henkelman, J. B. Goodenough, Journal of the American Chemical Society, 137 (2015) 2658-2664.

[183]. K. M. P. Novak, K.S.V.Santhanam, O.Haas, Chemical Reviews, 97 (1997) 207-282.

[184]. H. Chen, M. Armand, G. Demailly, F. Dolhem, P. Poizot, J. M. Tarascon, ChemSusChem, 1 (2008) 348-355.

[185]. P. Poizot, F. Dolhem, Energy & Environmental Science, 4 (2011) 2003.

[186]. Z. Song, H. Zhou, Energy & Environmental Science, 6 (2013) 2280.

[187]. Y. Liang, Z. Tao, J. Chen, Advanced Energy Materials, 2 (2012) 742-769.

[188]. S. O. H.Tsutsumi, T. Oishi, Electrochimica Acta, 43 (1998) 427-429.

[189]. L. Nyholm, G. Nystrom, A. Mihranyan, M. Stromme, Advanced Materials, 23 (2011) 3751-3769.

[190]. M. Armand, S. Grugeon, H. Vezin, S. Laruelle, P. Ribiere, P. Poizot, J. M. Tarascon, Nature Materials, 8 (2009) 120-125.

[191]. S. G. W. Walker, O. Mentre, S. Laruelle, J. M. Tarascon, F. Wudl, Journal of the American Chemical Society, 132 (2010) 6517-6523.

[192]. S. Wang, L. Wang, K. Zhang, Z. Zhu, Z. Tao, J. Chen, Nano Letters, 13 (2013) 4404-4409.

[193]. W. Huang, Z. Zhu, L. Wang, S. Wang, H. Li, Z. Tao, J. Shi, L. Guan, J. Chen, Angewandte Chemie International Edition, 52 (2013) 9162-9166.

[194]. Z. Zhu, M. Hong, D. Guo, J. Shi, Z. Tao, J. Chen, Journal of the American Chemical Society, 136 (2014) 16461-16464.

[195]. Y. Park, D. S. Shin, S. H. Woo, N. S. Choi, K. H. Shin, S. M. Oh, K. T. Lee, S. Y. Hong, Advanced Materials, 24 (2012) 3562-3567.

[196]. K. Zhang, C. Guo, Q. Zhao, Z. Niu, J. Chen, Advanced Science, 2 (2015) n/a-n/a.

[197]. A. Abouimrane, W. Weng, H. Eltayeb, Y. Cui, J. Niklas, O. Poluektov, K. Amine, Energy & Environmental Science, 5 (2012) 9632.

[198]. S. Zhang, W. Huang, P. Hu, C. Huang, C. Shang, C. Zhang, R. Yang, G. Cui, Journal of Material Chemistry A, 3 (2015) 1896-1901.

[199]. C. Wang, Y. Xu, Y. Fang, M. Zhou, L. Liang, S. Singh, H. Zhao, A. Schober, Y. Lei, Journal of the American Chemical Society, 137 (2015) 3124-3130.

[200]. W. Luo, M. Allen, V. Raju, X. Ji, Advanced Energy Materials, 4 (2014) n/a-n/a.

[201]. S. Y. H. G. Wang, D. L. Ma, X. L. Huang, F. Meng, X. Zhang, Advanced Energy Materials, 4 (2014) 1301651.

[202]. J. Hong, M. Lee, B. Lee, D. H. Seo, C. B. Park, K. Kang, Nature Communications, 5 (2014) 5335.

[203]. L. Zhu, Y. Shen, M. Sun, J. Qian, Y. Cao, X. Ai, H. Yang, Chemical Communications, 49 (2013) 11370-11372.

[204]. T. Nokami, T. Matsuo, Y. Inatomi, N. Hojo, T. Tsukagoshi, H. Yoshizawa, A. Shimizu, H. Kuramoto, K. Komae, H. Tsuyama, J. Yoshida, Journal of the American Chemical Society, 134 (2012) 19694-19700.

[205]. B. Genorio, K. Pirnat, R. Cerc-Korosec, R. Dominko, M. Gaberscek, Angewandte Chemie International Edition, 49 (2010) 7222-7224.

[206]. M. Dahbi, N. Yabuuchi, K. Kubota, K. Tokiwa, S. Komaba, Physical Chemistry Chemical Physics, 16 (2014) 15007-15028.

[207]. G. Schmuelling, T. Placke, R. Kloepsch, O. Fromm, H. W. Meyer, S. Passerini, M. Winter, Journal of Power Sources, 239 (2013) 563-571.

[208]. K. Nobuhara, H. Nakayama, M. Nose, S. Nakanishi, H. Iba, Journal of Power Sources, 243 (2013) 585-587.

[209]. B. Jache, P. Adelhelm, Angewandte Chemie International Edition, 53 (2014) 10169-10173.

[210]. Y. X. Wang, S. L. Chou, H. K. Liu, S. X. Dou, Carbon, 57 (2013) 202-208.

[211]. K. Tang, L. Fu, R. J. White, L. Yu, M. M. Titirici, M. Antonietti, J. Maier, Advanced Energy Materials, 2 (2012) 873-877.

[212]. Y. Cao, L. Xiao, M. L. Sushko, W. Wang, B. Schwenzer, J. Xiao, Z. Nie, L. V. Saraf, Z. Yang, J. Liu, Nano Letters, 12 (2012) 3783-3787.

[213]. J. P. Huang, D. D. Yuan, H. Z. Zhang, Y. L. Cao, G. R. Li, H. X. Yang, X. P. Gao, RSC Advances, 3 (2013) 12593.

[214]. A. Rudola, K. Saravanan, C. W. Mason, P. Balaya, Journal of Materials Chemistry A, 1 (2013) 2653-2662.

[215]. P. Senguttuvan, G. Rousse, V. Seznec, J.-M. Tarascon, M. R. Palac ń, Chemistry of Materials, 23 (2011) 4109-4111.

[216]. W. Wang, C. Yu, Z. Lin, J. Hou, H. Zhu, S. Jiao, Nanoscale, 5 (2013) 594-599.

[217]. W. Wang, C. Yu, Y. Liu, J. Hou, H. Zhu, S. Jiao, RSC Advances, 3 (2013) 1041-1044.

[218]. A. Rudola, K. Saravanan, S. Devaraj, H. Gong, P. Balaya, Chemical Communications, 49 (2013) 7451-7453.

[219]. X. Yu, H. Pan, W. Wan, C. Ma, J. Bai, Q. Meng, S. N. Ehrlich, Y. S. Hu, X. Q. Yang, Nano Letters, 13 (2013) 4721-4727.

[220]. Y. Sun, L. Zhao, H. Pan, X. Lu, L. Gu, Y. S. Hu, H. Li, M. Armand, Y. Ikuhara, L. Chen, X. Huang, Nature Communications, 4 (2013) 1870.

[221]. Y. Wang, X. Yu, S. Xu, J. Bai, R. Xiao, Y.-S. Hu, H. Li, X. Q. Yang, L. Chen, X. Huang, Nature Communications, 4 (2013)

[222]. M. Valvo, F. Lindgren, U. Lafont, F. Björefors, K. Edström, Journal of Power Sources, 245 (2014) 967-978.

[223]. B. Koo, S. Chattopadhyay, T. Shibata, V. B. Prakapenka, C. S. Johnson, T. Rajh, E. V. Shevchenko, Chemistry of Materials, 25 (2013) 245-252.

[224]. S. Hariharan, K. Saravanan, V. Ramar, P. Balaya, Physical Chemistry Chemical Physics, 15 (2013) 2945-2953.

[225]. M. C. López, P. Lavela, G. F. Ortiz, J. L. Tirado, Electrochemistry Communications, 27 (2013) 152-155.

[226]. S. Yuan, X. L. Huang, D. L. Ma, H. G. Wang, F. Z. Meng, X. B. Zhang, Advanced Materials, 26 (2014) 2273-2279, 2284.

[227]. M. J. R. Alcántara, P. Lavela, J. L. Tirado, Chemistry of Materials, 14 (2002) 2847-2848.

[228]. D. Su, H. J. Ahn, G. Wang, Chemical Communications, 49 (2013) 3131-3133.

[229]. K. Zhang, Z. Hu, X. Liu, Z. Tao, J. Chen, Advanced Materials, 27 (2015) 3305-3309.

[230]. Z. Hu, L. Wang, K. Zhang, J. Wang, F. Cheng, Z. Tao, J. Chen, Angewandte Chemie International Edition, 126 (2014) 13008-13012.

[231]. R. B. L. David, G. Singh, ACS Nano, 8 (2014) 1759-1770.

[232]. X. Xiong, W. Luo, X. Hu, C. Chen, L. Qie, D. Hou, Y. Huang, Scientific Reports, 5 (2015) 9254.

[233]. D. Y. W. Yu, P. V. Prikhodchenko, C. W. Mason, S. K. Batabyal, J. Gun, S. Sladkevich, A. G. Medvedev, O. Lev, Nature Communications, 4 (2013)

[234]. J. S. Kim, H. J. Ahn, H. S. Ryu, D. J. Kim, G. B. Cho, K. W. Kim, T. H. Nam, J. H. Ahn, Journal of Power Sources, 178 (2008) 852-856.

[235]. Z. Hu, Z. Zhu, F. Cheng, K. Zhang, J. Wang, C. Chen, J. Chen, Energy & Environmental Science, 8 (2015) 1309-1316.

[236]. J. Park, J. S. Kim, J. W. Park, T. H. Nam, K. W. Kim, J. H. Ahn, G. Wang, H. J. Ahn, Electrochimica Acta, 92 (2013) 427-432.

[237]. R. B. L. David, G. Singh, ACS nano, 8 (2014) 1759-1770.

[238]. T. B. Kim, W. H. Jung, H. S. Ryu, K. W. Kim, J. H. Ahn, K. K. Cho, G. B. Cho, T. H. Nam, I. S. Ahn, H. J. Ahn, Journal of Alloys and Compounds, 449 (2008) 304-307.

[239]. L. Xiao, Y. Cao, J. Xiao, W. Wang, L. Kovarik, Z. Nie, J. Liu, Chemical Communications, 48 (2012) 3321-3323.

[240]. J. C. Kim, D. W. Kim, Electrochemistry Communications, 46 (2014) 124-127.

[241]. K. C. Behdokht Farbod, W. Peter Kalisvaart, Martin Kupsta, Beniamin Zahiri, Alireza Kohandehghan, Elmira Memarzadeh Lotfabad, Zhi Li, Erik J. Luber, and David Mitlin, ACS Nano, 8 (2014) 4415-4429.

[242]. J. Qian, Y. Xiong, Y. Cao, X. Ai, H. Yang, Nano Letters, 14 (2014) 1865-1869.

[243]. Y. M. N. Yabuuchi, T. Ishikawa, S. Kuze, J. Y. Son, Y. T. Cui, H. Oji, S. Komaba, ChemElectroChem, 1 (2014) 580-589.

[244]. M. K. Datta, R. Epur, P. Saha, K. Kadakia, S. K. Park, P. N. Kumta, Journal of Power Sources, 225 (2013) 316-322.

[245]. J. W. Wang, X. H. Liu, S. X. Mao, J. Y. Huang, Nano Letters, 12 (2012) 5897-5902.

[246]. H. Zhu, Z. Jia, Y. Chen, N. Weadock, J. Wan, O. Vaaland, X. Han, T. Li, L. Hu, Nano Letters, 13 (2013) 3093-3100.

[247]. A. Darwiche, C. Marino, M. T. Sougrati, B. Fraisse, L. Stievano, L. Monconduit, Journal of the American Chemical Society, 134 (2012) 20805-20811.

[248]. J. Qian, Y. Chen, L. Wu, Y. Cao, X. Ai, H. Yang, Chemical Communications, 48 (2012) 7070-7072.

[249]. M. Wang, Z. Yang, J. Wang, W. Li, L. Gu, Y. Yu, Small, 40 (2015) 5381-5387.

[250]. C. M. Park, H. J. Sohn, Advanced Materials, 19 (2007) 2465-2468.

[251]. L. Wang, X. He, J. Li, W. Sun, J. Gao, J. Guo, C. Jiang, Angewandte Chemie International Edition, 51 (2012) 9034-9037.

[252]. Y. Kim, Y. Park, A. Choi, N. S. Choi, J. Kim, J. Lee, J. H. Ryu, S. M. Oh, K. T. Lee, Advanced Materials, 25 (2013) 3045-3049.

[253]. A. Ponrouch, D. Monti, A. Boschin, B. Steen, P. Johansson, M. R. Palac ń, Journal of Material Chemistry A, 3 (2015) 22-42.

[254]. C. Weidenthaler, Nanoscale, 3 (2011) 792-810.

[255]. R. K. Khanna, D. D. Stranz, B. Donn, The Journal of Chemical Physics, 74 (1981) 2108-2115.

[256]. H. K. B. Dunn, J. M. Tarascon, Science 334 (2011) 928-935.

[257]. Z. Yang, J. Zhang, M. C. Kintner-Meyer, X. Lu, D. Choi, J. P. Lemmon, J. Liu, Chemical Reviews, 111 (2011) 3577-3613.

[258]. V. Palomares, P. Serras, I. Villaluenga, K. B. Hueso, J. Carretero-González, T. Rojo, Energy & Environmental Science, 5 (2012) 5884.

[259]. R. Berthelot, D. Carlier, C. Delmas, Nature Materials, 10 (2011) 74-80.

[260]. N. Yabuuchi, M. Kajiyama, J. Iwatate, H. Nishikawa, S. Hitomi, R. Okuyama, R. Usui, Y. Yamada, S. Komaba, Nature Materials, 11 (2012) 512-517.

[261]. R. Alcántara, J. M. Jiménez Mateos, J. L. Tirado, Journal of The Electrochemical Society, 149 (2002) A201.

[262]. P. L. R. Alcántaraz, G. F. Ortiz, J. L. Tirado, Electrochemical and Solid-State Letters, 8 (2005) A222-A225.

[263]. S. Komaba, W. Murata, T. Ishikawa, N. Yabuuchi, T. Ozeki, T. Nakayama, A. Ogata, K. Gotoh, K. Fujiwara, Advanced Functional Materials, 21 (2011) 3859-3867.

[264]. J. R. D. W. Xing, Journal of the Electrochemical Society, 144 (1997) 1195-1201.

[265]. L. Xiao, Y. Cao, J. Xiao, W. Wang, L. Kovarik, Z. Nie, J. Liu, Chemical Communications, 48 (2012) 3321-3323.

[266]. J. Qian, Y. Chen, L. Wu, Y. Cao, X. Ai, H. Yang, Chemical Communications, 48 (2012) 7070-7072.

[267]. C. Marino, L. Boulet, P. Gaveau, B. Fraisse, L. Monconduit, Journal of Materials Chemistry, 22 (2012) 22713-22720.

[268]. S. W. Lee, N. Yabuuchi, B. M. Gallant, S. Chen, B.-S. Kim, P. T. Hammond, Y. Shao-Horn, Nature Nanotechnology, 5 (2010) 531-537.

[269]. P. N. K. W. Wang, ACS Nano, 4 (2010) 2233-2241.

[270]. W. Tang, X. Gao, Y. Zhu, Y. Yue, Y. Shi, Y. Wu, K. Zhu, Journal of Materials Chemistry, 22 (2012) 20143-20145.

[271]. W. Tang, Y. Y. Hou, X. J. Wang, Y. Bai, Y. S. Zhu, H. Sun, Y. B. Yue, Y. P. Wu, K. Zhu, R. Holze, Journal of Power Sources, 197 (2012) 330-333.

[272]. Y. Wang, M. Wu, Z. Jiao, J. Y. Lee, Chemistry of Materials, 21 (2009) 3210-3215.

[273]. J. M. Zaug, A. K. Soper, S. M. Clark, Nature Materials, 7 (2008) 890-899.

[274]. W. Wang, P. N. Kumta, ACS Nano, 4 (2010) 2233-2241.

[275]. G. Chen, Z. Wang, D. Xia, Chemistry of Materials, 20 (2008) 6951-6956.

[276]. M. S. Park, S. A. Needham, G. X. Wang, Y. M. Kang, J. S. Park, S. X. Dou, H. K. Liu, Chemistry of Materials, 19 (2007) 2406-2410.

[277]. W. X. Chen, J. Y. Lee, Z. Liu, Carbon, 41 (2003) 959-966.

[278]. Y. Wang, D. Su, C. Wang, G. Wang, Electrochemistry Communications, 29 (2013) 8-11.

[279]. U. Kasavajjula, C. Wang, A. J. Appleby, Journal of Power Sources, 163 (2007) 1003-1039.

[280]. S. L. Chou, Y. Pan, J. Z. Wang, H. K. Liu, S. X. Dou, Physical Chemistry Chemical Physics, 16 (2014) 20347-20359.

[281]. S. Li, Y. Dong, L. Xu, X. Xu, L. He, L. Mai, Advanced Materials, 26 (2014) 3545-3553.

[282]. Y. Dong, S. Li, K. Zhao, C. Han, W. Chen, B. Wang, L. Wang, B. Xu, Q. Wei, L. Zhang, X. Xu, L. Mai, Energy & Environmental Science, 8 (2015) 1267-1275.

[283]. W. J. Li, S. L. Chou, J. Z. Wang, Y. M. Kang, J. L. Wang, Y. Liu, Q. F. Gu, H. K. Liu, S. X. Dou, Chemistry of Materials, 27 (2015) 1997-2003.

[284]. Z. Wang, L. Qie, L. Yuan, W. Zhang, X. Hu, Y. Huang, Carbon, 55 (2013) 328-334.

[285]. T. Chen, Y. Liu, L. Pan, T. Lu, Y. Yao, Z. Sun, D. H. C. Chua, Q. Chen, Journal of Materials Chemistry A, 2 (2014) 4117-4121.

[286]. Y. Liu, N. Zhang, L. Jiao, Z. Tao, J. Chen, Advanced Functional Materials, 25 (2015) 214-220.

[287]. M. Walter, R. Erni, M. V. Kovalenko, Scientific Reports, 5 (2015) 8418.

[288]. M. He, K. Kravchyk, M. Walter, M. V. Kovalenko, Nano Letters, 14 (2014) 1255-1262.

[289]. W. J. Li, S. L. Chou, J. Z. Wang, H. K. Liu, S. X. Dou, Nano Letters, 13 (2013) 5480-5484.

[290]. I. Y. Jeon, H. J. Choi, S. M. Jung, J. M. Seo, M. J. Kim, L. Dai, J. B. Baek, Journal of the American Chemical Society, 135 (2013) 1386-1393.

[291]. J. Sun, G. Zheng, H. W. Lee, N. Liu, H. Wang, H. Yao, W. Yang, Y. Cui, Nano Letters, 14 (2014) 4573-4580.

[292]. L. M. Malard, M. A. Pimenta, G. Dresselhaus, M. S. Dresselhaus, Physics Reports, 473 (2009) 51-87.

[293]. P. L. R. Alcántara, G. F. Ortiz, J. L. Tirado, Electrochemical and Solid-State Letters, 8 (2005) A222-A225.

[294]. S. Komaba, Y. Matsuura, T. Ishikawa, N. Yabuuchi, W. Murata, S. Kuze, Electrochemistry Communications, 21 (2012) 65-68.

[295]. S. Komaba, T. Ishikawa, N. Yabuuchi, W. Murata, A. Ito, Y. Ohsawa, ACS Applied Materials & Interfaces, 3 (2011) 4165-4168.

[296]. Y. Liu, Y. Xu, Y. Zhu, J. N. Culver, C. A. Lundgren, K. Xu, C. Wang, ACS Nano, 7 (2013) 3627-3634.

[297]. Y. U. Kim, S. I. Lee, C. K. Lee, H. J. Sohn, Journal of Power Sources, 141 (2005) 163-166.

[298]. M. Z. Xue, J. Yao, S. C. Cheng, Z. W. Fu, Journal of The Electrochemical Society, 153 (2006) A270.

[299]. J. W. Wang, X. H. Liu, S. X. Mao, J. Y. Huang, Nano Letters, 12 (2012) 5897-5902.

[300]. J. J. Wu, Z. W. Fu, Journal of The Electrochemical Society, 156 (2009) A22.

[301]. Y. X. Wang, Y. G. Lim, M. S. Park, S. L. Chou, J. H. Kim, H. K. Liu, S. X. Dou, Y. J. Kim, Journal of Materials Chemistry A, 2 (2014) 529-534.

[302]. H. He, G. Jin, H. Wang, X. Huang, Z. Chen, D. Sun, Y. Tang, Journal of Materials Chemistry A, 2 (2014) 3563-3570.

[303]. H. He, X. Zeng, H. Wang, N. Chen, D. Sun, Y. Tang, X. Huang, Y. Pan, Journal of the Electrochemical Society, 162 (2014) A39-A43.

[304]. H. Wang, Z. Wu , F. Meng , D. Ma , X. Huang , L. Wang, X. Zhang, ChemSusChem, 6 (2013) 56-60.

[305]. I. T. Kim, E. Allcorn, A. Manthiram, Energy Technology, 1 (2013) 319-326.

[306]. Y. M. Lin, P. R. Abel, A. Gupta, J. B. Goodenough, A. Heller, C. B. Mullins, ACS Applied Materials & Interfaces, 5 (2013) 8273-8277.

[307]. W. Li, S. L. Chou, J. Z. Wang, J. H. Kim, H. K. Liu, S. X. Dou, Advanced Materials, 26 (2014) 4037-4042.

[308]. Y. Kim, Y. Kim, A. Choi, S. Woo, D. Mok, N.-S. Choi, Y. S. Jung, J. H. Ryu, S. M. Oh, K. T. Lee, Advanced Materials, 26 (2014) 4139-4144.

[309]. Y. Liang, Q. Liu, A. M. Asiri, X. Sun, Y. Luo, ACS Catalysis, 4 (2014) 4065-4069.

[310]. B. Koo, H. Kim, Y. Cho, K. T. Lee, N. S. Choi, J. Cho, Angewandte Chemie International Edition, 51 (2012) 8762-8767.

[311]. S. Wang, L. Wang, Z. Zhu, Z. Hu, Q. Zhao, J. Chen, Angewandte Chemie International Edition, 53 (2014) 5892-5896.

[312]. L. Wu, X. Hu, J. Qian, F. Pei, F. Wu, R. Mao, X. Ai, H. Yang, Y. Cao, Energy & Environmental Science, 7 (2014) 323-328.

[313]. H. Li, J. Wang, Q. Chu, Z. Wang, F. Zhang, S. Wang, Journal of Power Sources, 190 (2009) 578-586.

[314]. S. Zhou, X. Liu, D. Wang, Nano Letters, 10 (2010) 860-863.

[315]. K. Dai, H. Zhao, Z. Wang, X. Song, V. Battaglia, G. Liu, Journal of Power Sources, 263 (2014) 276-279.

[316]. J. Ren, X. He, W. Pu, C. Jiang, C. Wan, Electrochimica Acta, 52 (2006) 1538-1541.

[317]. S. L. C. W. J. Li, J. Z. Wang, H. K. Liu, S. X. Dou, Chemical Communications, 51 (2015) 3682-3685.

[318]. M. C. Biesinger, B. P. Payne, A. P. Grosvenor, L. W. M. Lau, A. R. Gerson, R. S. C. Smart, Applied Surface Science, 257 (2011) 2717-2730.

[319]. B. L. Ellis, W. R. M. Makahnouk, Y. Makimura, K. Toghill, L. F. Nazar, Nature Materials, 6 (2007) 749-753.

[320]. Y. Liu, Y. Xu, X. Han, C. Pellegrinelli, Y. Zhu, H. Zhu, J. Wan, A. C. Chung, O. Vaaland, C. Wang, L. Hu, Nano Letters, 12 (2012) 5664-5668.

[321]. Z. Jian, W. Han, X. Lu, H. Yang, Y.-S. Hu, J. Zhou, Z. Zhou, J. Li, W. Chen, D. Chen, L. Chen, Advanced Energy Materials, 3 (2013) 156-160.

[322]. H. Kim, I. Park, D. H. Seo, S. Lee, S. W. Kim, W. J. Kwon, Y. U. Park, C. S. Kim, S. Jeon, K. Kang, Journal of the American Chemical Society, 134 (2012) 10369-10372.

[323]. K. Sakaushi, E. Hosono, G. Nickerl, T. Gemming, H. Zhou, S. Kaskel, J. Eckert, Nature Communications, 4 (2013) 1485.

[324]. S. H. Yu, M. Shokouhimehr, T. Hyeon, Y. E. Sung, ECS Electrochemistry Letters, 2 (2013) A39-A41.

[325]. H. Ma, S. Zhang, W. Ji, Z. Tao, J. Chen, Journal of the American Chemical Society, 130 (2008) 5361-5367.

[326]. S. L. Chou, J. Z. Wang, H. K. Liu, S. X. Dou, The Journal of Physical Chemistry C, 115 (2011) 16220-16227.

[327]. B. Zhang, Y. Liu, X. Wu, Y. Yang, Z. Chang, Z. Wen, Y. Wu, Chemical Communications, 50 (2014) 1209-1211.

[328]. Q. T. Qu, Y. Shi, S. Tian, Y. H. Chen, Y. P. Wu, R. Holze, Journal of Power Sources, 194 (2009) 1222-1225.

[329]. B. H. Toby, R. B. Von Dreele, Journal of Applied Crystallography, 46 (2013) 544-549.

[330]. E. J. M. Vertelman, T. T. A. Lummen, A. Meetsma, M. W. Bouwkamp, G. Molnar, P. H. M. van Loosdrecht, P. J. van Koningsbruggen, Chemistry of Materials, 20 (2008) 1236-1238.

[331]. L. Samain, F. Grandjean, G. J. Long, P. Martinetto, P. Bordet, D. Strivay, The Journal of Physical Chemistry C, 117 (2013) 9693-9712.

[332]. H. Liu, F. C. Strobridge, O. J. Borkiewicz, K. M. Wiaderek, K. W. Chapman, P. J. Chupas, C. P. Grey, Science, 344 (2014).

Appendix

List of publications

[1] Weijie Li, Shulei Chou, Jiazhao Wang, Huakun Liu, Shixue Dou, Simply mixed commercial red phosphorus ans carbon nanotube composite with exceptionally reversible sodium-ion storage, ***Nano Letters(IF=13.6),*** 2013,13, 5480-5484.

[2] Weijie Li, Shulei Chou, Jiazhao Wang, Jung Ho Kim, Huakun Liu, Shixue Dou, $Sn_{4+x}p_3$@ amorphous Sn-P composites as anodes for sodium-ion batteries with low cost, high capacity, long life, and superior rate capability, ***Advanced Materials(IF=17.4)***, 2014, 26,4037-4042.

[3] Wei-Jie Li, Shu-Lei Chou, Jia-Zhao Wang, Yong-Mook Kang, Jian-Li Wang, Yong Liu, Qin-Fen Gu, Hua-Kun Liu, Shi-Xue Dou, A facile method to synthesize Na-enriched $Na_{1+x}FeFe(CN)_6$ frameworks as cathode with superior electrochemical performance for sodium-ion batteries. ***Chem. Mater (IF=8.3)***. 2015, 27(6), 1997-2003.

[4] Wei-Jie Li, Shu-Lei Chou, Jia-Zhao Wang, Hua-Kun Liu and Shi-Xue Dou, A new, cheap, productive FeP anode material for sodium-ion batteries. ***Chem. Commun.(IF=6.8)***, 2015, 51, 3682-3685.

[5] Wei-Jie Li, Shu-Lei Chou, Jia-Zhao Wang, Jian-Li Wang, Qin-Fen Gu, Hua-Kun Liu and Shi-Xue Dou, Multifunctional conducing polymer coated Prussian blue-based cathode for sodium-ion batteries with superior performance via a facile and one-step chemistry approach, ***Nano Energy (IF=10.3)***, 2015, 13, 200-207.

[6] Wei-Jie Li, Shu-Lei Chou, Jia-Zhao Wang, Hua-Kun Liu, Cobalt phosphide as a new anode material for sodium storage. ***Journal of Power Sources (IF=6.2)***, 2015, 294, 627-632.

[7] Wei-Jie Li, Chao Han, Shu-Lei Chou, Jia-Zhao Wang, Zhen Li, Yong-Mook Kang, Hua-Kun Liu and Shi-Xue Dou, Graphite nanoplate coated Bi_2S_3 composite with high volume energy density and excellent cycle life for room-temperature sodium - sulfide batteries, ***Chem. Eur.J.*** (accepted)

[8] Wei-jie Li, Shu-lei Chou, Jia-zhao Wang, Hua-kun Liu and Shixue Dou, Phosphorus and graphite composite as anode with enhanced cycling performance and rate capability for sodium ion storage . ***J. Mater. Chem. A(IF=7.4)*** (accepted)

[9] Chao Han, Zhen Li, **Weijie Li,** Shulei Chou, Shixue Dou,Controlled synthesis of copper telluride nanostructures for long-cycling anodes in lithium ion batteries. ***J. Mater. Chem. A(IF=7.4)***, 2014, 2, 11683-11690**.**

[10] Shaohua Zhang, **Weijie Li**, Bien Tan, Shulei Chou, Zhen Li, and Shixue Dou, One-pot synthesis of ultra-small magnetite nanoparticles on the surface of reduced graphene oxide nanosheets as anode for sodium-ion batteries. ***J. Mater. Chem. A(IF=7.4)***, 2015, 3, 4793-4798.

[11] Qiuran Yang, **Weijie Li**, Shulei Chou, Jiazhao Wang, and Huakun Liu, Ball-milled FeP/graphite as a low-cost anode material for the sodium-ion battery. ***RCS Adv***. 2015, 5, 80536-80541.

[12] Jinyan Xiong, Chao Han, **Weijie Li**, Qiao Sun, Jun Chen, Shulei Chou, Zhen Li, Shixue Dou, Ambient Synthesis of a Multifunctional 1D/2D Hierarchical Ag-Ag_2S Nanowire/Nanosheet Heterostructure with Diverse Applications. ***CrystEngComm (IF=4.03)*** (accepted)

Received Awards:

[1] International Postgraduate Tuition Award (IPTA), 2011-2014, University of Wollongong;

[2] Chinese Government Scholarship, 2011-2014, China Scholarship Council;

[3] Excellent Research Top-Up Award, 2014, University of Wollongong;

[4] 2013 postgraduate student best paper award, 2014, University of Wollongong;

[5] 2015 Innovation works – Highly commended Award, 2015, University of Wollongong.